An investigation into Eoarchean geodynamics via multiple sulfur isotopes

Jonathan Aaron Lewis

Dissertation

zur Erlangung des Grades eines

Doktors der Naturwissenschaften

(doctor rerum naturalium)

am Fachbereich Geowissenschaften

der Freien Universität Berlin

November 2023 – Berlin, Germany

Erstgutachter: Prof. Dr. Esther M. Schwarzenbach, Universität Freiburg, Freiburg (Schweiz)
Zweitgutachter: Priv.-Doz. Dr. J. Elis Hoffmann, Freie Universität Berlin, Berlin
Drittgutachter: Prof. Dr. Harry Becker, Freie Universität Berlin, Berlin

Tag der Disputation: 15.02.2024

Erklärung

Hiermit erkläre ich, Jonathan A. Lewis, dass diese Arbeit ausschließlich auf Grundlage der angegebenen Hilfsmittel und Hilfen selbstständig von mir verfasst wurde. Diese Arbeit ist nicht in einem früheren Promotionsverfahren eingereicht worden.

Berlin, den 28. November 2023

Jonathan A. Lewis

Abstract

The geodynamic processes that gave rise to the first cratons on Earth remain controversial. Whether the first preserved cratons formed through horizontal tectonic processes similar to those operating on Earth today or in a stagnant lid regime dominated by vertical stacking and reworking of crustal material continues to be debated. Central to the question of Eoarchean geodynamics is whether and to what extent material from Earth's surface was recycled into the magmatic system and mantle. Horizontal tectonic processes similar to those active today would be expected to rework material including sulfur from the Earth's surface into igneous rocks and the mantle. In contrast, significant reworking of sulfur from the crust into the mantle under proposed vertical tectonic regimes is not expected.

Multiple sulfur isotopes provide a valuable window into early Earth processes. They can preserve a record of mass independent fractionation (MIF-S) that took place as a result of photolytic processes in the atmosphere prior to the Great Oxidation Event (GOE). This MIF-S was preserved in sediment and hydrothermal deposits that incorporated sulfur species fractionated in the atmosphere. Large MIF-S signatures are a unique feature of surface deposits formed prior to the GOE, and these signatures are robust enough to survive reworking into the magmatic system. The occurrence of MIF-S in igneous lithologies is therefore an indication that the rocks include material recycled from Earth's surface in the Archean or before. In this dissertation, the results of multiple sulfur isotope analyses of igneous lithologies from the Eoarchean Itsaq Gneiss Complex (IGC) in southern West Greenland are reported, alongside petrographic observations and additional supporting analyses of the same.

Investigated lithologies include tonalite-trondhjemite-granodiorites (TTGs), amphibolites, and peridotites from the IGC. The TTGs were subject to bulk multiple sulfur isotope and petrographic analysis. The majority of measured TTGs were found to contain MIF-S (positive $\Delta^{33}S$ values up to +0.30‰), indicating incorporation of surface-derived sulfur dominated by sedimentary material. Elevated $\Delta^{36}S$ up to +0.80‰ and $\delta^{34}S$ up to +3.36‰ in IGC TTG samples point to additional incorporation of seawater sulfate. The surface-derived material is interpreted to have been incorporated into the TTGs in the context of modern-like arc accretion. Two IGC amphibolites with tholeiite-like compositions were concurrently analyzed for multiple sulfur isotopes. One of the two amphibolites was found to contain positive bulk $\Delta^{33}S$ (+0.14‰), similar to other IGC amphibolites reported in the literature.

These tholeiite-like amphibolites are interpreted to represent the source rocks of the TTGs and to have incorporated sediment-dominated sulfur during subduction in the Eoarchean.

Peridotites found in ultramafic enclaves in the IGC were also investigated. These rocks have been well characterized by previous investigations and have been interpreted to represent the oldest remnants of obducted mantle. A mantle origin for these peridotites remains controversial, however, with some researchers arguing that they are ultramafic cumulates. The peridotites were found to contain positive bulk $\Delta^{33}S$ values between +0.04‰ and +0.21‰, indicating that they incorporated sulfur dominated by sedimentary material. Trends emerge when plotting the $\Delta^{33}S$ and $\delta^{34}S$ values of the peridotites against trace and major element concentration data on these rocks from the literature, as well as Hf isotope data published in previous studies. The trends indicate that the peridotites incorporated sediment derived sulfur early in their history, prior to variable melt overprinting that delivered additional sulfur of seawater sulfate origin. The complex history of multiple overprinting events in the Eoarchean is interpreted to have taken place in a mantle wedge. The presence of MIF-S in peridotites originating in the mantle is a significant line of evidence in support of Eoarchean subduction.

Additional in-situ sulfur and lead isotope analysis of sulfides in the studied peridotites was conducted by secondary ion mass spectrometry (SIMS), in conjunction with electron microscopy and electron microprobe analysis. The sulfides were predominantly pentlandite and pyrrhotite, typical mantle minerals, and their $\Delta^{33}S$ values were consistent with bulk analyses. Amphibole crosscutting the sulfides demonstrates that the sulfides predate amphibolite facies metamorphism the peridotites experienced in the Neoarchean. Highly unradiogenic lead isotope results are consistent with Eoarchean origins followed by partial reequilibration during metamorphism. Because lead is a trace component of the sulfides and sulfur is a major component, this reequilibration is not expected to have influenced $\Delta^{33}S$ values.

The presence of MIF-S in a majority of studied samples and in representatives of all studied rock types points strongly in the direction of widespread Eoarchean crustal recycling in the IGC. This is consistent with interpretations of Eoarchean geodynamics that include horizontal processes in which plates override one another.

Kurzfassung

Die geodynamischen Prozesse, die zur Entstehung der ersten kontinentalen Kruste auf der Erde führten, sind nach wie vor umstritten. Es wird debattiert, ob die ältesten noch erhaltenen Kratone durch horizontale plattentektonische Prozesse, wie sie heute auf der Erde ablaufen, oder durch vertikale Prozesse entstanden. Bei den letztgenannten Prozessen wird die Kruste durch vulkanische Prozesse vertikal verdickt und gestapelt. Die Frage, ob und in welchem Ausmaß Material von der Erdoberfläche in den Erdmantel recycelt wurde, ist von zentraler Bedeutung für die Geodynamik des Eoarchaikums. Bei horizontalen tektonischen Prozesse würde Material (einschließlich Schwefel) von der Erdoberfläche über Subduktionszonen in den Erdmantel transportiert und Gesteine, die aus dem Mantel schmelzen, würden dieses inkorporieren Dagegen ist eine signifikante Umverteilung von Schwefel aus der Kruste in den Erdmantel in einem vertikalen tektonischem Regime nicht zu erwarten.

Multiple Schwefelisotope bieten einen wertvollen Einblick in frühe Erdprozesse, da sie eine massenunabhängige Fraktionierung (MIF-S) anzeigen, die als Ergebnis photolytischer Prozesse in der Atmosphäre vor dem Great Oxidation Event (GOE) entstanden. Diese MIF-S Signaturen sind in Sedimenten und hydrothermalen Ablagerungen erhalten, die in der Atmosphäre fraktionierte Schwefelspezies in Mineralen einbauten. Deutliche MIF-S-Signale sind ein einzigartiges Merkmal von Oberflächenablagerungen, die vor dem GOE entstanden sind, und diese Signale sind robust genug, um nicht durch Umverteilung im magmatischen System modifiziert zu werden. Das Auftreten von MIF-S in magmatischen Lithologien ist daher ein Hinweis darauf, dass die Gesteine recyceltes Material enthalten, welches sich während des Archaikums oder davor, an der Erdoberfläche befunden hat. In dieser Dissertation werden die Ergebnisse mehrerer Schwefelisotopenanalysen von magmatischen Lithologien aus dem eoarchaischen Itsaq-Gneis-Komplex (IGC) im südlichen Westgrönland präsentiert. zusammen mit petrographischen Beobachtungen und zusätzlichen Analysen derselben. Zu den untersuchten Lithologien gehören Tonalit-Trondhjemit-Granodiorite (TTGs), Amphibolite und Peridotite aus dem IGC. Die TTGs wurden einer multiplen Schwefelisotopen- sowie einer petrographischen Analyse unterzogen. Die Mehrheit der gemessenen TTGs enthielt MIF-S Signale (positive Δ^{33}S-Werte von bis zu +0,30‰). Dies weist auf den Einbau von Schwefel hin, der von sedimentärem Material stammt. Erhöhte Δ^{36}S-Werte von bis zu +0,80‰ und δ^{34}S von bis zu +3,36‰ in den TTG-Proben des IGC deuten auf zusätzlichen Einbau von Meerwassersulfat hin. Es wird davon ausgegangen, dass

das von der Oberfläche stammende Material durch Prozesse, ähnlich wie sie in modernen Inselbögen stattfinden, in die TTGs eingebaut wurde. An zwei Amphiboliten des IGC mit tholeiit-ähnlicher Zusammensetzung wurden gleichzeitig mehrere Schwefelisotope analysiert. Einer der beiden Amphibolite enthielt ein positives $\Delta^{33}S$ (+0,14‰) Signal, vergleichbar mit anderen in der Literatur beschriebenen Amphiboliten des IGC. Es ist anzunehmen, dass diese tholeiit-ähnlichen Amphibolite das Ausgangsgestein der TTGs darstellen und während der Subduktion im Eoarchikum hauptsächlich sedimentären Schwefel aufgenommen haben.

Peridotite, die in ultramafischen Enklaven im IGC gefunden wurden, wurden ebenfalls untersucht. Diese Gesteine wurden in der Vergangenheit bereits ausführlich beschrieben und als das älteste obduzierte Mantelmaterial der Erde interpretiert. Dies ist jedoch nach wie vor umstritten, wobei einige Forscher die Ansicht vertreten, dass es sich um ultramafische Kumulate handelt. Die untersuchten Peridotite weisen positive $\Delta^{33}S$-Werte zwischen +0,04‰ und +0,21‰ auf, was darauf hindeutet, dass diese in erster Linie sedimentären Schwefel enthalten. Beim Vergleich der $\Delta^{33}S$- und $\delta^{34}S$-Werte der Peridotite mit den Spuren- und Hauptelementen dieser Gesteine aus der Literatur und mit denen, in früheren Studien veröffentlichten Hf-Isotopendaten zeichnen sich Trends ab. Diese Trends deuten darauf hin, dass die Peridotite schon früh in ihrer Geschichte Schwefel aus Sedimenten aufgenommen haben, noch bevor es zur Überprägung kam. Hierbei wurde zusätzlicher Schwefel aus Meerwassersulfaten aufgenommen. Das Vorhandensein von MIF-S Signaturen in Peridotiten, die aus dem Erdmantel stammen, ist ein wichtiger Hinweis auf Subduktionsprozesse im Eoarchaikum.

Zudem wurden in-situ Schwefel- und Blei-Isotopenanalysen der Sulfide in den untersuchten Peridotiten mittels Sekundärionen-Massenspektrometrie (SIMS) in Verbindung mit Elektronenmikroskopie und Elektronenmikrosondenanalyse durchgeführt. Bei den Sulfiden handelte es sich überwiegend um Pentlandit und Pyrrhotin, typische Mantelsulfide deren $\Delta^{33}S$-Werte mit den Gesamtgesteinsanalysen übereinstimmen. Amphibole, die während der Metamorphose im Neoarchaikum gebildet wurden durchschlagen die Sulfide und zeigen, dass die Sulfide vor der Metamorphose gebildet wurden. Blei-Isotopenanalysen zeigen stark unradiogene Werte. Dies deutet auf einen Ursprung im Eoarchaikum hin, gefolgt von einer teilweisen Reequilibrierung während der neoarcheaischen Metamorphose. Da Blei nur in Spuren in Sulfiden vorkommt, während Schwefel ein Hauptbestanteil ist, dürfte diese Reequilibrierung die $\Delta^{33}S$-Werte nicht beeinflusst haben.

Das Vorhandensein von MIF-S in der Mehrzahl der untersuchten Proben und in allen untersuchten Gesteinsarten deutet stark auf ein weit verbreitetes eoarchaisches Krustenrecycling im IGC hin. Dies steht im Einklang mit Interpretationen der eoarchaischen Geodynamik, die horizontale Prozesse favorisiert, bei denen sich die Platten gegenseitig überlagern und krustenmaterial in den Mantel recycelt wird.

Acknowledgements

First, I would like to thank Elis Hoffmann for his mentorship and infinite patience over the past years. Without our near-daily conversations about the content of this dissertation among many other things this work would not have been possible.

Thanks also to Esther Schwarzenbach, without whose insistence that I keep some semblance of a timetable and actually finish papers, I might still be working on the first chapter of this document.

Thanks to Harald Strauss for welcoming me into his lab in Muenster and providing much needed insights about multiple sulfur analysis. Additional thanks to Martin Whitehouse and Heejin Jeon for doing the same in Stockholm and for their help with the fourth chapter of this manuscript. I would also like to acknowledge once again the contributions of my other coauthors in following chapters, Moritz Liesegang, Minik Rosing, Chunhui Li, Carsten Münker, Julia van de Löcht, and Alex Schwarz. Thanks also to Dirk Scherler, Anne Bernhardt, Friedhelm von Blanckenburg, Uwe Weichert, and Harry Becker (also for his leadership of the Geochemistry group here at FU Berlin) for agreeing to join Elis, Esther, and Harald on my committee and review this dissertation. Thanks once again to those also acknowledged in following chapters for their contributions, Andreas Lutter, Yogita Kadlag, Frédéric Moynier, Michael Antonelli, Sonja Aulbach, Pedro Waterton, Julia van de Löcht, Hans Vrijmoed, Konstantin Huber, and Daniel Dunkley. Thanks also to the anonymous peer reviewers whose valuable feedback improved the second and third chapters. Thanks to Austin Jarl Boyd and Kristoffer Szilas for providing additional samples that were analyzed over the course of this research with results reported in the fifth chapter of this manuscript.

Thanks to the German Science Foundation (DFG) and its SPP 1833 ‘Building a Habitable Earth’ priority program for funding this research and making my dissertation possible. Thanks to Daniela Hülle and all other organizers of the SPP 1833 program for putting together many great meetings and unforgettable field workshops in India and Greenland. Additional thanks to the National Natural Science Foundation of China for supporting the acquisition of sulfur concentration data reported in the third chapter and to the Danish National Research Fund for grants to Nord CEE.

Thanks to Michaela Schreiber, Pietro Potenza, and Elfrun Lehmann for much needed administrative support.

Thanks to Linus Streicher, who generously offered me a place to stay while finding an apartment after moving to Berlin. Thanks to my first officemates, Julia Schmidt and Sara Vulpius, who made me feel welcome and helped me with many aspects of adjusting to life in a totally new city and country. Additional thanks to Julia and Sara, as well as Guillame Florin and Max Thiemens for their help proofreading parts of this document. Any errors that remain are my own. Thanks also to Julia, Sara, Guillame, and Max, as well as Alex Rodler-Rørbo, Anselm Loges, Aurélie Gérard, Lingzhi Hu, Marina Vergotti, Phillip Kingsbery, Josephine Moore, Hans Vrijmoed, Shilei Qiao, Xin Zhong, and Zoe Kaehne for listening to rehearsals of my defense and for their valuable feedback contributing to the final, successful version. Other friends and colleagues who made my time as a doctoral student better include (but are not limited to): Alex Balduin, Carina Gerritzen, Dennis Vanderleik, Evan DeMers, Jian Kuang (thanks also for the great figure reproduced in the Conclusions section), Lisa Schmidt, Maja Bunke, Milena Waag, Patrick Gans, Thomas Ferrand, Tim Roth, and Dan Fionte (even from overseas).

Thanks to Mang Lin for the invitation to present my research at his institute, providing a needed confidence boost to finish this dissertation and the opportunity to put together an early version of my defense talk, an important exercise not just for my final defense but for conceptualizing the first and final chapters of this document.

I would like to thank Haruna Grema for a valuable discussion contributing to the Outlook section about methods of finding evidence for barite replacement in altered lithologies.

Thanks to Kathrin Schneider for her example of what a successful dissertation from this department looks like, an invaluable resource in the preparation of this document.

Thanks to Brad Hubeny and Jen Smith for their mentorship as I pursued my previous degrees in earth science, and for their encouragement and support in my pursuing this one.

Special thanks to Max Thiemens for providing an example of moving to Germany to do a Ph.D., a possibility whose reality I might not otherwise have imagined, and for convincing me to do the same, as well as for help connecting to this particular opportunity.

Thanks to my parents, Larry and Karen Lewis, for their example of pursuing doctoral education, and for their help getting me to where I am in life now, including with the logistics of moving overseas. Thanks also to Gill Sigmon for helping Ashely and I with our move.

Finally and most importantly, I thank my wife, Ashley Sigmon, for agreeing to move to Berlin with me (for threatening to be angry at me if I turned this opportunity down in fact) and her constant support as I wrote this dissertation.

Table of Contents

List of Figures

List of Tables

Microsoft office compatible versions of the tables are also available in the CD included with the print version of this dissertation.

Chapter 1

1.1. Introduction

The geodynamic processes shaping the early Earth's crust in the Archean and before (>2.5 Ga) remain mysterious and the subject of continuing debate (e.g., Hastie et al., 2023; Hawkesworth et al., 2020; Johnson et al., 2017; Kuang et al., 2023; Nutman, 2023; Webb et al., 2020). The timing of the onset of modern plate tectonics has not been definitively established, with estimates ranging from the early Hadean to the Neoproterozoic (e.g., Hawkesworth et al., 2020; Kuang et al., 2023 and citations therein). An important challenge facing researchers attempting to unravel the early history of our planet is the scarcity of geological material dating from the Earth's most distant past, with rocks of Paleoarchean and older age (>3.2 Ga) cropping out only in a few tens of localities worldwide (Figure 1.1). Rocks of Eoarchean age and older (>3.6 Ga) are still rarer, representing well under 1% of the existing crust (Löcht, 2019; Nutman et al., 1996). Much of what we know about the history of the early Earth has been gleaned from intensive study of these unusual, ancient lithologies (e.g., Van Kranendonk et al., 2019a).

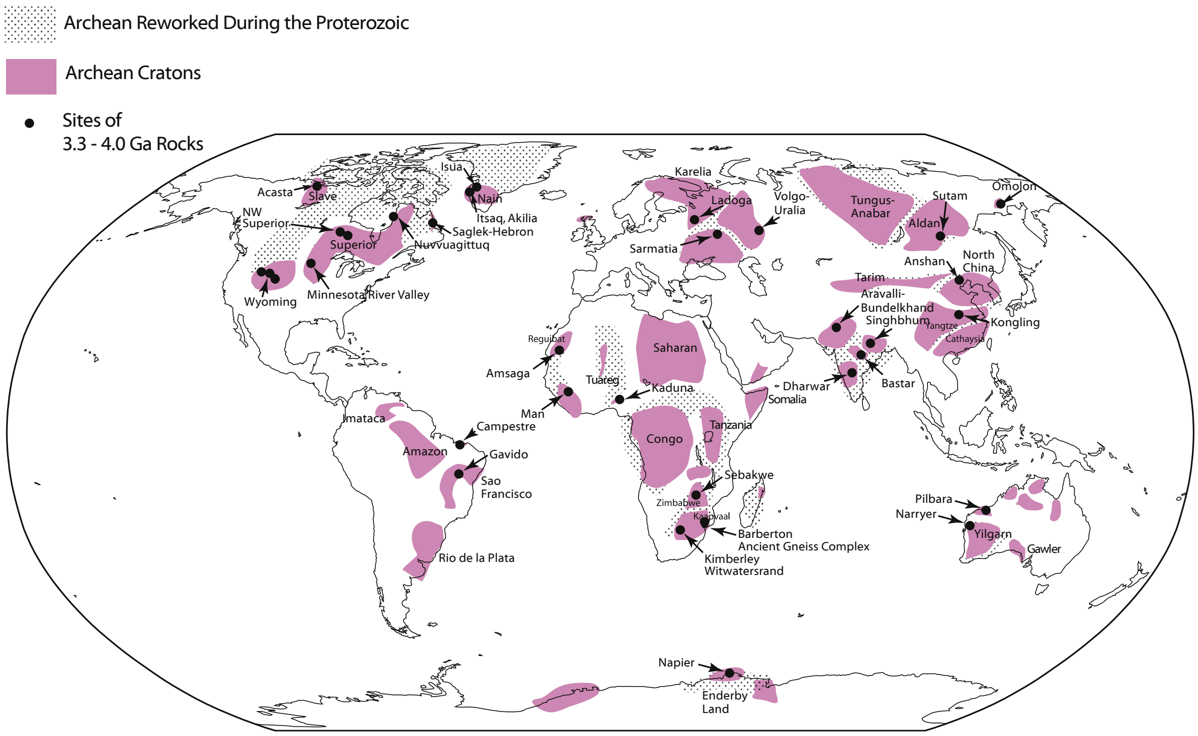

Figure 1.1: Global distribution of Archean cratons and rocks of Paleoarchean age and older (>3.2Ga), reprinted from Condie (2019).

The information available to us concerning the Earth's first half billion years (the Hadean) is limited by the paucity of preserved rocks from this time, but ongoing research has provided a few clues. Following the moon forming impact (e.g., Hartmann and Davis, 1975; Wiechert et al., 2001), which took place ca. 50 million years after the formation of the Solar System (Thiemens et al., 2019), the Earth began to cool, and a solid protocrust formed above the magma ocean that was generated by this violent collision (e.g., Kamber, 2007). The Earth's earliest protocrust has not been preserved, but indirect isotopic evidence for this protocrust's formation within the first 60 million years of the solar system's existence has recently been identified in Archean rocks from the Kapvaal Craton in southern Africa (Tusch et al., 2022). Isotopic evidence for mantle domains likely depleted in the Hadean as a result of melt extraction that formed Earth's first crust has also been identified in mafic and ultramafic lithologies from the Itsaq Gneiss Complex of southern West Greenland (Hoffmann et al., 2010; van de Löcht et al., 2020). The oldest minerals on Earth that have been preserved to this day, detrital zircons of up to 4.4 Ga (Wilde et al., 2001), were found in 3.3 Ga metasediments in the Jack Hills and Mt. Narryer, within the Yilgarn Craton of Western Australia (e.g., Amelin et al., 1999; Cavosie et al., 2019; Froude et al., 1983; Harrison et al., 2005; Valley et al., 2014; Wilde et al., 2001). These detrital grains provide evidence that a crust had already begun to form and differentiate by the early Hadean. While the majority of Hadean zircons come from Yilgarn (Whitehouse et al., 2017), younger Hadean zircon grains have been found outside of this craton in other contexts, such as xenocrysts in igneous lithologies (e.g., Chaudhuri et al., 2018; Cui et al., 2013; Nadeau et al., 2013; Wan et al., 2023). The available Hadean zircon record remains extremely limited. As of 2019, all of the terrestrial Hadean zircons yet identified amount to less than a gram of material (Nutman and Bennett, 2019). The mechanisms by which the Earth's earliest crust formed and differentiated in the Hadean remain controversial, as what limited information the zircon record offers us about Hadean geodynamics is ambiguous (e.g., Whitehouse et al., 2017).

The geological record improves around the time of the Hadean-Archean transition at 4 Ga. The oldest unambiguously dated whole rocks on Earth come from parts of the Acasta Gneiss Complex in the Northwest Territories of Canada, representing the very end of the Hadean at 4.03-4.00 Ga (Bowring and Williams, 1999; Stern and Bleeker, 1998). Based on the Nd isotope systematics of mafic lithologies, it has been suggested that the Nuvvuagittuq Greenstone Belt in Canada hosts even older rocks, at 4.3 Ga (O'Neil et al., 2008; O'Neil et al., 2012). However, this interpretation remains controversial, and the oldest unambiguously dated zircons from the heavily metamorphosed Nuvvuagittuq Greenstone Belt are of

Eoarchean age (Cates et al., 2013; O'Neil et al., 2019). The Eoarchean (4.0-3.6 Ga) rock record is far more extensive than what little remains from Hadean time, though it still represents a vanishingly small fraction of Earth's surface (Nutman et al., 1996). While the Eoarchean rock record is more extensive than the Hadean one, offering the possibility that Eoarchean geodynamic processes might be better understood, geodynamic interpretations of the Eoarchean rock record vary dramatically and continue to be vigorously debated (e.g., Antonelli et al., 2021; Drabon et al., 2022; Garde et al., 2020; Hastie et al., 2023; Johnson et al., 2017; Nutman, 2023; Nutman et al., 2021; Webb et al., 2020; Windley et al., 2021). The Eoarchean represents a crucial period in the development of our planet, as it was during this era that the cores of the oldest existing cratons formed (e.g., Hoffmann et al., 2019). This era was therefore a time of critical processes that made our planet recognizable to us today, and habitable for terrestrial life forms such as ourselves, whose existence depends on large, emergent landmasses.

While the role of continental crust in supporting the modern biosphere is evident, cratons also played important roles in the early development of life. The precise timing of life's first emergence continues to be debated. ^{13}C depleted carbon has been identified in metasediments found within the 3.95 Ga Uivak Gneiss in Saglek Block, northern Labrador, and attributed to biological processes (Tashiro et al., 2017). Similar carbon isotope evidence strongly suggestive of biological activity is found in 3.7 Ga metasediments in the Itsaq Gneiss Complex of southern West Greenland (Rosing, 1999). Stromatolites have also been reported in the latter locality (e.g., Nutman et al., 2016). Structures that some researchers have described as microfossils have also been found in the 3.77 Ga (and possibly older; see O'Neil et al. (2019) and citations therein) Nuvvuagittuq Greenstone Belt (Dodd et al., 2017). The earliest microfossils including unambiguously biogenic structures date from the Paleoarchean 3.5 Ga Dresser Formation (e.g., Baumgartner et al., 2019) and the 3.4 Ga Strelley Pool Formation (e.g., Sugitani et al., 2015; Wacey et al., 2011) in Australia's East Pilbara Craton. Genomic studies, however, point to an origin of life before any of the aforementioned times, in the Hadean (e.g, Betts et al., 2018). The available evidence strongly suggests that life first emerged in the Eoarchean or before, concurrent with (or possibly predating) the first nucleation of the cratons. It has been argued that the emergence of land from the world ocean may have been required for life to have begun, as the emergence of life may have required concentrations of compounds that were only possible in small ponds, isolated from the world ocean on emergent land (e.g., Damer, 2016; Darwin, 1871; Ranjan et al., 2019). Uncertainties surround the volume of the early Earth's ocean, which was likely greater than that of the ocean today (e.g., Kasting, 2019; Korenaga, 2021). As a result, it is possible that only a few ocean islands were subaerially exposed in the Eoarchean, and that only by the end of the Archean did extensive continental landmasses emerge from the ocean (e.g., Korenaga, 2021). Therefore, given what we know about the timing of the earliest life on Earth, continental freeboard did not necessarily play a direct role in life's first emergence. However, shallow water environments such as those provided by early cratons were important habitats for marine ecosystems in the Archean such as the 3.43 Ga stromatolite reef found in the Pilbara Craton of Australia (e.g., Allwood et al., 2007; Lowe, 1983). Furthermore, even after the evolution of photosynthetic cyanobacteria, the reducing nature of the first mafic crust that was exposed on Earth may have prevented the oxygenation of the ocean and atmosphere necessary for the evolution of aerobic life (Hoffmann, 2017; Smit and Mezger, 2017). The subaerial exposure of extensive areas of evolved rock characteristic of continental crust may have been required for the oxygenation of the atmosphere ca. 2.4-2.3 Ga (Hoffmann, 2017; Smit and Mezger, 2017). Crucial to the extensive emergence of subaerially exposed, evolved rock was the formation of thick continental crust, and crucial to the formation of continental crust was a geodynamic regime capable of generating that crust. The work presented in this thesis is an attempt to shed light on the nature of this geodynamic regime.

1.2. Eoarchean geodynamics

The primary mechanism shaping the surface of the Earth today is modern plate tectonics. Under this geodynamic regime, the planet is dominated by an interlocking set of rigid, mobile tectonic plates, including relatively short-lived oceanic crust formed along mid-ocean ridges and subducted beneath other plates, and essentially permanent continental crust dominated by intermediate to felsic rock (e.g., Dietz and Holden, 1970). On the modern Earth, this process contributes to the continued formation of evolved melts and continental crust at subduction zones, and it is the dominant mechanism of continental crust formation (e.g., Hawkesworth et al., 2019). It has been suggested that plate tectonics of some kind began as early as the Hadean (e.g., Miyazaki and Korenaga, 2022; Rosas and Korenaga, 2018), potentially initiated by the numerous bolide impacts that the Earth experienced at this time (e.g., Maruyama et al., 2018). This type of early tectonism may have been episodic in nature, including brief periods of active subduction followed by longer stretches of stagnant lid tectonics characterized by processes such as heat-pipe volcanism building the crust vertically (e.g., Kuang et al., 2023; O'Neill and Debaille, 2014; O'Neill and Zhang, 2019; van Hunen and Moyen, 2012). Several lines of evidence point to the onset of tectonic processes similar to those operating today, including the horizontal movement of plates relative to one another and subduction, by at least the Eoarchean (e.g., Antonelli et al., 2021; Drabon et al., 2022; Garde et al., 2020; Hastie et al., 2016; Hastie et al., 2023; Nutman, 2023; Nutman et al., 2020; Nutman et al., 2021; Windley et al., 2021). These include field relations of Eoarchean supracrustal rocks juxtaposed in ways strongly suggestive of modern-like tectonic processes (e.g., Nutman and Bennett, 2019; Nutman et al., 1996), evidence for high pressure, low temperature metamorphism in some Eoarchean lithologies (e.g., Nutman et al., 2020), as well as stable isotope and other geochemical data from Eoarchean minerals and rocks such as zircons (e.g., Drabon et al., 2022; Ge et al., 2023) and granitoids (e.g., Antonelli et al., 2021) suggesting an Eoarchean onset of mobile-lid or horizontal tectonics. Experiments melting basalts under temperature and pressure conditions consistent with subduction settings produce melts with compositions consistent with Eoarchean granitoids (e.g., Hastie et al., 2016; Hastie et al., 2023). This points further to a modern-like, horizontal tectonic mechanism forming the Earth's first cratons.

However, models of Eoarchean modern-like tectonics have been challenged by researchers arguing that other processes were responsible for the nucleation of Earth's first cratons. Some researchers have suggested that the Eoarchean Earth was driven by heat pipe tectonics vertically building the crust in a similar manner to what is observed on Jupiter's moon Io (e.g., Moore and Webb, 2013). Others suggest that the first cratons formed through vertical thickening and reworking of mafic crust without subduction in settings similar to oceanic plateaus (e.g., Johnson et al., 2017). Like some models of modern-like but episodic subduction, some non-uniformitarian models of Eoarchean geodynamics include the potential for bolides to play a role in craton formation (e.g., Johnson et al., 2022). Furthermore, non-uniformitarian explanations involving vertical tectonism have been proposed for field relations of Eoarchean rocks that suggest horizontal tectonic juxtaposition (e.g., Webb et al., 2020). It has even been argued, based on the absence of bluseschists (formed at high pressure and low temperature) older than ca. 800 Ma in the geologic record, that modern plate tectonics began as late as the Neoproterozoic (e.g., Stern, 2005). Additionally, a few models have attempted to split the difference between subduction and non-subduction in the Eoarchean, invoking processes such as drip tectonics and sagduction that allow for limited recycling of crustal material into the mantle but, lacking rigid plates interacting with one another as they do in modern convergent plate boundaries, would not allow for the formation of ophiolites (e.g., Nebel et al., 2018).

It is worth noting that evidence for vertical tectonic processes, including vertical stacking of volcanic rocks followed by internal crustal reworking, is clearly preserved in the dome and keel structures found in Paleoarchean terranes such as the East Pilbara in Australia (e.g., Van Kranendonk et al., 2019b) and Neoarchean terranes such as those in the North China Craton (e.g., Liu et al., 2023). This shows that vertical tectonism persisted at least to some extent after Eoarchean time. The persistence of vertical tectonic processes into the Paleoarchean and beyond does not mean there was no subduction prior to this time. Furthermore, dome and keel structures are not obviously present in all Archean terrains. The Eoarchean Itsaq Gneiss Complex (IGC) of southern West Greenland is an excellent example of a terrain showing structural evidence of processes at work in the Eoarchean that are not the same as those that formed dome and keel structures found elsewhere (e.g., Nutman et al., 1996).

The geodynamic processes active in the Eoarchean remain controversial. The timing of the onset of horizontal tectonics and subduction, as well as the extent to which nonuniformitarian processes played a role in forming the Earth's first cratons, continue to be debated. The work presented in this dissertation aims to offer fresh insights into the geodynamic processes active on the Eoarchean Earth.

1.3. The Itsaq Gneiss Complex

Arguably the most extensive, best exposed, and best-preserved example of Eoarchean crust is found in the Itsaq Gneiss Complex in southern West Greenland, which is part of the North Atlantic Craton (e.g., Garde et al., 2020; Nutman and Bennett, 2019; Nutman et al., 1996). The IGC consists primarily of tonalite-trondjemite-granodiorites (TTGs), and also contains numerous other Eoarchean lithologies (Nutman and Bennett, 2019). The IGC includes two Eoarchean terranes, the Isukasia Terrane in the northeast and the Færingehavn Terrane in the southwest (e.g, Nutman and Bennett, 2019). In addition to the TTGs of Eoarchean age, the IGC has been intruded by various swarms of basic dykes as well as pegmatites and granites until ca. 1.6 Ga (e.g., Nutman et al., 1984; Nutman and Bennett, 2019; Nutman et al., 1996). The northern part of the IGC has been subject to remarkably little metamorphism among rocks of Eoarchean age, having locally experienced only amphibolite facies metamorphism, which took place in the Neoarchean ca. 2.6-2.7 Ga (Eskesen et al., 2023; Nutman and Bennett, 2019). Granulite facies conditions were reached elsewhere in the IGC at this time (Eskesen et al., 2023; Nutman and Friend, 2007). The IGC was tectonically juxtaposed with younger terranes of Mesoarchean age in the Neoarchean as well (Nutman et al., 1996).

Notably, the northern part of the IGC includes the 3.7-3.8 Ga Isua Crustal Belt (ISB), the oldest supracrustal belt in the world (Garde et al., 2020). The low degree of deformation and metamorphism experienced by lithologies in the northern part of the IGC, including the ISB and surrounding area, make them unique among rocks of Eoarchean age (Nutman and Bennett, 2019). Crosscutting 3.5 Ga dykes show that while the ISB underwent deformation in the Eoarchean, it has experienced little strain since this time, including during Neoarchean metamorphism (e.g., Nutman and Bennett, 2019). The ISB contains a more diverse and extensive inventory of supracrustal rocks than anywhere else on Earth and notably includes low-strain domains in which the primary structures and textures of supracrustal lithologies are preserved (e.g., Nutman and Bennett, 2019). These supracrustal rocks include pillow basalts with visually discernable and geochemically distinct rims and cores (e.g., Nutman et al., 1984; Polat et al., 2003), metabasalts with geochemical characteristics similar to those found in modern island arcs (e.g., Nutman and Friend, 2009; Polat et al., 2002), and metasediments such as banded iron formations (e.g., Baublys et al., 2004; Mojzsis et al., 2003; Nutman et al., 1984; Nutman and Friend, 2009; Nutman et al., 1996; Papineau and Mojzsis, 2006; Whitehouse, 2013; Whitehouse et al., 2005) and metapelites (e.g., Mojzsis et al., 2003; Nutman and Friend, 2009; Nutman et al., 1996; Papineau and Mojzsis, 2006). Another notable feature of the ISB is the juxtaposition of its two constituent terranes, a 3.8 Ga southern terrane and a 3.7 Ga northern terrane (Nutman and Friend, 2009). These terranes were juxtaposed in the Eoarchean between 3.7 Ga, the age of the youngest sedimentary deposits, and 3.66 Ga, the age of the oldest intrusions crosscutting both terranes (Crowley, 2003; Nutman and Friend, 2009). This juxtaposition points in the direction of modern-like, horizontal tectonic processes (Nutman and Friend, 2009), though this interpretation has been challenged by researchers who argue that non-uniformitarian, vertical tectonic processes can explain the observed field relationships in the ISB (Webb et al., 2020). An additional compelling line of evidence for early crustal recycling in the ISB, potentially including subduction, has been found in the form of mass independently fractionated sulfur in metabasalts found within the ISB, indicating that these igneous rocks incorporated sulfur recycled from Earth's surface during their petrogenesis (Siedenberg et al., 2016).

Another remarkable feature of the IGC is the local preservation of original magmatic (non-gneissic) textures in igneous rocks, including TTGs (e.g., Hoffmann et al., 2014;

Nutman and Bennett, 2019; Nutman et al., 1996). The occurrence of these TTGs is particularly significant because they represent the most pristine known examples of the most common lithology in Eoarchean cratons worldwide (Hoffmann et al., 2014; Nutman and Bennett, 2019). Indeed, the non-gneissic TTGs found in the IGC are among the most well-preserved plutonic rocks of Eoarchean age found anywhere in the world (Nutman and Bennett, 2019).

Enclaves of ultramafic rock, metagabbros, amphibolites, and sedimentary rock are also found to the south of the ISB (SOISB), intruded by TTGs of Eoarchean age (e.g., Nutman et al., 1996). Some ultramafic rocks in the IGC, such as those found within the ISB, are crustal cumulates (e.g., Szilas et al., 2015). However, certain peridotites found in the enclaves to the south of the ISB have petrographic characteristics, major element geochemistry, platinum group element and trace element compositions, as well as Re-Os and Lu-Hf isotope systematics consistent with origins in a mantle wedge in the Eoarchean (Bennett et al., 2002; Friend et al., 2002; van de Löcht et al., 2018a; van de Löcht et al., 2020). These lines of evidence have led to the interpretation that these SOISB peridotites represent the oldest pieces of Earth's mantle found anywhere on Earth (e.g., van de Löcht et al., 2018a; van de Löcht et al., 2020). This interpretation has, however, been challenged by researchers arguing that all of the ultramafic rocks found in the IGC are cumulates (Waterton et al., 2022).

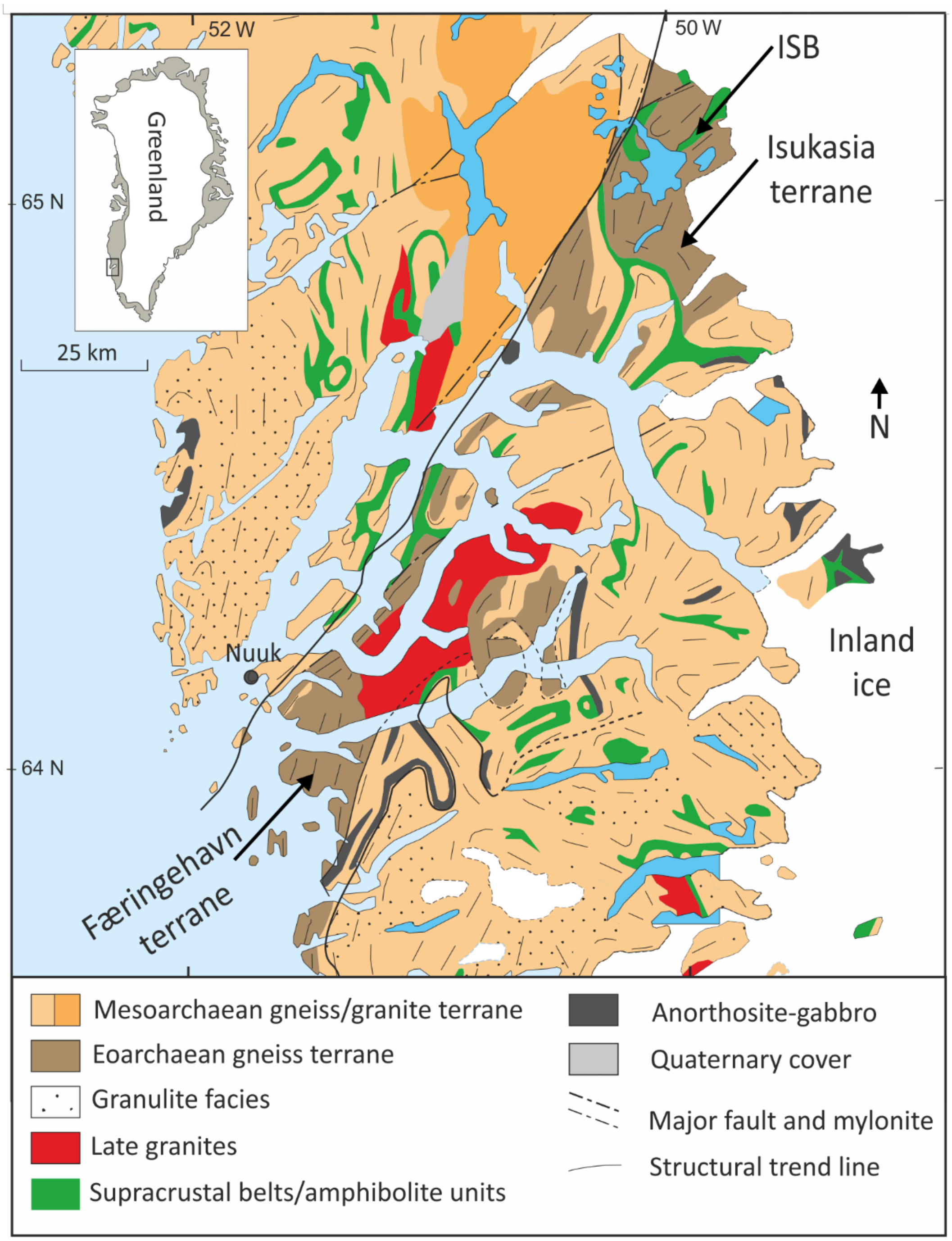

Figure 1.2: Geological map of the IGC including the Isukasia and Færingehavn Terranes. The ISB is also indicated in the northeast. Modified from Næraa et al. (2012).

The IGC's geological diversity, unique state of preservation, and constituent rocks and terranes that previous studies show are suggestive of early horizontal tectonics make the IGC an ideal locality to search for new lines of evidence for Eoarchean tectonic processes. This is why the IGC was chosen as the source for the studied rocks in this dissertation. While many of the studied rocks have been well characterized (Hoffmann et al., 2014; van de Löcht et al., 2018a; van de Löcht et al., 2020), geochemical methods that have not previously been applied to these rocks have the potential to offer new insights into the geodynamic processes that formed the IGC. An especially valuable tool for elucidating the history of Eoarchean rocks is multiple sulfur isotope analysis.

1.4. Sulfur isotopes in the Archean: a tracer of surface-derived material

Four stable isotopes of sulfur are found in nature, ^{32}S, ^{33}S, ^{34}S, and ^{36}S. A variety of natural processes fractionate these isotopes in different proportions to different degrees, resulting in discrete reservoirs containing these isotopes in different proportions. Most processes that fractionate sulfur isotopes on and within the modern Earth, including equilibrium and kinetic processes, are said to be mass dependent, which means that isotopes are fractionated as an approximately linear function of their mass (Hulston and Thode, 1965; O'Neil, 1986). This means that, in proportion to the most common sulfur isotope, ^{32}S, mass dependent processes fractionate ^{34}S approximately twice as much as ^{33}S and fractionate ^{36}S approximately twice as much as ^{34}S. Certain processes can also result in mass independent fractionation of sulfur (MIF-S), in which the four sulfur isotopes are not fractionated as a direct function of their relative mass (Farquhar et al., 2000). The relative abundance of sulfur isotopes in natural materials including rock offers insight into processes the sulfur has undergone.

Researchers have developed specialized notation to illustrate differences in sulfur isotopic compositions and the degree to which those compositions differ from ones expected as a result of purely mass-dependent processes. In this and following chapters, sulfur isotope ratios are reported vs. the standard Vienna Canyon Diablo Troilite (V-CDT) in per mil (‰), using conventional notation following Farquhar et al. (2000) and Johnston et al. (2008), defined as follows:

For 3i = 33, 34, or 36:

$\delta^{3i}(‰) = ((^{3i}/^{32}S)_{\mathrm{Sample}}/(^{3i}S/^{32}S)_{\mathrm{Standard}} - 1) \times 1000$

$\Delta^{33}S = \delta^{33}S - 1000 \times [(1 + \delta^{34}S / 1000)^{0.515} - 1]$

$\Delta^{36}S = \delta^{36}S - 1000 \times [(1 + \delta^{34}S / 1000)^{1.90} - 1]$

Multiple sulfur isotopes provide a valuable window into processes that took place on Earth in the Archean. The four stable isotopes of volcanogenic sulfur underwent mass independent fractionation as a result of photolytic processes in the reducing atmosphere that existed prior to the Great Oxidation Event (e.g., Farquhar et al., 2000; Figure 1.3). These photolytic processes enriched reduced species in ^{33}S relative to ^{34}S to a greater extent than mass dependent processes, resulting in positive Δ^{33}S values in sedimentary pyrite in marine settings (Farquhar et al., 2002). Oxidized sulfur species with complementary, negative Δ^{33}S values were dissolved in seawater until hydrothermal processes caused the oxidized sulfur to precipitate (Farquhar et al., 2002). Nonzero Δ^{33}S values on the order of up to several ‰ have been documented in numerous Archean surface deposits including Eoarchean sediments in the ISB as a result of these processes (e.g., Baublys et al., 2004; Mojzsis et al., 2003; Papineau and Mojzsis, 2006; Whitehouse, 2013; Whitehouse et al., 2005). Large, nonzero Δ^{33}S values resulting from mass independent fractionation in the Earth's reducing atmosphere disappear from the geologic record after the Great Oxidation Event and are a unique feature of surface deposits of Archean age and older on Earth (Farquhar et al., 2000).

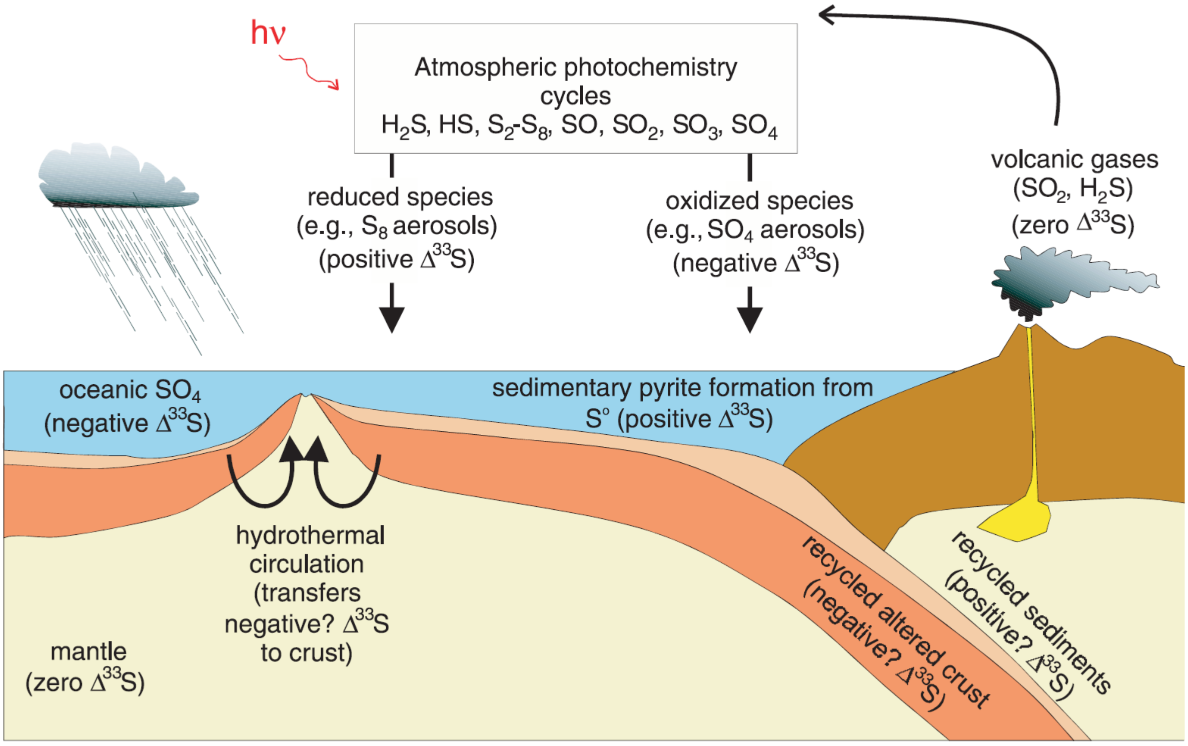

Figure 1.3: The sulfur cycle in the Archean, including the formation of MIF-S in the atmosphere, its deposition, and its anticipated recycling into the mantle via subduction under a tectonic regime similar to the modern one, reprinted from Farquhar et al. (2002).

Until recently, relatively small nonzero Δ^{33}S values within 0 ±0.2‰ were not considered to be unambiguous indications of MIF-S, as deposits formed after the Great Oxidation Event occasionally have small nonzero Δ^{33}S values that generally fall within this range (e.g., Farquhar and Wing, 2003). However, recent work has shown that such small, nonzero Δ^{33}S values are indicative of MIF-S when combined with sufficiently low δ^{34}S values in rocks of Archean age (LaFlamme et al., 2018b). While mass dependent processes such as Rayleigh fractionation can also produce small nonzero $\Delta^{33}S$ values, these processes typically produce large $\delta^{34}S$ offsets on the order of multiple tens of per mils (LaFlamme et al., 2018b). Furthermore, such mass dependent processes have been found to fractionate sulfur isotopes along a line with a slope of $\Delta^{33}S/\Delta^{36}S = -6.85$ (Ono et al., 2006), producing an array with a much more steeply negative slope in $\Delta^{33}S$-$\Delta^{36}S$ space than that defined by most Archean sulfur subject to MIF-S, which typically has $\Delta^{33}S/\Delta^{36}S$ between -0.9 and -1.5 (Farquhar et al., 2000; Zerkle et al., 2012; Figure 1.4). Mixing of sulfur reservoirs with differences in $\delta^{34}S$ on the order of several tens of per mils can also result in small nonzero $\Delta^{33}S$ values (e.g., LaFlamme et al., 2018b; Schwarzenbach et al., 2018), however, fractionations on the necessary scale to produce such offsets through mixing are not typically found in Archean lithologies and are absent in rocks of Eoarchean age (e.g., Fike et al., 2015; LaFlamme et al., 2018b). There is also evidence that MIF-S also occurs on the modern Earth to a limited extent in spite of the oxidizing atmosphere and ozone layer. In certain contexts, small MIF-S anomalies (nonzero $\Delta^{33}S$) have been observed in modern settings, such as in sulfates released into the atmosphere through volcanism or combustion (e.g., Lin et al., 2018; Savarino et al., 2003). However, these anomalies, generally on the order of no more than a few tenths of a per mil, are much smaller than those found in Archean sedimentary settings, and would not be expected to survive mixing with much larger reservoirs of sedimentary or magmatic sulfur with $\Delta^{33}S=0$ during sedimentary reworking or crustal recycling. Additionally, there is no known process within the Earth's deep interior that can produce MIF-S (Farquhar et al., 2002). Hence, the presence of nonzero $\Delta^{33}S$ in igneous lithologies is a strong indication that the rocks have incorporated material recycled from the Archean Earth's surface (e.g., Cabral et al., 2013; Caruso et al., 2022b; Dottin et al., 2020; Farquhar et al., 2002; LaFlamme et al., 2018a; Siedenberg et al., 2016).

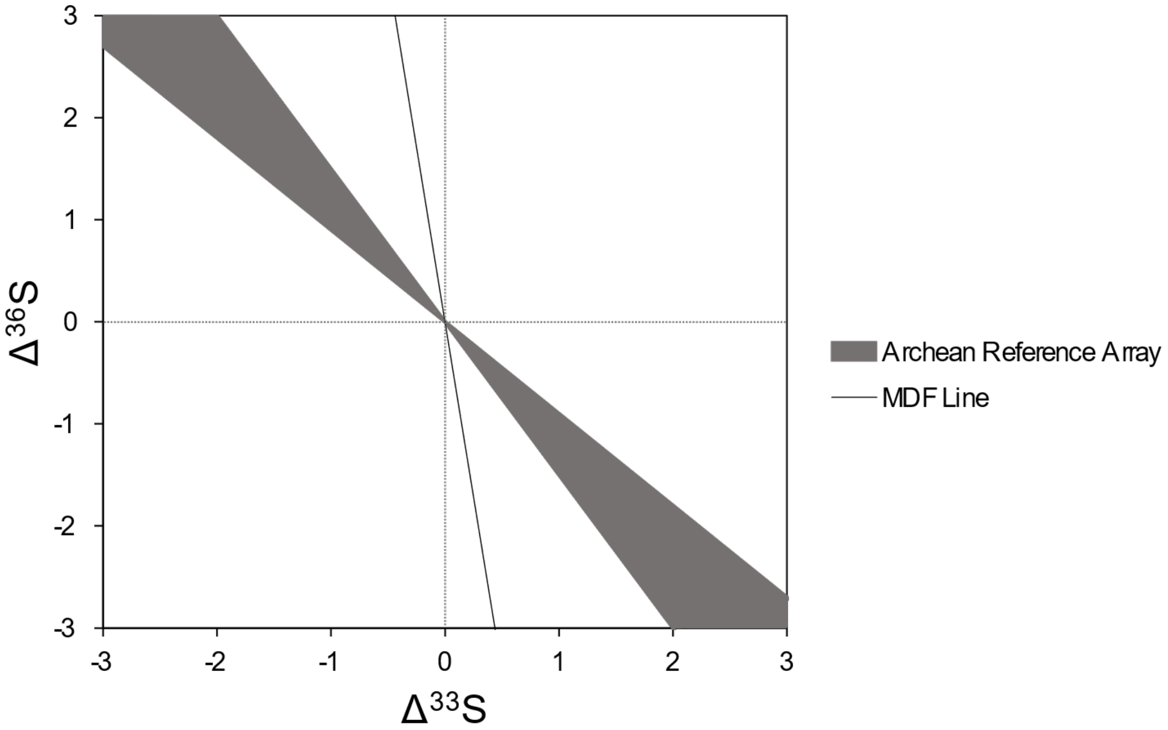

Figure 1.4: Mass dependent fractionation (MDF) line with $\Delta^{33}S/\Delta^{36}S = -6.85$ (Ono et al., 2006) compared to the Archean reference array defined by most Archean sulfur subject to MIF-S (Farquhar et al., 2000; Zerkle et al., 2012).

Modern subduction transfers elements including sulfur into the mantle wedge above subducting slabs (Li et al., 2020), and if subduction was active in the Eoarchean and mantle rocks dating from this time may be found, we would expect to find surface-derived sulfur in those mantle rocks, with characteristic MIF-S. We would also expect to find evidence for surface-derived sulfur in any mafic and evolved melts that incorporated subduction-derived material during their petrogenesis in the Eoarchean. Certain arc-like metabasalts in the ISB were already found to contain MIF-S prior to the research presented in this thesis (Siedenberg et al., 2016), hinting that surface-derived material may be found in other igneous lithologies in the IGC. However, further work was needed to trace the movement of sulfur through the entire magmatic system, demonstrating the presence of surface-derived sulfur in all parts of a potential crustal recycling process from a hypothetical Eoarchean mantle wedge to evolved cratonic crust. The work presented in this thesis includes both bulk and in-situ measurements of multiple sulfur isotopes in Eoarchean lithologies from the IGC, in addition to petrographic observations and (in the third chapter) lead isotope measurements. This thesis aims to find evidence for crustal recycling processes in the Eoarchean by tracing surface-derived sulfur through various igneous lithologies from the IGC including TTGs, amphibolites, and the SOISB peridotites.

1.5. Outline of this thesis

The following chapters include two manuscripts that have been published in peer-reviewed scientific journals as part of my doctoral research. An additional manuscript is in preparation for future publication. This work has been funded by a grant from the German Research Foundation's (Deutsche Forschungsgemeinschaft; DFG) priority program SPP1833 "Building a Habitable Earth," which has the goal of improving our understanding of how the Earth became a habitable planet. The funded project that supported my research was proposed by Drs. J. Elis Hoffmann, Esther M. Schwarzenbach, and Harald Strauss.

Chapter 2 presents the first systematic study of quadruple sulfur isotopes in Eoarchean TTGs ever conducted. This study was published in *Earth and Planetary Science Letters,* (Lewis, J.A., Hoffmann, J.E., Schwarzenbach, E.M., Strauss, H., Liesegang, M., Rosing, M.T.), with the title "Sulfur isotope evidence for surface-derived sulfur in Eoarchean TTGs" (https://doi.org/10.1016/j.epsl.2021.117218). It includes bulk multiple sulfur isotope measurements of nine non-gneissic TTGs from the vicinity of the ISB, two migmatized TTGs from the IGC, as well as two amphibolites from the ISB for comparison. Our results show MIF-S (nonzero $\Delta^{33}S$ values) in a majority of measured TTG samples and one of the two amphibolites, indicating that these rocks incorporated surface-derived material during petrogenesis. The generally positive measured $\Delta^{33}S$ values (0.00‰ to +0.30‰) indicate that the surface-derived sulfur was dominated by sedimentary sulfide, but $\Delta^{36}S$ values up to +0.80‰ and $\delta^{34}S$ values up to +3.35‰ point to incorporation of hydrothermally-derived sulfur as well. We interpret the incorporation of this surface-derived material to have taken place in the context of arc accretion in a modern-like tectonic setting, and present a three-component isotope mixing model that includes two distinct surface-derived sulfur sources (sedimentary and hydrothermally-derived), as well as sulfur from a previously measured ISB metabasalt to explain the observed sulfur isotope compositions of the IGC TTGs.

For this chapter, I prepared the samples for analysis, participated in isotope analytical work, conducted light microscopy, collected the BSE images and microprobe data, interpreted the results, developed the isotope mixing model, created the original figures, and wrote the original manuscript. J. Elis Hoffmann co-supervised the project, provided the samples for analysis, and reviewed and edited the manuscript. Esther Schwarzenbach co-supervised the project, developed and oversaw the sample preparation method, and also reviewed and edited the manuscript. Harald Strauss co-supervised the project, conducted and supervised the isotope analytical work, and reviewed and edited the manuscript. Moritz Liesegang supervised the microprobe work, and also reviewed and edited the manuscript. Minik Rosing provided samples and sample locations, and also reviewed and edited the manuscript. Andreas Lutter conducted isotope analytical work. Yogita Kadlag assisted with error propagation. Michael Antonelli and three anonymous reviewers provided valuable feedback to improve this chapter, and Frédéric Moynier provided editorial handling for the published version in *Earth and Planetary Science Letters.*

Chapter 3 is a quadruple sulfur isotope study of dunite and harzburgite samples from ultramafic enclaves located south of the ISB that have been interpreted to represent the oldest pieces of Earth's mantle ever found (e.g., Bennett et al., 2002; Friend et al., 2002; van de Löcht et al., 2018a; van de Löcht et al., 2020). This study was published in *Chemical Geology,* (Lewis, J.A., Hoffmann, J.E., Schwarzenbach, E.M., Strauss, H., Li, C., Münker, C., Rosing, M.T.), and titled "Sulfur isotope evidence from peridotite enclaves in southern West Greenland for recycling of surface material into Eoarchean depleted mantle domains" (https://doi.org/10.1016/j.chemgeo.2023.121568). It includes bulk multiple sulfur isotope measurements of eight SOISB peridotite samples. All measured samples contain positive $\Delta^{33}S$ (+0.04‰ to +0.21‰), indicating that they have incorporated surface-derived sulfur dominated by sedimentary sulfide. Notably, the peridotites show signs of variable early melt metasomatism (van de Löcht et al., 2018a; van de Löcht et al., 2020), and the samples that experienced the least melt metasomatism were found to have the highest $\Delta^{33}S$, indicating that the sedimentary input is unrelated to and predates this metasomatism. The sulfur isotope results are compared to a variety of previously published geochemical data on these rocks, and negative trends are found between $\Delta^{33}S$ and melt-mobile, fluid-immobile elements as well as εHf(t) values. Lower $\Delta^{33}S$ values are also associated with higher $\delta^{34}S$ values, with the highest measured $\delta^{34}S$ values up to +4.94‰. The relatively high $\delta^{34}S$ and low $\Delta^{33}S$ values associated with rocks preferentially influenced by the overprinting melt are interpreted to indicate that this melt also carried surface-derived sulfur form a distinct, seawater sulfate dominated source. Additionally, light microscopy was conducted on the peridotites in thin section and it was noted that amphibole overgrows the sulfides found within the peridotites, indicating that the sulfides predate amphibolite-facies metamorphism. Sulfur concentration data are also presented, which range from 95 μg/g to 800 μg/g. The history of two overprinting events in the Eoarchean bearing distinct surface-derived sources of sulfur is interpreted to most likely have occurred in a mantle wedge, reinforcing previous interpretations that the SOISB peridotites originate in the mantle, and adding a new line of evidence for recycling of surface material into the mantle in the Eoarchean.

For this chapter, I prepared the samples for analysis, participated in isotope analytical work, conducted light microscopy, interpreted the results, created the original figures, and wrote the original manuscript. J. Elis Hoffmann co-supervised the project, provided the samples for analysis, and reviewed and edited the manuscript. Esther Schwarzenbach co-supervised the project, developed and oversaw the sample preparation method, and also reviewed and edited the manuscript. Harald Strauss co-supervised the project, conducted and supervised the isotope analytical work, and reviewed and edited the manuscript. Chunhui Li conducted the sulfur concentration analyses and also reviewed and edited the manuscript. Carsten Münker and Minik Rosing provided samples and sample locations, and also reviewed and edited the manuscript. Andreas Lutter conducted isotope analytical work, and Julia van de Löcht provided valuable petrographic information about the peridotites. Pedro Waterton and an anonymous reviewer made valuable constructive comments improving this manuscript. Sonja Aulbach made additional comments and provided editorial handling for the published version in *Chemical Geology.*

Chapter 4 is a study of the in-situ mineralogy, petrography, chemical composition, as well as sulfur and lead isotope composition of sulfides found within the SOISB peridotites. This manuscript is in preparation for submission to a peer-reviewed journal and is currently titled "Evidence for Eoarchean crustal recycling from In-situ sulfur and lead isotope analyses of peridotite enclaves (southern West Greenland)," with coauthors Lewis, J.A., Schwarzenbach, E.M., Liesegang, M., van de Löcht, J., Schwarz, A., Strauss, H., Münker, C., Rosing, M.T., Whitehouse, M. J., Jeon, H., and Hoffmann, J.E. The mineralogy and composition of sulfides in the SOISB peridotites are consistent with origins in the Earth's mantle, and the presence of overgrowing amphibole (hornblende) is confirmed. In-situ $\Delta^{33}S$ results are on average very consistent with bulk results presented in the third chapter, confirming the presence of MIF-S in the SOISB peridotites. In-situ lead isotope results are highly unradiogenic, and appear to reflect a mixture of Eoarchean lead and lead introduced during Neoarchean metamorphism. Because lead is only a trace component of the sulfides and was only partly re-equilibrated during metamorphism, this is consistent with sulfur, a major component of the sulfides, retaining its Eoarchean isotopic composition. The results are interpreted to reinforce the findings and interpretations of the third chapter, including the onset of crustal recycling processes in the IGC in the Eoarchean.

For this chapter, I participated in all analytical work including scanning electron microscopy, electron microprobe analysis, and SIMS analysis of the SOISB peridotite sulfides. I interpreted the results, created the original figures, and wrote the original manuscript. Esther Schwarzenbach co-supervised the project, supervised some of the microprobe work, and also reviewed and edited the manuscript. Moritz Liesegang also co-supervised the microprobe work and also reviewed and edited the manuscript. Julia de Löcht provided initial petrographic analysis. Alexander Schwarz conducted some of the EMP analysis. Harald Strauss co-supervised the project and reviewed the manuscript. Carsten Münker and Minik Rosing provided samples and sample locations. Martin Whitehouse supervised and participated in the SIMS work and some of the electron microprobe work. Heejin Jeon also participated in the SIMS analytical work. J. Elis Hoffmann co-supervised the project, provided the samples for analysis, and reviewed and edited the manuscript. Johannes C. Vrijmoed supervised the initial SEM work and also developed the method for creating the navigable sulfide maps used during SIMS analysis. Konstantin Huber created the script to visualize the microprobe element mapping results. I would also like to thank Daniel Dunkley for a valuable conversation about the tectonic context of the SOISB peridotites during development of this chapter.

Chapter 5 includes concluding remarks, potential future research directions, as well as bulk multiple sulfur isotope data measurements on additional lithologies from the IGC that do not appear elsewhere in the text and have not yet been published elsewhere. I prepared the samples for analysis and the measurements were made in Harald Strauss' lab under his supervision in collaboration with Andreas Lutter. The samples were generously provided by Christopher Szilas, Austin Jarl Boyd, Carsten Münker, Minik Rosing, and J. Elis Hoffmann.

Chapter 2

Sulfur isotope evidence for surface-derived sulfur in Eoarchean TTGs

This chapter was published in *Earth and Planetary Science Letters* Volume 576, 15 December 2021, 117218

https://doi.org/10.1016/j.epsl.2021.117218

by

Lewis, J.A.[1], Hoffmann, J.E.[1], Schwarzenbach, E.M.[1], Strauss, H.[2], Liesegang, M. ,[1] Rosing, M.T.[3]

[1]Institut für Geologische Wissenschaften, Freie Universität Berlin, Malteserstr. 74-100, 12249 Berlin, Germany

[2]Institut für Geologie und Paläontologie, Westfälische Wilhelms-Universität Münster, Corrensstr. 24, 48149 Münster, Germany

[3]GLOBE Institute, University of Copenhagen, Øster Voldgade 5, DK-1350 Copenhagen, Denmark

This chapter was modified for publication in this doctoral thesis.

2.1. Abstract

The conditions giving rise to the first evolved melts preserved on Earth remain a subject of debate. These melts formed tonalite-trondhjemite-granodiorites (TTGs) comprising the first cratonic cores. Constraining the nature of the rocks that melted to form these TTGs is crucial to understanding the mechanism that produced the first continents. Previous studies have indicated that TTGs' source rocks are hydrated mafic lithologies similar to modern arc tholeiitic basalts, comparable to amphibolites embedded in greenstone belts within Archean cratons.

To elucidate the geodynamic setting of TTG formation, we investigated 3.9-3.6 Ga TTGs and amphibolites from the Itsaq Gneiss Complex (IGC), southern West Greenland using multiple sulfur isotope signatures, as well as textural and compositional analysis of selected sample sulfides. Small but significant nonzero $\Delta^{33}S$ and $\Delta^{36}S$ values were measured in the TTGs, with $\Delta^{33}S$ values from 0.00‰ to +0.30‰, and $\Delta^{36}S$ values from -0.13‰ to +0.80‰. Amphibolites yielded $\Delta^{33}S$ values of -0.01‰ and +0.14‰, and $\Delta^{36}S$ values of +0.08‰ and +0.23‰. These values are consistent with the presence of sedimentary sulfur, likely introduced to the sources

of the TTGs' precursor rocks via horizontal tectonics. Sulfur in the TTGs was likely subject to mass independent fractionation on Earth's surface and may have experienced subsequent ^{34}S enrichment during metamorphism in the TTGs' source rocks. Relative enrichment in ^{34}S and ^{36}S in TTGs may be explained by incorporation of fluid sampling hydrothermal deposits within the thickened mafic crust, released during arc accretion. This fluid may have triggered partial melting, forming the TTGs. Hence, the sulfur isotope composition of the TTGs represent a mixture of material derived from the source rocks by melting and from fluid released from other rocks bearing hydrothermally derived sulfur. Our results add weight to existing models of modern-like tectonic processes active in the Eoarchean.

2.2. Introduction

Earth's earliest remnants of preserved continental crust are sodic granitoids of Eoarchean (4.0-3.6 Ga) age with tonalitic-trondhjemitic-granodioritic (TTG) composition. They represent the majority of Eoarchean rocks found on Earth's surface, yet their origins remain subject to debate. Competing hypotheses concerning the geodynamic setting in which TTGs formed continue to be investigated. It is commonly agreed that the source rocks of TTGs were hydrated mafic lithologies generated from an enriched source (e.g., Smithies et al., 2009). These source rocks melted either at the base of thick oceanic plateaus, or within modern arc-like geodynamic environments to form TTG plutons (see Hoffmann et al. (2019) for a review). Recent work has revealed evidence suggesting that some source rocks of TTGs have incorporated surface-derived components that melted under temperature and pressure conditions reminiscent of modern hot subduction zones (Antonelli et al., 2021; Deng et al., 2019), as well as hydrothermally altered rocks (André et al., 2019; Vezinet et al., 2018; Vezinet et al., 2019). However, a paucity of Eoarchean rocks subject only to low pressure/temperature metamorphism and the fact that modeling of the thermal evolution of the Earth's mantle can accommodate both modern and non-uniformitarian, stagnant lid tectonic regimes on the early Earth, (e.g. Brown and Johnson, 2019), means that the geodynamic mechanism giving rise to Earth's earliest TTGs continues to be debated.

Several lines of evidence point to a genetic link between the Eoarchean TTGs and amphibolites found in the 3.9-3.6 Ga Itsaq Gneiss Complex (IGC) of southern West Greenland, and the formation of the TTGs in a geodynamic setting resembling a modern island arc accretionary complex. Trace element concentrations and other geochemical systematics of co-occurring basaltic amphibolites in the Isua Supracrustal Belt (ISB) strongly resemble those of modern arc tholeiites and boninites, and have been interpreted to have formed under similar geodynamic conditions (Polat and Hofmann, 2003a). Furthermore, petrological phase equilibrium modeling, major and trace element compositions, and Hf-Nd isotope systematics have shown that the source rocks of Archean TTGs are likely to be amphibolites with arc tholeiite-like compositions similar to those found in the ISB (Hoffmann et al., 2011b; Hoffmann et al., 2019). In addition, the episodic nature of TTG formation in the IGC as evidenced by peaks of ^{207}Pb/^{206}Pb ages in IGC TTG samples analyzed in previous studies (Nutman and Bennett, 2019) supports the hypothesis that they formed during episodes of crustal thickening during arc accretion. While the rocks that partially melted to form the TTGs were likely subject to a higher degree of metamorphism than the basaltic amphibolites exposed in the ISB, they likely were of similar origin and composition (Nagel et al., 2012). If robustly proven, a horizontal tectonic origin for Eoarchean amphibolites and TTGs would preclude a plateau-like formation setting.

Recycling of material derived from Earth’s surface by subduction is a feature of modern horizontal tectonics that would not be expected in vertical tectonic systems. Stable isotopes of sulfur (^{32}S, ^{33}S, ^{34}S, and ^{36}S) provide a unique tracer for surface-derived material in the Archean. Prior to the Great Oxidation Event (GOE) at approximately 2.45 Ga, photolytic processes in Earth's atmosphere caused mass independent isotope fractionation (MIF) of volcanogenic sulfur species, (e.g., Farquhar et al., 2000). This resulted in reduced sulfur species with higher ^{33}S content than would be expected from mass dependent fractionation processes (expressed by positive Δ^{33}S values) forming sedimentary pyrite in marine environments (Farquhar et al., 2002). Oxidized species with more negative Δ^{33}S values remained dissolved in seawater until they were precipitated within the crust through hydrothermal processes (Farquhar et al., 2002). After the GOE the presence of atmospheric ozone mostly prevented such mass independent sulfur isotope fractionation processes, and thus the processes leading to large variations in Δ^{33}S are unique to the Earth's surface and the Archean. No process in the Earth's deep interior has been shown to produce MIF, and the relative homogeneity of Δ^{33}S values in meteorites precludes the possibility of Δ^{33}S variability in the early Earth's mantle leftover from its accretion on the order of more than +/- 0.031‰ (Antonelli et al., 2014; Farquhar et al., 2002).

While numerous multiple sulfur isotope studies on Archean sedimentary and hydrothermally derived rocks have been conducted in the past, (e.g., Farquhar et al., 2000), evidence also arises from the igneous rock record for the incorporation of surface-derived mass independently fractionated sulfur (MIF-S) (e.g., Dottin et al., 2020; Farquhar et al., 2002; Siedenberg et al., 2016). Notably, previous work has identified small but significant nonzero $\Delta^{33}S$ signatures in amphibolites with tholeiitic and boninitic composition in the ISB, suggesting that these rocks have incorporated surface derived sulfur that was introduced into their mantle source and supporting a subduction-related formation setting (Siedenberg et al., 2016).

Here, we use multiple sulfur isotope signatures as a new tool to explore the origins of Eoarchean TTGs from the Itsaq Gneiss Complex of southern West Greenland. The potential for multiple sulfur isotopes to trace a genetic link between Eoarchean amphibolites and TTGs is investigated for the first time. The results presented in this study cast fresh light on questions of how and from what source rocks Eoarchean TTGs formed. We combine these results with textural and mineralogical data in order to constrain the processes involved. These results are interpreted to represent a new line of evidence for Eoarchean crustal recycling, implying an early onset of at least localized horizontal tectonics.

2.3. Geology of the Itsaq Gneiss Complex

The 3.66-3.90 Ga Itsaq Gneiss Complex (IGC), located in the Nuùk region of southern West Greenland, consists of two Eoarchean terranes, the Isukasia and the Færingehavn Terrane (Figure 2.1)., both consisting of 90% orthogneiss with primarily TTG composition. The terranes were juxtaposed in the Neoarchean in a collage of younger terranes. Both terranes were overprinted by amphibolite and granulite facies metamorphism (Nutman et al., 1996). The IGC includes the 3.7-3.8 Ga Isua Supracrustal Belt (ISB), representing the largest body of Eoarchean supracrustal rocks in the world (Nutman and Friend, 2009). The ISB and adjacent areas include a wide variety of lithologies, including altered sedimentary rocks, as well as amphibolites of boninitic and tholeiitic compositions similar to modern island arc basalts (Jenner et al., 2009; Nutman and Friend, 2009; Polat and Hofmann, 2003a; Polat et al., 2002), as well as ultramafic rocks interpreted to represent Eoarchean mantle (e.g., Friend and Nutman, 2011) and ultramafic cumulates (e.g., Szilas et al., 2015). TTGs on both the northern and southern sides of the ISB formed prior to the event between 3.66 and 3.69 Ga that juxtaposed the northern and southern terranes (Nutman and Friend, 2009).

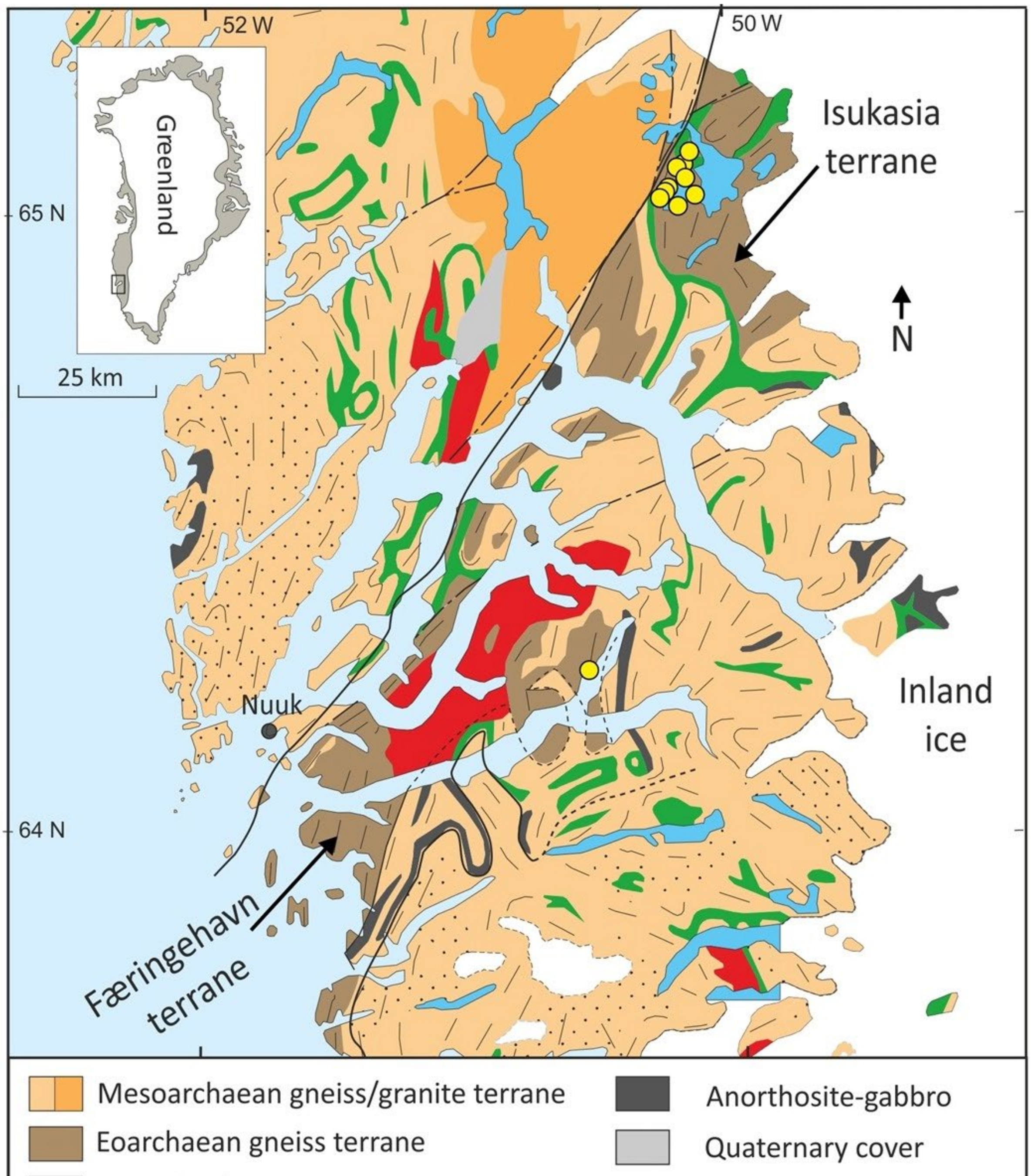

Figure 2.1: Simplified geological map showing approximate locations of all samples investigated in this study except for 2000-010, whose coordinates are not available (modified from Næraa et al. (2012)).

The IGC TTGs intruded mafic and ultramafic lithologies of the ISB and other enclaves that were deformed and metamorphosed prior to the TTG intrusion (Hoffmann et al., 2014;

Nutman and Friend, 2009). In the area south of the ISB, rare outcrop localities preserve unique non-gneissic TTGs with magmatic textures (e.g., Hoffmann et al., 2014; Nutman and Friend, 2009). Between 3.66 and 3.45 Ga the IGC was intruded by the Ameralik and Inaluk dyke suite followed by superimposed lower amphibolite metamorphism (e.g., Nutman and Friend, 2009 and citations therein).

2.4. Analytical Methods

In this study, nine well-characterized non-gneissic TTGs from the IGC representing some of the best preserved single phase Eoarchean TTGs yet identified (e.g., Hoffmann et al., 2011a; Hoffmann et al., 2014; Næraa et al., 2012), two Eoarchean TTG migmatites (Hoffmann et al., 2011a; Næraa et al., 2012; Nutman et al., 1999) as well as two amphibolites from the ISB (Hoffmann et al., 2011b; Polat and Hofmann, 2003a) were selected for multiple sulfur isotope measurements. Sample locations are provided in Figure 2.1 and GPS coordinates and ages are provided in the supplementary material (Supplementary table 2.10.B; further details on samples including major and trace element data can be found in Hoffmann et al. (2011a), Hoffmann et al. (2011b), Hoffmann et al. (2014), and Polat and Hofmann (2003a)).

For each sample, 16-35 g of powdered rock was placed in a round bottomed flask with 5-6 g of $Sn(II)Cl_2$, and then was heated and reacted under nitrogen gas with a $CrCl_2$ solution in order to liberate sulfide sulfur as H_2S. Hydrogen sulfide from the sample was captured in a 3% zinc acetate trap solution and reacted with silver nitrate to precipitate the sulfur as Ag_2S. Subsequently, 1-3 mg aliquots of extracted Ag_2S samples were reacted with F_2 gas to form SF_6, which was purified cryogenically and by gas chromatography, and subjected to multiple sulfur isotope analysis (^{32}S, ^{33}S, ^{34}S, ^{36}S) with a Thermo Fisher Scientific MAT 253 isotope ratio mass spectrometer following the method of Siedenberg et al. (2016). Duplicate samples were extracted following the same methods in labs at Freie Universität Berlin and Westfälische Wilhelms-Universität Münster (designated Munster Dup on Table 2.1). Fluorination and sulfur isotope analysis on SF_6 was performed at Westfälische Wilhelms-Universität Münster. Sulfur isotope ratios are reported using the conventional delta-notation relative to the Vienna Canyon Diablo Troilite (V-CDT) in per mil (‰), with mass dependent signals in terms of $\delta^{34}S$ and mass independent signals in terms of $\Delta^{33}S$ and $\Delta^{36}S$. These are defined after Farquhar et al. (2000) and Johnston et al. (2008) as:

For 3i = 33, 34, or 36:

δ^{3i}(‰) = $((^{3i}/^{32}S)_{Sample}/(^{3i}S/^{32}S)_{Standard} - 1) \times 1000$

$\Delta^{33}S = \delta^{33}S - 1000 \times [(1 + \delta^{34}S / 1000)^{0.515} - 1]$

$\Delta^{36}S = \delta^{36}S - 1000 \times [(1 + \delta^{34}S / 1000)^{1.90} - 1]$

The 2σ analytical error based on ^{36}S standard measurements over the year in which the study was conducted was ±0.13‰ for δ^{34}S, ±0.01‰ for Δ^{33}S, and ±0.23‰ for Δ^{36}S. 2σ internal measurement errors ranged from 0.002‰ to 0.018‰ for δ^{34}S, 0.013‰ to 0.038‰ for Δ^{33}S, and 0.069‰ to 0.292‰ for Δ^{36}S and are provided in Table 2.1.

Selected TTG samples were examined by transmitted and reflected light microscopy in thin sections in order to determine the presence of sulfides suitable for electron microprobe (EMP) analysis. Selected amphibolite samples from the ISB including the two subject to isotope analysis in this study and three with sulfur isotope results reported in (Siedenberg et al., 2016) were similarly examined by reflected light microscopy in thick sections. These thin and thick sections were then subject to EMP analyses to determine their sulfide mineralogy (see Supplementary table 2.10.C). EMP analyses at 1 µm beam diameter were conducted on a JEOL JXA 8200 Superprobe at the Freie Universität Berlin. Sulfides were analyzed for Ni, S, As, Fe, Cu, Co, and Zn concentrations, in most cases (178 measurements) with an acceleration voltage of 20 kV and 20 nA beam current, measured for 30 seconds on peak and 15 seconds on background, whereas 30 measurements were taken at 15kV, 20 nA beam current and measured at 10 s on the peak and 5 s on the background (see Supplementary table 2.10.C).

2.5. Results

2.5.1. Multiple sulfur isotope signatures

Small but significant nonzero Δ^{33}S and Δ^{36}S values were measured in several of the TTGs and one of the amphibolites (Table 2.1). The TTGs have δ^{34}S values ranging from +1.63‰ to +3.35‰, Δ^{33}S values ranging from 0.00‰ to +0.30‰, and Δ^{36}S values ranging from -0.08‰ to +0.80‰. In the migmatitic TTGs δ^{34}S values are +2.78‰ and +2.60‰, Δ^{33}S values are +0.14‰ and +0.05‰, and Δ^{36}S values are -0.13‰ and +0.35‰ for samples 498027 and JEH-SG-07, respectively. The amphibolites have δ^{34}S values of +2.32‰ and +0.42‰, Δ^{33}S values of -0.01‰ and +0.14‰, and Δ^{36}S values of +0.08‰ and +0.23‰ for samples JEH-2007-01 and 2000-10, respectively. Both sets of duplicates show differences in δ^{34}S up to 0.4‰ and one set of duplicates (010-038) shows a significant difference in Δ^{36}S values of 0.15‰. We attribute these differences to sample heterogeneity. Other differences between duplicates are less than the 2σ measurement error.

Table 2.1: Analytical Results for multiple sulfur isotope compositions of Eoarchean TTGs and amphibolites from the IGC.

Sample	Type	$\delta^{34}S$ [‰] (VCDT)	σ ($\delta^{34}S$) [‰]	2*σ ($\delta^{34}S$) [‰]	$\delta^{33}S$ [‰]	σ ($\delta^{33}S$) [‰]	$\delta^{36}S$ [‰]	σ ($\delta^{36}S$) [‰]	$\Delta^{33}S$ [‰]	2*σ ($\Delta^{33}S$) [‰]	$\Delta^{36}S$ [‰]	2*σ ($\Delta^{36}S$) [‰]
JEH-2007-01	Amphibolite (metagabbro)	2.317	0.003	0.006	0.367	0.015	2.256	0.109	-0.005	0.030	0.082	0.218
2000-010	Amphibolite (metabasalt)	0.416	0.009	0.018	-0.469	0.017	-1.201	0.122	0.136	0.035	0.230	0.246
498027	Migmatitic tonalite	2.782	0.006	0.012	0.748	0.016	2.928	0.114	0.137	0.033	-0.129	0.229
JEH-SG-07	Migmatitic tonalite	2.604	0.006	0.012	0.568	0.006	3.072	0.123	0.048	0.013	0.354	0.247
010-018	TTG	1.989	0.008	0.016	0.393	0.015	1.475	0.081	0.190	0.031	-0.076	0.165
010-024	TTG	2.214	0.006	0.012	0.515	0.007	2.104	0.065	0.196	0.015	0.126	0.132
010-025	TTG	3.355	0.007	0.014	1.032	0.018	4.723	0.101	0.127	0.037	0.578	0.204
010-038	TTG	2.157	0.008	0.016	0.285	0.012	2.087	0.135	-0.005	0.025	0.217	0.272
010-038 Munster Dup	TTG	1.766	0.004	0.008	0.099	0.011	1.199	0.146	0.010	0.022	0.070	0.292
010-039	TTG	2.298	0.007	0.014	0.435	0.015	2.937	0.106	0.073	0.031	0.799	0.214
JEH-2007-05	TTG	2.869	0.007	0.014	0.955	0.012	3.346	0.087	0.299	0.025	0.124	0.176
JEH-SG-04	TTG	1.632	0.005	0.010	0.212	0.014	0.033	0.033	0.192	0.028	0.219	0.069
JEH-SG-04 Munster Dup	TTG	1.817	0.005	0.010	0.292	0.007	1.948	0.109	0.177	0.015	0.722	0.219
JEH-SG-05	TTG	2.870	0.005	0.010	0.803	0.006	3.416	0.085	0.147	0.013	0.192	0.171
JEH-SG-09	TTG	3.123	0.001	0.002	0.875	0.008	4.287	0.073	0.088	0.016	0.582	0.146
IAEA-S1	Standard	-0.279	0.004	0.008	-0.895	0.019	-3.691	0.121	0.068	0.038	-0.943	0.242
IAEA-S1	Standard	-0.282	0.009	0.018	-0.887	0.009	-3.636	0.113	0.078	0.020	-0.882	0.229
IAEA-S1	Standard	-0.280	0.003	0.006	-0.899	0.015	-3.405	0.067	0.064	0.030	-0.655	0.134
IAEA-S1	Standard	-0.291	0.008	0.016	-0.887	0.016	-3.427	0.071	0.082	0.033	-0.656	0.145
Ag2S (Lab.)	Standard	2.834	0.005	0.010	0.602	0.014	3.658	0.144	-0.036	0.028	0.503	0.289

2.5.2. *Sulfide mineral compositions and textures*

Sulfides in TTGs were rare with most grains around 10-100 µm long, along their longest axes. Pyrite and chalcopyrite were the dominant minerals, with pyrrhotite only observed in JEH-SG-05 and 010-038 (Supplementary table 2.10.C). In the TTGs, sulfides are often rimmed by magnetite, with sulfides locally showing signs of decomposition such as lamellar and symplectic interfingering of pyrrhotite with magnetite (Figure 2.2A) and porous pyrite (Figure 2.2B).

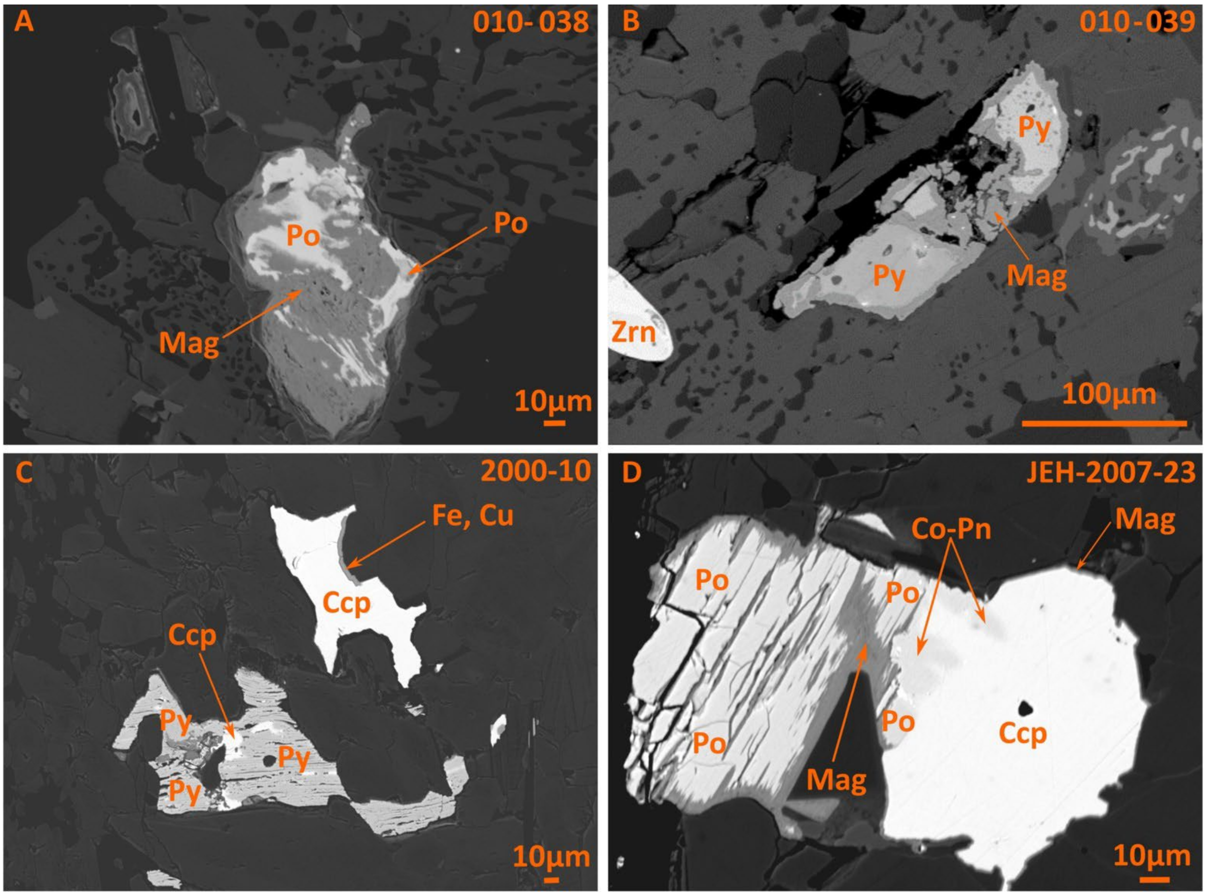

Figure 2.2: Backscattered electron (BSE) images of sulfides from TTGs (A and B) and amphibolites (C and D). A: Pyrrhotite rimmed by magnetite. B: Pyrite decomposing into magnetite in a TTG. C: Porous pyrite with inclusions of chalcopyrite and a chalcopyrite grain partially rimmed by an iron and copper bearing oxide in an amphibolite. D: Chalcopyrite thinly rimmed by magnetite to the right, intergrown with slightly decomposed pyrrhotite in an amphibolite. Abbreviations are: Py - pyrite, Ccp - chalcopyrite, Po - pyrrhotite, Co-Pn - cobalt rich pentlandite, Mag - magnetite, Zrn - zircon.

The sulfide mineralogy in the amphibolites is dominated in most samples by chalcopyrite and pyrrhotite, as well as smaller amounts of pyrite in some cases. Locally, these phases are intergrown (Supplementary table 2.10.C). Chalcopyrite is almost always rimmed by either magnetite or a Cu-bearing Fe-silicate. Chalcopyrite commonly forms euhedral grains, in most cases without corrosion features, whereas pyrrhotite and pyrite are always either porous or strongly corroded along cleavage planes (Figure 2.2 C, D), except where they are armored by silicate phases. In three samples, pentlandite was also detected containing between 0.14 and 21.96wt.% Co, locally intergrown with chalcopyrite.

In the TTGs, pyrite contains up to 2.24 wt. % Co, with Ni, Cu, Zn, and As being <0.15wt. %. Pyrrhotite contains <0.37wt. % Ni, <1.70 wt.% Cu, <0.12 wt. % Co, and for Zn and As contents are below detection limit. Chalcopyrite has a stoichiometric composition with trace element contents below detection limit. In the amphibolites, pyrite contains considerable Ni, up to 6.78 wt. % in sample 2000-10, whereas Co is <1.31 wt. % and Cu is <0.3 wt. %. Pyrrhotite contains up to 2.32 wt. % Ni, <0.65 wt. % Cu, and <0.23 wt. % Co, and chalcopyrite typically contains <0.1 wt.% of trace elements. Zn and As are below detection limits in most amphibolite sulfides. Results are given in Supplementary table 2.10.C.

2.6. Discussion

2.6.1. A mass independent sulfur signature in Eoarchean amphibolites and TTGs

Most modern rocks have $\Delta^{33}S$ and $\Delta^{36}S$ values near zero, which can be ascribed to purely mass dependent processes involved in their formation (e.g., Farquhar et al., 2011). However, the TTGs and amphibolites from the IGC show small but significant non-zero $\Delta^{33}S$ and $\Delta^{36}S$ values of 0.00‰ to +0.30‰ and -0.01‰ and +0.14‰, respectively (Table 2.1, Siedenberg et al., 2016). Non-zero $\Delta^{33}S$ and $\Delta^{36}S$ values have previously been inferred to be evidence for the input of Archean surface-derived sulfur (e.g., Farquhar et al., 2011). Archean sediments and hydrothermal deposits have $\Delta^{33}S$ and $\Delta^{36}S$ values in the range of ~-2.0 to 10‰ and ~ -9, to +2‰, respectively (e.g., Johnston, 2011 and references therein). Mixing of such signals with magmatic sulfur ($\Delta^{33}S = \Delta^{36}S = 0$‰) during recycling of surface-derived material into the mantle and ultimately into mantle-derived and crustal rocks could attenuate the signal and produce relatively small deviations from zero. However, mass dependent processes can similarly produce minor variations in $\Delta^{33}S$ values in the range of 0 ± 0.2‰ (Farquhar and Wing, 2003). These small, non-zero $\Delta^{33}S$ values are produced by thermochemical and biological processes such as Rayleigh fractionation, and are associated with significant fractionations in $\delta^{34}S$ relative to $\Delta^{33}S$ (LaFlamme et al., 2018). Similarly, mixing of two endmembers with different $\delta^{34}S$ values can produce offsets in $\Delta^{33}S$ and $\Delta^{36}S$, but with input values typical of Archean sedimentary and hydrothermal deposits these offsets are much smaller than those we observe in our study (see Supplementary Figure 2.A.5). According to

LaFlamme et al. (2018), nonzero Δ^{33}S values produced by mass dependent processes, denoted as $\Delta^{33}S_B$, have λ^{33} values ranging from 0.508 to 0.519, with the mass dependent relationship λ between Δ^{33}S and δ^{34}S defined as:

$$\Delta^{33}S_B = 1000 \times [(1 + \delta^{34}S / 1000)^{0.515} - 1] - 1000 \times [(1 + \delta^{34}S / 1000)^{\lambda} - 1].$$

As shown in Figure 2.3A, the majority of the IGC TTG samples, one of the amphibolites analyzed in this study, and the majority of amphibolite isotopic compositions from Siedenberg et al. (2016) fall significantly outside of the range of values expected to result from most mass dependent processes (LaFlamme et al., 2018). Thus, we infer that the observed variation in Δ^{33}S most likely carries a component of surface-derived, mass independently fractionated sulfur.

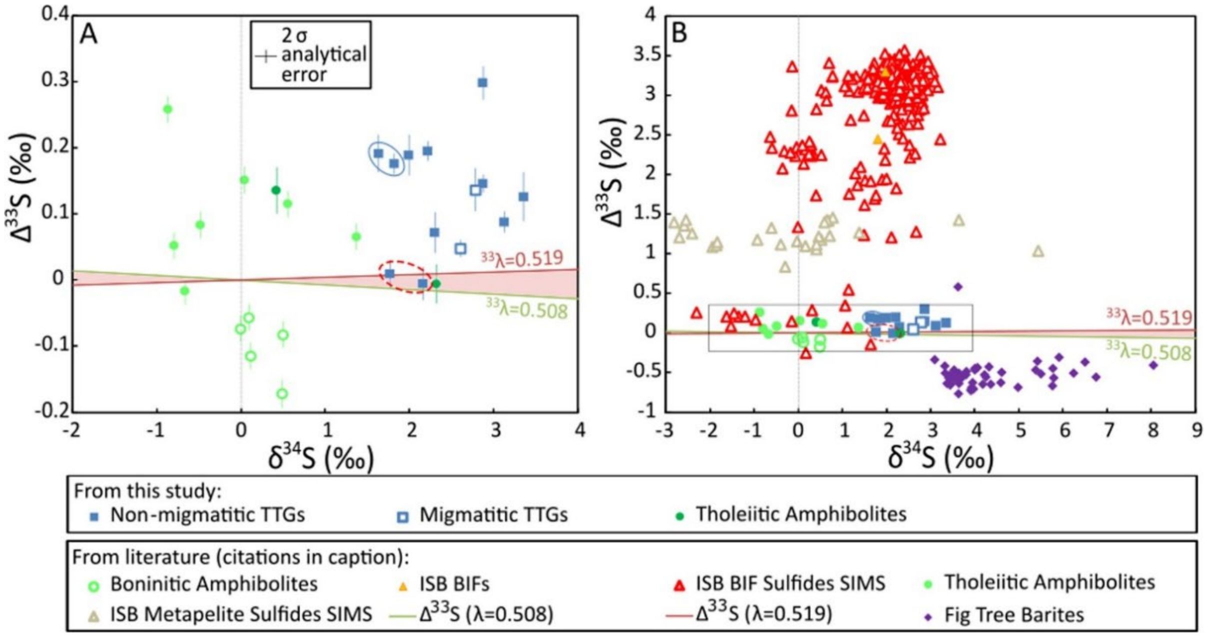

Figure 2.3: A: TTG and amphibolite δ^{34}S and Δ^{33}S results from this study compared to previously published sulfur isotope values for amphibolites of oceanic crustal origin from the ISB, including undifferentiated amphibolites with tholeiitic composition and slightly enriched trace element patterns, and more depleted amphibolites with boninitic affinity (Siedenberg et al., 2016). Duplicate results are shown in ovals (dotted red for TTG sample 010-038, solid blue for TTG sample JEH-SG-04). 2σ analytical errors for δ^{34}S and Δ^{33}S in this study are shown in the inset box, and 2σ measurement error bars are shown on data points representing measurements from this study. 2σ analytical errors for samples from Siedenberg et al. (2016) are shown as error bars on the relevant data points. The range of values expected to be produced by mass dependent isotopic fractionation (λ33 values between 0.508 and 0.519) (LaFlamme et al., 2018) is also shown in the red shaded area. B: Data as in A is compared to sediments from the ISB including BIFs (Baublys et al., 2004; Mojzsis et al., 2003; Papineau and Mojzsis, 2006; Whitehouse, 2013; Whitehouse et al., 2005) and metapelites (Mojzsis et al., 2003;

Papineau and Mojzsis, 2006), as well as Mesoarchean barites from the Fig Tree Group in South Africa (Bao et al., 2007; Farquhar et al., 2000; Montinaro et al., 2015). Note that measurement and analytical errors for samples measured in this study are smaller than the data points, and measurement errors for other points are available in the relevant references. Note that for BIFs, samples measured by bulk analysis and SIMS are symbolized separately. All metapelite measurements displayed were done by SIMS on individual sulfide grains (Mojzsis et al., 2003; Papineau and Mojzsis, 2006). Area covered by part A of the figure is outlined by the black rectangle.

2.6.2. Sources of Sulfur in Itsaq TTGs

The presence of surface-derived sulfur with similar MIF-S signatures in the amphibolites and TTGs is consistent with previous models that propose formation of the IGC rocks in a suprasubduction setting, where the TTGs were emplaced after crustal thickening by arc-accretion processes and partial melting of the amphibolites (Hoffmann et al., 2011a; Hoffmann et al., 2014; Nagel et al., 2012). In such a setting, subduction is necessary to transport surface-derived sulfur into the mantle source of tholeiitic rocks (Siedenberg et al., 2016). In modern arc systems, subducting slabs release sulfur-bearing fluids derived from pore fluid release and dehydration of sediments, altered oceanic crust, and upper mantle that can be transferred into the overlying mantle wedge (Li et al., 2020; Su et al., 2019), eventually promoting mantle metasomatism and melting. If such a process was already in progress during the Archean, the surface-derived sulfur sources would be expected to have distinct multiple sulfur isotope compositions. The hydrothermal or sedimentary-derived sulfur would have nonzero $\Delta^{33}S$ compositions with opposite signs, i.e., negative or positive $\Delta^{33}S$ compositions, respectively (e.g. Farquhar et al., 2000).

Potential sources for a sedimentary component of sulfur introduced to ISB amphibolites by slab dehydration are present in the ISB. ISB metasediments include banded iron formations with in situ $\delta^{34}S$ values ranging from -2.31‰ to +2.67‰, $\Delta^{33}S$ values ranging from -0.25‰ to +3.41‰, and generally negative $\Delta^{36}S$ values (Figures 2.3B and 2.4B) (Baublys et al., 2004; Mojzsis et al., 2003; Papineau and Mojzsis, 2006; Whitehouse et al., 2005) as well as ISB metapelites containing pyrite grains that yield $\delta^{34}S$ values ranging from -2.82‰ to +5.44‰ and $\Delta^{33}S$ values ranging from +0.84‰ to +1.43‰, respectively (Figure 2.3B) (Mojzsis et al., 2003; Papineau and Mojzsis, 2006). Additionally, bulk isotopic analysis of a variety of sedimentary pyrites from the ISB yielded $\delta^{34}S$ compositions between -3.8‰ and +3.4‰ (Grassineau et al., 2006; Monster et al., 1979; Strauss, 2002; Strauss, 2003). Taken together, the sulfur isotope compositions of these metasediments cover the range of $\delta^{34}S$ values and exceed the positive $\Delta^{33}S$ values found in the ISB TTGs and amphibolites analyzed in this study, and amphibolites from Siedenberg et al. (2016) (Figure 2.3B). Introduction of such material to a magmatic source with δ^{34}S = 0±0.5‰ (e.g., Kanehira et al., 1973; Labidi et al., 2015) would be expected to variably scatter δ^{34}S values in the amphibolites, potentially in both positive and negative directions (Figure 2.3). It would also be expected to move Δ^{33}S and Δ^{36}S compositions from the origin in the direction of sediments with positive Δ^{33}S and negative Δ^{36}S compositions, roughly along the Archean array (Figure 2.4, Figure 2.5A).

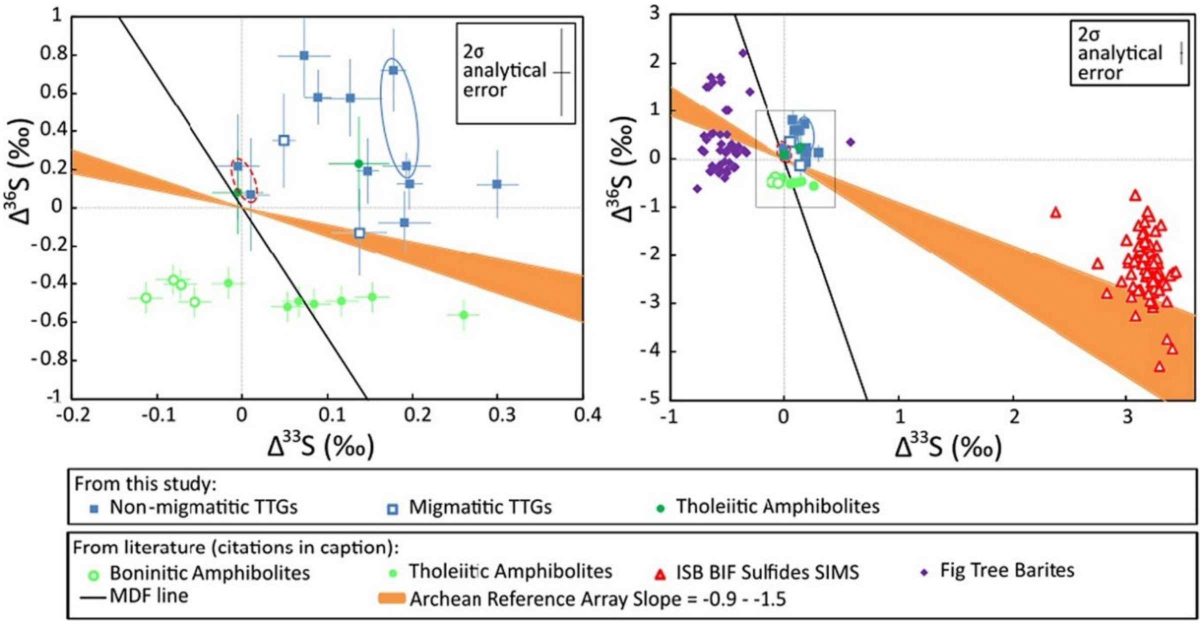

Figure 2.4: A: Results are displayed and compared with the same published data as in Figure 2.3A (Siedenberg et al., 2016), with Δ33S plotted against Δ^{36}S. 2σ analytical and measurement errors for Δ^{33}S and Δ^{36}S in this study are shown as in Figure 2.3A. Additionally, lines showing expected results for mass dependently fractionated sulfur based on modeling of mass dependent fractionation (MDF) processes consistent with measured isotopic values of Phanerozoic sedimentary pyrite (Ono et al., 2006), and the Archean reference array showing typical values for mass independently fractionated sulfur in the Archean (Farquhar et al., 2000; Zerkle et al., 2012) are also shown for comparison. 2σ analytical errors for Δ^{33}S and Δ^{36}S in this study are shown in the inset box, and 2σ measurement error bars are shown on data points representing measurements from this study. 2σ analytical errors for samples from (Siedenberg et al., 2016) are shown as error bars on the relevant data points. B: Data as in A is compared to sediments from the ISB including BIFs (Whitehouse, 2013) and Mesoarchean barites from the Fig Tree Group in South Africa (Bao et al., 2007; Farquhar et al., 2000; Montinaro et al., 2015). Note that results from (Montinaro et al., 2015) have been corrected for a systematic offset of 0.8‰ detected since publication of the original data. 2σ analytical errors for Δ^{33}S and Δ^{36}S for this study are shown in the inset box, and 2σ measurement error bars are shown on data points representing

measurements from this study. Measurement errors for other points are available in the relevant references. Area covered by part A of the figure is outlined by the black rectangle.

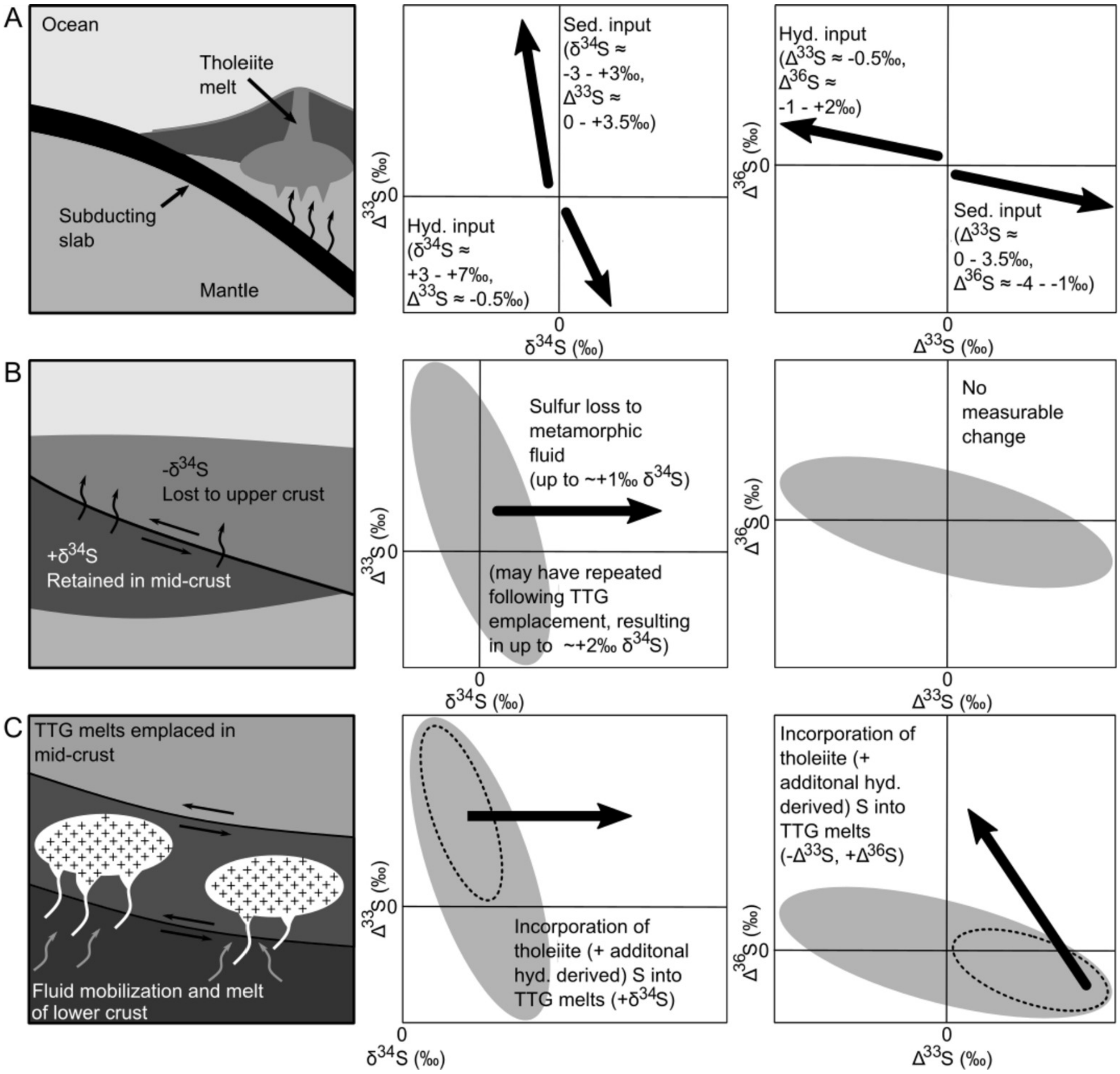

Figure 2.5: Schematic of processes influencing the sulfur isotopic composition of IGC amphibolites and TTGs in the Eoarchean. A) Sulfur derived from sediments (positive Δ^{33}S, negative δ^{34}S) is transferred into the mantle wedge where the sulfur is incorporated into tholeiites, the protoliths of the amphibolites, by partial melting. Hydrothermally altered oceanic crust (negative Δ^{33}S, positive δ^{34}S) was also mobilized by this process and appears to dominate mass independently fractionated sulfur in the boninites reported in (Siedenberg et al., 2016), which are not source rocks of the measured TTGs. B) The basalts produced in A (grey oval) experience amphibolite-facies metamorphism associated with sulfur loss causing an enrichment in ^{34}S in the residual amphibolites. C) The amphibolites (grey oval) are partially molten to produce the TTGs. The melting is driven by fluid incorporating sulfur from the dehydration of similar amphibolites as well as fluids formed by the dehydration of hydrothermal deposits in the lower crust. The hydrothermal material adds an additional component

with positive $\Delta^{36}S$ and $\delta^{34}S$, and negative $\Delta^{33}S$. The TTGs sample amphibolites incorporating sulfur with dominantly sediment-derived, positive $\Delta^{33}S$ values (dotted oval within grey oval), not boninites with negative $\Delta^{33}S$ values.

In contrast to sediments, hydrothermal deposits in the altered oceanic crust are likely to have incorporated seawater sulfate with $\Delta^{33}S$ compositions < 0‰, (e.g., Bao et al., 2007; Farquhar et al., 2000; Montinaro et al., 2015). Hydrothermal systems have been documented in the ISB (Appel et al., 2001; Touret, 2003), but these have not yet been measured for sulfur isotopes. However, mesoarchean barites from the Fig Tree Group in South Africa have been shown to have generally negative $\Delta^{33}S$ values, and their $\Delta^{36}S$ values range from -0.62 to 2.2‰ (Bao et al., 2007; Farquhar et al., 2000; Montinaro et al., 2015), possibly representing an analogue for seawater-derived hydrothermal deposits contributing to slab fluids that formed the ISB amphibolites. The negative $\Delta^{33}S$ values of boninitic amphibolites in the ISB point towards a surface-derived, hydrothermally processed sulfur component as well (Siedenberg et al., 2016) (Figure 2.5A). Importantly, seawater sulfate derived from pore fluid release during initial stages of subduction (e.g., Schwarzenbach et al., 2018a) could have caused metasomatism of the forearc region of the mantle wedge and contributed to positive $\delta^{34}S$ and negative $\Delta^{33}S$ values in the boninitic amphibolites (Bao et al., 2007; Farquhar et al., 2000; Montinaro et al., 2015). Hence, based on the sulfur isotopic evidence, it is most likely that the amphibolites measured in this study and in Siedenberg et al. (2016) have variably incorporated surface-derived sulfur of both sedimentary and hydrothermal origins, with sedimentary derived sulfur dominating the tholeiitic rocks and hydrothermally derived sulfur with a stronger seawater sulfate component dominating the boninitic rocks. It is most likely that the tholeiitic and boninitic amphibolites were fed by different sulfur sources within the slab since different lithologies dehydrate at different pressure and temperature conditions, contributing to varying degrees to the sulfur fluxes within subduction zones (e.g., Tomkins and Evans, (2015); Li et al., (2020)).

The overlap between the IGC TTGs and ISB amphibolites with tholeiitic composition in their $\Delta^{33}S$ (Figure 2.3A) adds weight to previous models suggesting a genetic link between these two rock types (Nagel et al., 2012; Hoffmann et al., 2014) since melting processes would not induce changes in the $\Delta^{33}S$ composition. Along other sulfur isotopic axes, however, the TTGs are systematically offset from the majority of measured tholeiitic amphibolites. They are elevated by ~2-3‰ in $\delta^{34}S$ and ~0.4-1‰ in $\Delta^{36}S$ (Figures 2.3A and 2.4A). The sulfur isotopic compositions of the TTGs must therefore have been modified in some way after the emplacement of the source amphibolites and prior to TTG crystallization, moving the sulfur isotopic compositions of the TTGs away from the $\Delta^{36}S/\Delta^{33}S$ array typical of sulfur subject only to mass independent fractionation.

The effect of mass dependent Rayleigh fractionation processes can be distinguished from MIF-S by the slope of the $\Delta^{36}S/\Delta^{33}S$ array. These processes will move isotopic compositions along steep, negative arrays in $\Delta^{36}S/\Delta^{33}S$ space that may be distinguished from the relatively shallow mass independent array (Ono et al., 2006). Archean sedimentary sulfides usually tend to fall along a $\Delta^{36}S/\Delta^{33}S$ array with a slope of approximately -1 (e.g., (Farquhar et al., 2000; Johnston, 2011). This slope is known to have changed during the Archean, for example achieving values as negative as -3.6 in Paleoarchean deposits from the Dresser Formation in Australia (Wacey et al., 2015). These variations in mass independent $\Delta^{36}S/\Delta^{33}S$ fractionation ratios have generally been attributed to changes in atmospheric chemistry and resulting transparency to different wavelengths of light, (e.g., Farquhar et al., 2007). Importantly, despite these variations, Archean MIF-S still plots along $\Delta^{36}S/\Delta^{33}S$ trends that contrast strongly with Phanerozoic sedimentary sulfides subject only to MDF, which have a slope in the range of -6.85 (Ono et al., 2006; Schwarzenbach et al., 2018b) (See also Figure 2.4). This contrast allows mass dependent and mass independent fractionation processes to be discerned from one another in $\Delta^{36}S/\Delta^{33}S$ space.

While the TTGs appear to include sulfur isotopic signatures consistent with a component subject to mass dependent fractionation following a steep $\Delta^{36}S – \Delta^{33}S$ array, most of the ISB amphibolites are spread along a much shallower array consistent with mass independent fractionation (Figure 2.4A). The fact that the amphibolites with tholeiitic and boninitic composition reported by Siedenberg et al. (2016) fall along an array crossing slightly below the origin (Figure 2.4A) suggests they may have incorporated a relatively minor component subject to mass dependent fractionation. However, only input of material subject to mass independent fractionation can explain their horizontal spread along the $\Delta^{33}S$ axis (Figure 2.5A). The TTGs' scatter along the $\Delta^{36}S$ axis in the positive direction, opposite to most of the amphibolites and of greater magnitude, strongly suggests that they incorporated material subject to mass dependent fractionation that is not present in most of the amphibolites. All but one of the TTGs have compositions that, if moved parallel to a mass dependent array, would not cross within error of the origin where $\Delta^{33}S = \Delta^{36}S = 0$ (Figure 2.4A). The most reasonable explanation for the measured range of TTG compositions is that they first incorporated mass independently fractionated material with isotopic compositions largely in the range of the amphibolites with tholeiitic composition (Siedenberg et al., 2016), in some cases slightly exceeding the highest $\Delta^{33}S$ reported in these source rock analogues (Figure 2.4A). Subsequently, the TTGs appear to have variably incorporated another component with relatively low $\Delta^{33}S$ and high $\Delta^{36}S$ (Figure 2.5C). This two-step process, including an initial sulfur source subject to mass independent fractionation and incorporation of a second component subject to mass dependent fractionation, is the simplest and most likely path for the isotopic compositions of the TTGs to move into the upper right quadrant ($\Delta^{33}S$ and $\Delta^{36}S$ both positive) of $\Delta^{36}S - \Delta^{33}S$ space.

2.6.3. Metamorphic effects on S isotope compositions during prograde metamorphism

The studied samples all experienced variable degrees of metamorphic overprint. Previous studies have shown that metamorphism can result in sulfur loss induced by metamorphic devolatilization reactions, or gain or loss of sulfur during interaction with externally derived fluids during prograde metamorphism (e.g., Li et al., 2020). Temperatures during amphibolite facies metamorphic conditions in the Archean would have been favorable to the generation of sulfur bearing fluids from pyrite or other sulfide mineral decomposition associated with devolatilization reactions, and subsequent transport of the dissolved sulfur from the source rocks to higher crustal levels (Tomkins, 2010).

Disulfides such as pyrite and chalcopyrite dominate the sulfide content of basaltic amphibolites found in the ISB, along with traces of monosulfides such as pentlandite and pyrrhotite, as evidenced by the EMP results of this study (Supplementary table 2.10.C, Figure 2.2). The dominance of disulfides as compared to monosulfides in these rocks is further supported by a previous study in which measurable disulfide but not monosulfide sulfur could be extracted from these rocks (Siedenberg et al., 2016). Importantly, both pyrite and pyrrhotite are always either porous or strongly corroded along cleavage plains, and similarly, chalcopyrite grains often have S-free corrosion rims (Figure 2.2). We infer that these features reflect sulfide mineral breakdown, indicating that a low-fS_2 fluid interacted with these rocks to cause both disulfide and monosulfide decomposition (Li et al., 2021).

Pyrite decomposition and conversion to H_2S or HS^- species lost to metamorphic fluids would induce S isotope fractionation. While the ^{34}S fractionation factor between pyrite and dissolved H_2S is relatively small, between 1.2‰ at 300°C and 0.5‰ at 600°C (Ohmoto and Rye, 1979), open system Rayleigh fractionation in the TTGs' mafic source rocks prior to partial melting may, at least in part, explain the observed elevated $\delta^{34}S$ values of the TTGs (Bucholz et al., 2020; Evans et al., 2014). Modeling of this reaction at 550°C, where both pyrite and pyrrhotite lose sulfur to a transient H_2S fluid phase, and beginning with pyrite with $\delta^{34}S$ = -0.87‰ (the composition of the most ^{34}S depleted tholeiitic amphibolite measured by Siedenberg et al. (2016)) results in pyrite with $\delta^{34}S$ = 0.32‰ and pyrrhotite with $\delta^{34}S$ = -0.12‰ when 90% of the initial sulfur is removed. As pyrite is expected to dominate the final sulfide mineralogy of the rock if pyrrhotite is removed concurrently with pyrite decomposition, this process may induce an enrichment in ^{34}S of more than 1‰ (Figure 2.5B, Figure 2.6, see also supplementary material).

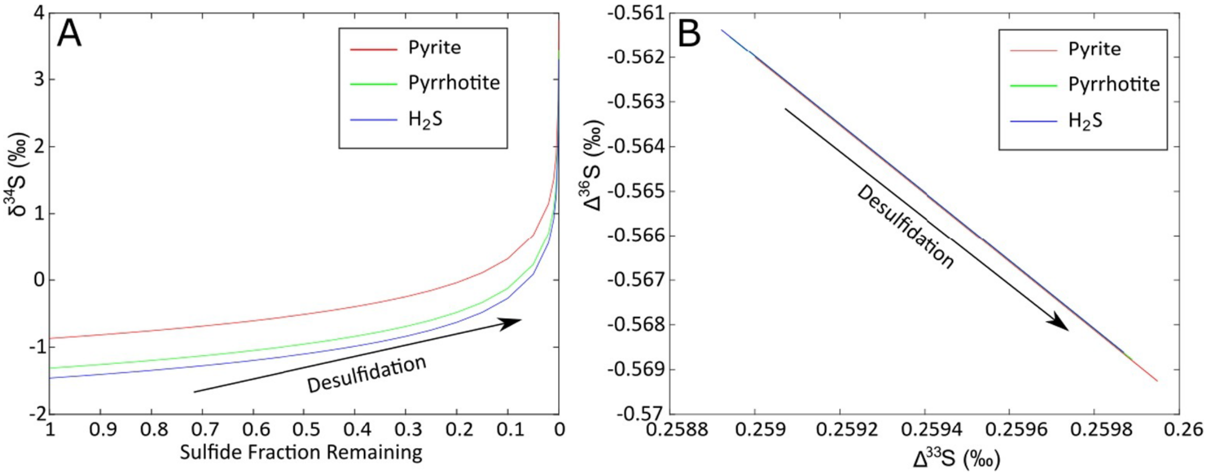

Figure 2.6: Model of pyrite desulfidation to pyrrhotite and H_2S, also described in Appendix B. Starting composition on both parts of the figure is the most $\Delta^{33}S$ enriched amphibolite reported by (Siedenberg et al., 2016). A) As the remaining fraction of pyrite becomes smaller, δ34S may increase by more than 1‰. $\delta^{34}S$ component of the model is based off of (Bucholz et al., 2020). B) The model predicts no measurable change in $\Delta^{33}S$ (<0.002‰) or $\Delta^{36}S$ (<0.01‰). Note the scale of the axes.

Hence, the mineralogy, textural evidence, and the TTGs' shift to positive $\delta^{34}S$ values point to sulfur loss associated with metamorphism. This likely took place during crustal thickening associated with arc accretion, prior to partial melting of the TTGs' source rocks. The lower $\delta^{34}S$ values of the amphibolites compared to the TTGs may be explained by the fact that these rocks were likely not subject to the same degree of desulfidation as the analogue rocks that ultimately melted at lower crustal levels to form the TTGs. It is notable that in the absence of a strong oxidative difference between phases, as in the case of partitioning between pyrite and H_2S, while measurable change in $\delta^{34}S$ can take place, any change in $\Delta^{33}S$ and $\Delta^{36}S$ is expected to be negligible (Figure 2.6B). Given the small magnitude of the fractionation involved, this process is unlikely to completely explain the high $\delta^{34}S$ of the TTGs as compared to the amphibolites, but it may have played an important role, especially if one considers that it may have been repeated in the TTGs following their crystallization.

Additional overprinting of the sulfur isotopic composition of ISB amphibolites and TTGs by metamorphic fluids mobilized from nearby sedimentary lithologies subsequent to their emplacement is possible but unlikely. Sharp isotopic boundaries between sedimentary and igneous lithologies are found in the Hadean/Eoarchean Nuvvuagittuq Greenstone Belt of Quebec (Thomassot et al., 2015). There, metamorphism induced reactive transport of sulfur from metasediments into igneous bodies was limited to less than ~10 m from the contacts (Thomassot et al., 2015). Samples in this study were taken from far greater distances from any metasedimentary rocks. In addition, metasediments in the area south of the ISB, where most TTGs studied here were collected, are very rare (Nutman and Friend, 2009).

2.6.4. Partial melting and hydrous melt fluid source

Previous modeling work based on phase equilibrium calculations indicates that partial melting of the TTGs' precursor tholeiitic amphibolites occurred at pressures between 10 and 14 kbar and temperatures between 860 and 980°C (Gardiner et al., 2019; Hoffmann et al., 2014; Hoffmann et al., 2019; Nagel et al., 2012). It is likely that partial melting was not only triggered by the breakdown of amphibole but also through infiltration of fluids derived from dehydrating underlying lithologies during crustal thickening in response to arc accretion processes (e.g., Hastie et al., 2016). As outlined in the previous section, the positive offset in the studied TTGs' $\Delta^{36}S$ signatures relative to those of their amphibolitic source rocks requires an additional process that involves sulfur input from other sources following source rock emplacement. This is because melting of such rocks at temperatures above 800°C should quantitively transfer sulfur to the melt, with no associated change in isotopic composition.

Modeling of mixing in quadruple sulfur isotope space between a low $\Delta^{33}S$ ISB amphibolite reported by Siedenberg et al. (2016), a selected high $\Delta^{36}S$ barite sample from Montinaro et al. (2015), as well as a high $\Delta^{33}S$ BIF sample from Whitehouse (2013), produces a mixing plane that agrees well with the array formed by the TTGs in this study (Figure 2.7). The fluid that induced partial melting of the TTGs' source rocks appears to have been dominated by sulfur from barite or similar hydrothermally derived material with high $\Delta^{36}S$, perhaps as a result of redox processes fractionating such material along an array similar to that reported by Ono et al. (2006) (Figure 2.7, see also supplementary Figure 2.A.1). Incorporation of such fluid would result in increased $\Delta^{36}S$ values, as well as decreased $\Delta^{33}S$ values and increased $\delta^{34}S$ values, as observed in the TTGs and some analyzed amphibolites (Figure 2.5C).

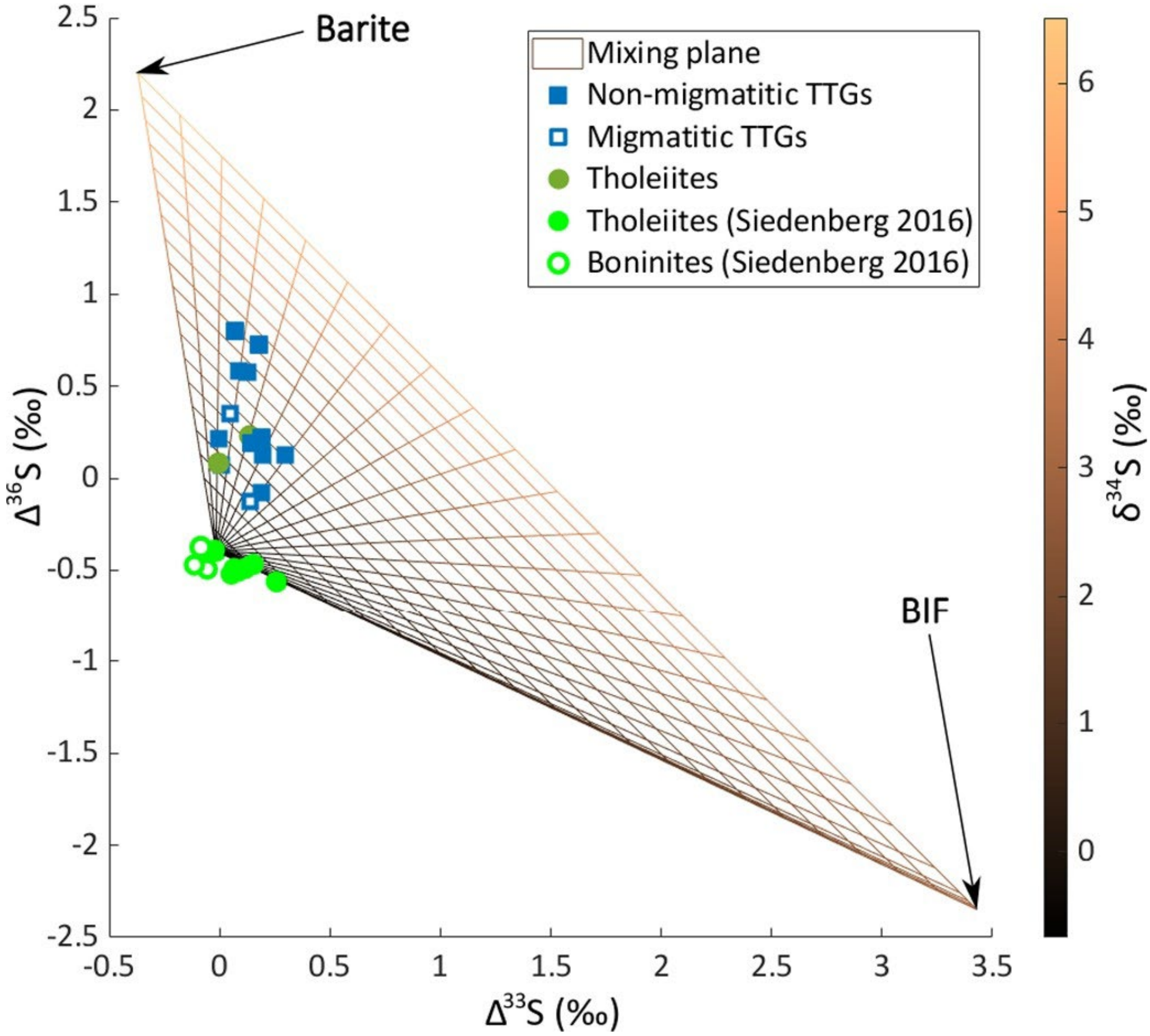

Figure 2.7: Three component isotope mixing model. The lower left endmember of the triangular mixing plane is a low $\Delta^{33}S$ ISB amphibolite from Siedenberg et al. (2016), the upper left endmember is a selected high $\Delta^{36}S$ barite sample from Bao et al. (2007), and the lower right endmember is a high $\Delta^{33}S$ BIF sample from Whitehouse, (2013). Note how the mixing line defining the bottom edge of the triangle between the low $\Delta^{33}S$ amphibolite and the BIF closely follows the distribution of points representing the tholeiitic amphibolites in $\Delta^{33}S$- $\Delta^{36}S$ space. Further explanation of the model and views of this triangle from multiple angles are available in supplementary Figures 2.10.A.2 to 2.10.A.4.

Mass dependent fractionation associated with redox processes can take place during dehydration of hydrothermally altered crustal rocks e.g., as sulfate is partly removed during dehydration and reduced to form H_2S. Similarly, sulfur fractionation would take place as sulfate bearing fluids move through the source rocks and are reduced in the process to form sulfide. Both processes would be associated with mass dependent Rayleigh fractionation to move its composition along a fractionation line in $\Delta^{33}S$-$\Delta^{36}S$ space steeper than that of the

Archean array (Ono et al., 2006). Such a process is hinted at in the slope of $\Delta^{36}S = -0.75 * \Delta^{33}S$ defined by the array of Isua BIF sulfide values (Whitehouse, 2013), subparallel to the mass-dependent fractionation line. It is notable that these sulfides, while clearly composed of sedimentary sulfur as a result of their $\Delta^{33}S$ composition, are also secondary (Whitehouse, 2013). Redox processes are also hinted at by the strong vertical scatter of sulfur isotopic compositions in Archean barites in $\Delta^{33}S$- $\Delta^{36}S$ space (Bao et al., 2007; Farquhar et al., 2000) (Figure 2.4B). Further isotope work on sedimentary and especially hydrothermally-derived Eoarchean sulfur from the ISB and the adjacent area may help to clarify whether a surface-derived component could have been introduced to these melts with or without such further isotopic modification.

2.6.5. Geodynamic implications

The sulfur isotope compositions and sulfide composition of ISB amphibolites and TTGs suggest that they have incorporated mass independently fractionated sulfur originally derived from sedimentary and hydrothermal material. This material was introduced to the mantle, possibly via subduction or a similar horizontal tectonic process, and variably mixed with magmatic sulfur to form the ISB tholeiitic basalts, the protoliths of the amphibolites. These tholeiitic basalts were subject to further isotopic modification, likely as a result of sulfur lost to metamorphic fluids under amphibolite facies conditions during arc accretion. During metamorphism of the amphibolites, it is likely that sulfur-bearing fluids escaped the rock, enriching the sulfur that remained in these rocks in ^{34}S by means of Rayleigh fractionation. Elevated $\Delta^{36}S$ in the TTGs relative to most tholeiitic metabasalts suggests that the metabasalts that melted to form the TTGs experienced additional input of sulfur from a fluid carrying hydrothermally derived sulfate, from a deeper part of the thickening crust. The sulfur in the amphibolites was incorporated into melts that produced the TTGs. These isotopically heterogeneous melts may have mixed to a limited degree, though not enough to obliterate their heterogeneity. These melts were emplaced to form the TTGs at mid-crustal levels. Subsequently, TTG sulfides may have been further modified by additional metamorphism and sulfide sulfur loss, causing further ^{34}S enrichment, but only very minor modification of $\Delta^{33}S$ and $\Delta^{36}S$.

2.7. Conclusions

This first systematic study of quadruple sulfur isotopes in Eoarchean TTGs indicates that they have incorporated surface-derived, mass independently fractionated sulfur during the process of their formation. A mass independently fractionated component is the most likely explanation for the elevated $\Delta^{33}S$ values of these rocks, concurrent with low $\delta^{34}S$ values. This MIF-S signal is also present in the TTGs' inferred amphibolitic source rocks. The TTGs' high $\Delta^{36}S$ values relative to most amphibolites suggests that they incorporated an additional hydrothermally derived component, likely by way of fluids released from the lower crust that triggered partial melting of the TTGs' source rocks. These results help to further establish the study of multiple sulfur isotopes as a powerful tool to trace the movement of sulfur throughout the magmatic system. They bring Eoarchean geodynamic processes into sharper focus, buttressing existing arguments for early horizontal plate tectonics and a genetic link between IGC amphibolites and TTGs, as well as providing new insights into the formation of the earliest continental crust.

2.8. Declaration of competing interest

The authors declare that they have no known competing financial interests or personal relationships that could have appeared to influence the work reported in this paper.

2.9. Acknowledgements

JEH, JAL, EMS, and HS would like to thank the German Science Foundation (DFG) for funding project HO4794/3-1 and SCHW1889/2-1 within the DFG priority program SPP1833 ‘Building a Habitable Earth.’ MR thanks the Danish National Research Fund for grants to NordCEE. We also thank Andreas Lutter for technical support, and Yogita Kadlag for assistance with error propagation. We would also like to thank Frédéric Moynier for editorial handling, Michael Antonelli and an anonymous reviewer of this manuscript for their helpful feedback, as well as the anonymous reviewers of a previous version of this manuscript for their constructive comments.

2.10. Supplementary material for the second chapter

2.10.A. Modeling information

2.10.A.1. Distillation of pyrite into pyrrhotite and H_2S:

All mathematical modeling was done in Matlab. The Rayleigh distillation model assumes an initial pyrite isotopic composition of the ISB amphibolite with the highest $\Delta^{33}S$ reported by (Siedenberg et al., 2016), with the following composition:

$\delta^{34}S = -0.87‰$

$\Delta^{33}S = 0.259‰$

$\Delta^{36}S$ = -0.562‰

All values are converted into δ notation for ease of computation. Fractionation factors with respect to $\delta^{34}S$ between phases at the appropriate temperatures are obtained from (Ohmoto and Rye, 1979):

ε34_FeS2_H2S = ((0.40 * 10^6) / (temperature^2))
ε34_FeS_H2S = ((0.1 * 10^6) / (temperature^2))

Temperature here is in Kelvin. To model multiple isotopes, typical mass dependent theta values are assumed (Farquhar et al., 2000; Johnston et al., 2008):

$\theta_{33} = 0.515$

$\theta_{36} = 1.90$

Vienna Canyon Diablo Troilite values for $\delta^{34}S$, $\Delta^{33}S$, and $\Delta^{36}S$ are obtained from (Ding et al., 2001).

The Rayleigh fractionation model follows Bucholz et al. (2020) at 550°C with ^{33}S and ^{36}S also modeled as above, and as shown in Figure 2.6 of the main text. No measurable change in $\Delta^{33}S$ or $\Delta^{36}S$ is indicated by the model (see Figure 2.10.A.1)

Note that this model can also produce measurable changes in $\Delta^{33}S$ and $\Delta^{36}S$ with the above assumed theta values when the reaction involves redox at lower temperatures. A simplified version of this model simulating a reaction between sulfate and H_2S at 300°C using the following value of epsilon from (Ohmoto and Lasaga, 1982):

ε34 = -((6.463 * 10^6) / (temperature^2) + (0.56 * 10^3/(temperature)))

yields a steep, negative slope and measurable change in $\Delta^{33}S$-$\Delta^{36}S$ space (Figure 2.10.A.1).

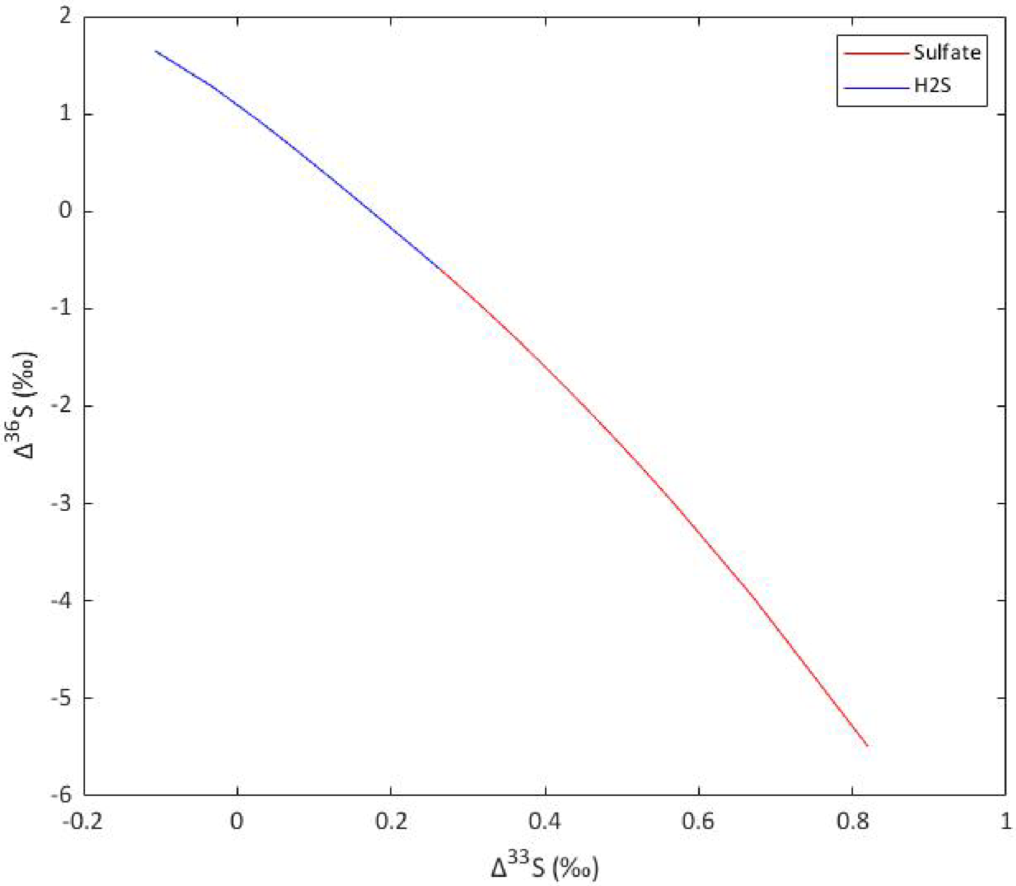

Figure 2.10.A.1: Modelled reaction between sulfate and H_2S at 300°C. Note that this reaction is not applicable to pyrite decomposition in the TTGs as no sulfate is present and temperatures are higher under metamorphism, but it may explain the range of $\Delta^{36}S$ values observed in surface-derived material such as hydrothermal deposits.

2.10.A.2. Mixing of Archean sedimentary, hydrothermal, and amphibolite endmembers:

This model is not intended to precisely simulate what happened in the Eoarchean at Isua but simply to demonstrate that it is reasonable for the mixing of three endmembers similar to this to produce the isotopic compositions we observe in the ISB TTGs.

The endmembers used to produce this model are:

Barite with the highest $\Delta^{36}S$ reported by Bao et al. (2007):

$\delta^{34}S = 6.512‰$

$\Delta^{33}S = -0.37‰$

$\Delta^{36}S = 2.2‰$

Banded Iron formation with the highest $\Delta^{33}S$ reported by Whitehouse (2013) (as determined by SIMS):

$\delta^{34}S = 0.53‰$

$\Delta^{33}S = 3.43‰$

$\Delta^{36}S = -2.35‰$

A tholeiitic amphibolite with the lowest $\Delta^{33}S$ reported by Siedenberg et al. (2016):

$\delta^{34}S = -0.669‰$

$\Delta^{33}S = -0.016‰$

$\Delta^{36}S = -0.396‰$

All melts are assumed to have equal concentrations of 50ppm S with complete transfer from source rocks into melts (no fractionation associated with melting).

Values of theta are assumed to be as in model 1 and all values are simplified using isotope ratios. These are subject to simple mixing and then converted back into delta notation. Over the relevant ranges of isotope values, we observe mixing lines to be essentially linear in $\delta^{34}S$-$\Delta^{33}S$-$\Delta^{36}S$ space, as LaFlamme et al. (2018) also notes. Different viewing angles are offered in three dimensions, with mixing plane $\delta^{34}S$ represented as in Figure 2.7 of the text and supplementary Figures 2.10.A.2 through 2.10.A.4.

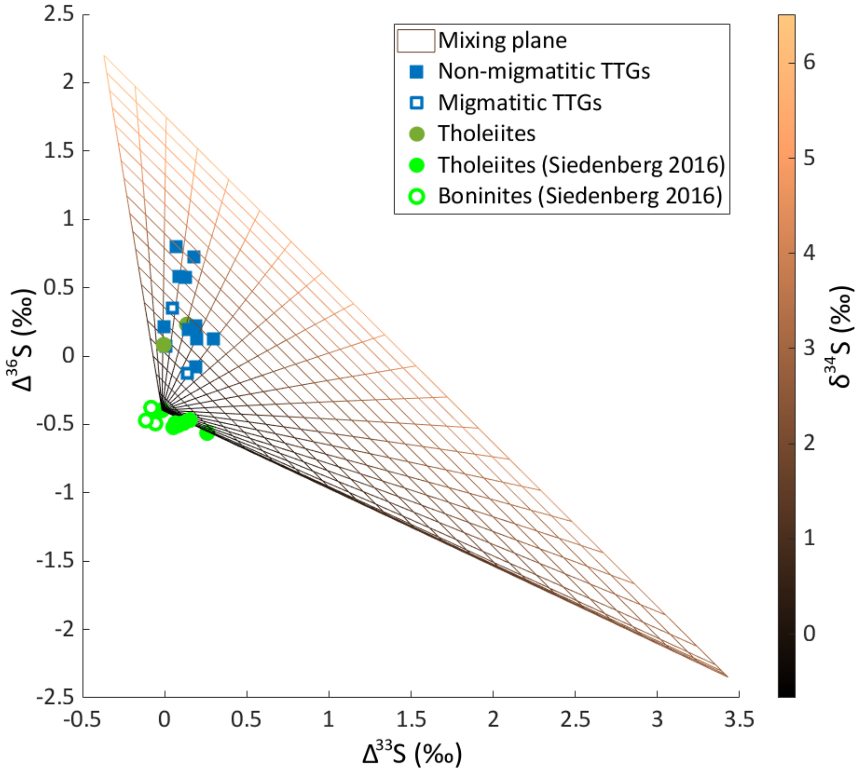

Figure 2.10.A.2: Mixing model in $\Delta^{33}S$-$\Delta^{36}S$ space. Note that here, unlike in Figure 2.7, the mixing plane is shown as a grid overlying some of the points beneath it (lower on the $\delta^{34}S$ axis).

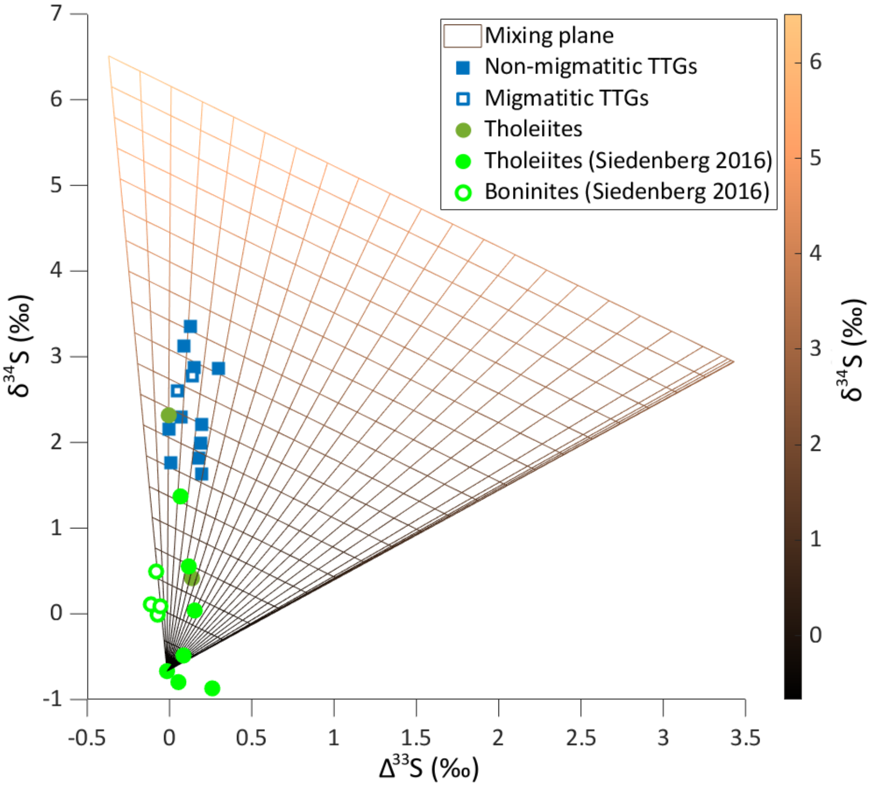

Figure 2.10.A.3: Mixing model in $\Delta^{33}S$- $\delta^{34}S$ space. The mixing plane color scheme shows the same information as the Y axis from this angle.

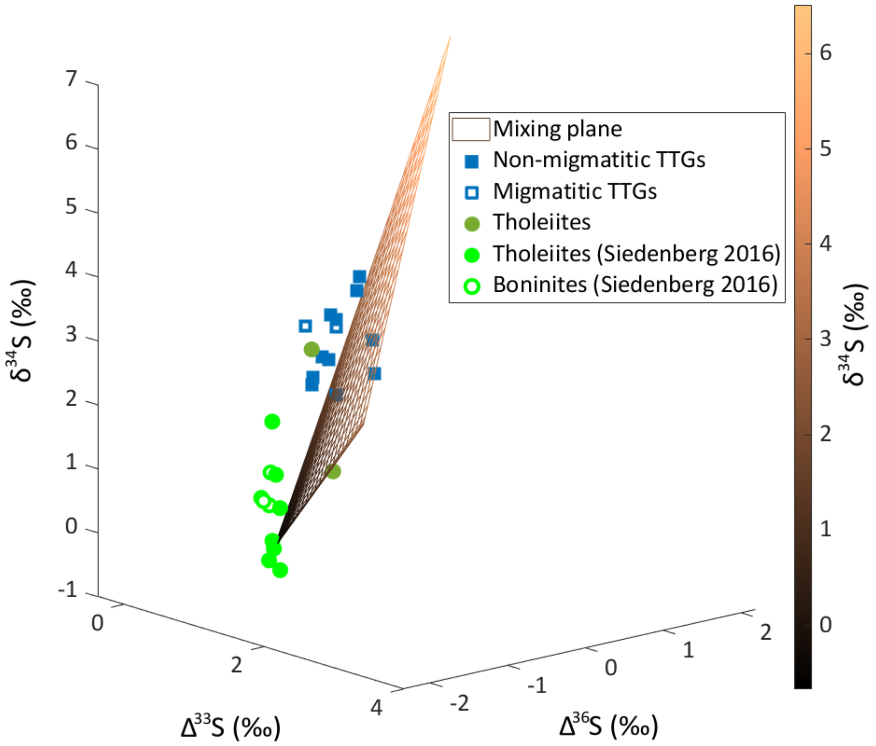

Figure 2.10.A.4: Isometric view of the mixing model.

The example endmembers are represented by vertices of the triangular surface. Divergence of presented data points, from this study and from Siedenberg et al. (2016), from the mixing array may be explained by mass dependent or mass independent isotopic variability in the mixing endmembers.

Note that the edges of the mixing plane appear as straight lines because offsets in $\Delta^{33}S$ and $\Delta^{36}S$ associated with mixing endmembers with such a small range of $\delta^{34}S$ values are not significant. Viewed at the appropriate scale, these mixing lines are in fact curves. To illustrate this, mixing of sulfur with $\delta^{34}S = -2.82$, as in the ISB metapelite with lowest $\delta^{34}S$ reported by Papineau and Mojzsis, (2006) and sulfur with $\delta^{34}S = 8.06$, as in the Mesoarchean barite with the highest $\delta^{34}S$ reported by (Montinaro et al., 2015), was modelled. The maximum offset in $\Delta^{33}S$ was 0.0037 and the maximum offset in $\Delta^{36}S$ was 0.025, far smaller than the anomalies observed in this study (Supplementary Figure 2.10.A.5).

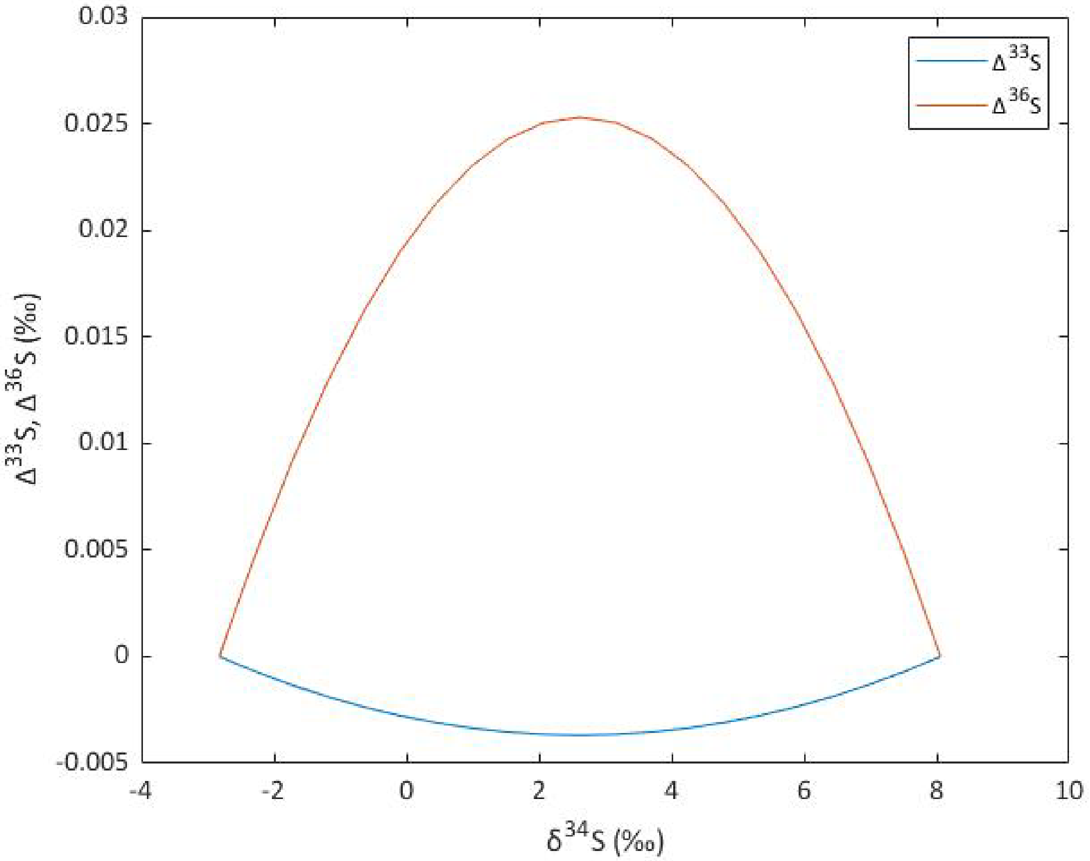

Figure 2.10.A.5: Small offsets in $\Delta^{33}S$ and $\Delta^{36}S$ produced by mixing endmembers with $\delta^{34}S$ values from Papineau and Mojzsis (2006) and Montinaro et al., (2015), as described above in the text. Note the scale of the Y axis. Endmember $\Delta^{33}S$ and $\Delta^{36}S$ values are set at zero to make the offset visible.

2.10.B. Sample locations

Supplementary table 2.10.B: Sample Locations

Sample	Type	Age [Ga]	Location	Age/ Location reference
JEH-2007-01	Amphibolite (metagabbro)	3.80	N 65°05.074’ W -50°09.924’	1, 2, 3
2000-010	Amphibolite (metabasalt)	3.72	ISB Northern ca. 3700 Ma terrane	2, 4, 5
498027	Migmatitic tonalite	3.87	N 64°16.373’ W -50°33.023’	1, 6
JEH-SG-07	Migmatitic tonalite	3.80	N 65°02.576’ W -50°08.115’	1, 6
010-018	TTG	3.80	N 65°02.338’ W -50°13.550’	7, 8
010-024	TTG	3.80	N 65°01.974’ W -50°15.891’	7, 8
010-025	TTG	3.80	N 65°02.231’ W -50°15.092’	7, 8
010-038	TTG	3.81	N 65°00.827’ W -50°13.744’	7, 8
010-038 Munster Dup	TTG	3.81	N 65°00.827’ W -50°13.744’	7, 8
010-039	TTG	3.81	N 65°00.824’ W -50°13.785’	7, 8
JEH-2007-05	TTG	3.68	N 65°06.103’ W -50°07.455’	1, 6
JEH-SG-04	TTG	3.77	N 65°04.103’ W -50°10.448’	1
JEH-SG-04 Munster Dup	TTG	3.77	N 65°04.103’ W -50°10.448’	1
JEH-SG-05	TTG	3.79	N 65°04.868’ W -50°10.734’	1, 6
JEH-SG-09	TTG	3.80	N 65°04.945’ W -50°10.692’	1, 8

References: 1. Hoffmann et al. (2011a) 2. Hoffmann et al. (2011b) 3. Crowley (2003) 4. Nutman and Friend (2009) 5. Polat and Hofmann (2003a) 6. Næraa et al. (2012) 7. Hoffmann et al. (2014) 8. Nutman et al. (1999)

2.10.C. Microprobe results

Supplementary table 2.10.C. microprobe results

Point name	Ni wt%	S wt%	As wt%	Fe wt%	Cu wt%	Co wt%	Zn wt%	Total wt%	Interpretation	Sample type	Measurement kV
010-018-S1-P1	<DL	35.21	<DL	30.60	33.57	<DL	<DL	99.38	Chalcopyrite	TTG	15
010-018-S1-P2	<DL	35.69	<DL	30.32	33.79	0.05	<DL	99.85	Chalcopyrite	TTG	15
010-024-S2-P1	0.14	53.59	<DL	48.05	<DL	<DL	<DL	101.78	Pyrite	TTG	15
010-024-S2-P2	0.07	53.51	<DL	47.98	<DL	<DL	<DL	101.56	Pyrite	TTG	15
010-024-S2-P5	0.04	52.49	0.12	47.05	<DL	<DL	<DL	99.70	Pyrite	TTG	15
010-024-S2-P6	<DL	52.84	0.23	47.20	<DL	<DL	0.08	100.34	Pyrite	TTG	15
010-038-S1-P1	<DL	54.97	<DL	44.29	<DL	2.24	0.08	101.57	Pyrite	TTG	15
010-038-S1-P2	<DL	34.95	<DL	30.28	33.92	0.05	<DL	99.19	Chalcopyrite	TTG	15
010-038-S1-P4	<DL	54.60	<DL	46.40	<DL	0.04	<DL	101.04	Pyrite	TTG	15
010-038-S2-P1	0.37	39.40	<DL	60.08	0.10	0.07	0.10	100.11	Pyrrhotite	TTG	15
010-038-S2-P2	0.21	39.76	<DL	59.49	0.35	0.10	<DL	99.91	Pyrrhotite	TTG	15
010-038-S2-P3	0.23	39.72	<DL	58.27	1.70	0.07	<DL	100.00	Pyrrhotite	TTG	15
010-039-S1-P16	<DL	52.80	<DL	48.20	<DL	<DL	<DL	101.00	Pyrite	TTG	15
010-039-S1-P3	<DL	34.64	<DL	33.08	32.71	<DL	<DL	100.43	Chalcopyrite	TTG	15
010-039-S1-P6	0.12	53.45	<DL	47.85	<DL	<DL	0.06	101.48	Pyrite	TTG	15
010-039-S1-P7	<DL	37.72	<DL	34.73	29.16	<DL	0.36	101.97	Chalcopyrite	TTG	15
2000-10-w-s1-p7	35.35	41.79	<DL	17.14	<DL	6.42	<DL	100.69	Pentlandite	Amphibolite	20
2000-10-w-s1-p9	2.71	54.09	<DL	43.54	0.30	0.24	<DL	100.89	Pyrite	Amphibolite	20
2000-10-w-s2-p11	2.71	53.93	<DL	42.99	0.04	0.81	<DL	100.48	Pyrite	Amphibolite	20
2000-10-w-s2-p2	41.69	33.20	<DL	25.45	<DL	0.19	<DL	100.54	Pentlandite	Amphibolite	20
2000-10-w-s2-p5	2.44	53.75	<DL	42.93	0.04	1.31	<DL	100.47	Pyrite	Amphibolite	20
2000-10-w-s2-p6	40.93	33.52	<DL	26.00	<DL	0.16	<DL	100.61	Pentlandite	Amphibolite	20
2000-10-w-s2-p7	41.08	33.52	<DL	25.45	<DL	0.14	<DL	100.19	Pentlandite	Amphibolite	20
2000-10-w-s2-p9	27.17	40.41	<DL	32.07	0.41	0.42	<DL	100.48	Pentlandite	Amphibolite	20
2000-10-w-s3-p1	<DL	35.22	<DL	30.66	34.22	0.03	<DL	100.13	Chalcopyrite	Amphibolite	20
2000-10-w-s3-p2	<DL	34.51	<DL	31.40	34.12	0.03	<DL	100.05	Chalcopyrite	Amphibolite	20
2000-10-w-s3-p3	1.69	53.66	<DL	45.04	0.04	0.19	<DL	100.63	Pyrite	Amphibolite	20
2000-10-w-s3-p4	2.22	53.80	<DL	44.76	0.04	0.08	<DL	100.89	Pyrite	Amphibolite	20
2000-10-w-s3-p6	2.40	53.88	<DL	44.21	0.08	0.28	<DL	100.83	Pyrite	Amphibolite	20

Supplementary table 2.10.C. microprobe results

Point name	Ni wt%	S wt%	As wt%	Fe wt%	Cu wt%	Co wt%	Zn wt%	Total wt%	Interpretation	Sample type	Measurement kV
2000-10-w-s3-p7	<DL	35.14	<DL	30.62	34.25	0.05	<DL	100.05	Chalcopyrite	Amphibolite	20
2000-10-w-s4-p1	<DL	35.54	<DL	30.59	34.28	0.03	<DL	100.44	Chalcopyrite	Amphibolite	20
2000-10-w-s4-p2	<DL	35.28	<DL	30.63	34.40	0.04	<DL	100.35	Chalcopyrite	Amphibolite	20
2000-10-w-s4-p3	<DL	35.55	<DL	30.58	34.39	0.05	<DL	100.56	Chalcopyrite	Amphibolite	20
2000-10-w-s4-p4	3.54	53.14	0.14	42.61	0.03	0.66	<DL	100.12	Pyrite	Amphibolite	20
2000-10-w-s4-p5	6.78	53.50	<DL	38.90	0.06	1.21	<DL	100.44	Pyrite	Amphibolite	20
2000-10-w-s4-p6	3.91	53.40	<DL	42.80	0.06	0.08	<DL	100.25	Pyrite	Amphibolite	20
2000-10-w-s4-p7	0.10	35.01	<DL	30.82	34.09	0.07	<DL	100.09	Chalcopyrite	Amphibolite	20
2000-10-w-s4-p8	0.19	36.39	<DL	31.17	33.15	0.09	<DL	100.99	Chalcopyrite	Amphibolite	20
2000-10-w-s5-p1	35.77	42.09	<DL	21.64	0.34	0.72	<DL	100.55	Pentlandite	Amphibolite	20
2000-10-w-s5-p10	1.89	53.75	<DL	44.79	0.01	0.09	0.04	100.55	Pyrite	Amphibolite	20
2000-10-w-s5-p2	1.66	53.60	<DL	44.94	<DL	0.07	<DL	100.27	Pyrite	Amphibolite	20
2000-10-w-s5-p3	0.06	34.48	<DL	31.32	34.09	0.05	<DL	99.98	Chalcopyrite	Amphibolite	20
2000-10-w-s5-p4	0.02	34.02	<DL	31.18	34.12	0.06	<DL	99.40	Chalcopyrite	Amphibolite	20
2000-10-w-s5-p5	0.02	34.81	<DL	31.28	33.91	0.05	<DL	100.07	Chalcopyrite	Amphibolite	20
2000-10-w-s5-p6	0.02	34.20	<DL	31.27	34.11	0.04	<DL	99.64	Chalcopyrite	Amphibolite	20
2000-10-w-s5-p7	2.13	53.68	<DL	44.63	0.08	0.07	<DL	100.59	Pyrite	Amphibolite	20
JEH-2007-01_S1	0.42	39.43	0.08	59.39	0.28	0.12	<DL	99.70	Pyrrhotite	Amphibolite	15
JEH-2007-01_S3_P1	<DL	35.18	<DL	29.92	34.11	0.04	<DL	99.24	Chalcopyrite	Amphibolite	15
JEH-2007-01_S3_P2	<DL	35.30	<DL	30.48	34.44	0.06	<DL	100.27	Chalcopyrite	Amphibolite	15
JEH-2007-01_S4_P1	0.04	35.49	<DL	29.96	33.57	0.08	<DL	99.13	Chalcopyrite	Amphibolite	15
JEH-2007-01-S10-P1	0.25	40.24	<DL	58.53	0.33	0.09	<DL	99.43	Pyrrhotite	Amphibolite	15
JEH-2007-01-S5-P1	0.11	35.33	<DL	30.61	32.92	0.05	<DL	99.01	Chalcopyrite	Amphibolite	15
JEH-2007-01-S6-P1	0.07	35.39	<DL	30.59	34.59	<DL	<DL	100.64	Chalcopyrite	Amphibolite	15
JEH-2007-01-S6-P2	0.06	52.25	<DL	46.05	1.11	0.15	<DL	99.60	Pyrite	Amphibolite	15
JEH-2007-01-S7-P1	<DL	35.48	<DL	29.89	33.82	0.04	<DL	99.24	Chalcopyrite	Amphibolite	15
JEH-2007-01-S7-P2	0.04	35.47	<DL	30.13	33.65	0.04	<DL	99.32	Chalcopyrite	Amphibolite	15
JEH-2007-01-S8-P1	<DL	35.56	<DL	30.31	34.34	<DL	<DL	100.21	Chalcopyrite	Amphibolite	15
JEH-2007-01-S9-P1	<DL	35.37	<DL	30.26	34.23	<DL	<DL	99.85	Chalcopyrite	Amphibolite	15

Supplementary table 2.10.C. microprobe results

Point name	Ni wt%	S wt%	As wt%	Fe wt%	Cu wt%	Co wt%	Zn wt%	Total wt%	Interpretation	Sample type	Measurement kV
JEH-2007-01-S9-P2	<DL	35.81	<DL	29.95	33.90	<DL	<DL	99.66	Chalcopyrite	Amphibolite	15
JEH-2007-08-s1-p1	1.26	40.47	<DL	58.63	<DL	0.09	<DL	100.46	Pyrrhotite	Amphibolite	20
JEH-2007-08-s1-p2	0.59	40.14	<DL	59.49	<DL	0.10	<DL	100.32	Pyrrhotite	Amphibolite	20
JEH-2007-08-s1-p3	2.18	54.02	<DL	44.79	0.02	<DL	<DL	101.00	Pyrite	Amphibolite	20
JEH-2007-08-s1-p4	4.18	53.83	<DL	42.74	0.05	0.21	<DL	101.00	Pyrite	Amphibolite	20
JEH-2007-08-s1-p5	0.73	39.71	<DL	59.12	0.08	0.11	<DL	99.75	Pyrrhotite	Amphibolite	20
JEH-2007-08-s2-p1	0.02	35.18	<DL	30.73	34.14	0.02	<DL	100.08	Chalcopyrite	Amphibolite	20
JEH-2007-08-s2-p2	<DL	34.24	<DL	31.71	34.00	0.05	<DL	99.99	Chalcopyrite	Amphibolite	20
JEH-2007-08-s2-p3	0.52	40.26	<DL	59.54	0.06	0.13	<DL	100.50	Pyrrhotite	Amphibolite	20
JEH-2007-08-s2-p4	0.51	40.22	<DL	59.57	<DL	0.13	<DL	100.43	Pyrrhotite	Amphibolite	20
JEH-2007-08-s2-p5	0.52	39.92	<DL	59.34	<DL	0.11	<DL	99.88	Pyrrhotite	Amphibolite	20
JEH-2007-08-s2-p6	0.54	39.83	<DL	59.37	<DL	0.13	<DL	99.87	Pyrrhotite	Amphibolite	20
JEH-2007-08-s4-p1	2.32	41.10	<DL	56.70	<DL	0.09	<DL	100.22	Pyrrhotite	Amphibolite	20
JEH-2007-08-s4-p2	1.75	40.64	<DL	57.49	<DL	0.09	<DL	99.97	Pyrrhotite	Amphibolite	20
JEH-2007-08-s4-p3	1.98	40.85	<DL	57.20	<DL	0.11	<DL	100.14	Pyrrhotite	Amphibolite	20
JEH-2007-08-s5-p1	0.77	40.14	<DL	59.37	<DL	0.12	<DL	100.40	Pyrrhotite	Amphibolite	20
JEH-2007-08-s5-p2	0.66	39.95	<DL	59.48	<DL	0.13	0.03	100.24	Pyrrhotite	Amphibolite	20
JEH-2007-08-s5-p3	0.69	40.17	<DL	59.19	0.04	0.13	<DL	100.20	Pyrrhotite	Amphibolite	20
JEH-2007-08-s5-p4	0.80	40.11	<DL	59.45	0.04	0.12	<DL	100.51	Pyrrhotite	Amphibolite	20
JEH-2007-08-s5-p5	0.47	39.93	<DL	59.41	<DL	0.12	<DL	99.93	Pyrrhotite	Amphibolite	20
JEH-2007-08-s5-p6	0.46	40.24	<DL	59.61	<DL	0.15	<DL	100.45	Pyrrhotite	Amphibolite	20
JEH-2007-08-s5-p7	0.43	40.08	<DL	59.63	<DL	0.13	<DL	100.27	Pyrrhotite	Amphibolite	20
JEH-2007-08-s5-p8	0.49	40.11	<DL	59.52	<DL	0.14	<DL	100.25	Pyrrhotite	Amphibolite	20
JEH-2007-08-s6-p1	0.16	40.05	<DL	59.55	0.05	0.23	<DL	100.02	Pyrrhotite	Amphibolite	20
JEH-2007-08-s6-p2	0.19	40.00	<DL	59.59	0.05	0.17	0.02	100.01	Pyrrhotite	Amphibolite	20
JEH-2007-08-s6-p3	<DL	35.19	<DL	30.92	34.10	0.05	<DL	100.27	Chalcopyrite	Amphibolite	20
JEH-2007-08-s6-p4	0.30	39.90	<DL	59.64	<DL	0.17	0.03	100.04	Pyrrhotite	Amphibolite	20
JEH-2007-08-s6-p5	0.27	40.15	<DL	59.43	0.04	0.17	<DL	100.05	Pyrrhotite	Amphibolite	20
JEH-2007-08-s6-p7	0.27	40.05	<DL	59.54	0.04	0.17	<DL	100.06	Pyrrhotite	Amphibolite	20

Supplementary table 2.10.C. microprobe results

Point name	Ni wt%	S wt%	As wt%	Fe wt%	Cu wt%	Co wt%	Zn wt%	Total wt%	Interpretation	Sample type	Measurement kV
JEH-2007-08-s6-p8	0.57	40.27	<DL	59.45	0.01	0.14	<DL	100.44	Pyrrhotite	Amphibolite	20
JEH-2007-08-s7-p1	0.69	40.11	<DL	59.13	<DL	0.11	<DL	100.03	Pyrrhotite	Amphibolite	20
JEH-2007-08-s7-p2	0.59	40.28	<DL	59.38	<DL	0.14	<DL	100.38	Pyrrhotite	Amphibolite	20
JEH-2007-08-s7-p3	0.58	39.97	<DL	59.32	<DL	0.14	<DL	100.00	Pyrrhotite	Amphibolite	20
JEH-2007-08-s7-p4	0.98	39.23	<DL	59.78	<DL	0.16	<DL	100.15	Pyrrhotite	Amphibolite	20
JEH-2007-08-s8-p1	1.00	40.04	<DL	58.82	<DL	0.11	<DL	99.96	Pyrrhotite	Amphibolite	20
JEH-2007-08-s8-p2	0.77	40.17	<DL	59.16	<DL	0.12	<DL	100.22	Pyrrhotite	Amphibolite	20
JEH-2007-08-s8-p3	0.81	40.15	<DL	59.22	0.02	0.12	<DL	100.31	Pyrrhotite	Amphibolite	20
JEH-2007-08-s8-p4	<DL	34.40	<DL	31.84	33.68	0.04	<DL	99.95	Chalcopyrite	Amphibolite	20
JEH-2007-14-s10-p1	<DL	35.39	<DL	31.11	34.28	0.04	<DL	100.83	Chalcopyrite	Amphibolite	20
JEH-2007-14-s10-p2	<DL	35.49	<DL	30.96	34.14	0.03	<DL	100.61	Chalcopyrite	Amphibolite	20
JEH-2007-14-s10-p3	<DL	35.30	<DL	30.72	34.43	0.05	0.10	100.60	Chalcopyrite	Amphibolite	20
JEH-2007-14-s11-p1	<DL	35.13	<DL	30.67	34.45	0.03	<DL	100.28	Chalcopyrite	Amphibolite	20
JEH-2007-14-s11-p2	<DL	35.10	<DL	30.69	34.48	0.05	<DL	100.32	Chalcopyrite	Amphibolite	20
JEH-2007-14-s11-p4	<DL	34.38	<DL	30.91	34.13	0.05	<DL	99.47	Chalcopyrite	Amphibolite	20
JEH-2007-14-s11-p5	0.01	35.30	<DL	30.83	34.35	0.05	<DL	100.54	Chalcopyrite	Amphibolite	20
JEH-2007-14-s11-p7	0.01	34.66	<DL	31.19	33.99	0.06	<DL	99.90	Chalcopyrite	Amphibolite	20
JEH-2007-14-s1-p1	<DL	35.19	<DL	30.68	34.28	0.03	<DL	100.19	Chalcopyrite	Amphibolite	20
JEH-2007-14-s1-p2	<DL	35.35	<DL	30.74	34.14	0.04	<DL	100.26	Chalcopyrite	Amphibolite	20
JEH-2007-14-s1-p3	<DL	35.20	<DL	30.57	34.19	0.05	<DL	100.01	Chalcopyrite	Amphibolite	20
JEH-2007-14-s1-p4	0.14	39.80	<DL	57.19	2.65	0.10	<DL	99.88	Pyrrhotite	Amphibolite	20
JEH-2007-14-s2-p1	<DL	35.23	<DL	30.57	34.44	0.04	<DL	100.27	Chalcopyrite	Amphibolite	20
JEH-2007-14-s2-p2	<DL	35.22	<DL	30.78	34.48	0.06	<DL	100.53	Chalcopyrite	Amphibolite	20
JEH-2007-14-s2-p3	<DL	35.06	<DL	30.52	34.58	0.04	<DL	100.20	Chalcopyrite	Amphibolite	20
JEH-2007-14-s3-p1	0.01	34.87	<DL	30.80	34.40	0.05	<DL	100.13	Chalcopyrite	Amphibolite	20
JEH-2007-14-s3-p2	<DL	35.13	<DL	30.85	34.39	0.05	<DL	100.42	Chalcopyrite	Amphibolite	20
JEH-2007-14-s4-p1	<DL	35.20	<DL	30.61	34.46	0.06	<DL	100.32	Chalcopyrite	Amphibolite	20
JEH-2007-14-s4-p2	<DL	35.20	<DL	30.71	34.38	0.05	<DL	100.34	Chalcopyrite	Amphibolite	20
JEH-2007-14-s4-p3	0.24	40.29	<DL	59.49	0.60	0.12	<DL	100.73	Pyrrhotite	Amphibolite	20

Supplementary table 2.10.C. microprobe results

Point name	Ni wt%	S wt%	As wt%	Fe wt%	Cu wt%	Co wt%	Zn wt%	Total wt%	Interpretation	Sample type	Measurement kV
JEH-2007-14-s4-p4	<DL	35.36	<DL	30.50	34.10	0.05	<DL	100.01	Chalcopyrite	Amphibolite	20
JEH-2007-14-s8-P1	<DL	35.30	<DL	30.85	34.21	0.06	<DL	100.42	Chalcopyrite	Amphibolite	20
JEH-2007-14-s8-P2	<DL	35.27	<DL	30.82	34.30	0.04	<DL	100.43	Chalcopyrite	Amphibolite	20
JEH-2007-14-s8-P3	<DL	35.19	<DL	30.76	34.06	0.04	<DL	100.05	Chalcopyrite	Amphibolite	20
JEH-2007-14-s8-P4	<DL	34.32	<DL	31.36	33.62	0.05	<DL	99.35	Chalcopyrite	Amphibolite	20
JEH-2007-14-s8-P5	<DL	35.54	<DL	30.87	34.23	0.03	<DL	100.67	Chalcopyrite	Amphibolite	20
JEH-2007-14-s8-P6	<DL	35.42	<DL	30.77	34.23	0.04	<DL	100.46	Chalcopyrite	Amphibolite	20
JEH-2007-14-s9-p1	0.31	40.02	<DL	59.30	0.19	0.12	<DL	99.94	Pyrrhotite	Amphibolite	20
JEH-2007-14-s9-p10	<DL	34.54	<DL	31.11	34.17	0.03	<DL	99.85	Chalcopyrite	Amphibolite	20
JEH-2007-14-s9-p2	0.30	39.87	<DL	59.00	0.65	0.12	<DL	99.94	Pyrrhotite	Amphibolite	20
JEH-2007-14-s9-p3	0.17	39.06	<DL	52.75	8.48	0.10	<DL	100.57	Pyrrhotite	Amphibolite	20
JEH-2007-14-s9-p4	<DL	35.16	<DL	30.95	34.36	0.04	<DL	100.50	Chalcopyrite	Amphibolite	20
JEH-2007-14-s9-p7	<DL	35.36	<DL	30.65	34.46	0.06	0.08	100.60	Chalcopyrite	Amphibolite	20
JEH-2007-14-s9-p8	<DL	35.27	<DL	30.74	34.54	0.04	<DL	100.58	Chalcopyrite	Amphibolite	20
JEH-2007-14-s9-p9	<DL	35.30	<DL	30.44	34.34	0.03	<DL	100.11	Chalcopyrite	Amphibolite	20
JEH-2007-23-s10-p3	1.04	39.56	<DL	59.04	0.09	0.12	<DL	99.84	Pyrrhotite	Amphibolite	20
JEH-2007-23-s10-p4	1.06	38.75	<DL	60.40	0.03	0.12	<DL	100.37	Pyrrhotite	Amphibolite	20
JEH-2007-23-s10-p5	<DL	34.80	<DL	30.57	34.58	0.04	<DL	99.98	Chalcopyrite	Amphibolite	20
JEH-2007-23-s10-p6	<DL	34.09	<DL	31.34	34.43	0.05	<DL	99.92	Chalcopyrite	Amphibolite	20
JEH-2007-23-s11-p1	<DL	54.00	<DL	46.49	0.05	0.07	<DL	100.61	Pyrite	Amphibolite	20
JEH-2007-23-s11-p2	<DL	53.76	<DL	46.48	0.04	0.06	<DL	100.34	Pyrite	Amphibolite	20
JEH-2007-23-s11-p3	<DL	53.84	<DL	46.46	0.03	0.06	<DL	100.40	Pyrite	Amphibolite	20
JEH-2007-23-s11-p4	<DL	53.81	<DL	46.22	0.05	0.07	<DL	100.15	Pyrite	Amphibolite	20
JEH-2007-23-s12-p1	<DL	33.98	<DL	31.14	34.21	0.05	<DL	99.38	Chalcopyrite	Amphibolite	20
JEH-2007-23-s12-p2	<DL	34.10	<DL	31.33	34.49	0.04	<DL	99.95	Chalcopyrite	Amphibolite	20
JEH-2007-23-s12-p3	<DL	34.21	<DL	31.32	34.37	0.04	<DL	99.94	Chalcopyrite	Amphibolite	20
JEH-2007-23-s1-p1	<DL	35.06	<DL	30.55	34.43	0.07	<DL	100.11	Chalcopyrite	Amphibolite	20
JEH-2007-23-s1-p10	25.63	41.54	<DL	10.58	0.35	21.96	<DL	100.06	Pentlandite	Amphibolite	20
JEH-2007-23-s1-p12	<DL	35.37	<DL	30.67	34.51	0.05	<DL	100.60	Chalcopyrite	Amphibolite	20

Supplementary table 2.10.C. microprobe results

Point name	Ni wt%	S wt%	As wt%	Fe wt%	Cu wt%	Co wt%	Zn wt%	Total wt%	Interpretation	Sample type	Measurement kV
JEH-2007-23-s1-p13	<DL	35.11	<DL	30.54	34.48	0.06	<DL	100.19	Chalcopyrite	Amphibolite	20
JEH-2007-23-s1-p2	24.94	41.21	<DL	11.21	1.05	21.90	<DL	100.31	Pentlandite	Amphibolite	20
JEH-2007-23-s1-p3	1.00	39.91	<DL	58.87	0.06	0.12	0.03	99.99	Pyrrhotite	Amphibolite	20
JEH-2007-23-s1-p4	0.97	41.04	<DL	58.81	0.05	0.11	<DL	100.97	Pyrrhotite	Amphibolite	20
JEH-2007-23-s1-p5	0.99	40.84	<DL	58.83	0.05	0.12	<DL	100.83	Pyrrhotite	Amphibolite	20
JEH-2007-23-s1-p6	1.01	38.76	<DL	60.36	0.04	0.12	<DL	100.28	Pyrrhotite	Amphibolite	20
JEH-2007-23-S1-P7	27.49	43.75	<DL	11.39	0.49	16.44	<DL	99.55	Pentlandite	Amphibolite	15
JEH-2007-23-s1-p7	1.01	39.67	<DL	58.85	0.06	0.13	<DL	99.71	Pyrrhotite	Amphibolite	20
JEH-2007-23-S1-P8	26.33	42.99	<DL	12.09	1.88	15.74	<DL	99.02	Pentlandite	Amphibolite	15
JEH-2007-23-s1-p8	1.03	38.77	<DL	60.15	0.22	0.15	<DL	100.33	Pyrrhotite	Amphibolite	20
JEH-2007-23-s1-p9	1.03	39.67	0.05	58.71	0.43	0.15	<DL	100.04	Pyrrhotite	Amphibolite	20
JEH-2007-23-s2-p1	<DL	33.89	<DL	31.35	34.43	0.04	<DL	99.71	Chalcopyrite	Amphibolite	20
JEH-2007-23-s2-p2	<DL	33.87	<DL	31.20	34.33	0.03	<DL	99.44	Chalcopyrite	Amphibolite	20
JEH-2007-23-s2-p3	<DL	34.21	<DL	31.26	34.52	0.06	<DL	100.04	Chalcopyrite	Amphibolite	20
JEH-2007-23-s2-p4	1.06	39.65	<DL	58.74	0.17	0.10	0.03	99.75	Pyrrhotite	Amphibolite	20
JEH-2007-23-s2-p5	1.08	39.57	<DL	59.11	0.20	0.10	<DL	100.06	Pyrrhotite	Amphibolite	20
JEH-2007-23-s3-p1	0.76	39.52	<DL	58.97	0.25	0.12	<DL	99.61	Pyrrhotite	Amphibolite	20
JEH-2007-23-s3-p2	<DL	34.04	<DL	31.40	34.40	0.06	<DL	99.90	Chalcopyrite	Amphibolite	20
JEH-2007-23-s3-p3	<DL	34.93	<DL	30.62	34.44	0.03	<DL	100.03	Chalcopyrite	Amphibolite	20
JEH-2007-23-s3-p4	1.04	38.96	<DL	59.96	0.22	0.13	<DL	100.30	Pyrrhotite	Amphibolite	20
JEH-2007-23-s3-p5	<DL	34.07	<DL	31.31	34.13	0.04	<DL	99.54	Chalcopyrite	Amphibolite	20
JEH-2007-23-s3-p6	1.07	39.74	<DL	58.79	0.05	0.10	<DL	99.76	Pyrrhotite	Amphibolite	20
JEH-2007-23-s3-p7	1.08	38.80	<DL	60.09	0.06	0.12	<DL	100.15	Pyrrhotite	Amphibolite	20
JEH-2007-23-s3-p8	1.05	38.49	<DL	60.02	0.04	0.11	<DL	99.71	Pyrrhotite	Amphibolite	20
JEH-2007-23-s4-p2	<DL	34.16	<DL	31.49	34.35	0.03	<DL	100.03	Chalcopyrite	Amphibolite	20
JEH-2007-23-s4-p3	<DL	34.36	<DL	31.46	34.05	0.05	<DL	99.92	Chalcopyrite	Amphibolite	20
JEH-2007-23-s4-p4	1.06	39.72	0.08	58.70	0.09	0.10	<DL	99.74	Pyrrhotite	Amphibolite	20
JEH-2007-23-s4-p5	1.06	39.72	<DL	58.78	0.05	0.12	<DL	99.73	Pyrrhotite	Amphibolite	20
JEH-2007-23-s4-p6	1.07	39.65	<DL	58.84	0.03	0.12	<DL	99.71	Pyrrhotite	Amphibolite	20

Supplementary table 2.10.C. microprobe results

Point name	Ni wt%	S wt%	As wt%	Fe wt%	Cu wt%	Co wt%	Zn wt%	Total wt%	Interpretation	Sample type	Measurement kV
JEH-2007-23-s4-p7	1.09	38.73	<DL	60.34	0.05	0.12	<DL	100.34	Pyrrhotite	Amphibolite	20
JEH-2007-23-s5-p1	1.38	38.23	<DL	59.76	0.05	0.12	<DL	99.53	Pyrrhotite	Amphibolite	20
JEH-2007-23-s5-p10	<DL	34.15	<DL	31.32	34.42	0.04	<DL	99.94	Chalcopyrite	Amphibolite	20
JEH-2007-23-s5-p11	1.11	39.00	<DL	60.06	0.06	0.12	<DL	100.35	Pyrrhotite	Amphibolite	20
JEH-2007-23-s5-p13	1.14	38.64	<DL	60.19	0.06	0.11	<DL	100.14	Pyrrhotite	Amphibolite	20
JEH-2007-23-s5-p14	1.17	38.55	<DL	60.22	0.08	0.11	<DL	100.13	Pyrrhotite	Amphibolite	20
JEH-2007-23-s5-p15	1.13	38.29	<DL	60.11	0.08	0.11	<DL	99.72	Pyrrhotite	Amphibolite	20
JEH-2007-23-s5-p2	1.41	38.54	<DL	60.03	0.06	0.10	<DL	100.14	Pyrrhotite	Amphibolite	20
JEH-2007-23-s5-p3	1.41	38.63	<DL	59.69	0.03	0.11	<DL	99.87	Pyrrhotite	Amphibolite	20
JEH-2007-23-s5-p4	1.39	38.61	<DL	60.07	0.05	0.11	<DL	100.23	Pyrrhotite	Amphibolite	20
JEH-2007-23-s5-p6	1.40	38.61	<DL	59.94	0.05	0.09	0.04	100.13	Pyrrhotite	Amphibolite	20
JEH-2007-23-s5-p7	<DL	33.86	<DL	31.25	34.36	0.04	<DL	99.51	Chalcopyrite	Amphibolite	20
JEH-2007-23-s5-p8	<DL	34.11	<DL	31.41	34.43	0.05	<DL	100.00	Chalcopyrite	Amphibolite	20
JEH-2007-23-s5-p9	<DL	34.13	<DL	31.25	34.38	0.03	<DL	99.78	Chalcopyrite	Amphibolite	20
JEH-2007-23-s6-p1	0.97	38.24	<DL	60.03	0.05	0.12	<DL	99.41	Pyrrhotite	Amphibolite	20
JEH-2007-23-s6-p2	0.98	38.53	<DL	60.43	0.11	0.12	<DL	100.17	Pyrrhotite	Amphibolite	20
JEH-2007-23-s6-p3	1.01	38.56	<DL	60.36	0.07	0.12	<DL	100.11	Pyrrhotite	Amphibolite	20
JEH-2007-23-s6-p4	0.99	38.63	<DL	60.57	0.06	0.11	<DL	100.36	Pyrrhotite	Amphibolite	20
JEH-2007-23-s6-p5	0.95	38.78	<DL	60.35	0.06	0.10	<DL	100.24	Pyrrhotite	Amphibolite	20
JEH-2007-23-s7-p1	<DL	34.11	<DL	31.49	34.07	0.04	<DL	99.70	Chalcopyrite	Amphibolite	20
JEH-2007-23-s7-p2	0.02	34.18	<DL	31.48	34.32	0.05	<DL	100.05	Chalcopyrite	Amphibolite	20
JEH-2007-23-s7-p3	<DL	34.15	<DL	31.34	34.39	0.03	<DL	99.90	Chalcopyrite	Amphibolite	20
JEH-2007-23-s7-p4	1.05	39.76	<DL	58.67	0.11	0.11	<DL	99.69	Pyrrhotite	Amphibolite	20
JEH-2007-23-s7-p5	1.08	38.73	0.06	60.26	0.14	0.10	<DL	100.37	Pyrrhotite	Amphibolite	20
JEH-2007-23-s7-p6	1.06	38.77	<DL	59.99	0.15	0.12	0.03	100.13	Pyrrhotite	Amphibolite	20
JEH-2007-23-s7-p7	1.06	38.74	<DL	60.29	0.09	0.11	<DL	100.30	Pyrrhotite	Amphibolite	20
JEH-2007-23-s8-p3	<DL	34.95	<DL	30.65	34.52	0.04	<DL	100.17	Chalcopyrite	Amphibolite	20
JEH-2007-23-s8-s1	<DL	33.93	<DL	31.49	34.45	0.04	<DL	99.91	Chalcopyrite	Amphibolite	20
JEH-2007-23-s8-s2	<DL	34.00	<DL	31.33	34.44	0.04	<DL	99.81	Chalcopyrite	Amphibolite	20

Supplementary table 2.10.C. microprobe results

Point name	Ni wt%	S wt%	As wt%	Fe wt%	Cu wt%	Co wt%	Zn wt%	Total wt%	Interpretation	Sample type	Measurement kV
JEH-2007-23-s9-p1	<DL	34.18	<DL	31.45	34.38	0.05	<DL	100.05	Chalcopyrite	Amphibolite	20
JEH-2007-23-s9-p2	<DL	34.12	<DL	31.43	34.36	0.05	<DL	99.95	Chalcopyrite	Amphibolite	20
JEH-2007-23-s9-p3	<DL	34.92	<DL	30.68	34.42	0.04	<DL	100.06	Chalcopyrite	Amphibolite	20
JEH-SG-05-s1-p1	0.16	38.51	<DL	61.06	0.17	0.11	<DL	100.01	Pyrrhotite	TTG	20
JEH-SG-05-s1-p2	0.15	38.29	<DL	61.09	0.14	0.12	<DL	99.79	Pyrrhotite	TTG	20
JEH-SG-05-s1-p3	0.14	38.10	<DL	61.10	0.15	0.12	<DL	99.60	Pyrrhotite	TTG	20
JEH-SG-05-s1-p5	0.04	36.77	<DL	62.57	0.07	0.10	<DL	99.55	Pyrrhotite	TTG	20

Chapter 3

Sulfur isotope evidence from peridotite enclaves in southern West Greenland for recycling of surface material into Eoarchean depleted mantle domains

This chapter was published in *Chemical Geology* Volume 633, 5 September 2023, 121568

https://doi.org/10.1016/j.chemgeo.2023.121568

by

Lewis, J.A.[1], Hoffmann, J.E.[1], Schwarzenbach, E.M.[1], Strauss, H.[2], Li, C.[3], Münker. C.[4], Rosing, M.T.[5]

[1]Institut für Geologische Wissenschaften, Freie Universität Berlin, Malteserstr. 74-100, 12249 Berlin, Germany

[2]Institut für Geologie und Paläontologie, Westfälische Wilhelms-Universität Münster, Corrensstr. 24, 48149 Münster, Germany

[3]International Center for Planetary Sciences, College of Earth Sciences, Chengdu University of Technology, Chengdu 610059, China

[4]Institut für Geologie und Mineralogie, Universität zu Köln, Zülpicher Str. 49b, 50674 Köln, Germany

[5]GLOBE Institute, University of Copenhagen, Øster Voldgade 5, DK-1350 Copenhagen, Denmark

This chapter was reformatted for publication in this doctoral thesis.

3.1. Abstract

Eoarchean peridotite enclaves found in southern West Greenland's Itsaq Gneiss Complex (IGC) represent an important and valuable record of Earth's early geodynamic history. However, the origins of these rocks and the processes acting on them in the Eoarchean remain a subject of debate. Some researchers have proposed that these peridotites represent the oldest preserved pieces of Earth's mantle, while others have suggested that they represent ultramafic cumulates. Similarly, the geodynamic context in which they formed and were emplaced is subject to multiple interpretations. Some researchers argue that only vertical tectonic processes operated in the Eoarchean and others contend that these peridotites were embedded in the crust by horizontal tectonic processes. We present multiple sulfur isotope data from

IGC peridotite enclaves, offering new insights into these rocks' origins and tectonic processes in the early Earth. Generally small but significant nonzero $\Delta^{33}S$ values of 0.04 to 0.21‰ were detected in the studied peridotites. Peridotites with almost no petrographic signs of metasomatic alteration have on average slightly higher $\Delta^{33}S$ values, whereas peridotites with clear petrographic and geochemical signatures of melt metasomatism were found to have slightly lower $\Delta^{33}S$ values. These $\Delta^{33}S$ values point to incorporation of surface-derived material of Archean age or older. Correlations between $\Delta^{33}S$ values and previously published major and trace element data support the view that these peridotites were subject to hydrous melt depletion of incompatible elements, followed by variable melt re-enrichment. Notably, a distinct correlation also exists between previously published Hf isotope data and $\Delta^{33}S$ values, indicating a depleted mantle source for melt percolating through the peridotites in the Eoarchean. The sulfur isotope data demonstrate that these processes included the introduction of surface-derived sulfur, pointing to an early onset of crustal recycling. These findings point to the existence of depleted mantle domains in the Hadean and suggest that crustal recycling processes operated during the Eoarchean or earlier.

3.2. Introduction

The timing of the onset of crustal recycling processes that moved material from the Earth's surface into the mantle and the nature of these mechanisms remain a subject of intensive debate. Some authors have proposed that processes similar to modern plate tectonics, including subduction zones and the formation of island arcs, were in operation as early as the Eoarchean (e.g., Nutman et al., 2021; Windley et al., 2021), whereas others argue that only nonuniformitarian, vertical tectonic processes operated at this time (Johnson et al., 2017; Rollinson, 2021; Webb et al., 2020). Relatedly, the extent to which felsic crust had differentiated (e.g., Hoffmann et al., 2019), and consequently the extent to which depleted mantle domains had formed in the Eoarchean also remains controversial (e.g., Hoffmann et al., 2010).

If recycling processes similar to subduction brought material from Earth's surface into the mantle in the Eoarchean, they would be expected to have fertilized mantle domains, or refertilized depleted mantle domains, with incompatible elements such as sulfur derived from the downgoing slab (e.g., Li et al., 2020). Direct and indirect evidence for such depleted and refertilized mantle domains have been reported from 3.81 Ga dunites and harzburgites (Bennett et al., 2002; Friend et al., 2002; Hasenstab-Dübeler et al., 2022; van de Löcht et al., 2018; van de Löcht et al., 2020) as well as 3.72 Ga depleted mantle-derived boninite-like metabasalts (Hasenstab-Dübeler et al., 2022; Hoffmann et al., 2010; Polat et al., 2002) from the Itsaq Gneiss Complex (IGC) of southern West Greenland. However, the mantle origin of the dunites and harzburgites remain controversial because rocks of similar composition from enclaves within the Isua Supracrustal belt (ISB) have been interpreted to represent either remnants of Eoarchean mantle (e.g., Friend and Nutman, 2011; Nutman et al., 2020) or ultramafic cumulates associated with local basalt flows (e.g., Szilas et al., 2015; McIntyre et al., 2019; Waterton et al., 2022).

Two ideal tracers to investigate Eoarchean geodynamic processes including crustal recycling and mantle differentiation are hafnium and multiple sulfur (^{32}S, ^{33}S, ^{34}S, ^{36}S) isotope compositions. Hafnium isotopes can serve as a powerful tool to elucidate the nature and extent of crust and mantle differentiation in the early Earth, as Hf is more incompatible than Lu, so ^{176}Lu, which decays into ^{176}Hf, preferentially remains in the mantle during melt extraction and enriches the depleted mantle in ^{176}Hf over time. This produces a positive εHf signature in the mantle, (e.g., Patchett and Tatsumoto, 1980). Thus, high εHf values in magmatic rocks can point to the existence of depleted mantle reservoirs. For example, εHf values in 3.72 Ga ISB boninite-like metabasalts and >3.8 Ga harzburgites and dunites from SOISB as high as +12.9 and +7.3, respectively (Hoffmann et al., 2010; van de Löcht et al., 2020), imply that these rocks sample mantle material already depleted in the Eoarchean or Hadean.

In contrast to the Hf isotope record in certain IGC peridotites and boninite-like metabasalts, near-zero εHf values of Eoarchean zircons from tonalites-trondhjemites-granodiorites (TTGs), felsic rocks that represent some of the earliest remnants of Earth's continental crust (Fisher and Vervoort, 2018; Guitreau et al., 2012; Hiess et al., 2008; Hoffmann et al., 2011a; Næraa et al., 2012; Vervoort and Blichert-Toft, 1999), as well as tholeiitic metabasalts from the IGC (Polat et al., 2003; Hoffmann et al., 2011a; Hoffmann et al., 2011b; Rizo et al., 2011) suggest mantle sources that had not yet undergone strong depletion in the Eoarchean. Because the Itsaq Gneiss Complex TTGs likely formed from melting of tholeiitic metabasalts (Hoffmann et al., 2011a; Hoffmann et al., 2014; Nagel et al., 2012) and not from boninite-like metabasalts (Hoffmann et al., 2014), it is unlikely that any depleted mantle reservoirs that already existed in the Eoarchean were sampled by the TTGs. This results in the TTG Hf isotope record providing a biased view of early mantle depletion (e.g., Hoffmann and Wilson, 2017; Liou et al., 2022) and thus in contrast to previous suggestions (e.g., Fisher and Vervoort, 2018), boninite-like metabasalts and peridotitic rocks provide direct insights into the earliest mantle depletion processes.

Depleted mantle domains may have formed either by high degrees of melt depletion in a single event, (e.g., Hoffmann and Wilson, 2017) or were depleted during multiple melting events that were likely triggered by fluids as is the case in modern mantle wedge domains e.g. by those producing boninites (König et al., 2010). Such depleted sources are ideal to study mantle metasomatism and crustal recycling because their incompatible element budget would be dominantly controlled by refertilizing aqueous fluids or melts (Hoffmann and Wilson, 2017; Tusch et al., 2022). These aqueous fluids and melts can either be related to (1) delaminated crustal material possibly related to non-uniformitarian vertical tectonic processes (e.g., Bédard, 2006; Johnson et al., 2017; Johnson et al., 2013; Rollinson, 2021; Webb et al., 2020) or (2) to horizontal tectonics involving some form of proto-subduction as also proposed for rocks from the IGC (e.g., Kamber et al., 2003; Nutman et al., 2021 and references therein). Such subduction-like processes would include the recycling of ocean floor and/or sedimentary material.

In this regard, multiple sulfur isotope signatures can provide a unique record. They can preserve distinct signals that were generated in the Earth's atmosphere prior to the Great Oxidation Event at ~2.45 Ga and serve as a tracer of material recycled from the Earth's surface into the mantle in the Archean (Farquhar et al., 2000; Farquhar et al., 2002). In the reduced atmosphere of the Archean, photolytic processes produced a mass independent difference in the relative abundance of ^{33}S compared to ^{32}S and ^{34}S (expressed as Δ^{33}S values) of reduced and oxidized sulfur species that became incorporated in sedimentary and hydrothermal sulfur-bearing deposits, producing distinct Δ^{33}S values (Farquhar et al., 2000; Farquhar et al., 2002). Notably, recent studies have shown that even small nonzero Δ^{33}S values in igneous lithologies provide strong evidence of mass independently fractionated sulfur (MIFS) input (e.g., LaFlamme et al., 2018a). In the past, nonzero Δ^{33}S values within 0.2‰ of 0 in terrestrial rocks were not considered indicative of MIF-S (Farquhar and Wing, 2003). However, it has recently been shown that when combined with sufficiently low δ^{34}S values, nonzero Δ^{33}S values of <0.2‰ are likely to represent incorporation of surface-derived material in Archean lithologies as no other S cycling processes existed in the Archean that could have produced these signatures (LaFlamme et al., 2018b). Furthermore, mass dependent processes that can produce nonzero Δ^{33}S fractionate sulfur along a specific slope in Δ^{33}S-Δ^{36}S space that mass independent processes do not (e.g., Ono, 2017; Ono et al., 2006). These insights, combined with improvements in the analytical precision of multiple sulfur isotope measurements, have allowed small, surface-derived MIF-S signatures to be identified in numerous igneous lithologies (e.g., Cabral et al., 2013; Caruso et al., 2022; Delavault et al., 2016; Farquhar et al., 2002; Kubota et al., 2022; Lewis et al., 2021; Ranta et al., 2022). These studies further corroborate the robust nature of MIF-S in magmatic systems, surviving within the Earth and during igneous processes over billions of years.

Here, we present the first multiple sulfur isotope analyses and sulfur concentration measurements of well-characterized peridotites previously interpreted to represent Eoarchean mantle enclaves (e.g., Bennett et al., 2002; Friend et al., 2002; van de Löcht et al., 2018; van de Löcht et al., 2020) to place constraints on Eoarchean recycling of surface-derived crustal material and mantle metasomatism. Combination of these results with compiled major and trace element concentrations, and Hf isotope data from previous studies (Hoffmann et al., 2010; van de Löcht et al., 2018; van de Löcht et al., 2020) allows for further constraints on the history of these rocks. The resulting correlations can elucidate processes of crustal differentiation and metasomatism and hint to a possible geodynamic setting in which these rocks formed, as well as provide further evidence for the early existence of highly depleted mantle reservoirs in the Eoarchean.

3.3. Geological overview and sample selection

The 3.9 to 3.6 Ga IGC, which is part of the North Atlantic Craton, is composed primarily of tonalitic-trondhjemitic-granodioritic (TTG) orthogneisses that have intruded into supracrustal packages including the Isua Supracrustal Belt (ISB) (e.g., Nutman and Bennett, 2019). The ISB represents one of the world's largest areas of coherent Eoarchean supracrustal rock, and includes low-strain domains in which rocks such as pillow basalts and layered sediments affected by amphibolite facies metamorphism have retained primary textures and structures, (e.g., Hoffmann et al., 2010; Nutman and Bennett, 2019). The field relationships of lithologies within the ISB strongly suggest that the ISB includes terranes that were tectonically intercalated in a convergent setting prior to 3.66 Ga (Nutman and Friend, 2009; Nutman et al., 1996).

Among the rocks found in the vicinity of the ISB are a number of mafic lithologies, including remnants of layered intrusions (e.g., Friend et al., 2002; McIntyre et al., 2021) and metabasalts with compositions resembling boninitic, tholeiitic, and picritic basalts. These metabasalts have major and trace element systematics similar to modern island arc basalts (Nutman and Friend, 2009; Polat et al., 2002). Remarkably well-preserved domains of dunite and harzburgite are also found in areas to the south of the ISB (SOISB) in the northern Isukasia Terrane of the IGC (Bennett et al., 2002; Nutman et al., 1996) as well as in the southern Faeringhaven Terrane on the Narssaq Peninsula south of Nuuk (Nutman et al., 2007b). Some of these rocks have also been interpreted to represent obducted pieces of Eoarchean mantle (Bennett et al., 2002; Friend et al., 2002; Nutman et al., 2007b; Rollinson, 2010; van de Löcht et al., 2018; van de Löcht et al., 2020). Others show cumulate textures and are unambiguously related to layered intrusions (Coggon et al., 2015; McIntyre et al., 2021). A minimum age of 3.81 Ga is defined by crosscutting TTGs (Friend et al., 2002; Nutman et al., 2007a). In contrast to peridotites found within the ISB, some of the peridotites found south of the ISB have been interpreted to be of mantle origin and have been found to possess platinum group element (PGE) patterns consistent with those of harzburgites from the modern mantle (van de Löcht et al., 2018). Additionally, the Re and Os isotope systematics of these rocks suggest a 3.8 Ga mantle source that was chondritic in its $^{187}Os/^{188}Os$ ratio (Bennett et al., 2002; van de Löcht et al., 2018). However, a mantle origin of all peridotites found in the IGC has been subject to some controversy, with recent studies suggesting the mantle-like compositions and textures of these rocks are not exclusively indicative of formation in the Earth’s mantle, and a cumulate origin in a stagnant lid setting cannot be ruled out (Waterton et al., 2022; Zuo et al., 2022). Because of their occurrence in isolated domains intruded by TTGs (Bennett et al., 2002; Friend et al., 2002; Nutman et al., 1996), the SOISB peridotites are tectonically decontextualized and the mechanism that originally emplaced them in the crust cannot be determined by field relations alone.

For this study, we selected 8 well-preserved peridotites from an area approximately 15 km to the south of the ISB (see Figure 3.1 and supplementary Table 3.10.B for GPS data). The samples were taken from ~50 m ultramafic domains that along the edges show signs of hydrous alteration as a result of mid to late Archean metamorphic events (van de Löcht et al., 2018; van de Löcht et al., 2020). However, the domain cores remained almost entirely free of phases attributed to hydrous metamorphism (Friend et al., 2002) and thus sampling was restricted to these domain cores. Accordingly, in thin sections these rocks display only very low amounts of micaceous and serpentine minerals (van de Löcht et al., 2018; van de Löcht et al., 2020). Dunite samples 010–022 and 010–023 comprise >90% olivine with <3% secondary phases by volume, whereas other samples include small amounts of serpentine and amphibole overgrowing the primary mineral phases (van de Löcht et al., 2020). The selected dunites and harzburgites form two distinct groups in terms of their PGE patterns and Re contents as identified by van de Löcht et al. (2018).

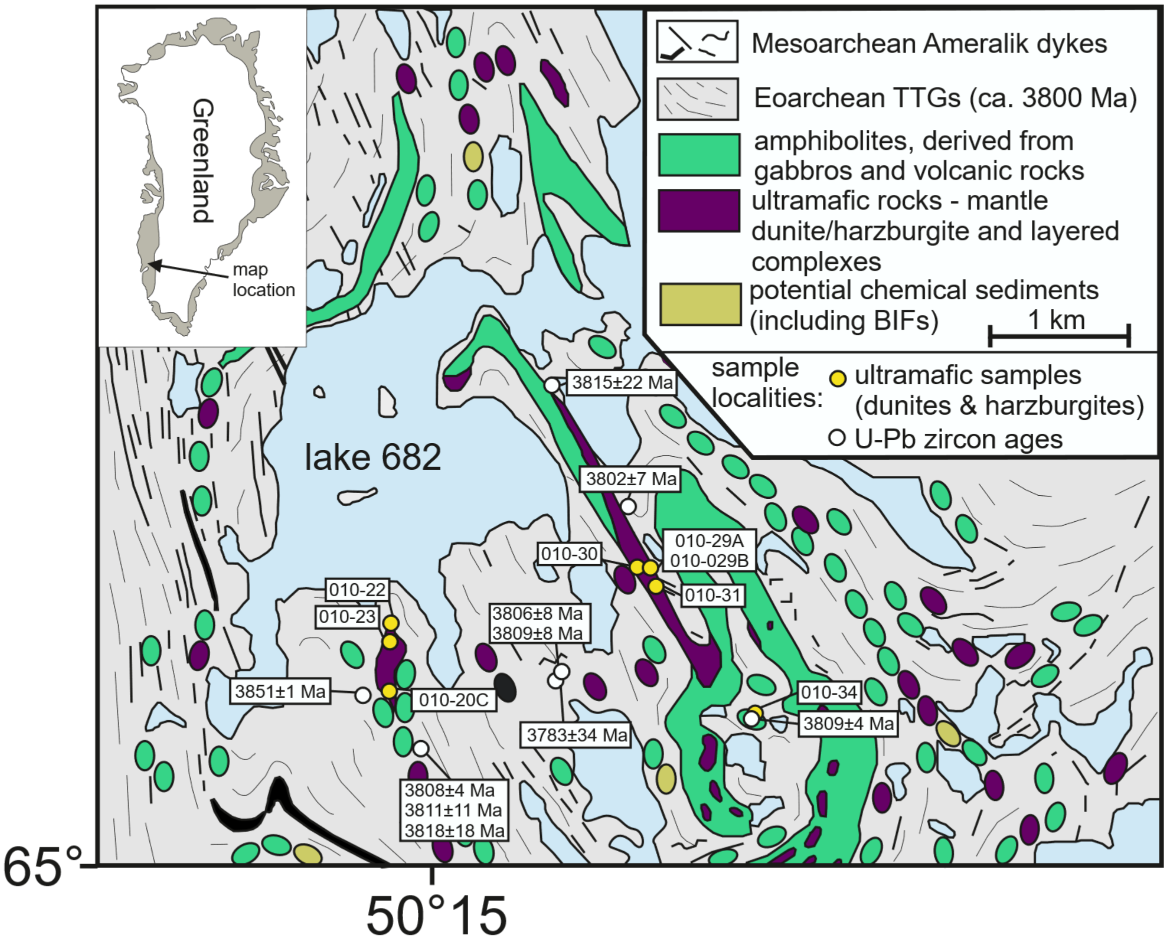

Figure 3.1. Simplified geology map of the SOISB area with sample locations, after Nutman and Friend (2009); van de Löcht et al. (2018); van de Löcht et al. (2020). Age data are from Amelin et al. (2010); (Nutman et al., 2007a); Nutman et al. (1999); Nutman et al. (2007b); Nutman et al. (1996), as compiled in van de Löcht et al. (2020).

Group 1 peridotites are characterized by strong depletions in Pd-group platinum group elements (PPGEs) relative to Ir-group platinum group elements (IPGEs), indicative of melt depletion assuming they are mantle peridotites, and by Eoarchean Re depletion ages (van de Löcht et al., 2018). These rocks have coarse grained microstructures consistent with primary magmatic processes and have features consistent with only very limited melt metasomatism including unzoned olivine with no signs of overgrowth and very low abundances of secondary minerals (van de Löcht et al., 2020).

Group 2 peridotites have relatively flat PGE patterns and their Re depletion ages are Paleoarchean and younger (van de Löcht et al., 2018), suggesting that Group 2 peridotites have experienced a re-fertilization event by a melt-like component that did not affect Group 1 peridotites to the same extent (van de Löcht et al., 2018; van de Löcht et al., 2020). Group 2 peridotites have heterogeneous grain sizes and display evidence for recrystallization (van de Löcht et al., 2020).

Notably, most of the SOISB Group 1 and 2 peridotites, and all of the ones selected for this study, have elevated initial εHf values of up to +7.2, consistent with origins in Earth's mantle (van de Löcht et al., 2020). Group 2 peridotite εHf initial values are more positive than Group 1 peridotite εHf values (van de Löcht et al., 2020). Both groups of peridotites display flat mantle-normalized REE patterns. These REE patterns are uncharacteristic of depleted mantle rocks and suggest that both groups of rocks have experienced re-fertilization following initial melt depletion, prior to the re-fertilization event preferentially experienced by Group 2 peridotites (van de Löcht et al., 2020). SOISB peridotites selected for this study have ^{176}Lu–^{177}Hf ages of 3780 ± 84 Ma (Group 1, MSWD = 0.84, n = 6); see supplementary Figure 3.10.A.1) and 3933 ± 180 Ma (Group 2, MSWD = 0.39; n = 4; see supplementary Figure 3.10.A.1). Combining both groups, the 176Lu–177Hf regression age is 3845 ± 140 Ma (MSWD = 2.4; n = 10), which is interpreted to record the re-fertilization event experienced by both groups of rocks (van de Löcht et al., 2020).

3.4. Analytical methods

Four Group 1 peridotites and four Group 2 peridotites were selected for sulfur isotopic analysis based on relatively high sulfur contents in these samples. For three of the four Group 1 samples and all of the Group 2 samples, acid volatile and chromium reducible sulfur were extracted and analyzed separately following a procedure slightly modified from the methods of Canfield et al. (1986) and Tuttle et al. (1986). Acid volatile sulfur (AVS or monosulfides such as pyrrhotite) and chromium reducible sulfur (CRS or disulfides such as pyrite) were extracted separately as they may trace different sulfur reservoirs in the rock.

For the investigated samples, 20–32 g of powdered sample material was placed in a flask with 5g Sn(*II*)Cl_2 and ethanol, heated to boiling, and reacted with 80ml 6M HCl in an inert N_2 atmosphere for two hours. Acid volatile sulfur released as H_2S gas was captured in a zinc acetate trap solution over the course of at least two hours. This trap solution was then reacted with silver nitrate to precipitate the sulfur as solid Ag_2S. Subsequently, the residual sample in the flask was heated to boiling and reacted with an additional 60 ml of acidified 1M $CrCl_2$-solution in an inert N_2 atmosphere to extract the chromium reducible sulfur as H2S for an additional two hours. The released H_2S was also captured in a zinc acetate trap solution and subsequently reacted to Ag_2S. For three of the Group 1 samples and one of the Group 2 samples, the sample powders were reacted only with the $CrCl_2$-solution to extract the AVS and CRS fractions simultaneously. These extractions are described as “combined” in Table 3.1. Sulfur extractions were primarily carried out at the Freie Universität Berlin (including five duplicate extractions labelled “DUP” in Table 3.1), and two additional duplicate extractions were done at Westfälische Wilhelms-Universität Münster (labelled “Münster DUP” in Table 3.1).

Sulfur isotope analyses were carried out at the University of Münster. For this, 1–3 mg aliquots of the Ag_2S extracts were reacted with F_2 gas to form SF_6, which was subsequently purified cryogenically and by gas chromatography, and then analyzed for multiple sulfur isotope (^{32}S, ^{33}S, ^{34}S, ^{36}S) compositions with a Thermo Fisher Scientific MAT 253 isotope ratio mass spectrometer following the method of e.g., Lewis et al. (2021); Siedenberg et al. (2016). Analytical results are expressed using the standard delta notation after Farquhar et al. (2000) and Johnston et al. (2008), for 3i = 33, 34, or 36:

$$\delta^{3i}(‰) = ((^{3i}/^{32}S)Sample/(^{3i}S/^{32}S)Standard – 1) \text{ x } 1000.$$

$$\Delta^{33}S = \delta^{33}S – 1000 \text{ x } [(1 + \delta^{34}S / 1000)^{0.515} – 1].$$

$$\Delta^{36}S = \delta^{36}S – 1000 \text{ x } [(1 + \delta^{34}S / 1000)^{1.90} – 1].$$

Results are reported relative to the standard Vienna Canon Diablo Troilite (VCDT). The IAEA S1 $\Delta^{36}S$ results were subject to a – 0.81‰ calibration against VCDT. The 2σ analytical error, based on standard measurements collected from the instrument over one year, was ±0.13‰ for $\delta^{34}S$, ±0.01‰ for $\Delta^{33}S$, and ± 0.23‰ for $\Delta^{36}S$. 2σ internal measurement errors are shown in Table 3.1 and ranged from 0.004‰ to 0.074‰ for δ34S, 0.007‰ to 0.164‰ for $\Delta^{33}S$, and 0.060‰ to 0.331‰ for $\Delta^{36}S$. Results for IAEA-S1 reference material run concurrently with the samples are presented in supplementary Table 3.10.C.

Additionally, selected peridotite samples were analyzed for bulk rock sulfur concentrations on the same bulk rock powders following the method of Wang et al. (2013). Sulfur was separated by means of two-step ion exchange chromatography followed by successive dissolution in HCl and HNO_3. Sulfur concentrations were then determined by sector-field inductively coupled plasma mass spectrometry (SF-ICPMS) using a ThermoElectron Element 2 XR at the Freie Universität Berlin.

3.5. Results

Sulfur isotope and S concentration results are presented in Table 3.1 and displayed in Figures 3.2 and 3.3. Group 1 peridotites analyzed for sulfur concentration contain between

455 µg/g and 800 µg/g sulfur. Group 2 peridotites contain between 95 µg/g and 733 µg/g sulfur. Inspection of the selected peridotites in thin section by reflected light microscopy revealed that major sulfide minerals in the peridotites included pentlandite and pyrrhotite, which were at times intergrown with each other (supplementary Figures 3.10.A.2, 3.10.A.3). In places, amphiboles overgrow sulfide minerals (supplementary Figure 3.10.A.3).

Table 3.1: Analytical results

Sample Name	**010-020C**	**010-020C DUP[2]**	**010-022**	**010-023**	**010-023 DUP[2]**	**010-034**	**010-029A**	**010-029A**	**010-029A Münster DUP[2]**	**010-029A Münster DUP[2]**	**010-029B**	**010-029B DUP[2]**	**010-030**	**010-030 DUP[2]**	**010-030 DUP[2] 2**	**010-031**
PGE Group[1]	1	1	1	1	1	1	2	2	2	2	2	2	2	2	2	2
AVS																
δ^{34}S vs CDT [‰]	2.85	2.78	1.40	3.84	3.85		3.45	3.87			4.94	4.90	3.07		2.76	1.57
$2\sigma(\delta^{34}$S) [‰]	0.01	0.02	0.01	0.01	0.01		0.00	0.01			0.01	0.01	0.01		0.01	0.02
Δ^{33}S [‰]	0.17	0.17	0.20	0.20	0.19		0.07	0.06			0.04	0.05	0.12		0.12	0.08
$2\sigma(\Delta^{33}$S) [‰]	0.03	0.04	0.01	0.02	0.03		0.03	0.03			0.02	0.02	0.02		0.01	0.04
Δ^{36}S [‰]			-0.37	-0.50	-0.28		-0.28	-0.06			-0.10	-0.29	0.03		-0.13	
$2\sigma(\Delta^{36}$S) [‰]			0.15	0.16	0.06		0.20	0.30			0.13	0.15	0.10		0.33	
CRS																
δ^{34}S vs CDT [‰]			1.79	4.01									3.34	3.32		
$2\sigma(\delta^{34}$S) [‰]			0.00	0.01									0.07	0.02		
Δ^{33}S [‰]			0.20	0.20									0.20	0.13		
$2\sigma(\Delta^{33}$S) [‰]			0.03	0.03									0.16	0.04		
Δ^{36}S [‰]			-0.03	0.15												
$2\sigma(\Delta^{36}$S) [‰]			0.21	0.25												
Combined																
δ^{34}S vs CDT [‰]	3.01		1.55			2.41		4.10	3.36	3.48			2.61			
$2\sigma(\delta^{34}$S) [‰]	0.01		0.01			0.02		0.01	0.01	0.01			0.01			
Δ^{33}S [‰]	0.20		0.21			0.14		0.05	0.05	0.07			0.13			
$2\sigma(\Delta^{33}$S) [‰]	0.02		0.02			0.02		0.03	0.03	0.05			0.01			
Δ^{36}S [‰]	-0.19		0.17			0.14		0.18	0.12	-0.02			0.22			
$2\sigma(\Delta^{36}$S) [‰]	0.28		0.20			0.27		0.14	0.17	0.23			0.09			
S (µg/g)																
	800	800	634	455	455		345	345	345	345	733	733	95	95	95	

Table 3.1. Sulfur isotope results of acid volatile sulfur (AVS) and chromium reducible sulfur (CRS), as well as combined sulfur isotope results where available. Sulfur concentration data are also shown. All results are reported relative to the Vienna Canon Diablo Troilite (VCDT). [1]PGE Groups from van de Löcht et al. (2018). [2]Duplicates labelled "DUP," duplicates extracted in Münster labelled "Münster DUP."

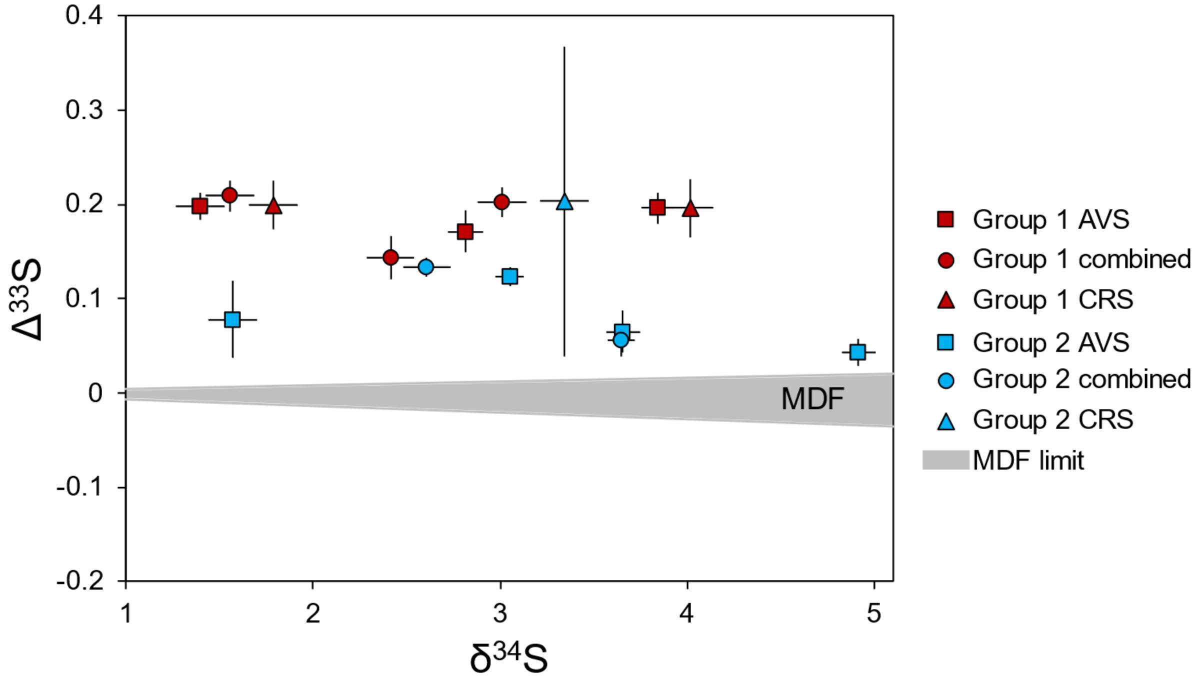

Figure 3.2. $\delta^{34}S$ versus $\Delta^{33}S$ values of SOISB peridotites shown by group (van de Löcht et al., 2018) and type of sulfide extracted. Sets of duplicate measurements with common extracted sulfide types are displayed as averages weighted according to their associated 2σ internal or external errors, whichever is greater, using IsoPlot v. 4.15 (Ludwig, 2012). 2σ errors are shown for each data point. Note that for duplicate samples, 2σ weighted average error bars are shown with internal or external errors considered in the weighted average calculation but not the scatter of measured duplicate results. Full results are given in Table 3.1. In gray, the range of isotopic values expected to be produced by most mass dependent processes is shown (LaFlamme et al., 2018b).

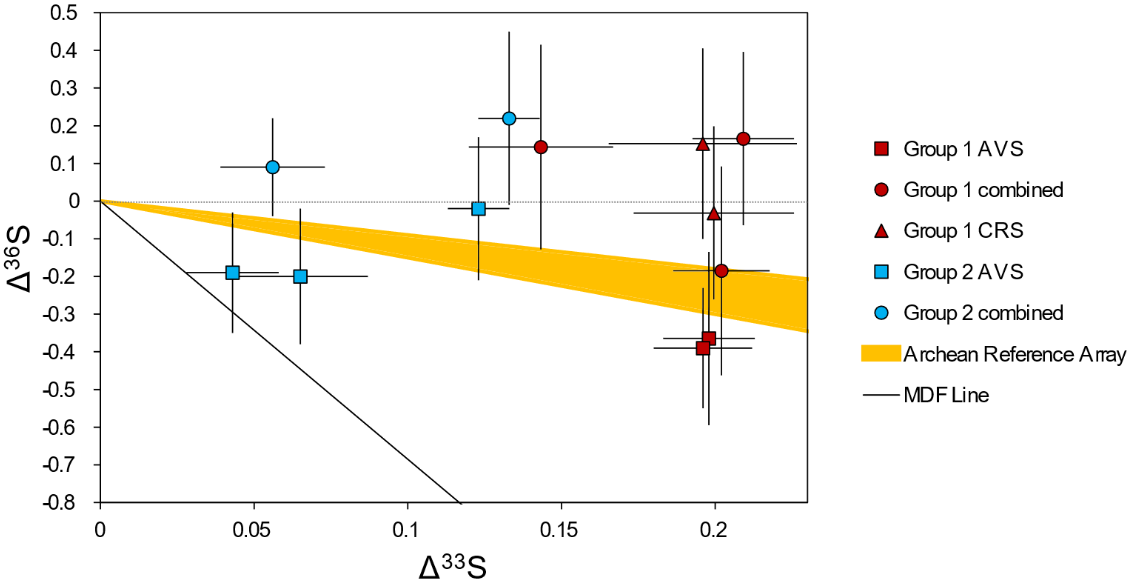

Figure 3.3. $\Delta^{33}S$ versus $\Delta^{36}S$ values of SOISB peridotites shown by group (van de Löcht et al., 2018) and type of sulfide extracted (as in Figure 3.2). 2σ errors and weighted average results are shown as in Figure 3.2. The Archean reference array is shown in yellow covering typical values of MIF-S (Farquhar et al., 2000; Ono, 2017; Zerkle et al., 2012). The expected array of values produced by mass dependent fractionation (MDF) resulting from microbial sulfate reduction consistent with Phanerozoic sedimentary pyrite is shown as a line (Ono et al., 2006).

All analyzed samples have positive $\delta^{34}S$ and $\Delta^{33}S$ values, though on average Group 1 peridotites have higher $\Delta^{33}S$ values and lower $\delta^{34}S$ values compared to Group 2 peridotites (Figure 3.2). AVS measurements of Group 1 peridotites (based on individual extractions, see Table 3.1) yielded $\delta^{34}S$ values ranging from 1.40‰ to 3.85‰, $\Delta^{33}S$ values ranging from 0.17‰ to 0.20‰, and $\Delta^{36}S$ values ranging from – 0.50‰ to – 0.28‰. CRS measurements of Group 1 peridotites yielded $\delta^{34}S$ values of 1.79‰ and 4.01‰, two $\Delta^{33}S$ values of 0.20‰, and $\Delta^{36}S$ values of 0.15‰ and – 0.03‰. Combined (AVS + CRS) measurements of Group 1 peridotites yielded $\delta^{34}S$ values ranging from 1.55‰ to 3.01‰, $\Delta^{33}S$ values ranging from 0.14‰ to 0.21‰, and $\Delta^{36}S$ values ranging from – 0.19‰ to 0.17‰. AVS measurements of Group 2 peridotites yielded $\delta^{34}S$ values ranging from 1.57‰ to 4.94‰, $\Delta^{33}S$ values ranging from 0.04‰ to 0.12‰, and $\Delta^{36}S$ values ranging from – 0.29‰ to 0.03‰. CRS measurements of Group 2 peridotites yielded $\delta^{34}S$ values of 3.32‰ and 3.34‰ and $\Delta^{33}S$ values of 0.13‰ and 0.20‰. Combined (AVS + CRS) measurements of Group 2 peridotites yielded $\delta^{34}S$ values ranging from 2.61‰ to 4.10‰, $\Delta^{33}S$ values ranging from 0.05‰ to 0.13‰, and $\Delta^{36}S$ values ranging from – 0.02‰ to 0.22‰. Generally, CRS is between 0.17 and 0.39‰ higher for $\delta^{34}S$ compared to the AVS fraction, whereas $\Delta^{33}S$ and $\Delta^{36}S$ variations between AVS and CRS for the same samples are within measurement error. These variations, as well as small differences between duplicate sample results (e.g., by up to 0.74‰ in δ^{34}S), and differences between combined (AVS + CRS) and separately extracted AVS and CRS fractions of the same sample, are attributed to sample heterogeneity.

3.6. Discussion

3.6.1. MIF-S in the SOISB peridotites

MIF-S has been reported from several lithologies within the IGC including igneous lithologies such as tholeiitic metabasalts (Siedenberg et al., 2016; Lewis et al., 2021), boninite-like metabasalts (Siedenberg et al., 2016) and TTGs (Lewis et al., 2021), as well as from metasediments and associated sulfide grains (e.g., Baublys et al., 2004; Mojzsis et al., 2003; Papineau and Mojzsis, 2006; Whitehouse, 2013; Whitehouse et al., 2005). Similarly, the nonzero Δ^{33}S values found in the SOISB peridotites (Figure 3.2) are best explained by the presence of mass independently fractionated sulfur (MIF-S) formed on Earth's surface in the Archean. Prior to the Great Oxidation Event, photolytic processes in the Earth's atmosphere produced reduced sulfur species (e.g., S^-, S^{2-}) with positive Δ^{33}S values that were incorporated primarily into sediments, and oxidized sulfur species (e.g., SO_4^{2-}) with negative Δ^{33}S values that were primarily incorporated into hydrothermal deposits (Farquhar et al., 2002). While mixing with sulfur not subject to MIF may result in an attenuated mass independent isotope signature, small nonzero values of Δ^{33}S from surface-derived sulfur components in rocks of Archean age can remain resolvable even after magmatic processes such as e.g., those taking place during subduction or crustal thickening (LaFlamme et al., 2018a; Lewis et al., 2021). However, nonzero Δ^{33}S signatures smaller than ±0.2‰ have traditionally not been interpreted to reflect MIF-S, but mass dependent processes (Farquhar and Wing, 2003). Mass dependent processes that can produce offsets in Δ^{33}S include mixing of isotopic endmembers with sufficiently different δ^{34}S values on the order of several tens of permils (e.g., LaFlamme et al., 2018b; Schwarzenbach et al., 2018) or biologically mediated Rayleigh fractionation (e.g., Ono et al., 2006). However, large isotope fractionations (of several tens of permils in δ^{34}S) produced by mass dependent processes are not found in the Eoarchean (e.g., Fike et al., 2015; LaFlamme et al., 2018b), and such processes are therefore unlikely to have produced the anomalous Δ^{33}S signatures concurrent with relatively low δ^{34}S values found in Eoarchean rocks (LaFlamme et al., 2018b, see also Figure 3.2). Furthermore, the measured results do not fall on the array typical of sulfur subject only to mass dependent fractionation in Δ^{33}S-Δ^{36}S space (Ono et al., 2006), and are scattered further along the axis of the Archean array representing typical isotopic values of deposits subject to MIF-S prior to the Great Oxidation Event (Farquhar et al., 2000; Ono, 2017; Zerkle et al., 2012, (Figure 3.3). Hence, such mass dependent processes are very unlikely to have influenced the $\Delta^{33}S$ compositions of the SOISB peridotites. We suggest that the positive $\Delta^{33}S$ values in both groups of peridotites indicate that they have incorporated surface-derived MIF-S because all but one individual measurement falls significantly outside the range of values with relatively low $\Delta^{33}S/\delta^{34}S$ produced by most mass dependent processes (Table 3.1) (LaFlamme et al., 2018b), all weighted average measurements fall significantly outside this range (Figure 3.2), and all but one result fall significantly outside the line in $\Delta^{33}S$-$\Delta^{36}S$ space followed by Rayleigh fractionation processes (Figure 3.3).

Notably, the Group 1 peridotites, which show the least evidence of melt overprint, are found to have higher average $\Delta^{33}S$ values and lower average $\delta^{34}S$ values than the Group 2 peridotites, which have experienced higher degrees of melt metasomatism (van de Löcht et al., 2020; van de Löcht et al., 2018). This indicates that the peridotites have incorporated two sulfur sources: one with relatively high $\Delta^{33}S$ and relatively low $\delta^{34}S$ that is found in both groups of rocks and is not associated with any clear sign of melt overprint, and a second with relatively low $\Delta^{33}S$ and relatively high $\delta^{34}S$ that was introduced by the melt that preferentially overprinted the Group 2 peridotites.

A simple explanation for the presence of sulfur with nonzero $\Delta^{33}S$ values in these rocks, along with the elevated Hf isotope compositions measured by van de Löcht et al. (2020), would be that S and Hf were incorporated by the peridotites from surrounding lithologies during emplacement, or by hydrous metamorphic processes following emplacement. In the event that the SOISB peridotites are crustal cumulates, the former possibility cannot be entirely ruled out. However, no lithologies have been detected that are similar in S and Hf isotopic composition to those that have been measured in the peridotites that could explain such a mass transfer or contamination (van de Löcht et al., 2020). This suggests that even if the SOISB peridotites are crustal cumulates, they may not have incorporated S and Hf during emplacement but through some other process. If the peridotites have their origin in the mantle, incorporation of material from partial melting of surrounding rocks during emplacement is less likely, but the possibility that they incorporated S and Hf during metamorphism within the crust remains, regardless of how the SOISB peridotites first formed. Introduction of MIF-S to these rocks following emplacement would mean that this signal does not necessarily have its origin in the mantle. This explanation is especially tempting in light of the up to amphibolite-granulite-facies metamorphism the IGC has experienced (e.g., Nutman et al., 1996). However, several lines of evidence argue that this is unlikely, and that a different explanation is required, as discussed in the following.

3.6.2. Absence of sulfur and Hf contamination during or following peak metamorphism

The IGC has been subject to a complex history of metamorphism following the Eoarchean (e.g., Nutman et al., 1996), with events generating metasomatizing fluids such as a ~2.56 Ga intrusion of granite that influenced many IGC lithologies (Nutman et al., 2007b). However, some isolated localities contain rocks that have been left largely unaffected by this overprint, including the SOISB peridotites investigated in this study (Friend et al., 2002; van de Löcht et al., 2020). This is reflected by their textural characteristics (van de Löcht et al., 2018; van de Löcht et al., 2020) and occurrence in the cores of ultramafic domains that have not been subject to hydrous alteration visible in the field (Friend et al., 2002).

It is also notable that the Group 1 peridotites, which have the most positive $\Delta^{33}S$ values, have Eoarchean Re-depletion ages and chondritic initial $^{187}Os/^{188}Os$ isotope compositions (Bennett et al., 2002; van de Löcht et al., 2018). As Re is strongly enriched in felsic crustal lithologies, this effectively rules out contamination from such crustal lithologies because it would lead to substantial radiogenic ingrowth in ^{187}Os. While the Re–Os systematics of the Group 2 peridotites show signs of radiogenic ingrowth (van de Löcht et al., 2018; van de Löcht et al., 2020), this is better explained by melt metasomatic processes, as evidenced by the Group 2 peridotites' relative enrichment in several melt mobile and fluid immobile elements such as Al and Sc as compared to the Group 1 peridotites (van de Löcht et al., 2020). Such melt metasomatism must predate the amphibolite facies metamorphism the SOISB peridotites experienced (e.g., Nutman and Bennett, 2019). Melt metasomatism can also explain the difference in S isotope compositions between the Group 1 and 2 peridotites as this process appears to have preferentially delivered an isotopically distinct source of sulfur to the Group 2 peridotites. Subsequent metamorphic processes have not erased these differences, and this argues against significant mobilization of sulfur during metamorphism. As shown in Figure 3.4, clear trends are observed when plotting fluid-immobile elements such as Al and Sc, as well as other melt proxies against $\Delta^{33}S$. These trends argue strongly for melt-related mobilization of sulfur in these rocks, which must predate metamorphism, and against subsequent disturbance.

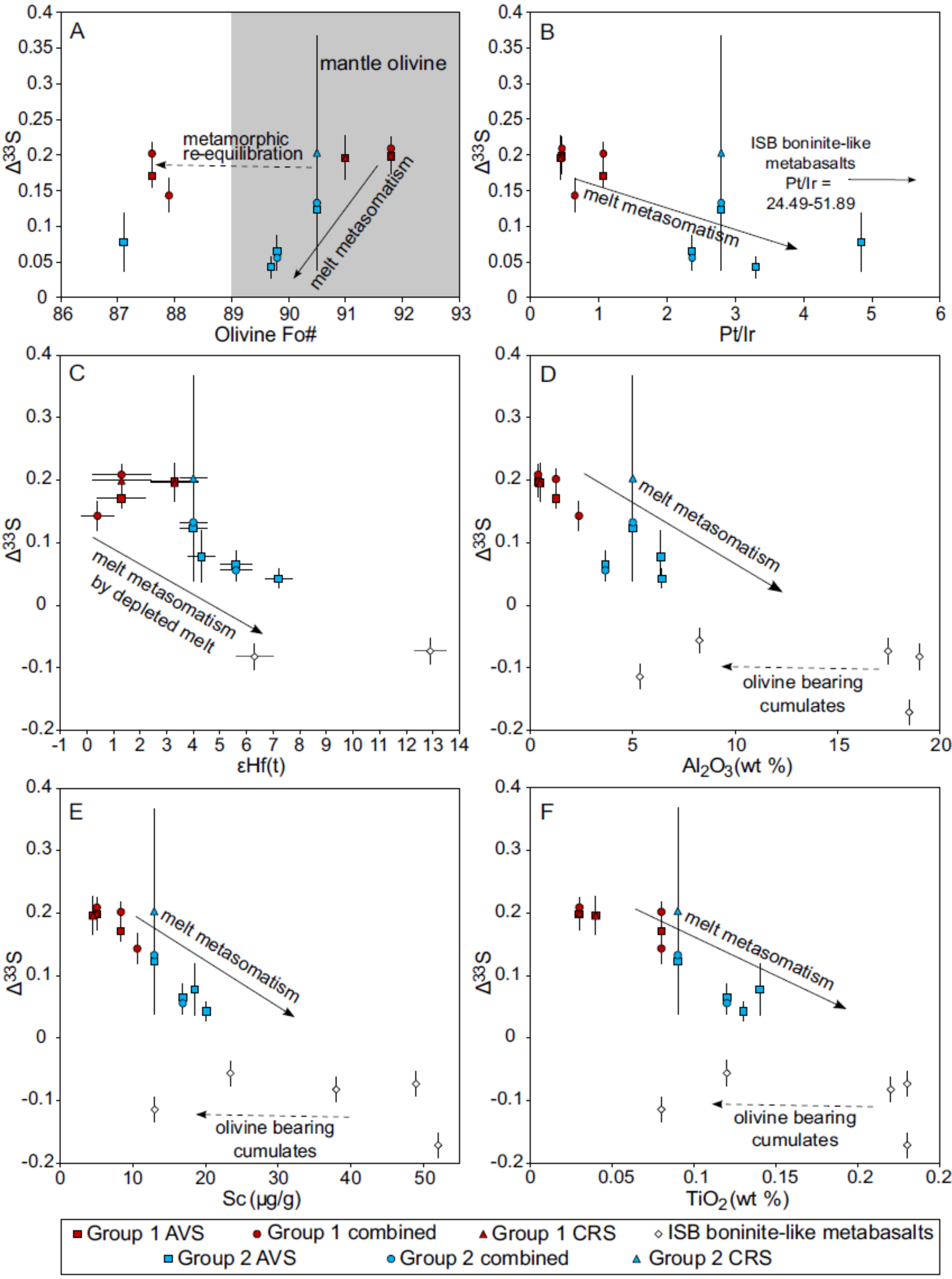

Figure 3.4. $\Delta^{33}S$ values of Group 1 and Group 2 peridotites shown against previously published data including A) olivine Fo# (van de Löcht et al., 2018; van de Löcht et al., 2020), B) Pt/Ir ratios (van de Löcht et al., 2018), C) εHf values (van de Löcht et al., 2018; van de Löcht et al., 2020), D) Al_2O_3 contents (van de Löcht et al., 2018; van de Löcht et al., 2020), E) Sc contents (van de Löcht et al., 2018; van de Löcht et al., 2020), and F) TiO2 contents (van de Löcht et al., 2018; van de Löcht et al.,

2020). B includes Pt/Ir ratios inferred from Szilas et al. (2015), C, D, E, and F also include data ranges for ISB boninite-like metabasalts from Polat and Hofmann (2003); Polat et al. (2002); Siedenberg et al. (2016). Black solid arrows indicate increasing melt metasomatism. C demonstrates that the metasomatizing melt has a depleted mantle source with elevated εHf. Dashed arrows indicate metamorphic re-equilibration of peridotite olivine with other minerals in A and compositional variation resulting from the formation of cumulates in the ISB boninite-like metabasalts in D-F.

Evidence from other Eoarchean terranes subject to similar metamorphic processes as the IGC reinforce this interpretation. Thomassot et al. (2015) investigated a transect between >3.8 Ga metasediments and igneous lithologies in the Nuvvuagittuq Greenstone Belt, Quebec that were, like the SOISB, subject to upper amphibolite facies metamorphism at ~2.7 Ga (Thomassot et al., 2015). Thomassot et al. (2015) found no evidence for the transfer of MIF-S signatures between sediments with $\Delta^{33}S$ values up to +2.27‰ and igneous lithologies within more than a few meters. This is much closer than the samples investigated in this study are to any exposed sedimentary rock. Hence, MIF-S signatures in the studied peridotites are unlikely to be transported from sediments following emplacement via reactive transport associated with metamorphism. Additionally, and as seen in supplementary Figure 3.10.A.3, amphibole can be seen overgrowing some sulfides, demonstrating that these sulfides predate amphibolite facies metamorphism.

Post-emplacement overprint by metamorphic fluid infiltration from crustal rocks is also not expected to have influenced the Hf isotope compositions of the SOISB peridotites. These peridotites and the boninite-like metabasalts in the ISB, the only lithologies with highly positive initial εHf values found in the IGC, occur in limited domains kilometers apart from one another, and the lithologies both yield Eoarchean isochron ages in agreement with the minimum ages obtained by U–Pb zircon dating (Hoffmann et al., 2010; van de Löcht et al., 2020). The two lithologies are separated by bodies of supracrustal rock and TTGs with initial εHf values of near-zero (e.g., Hoffmann et al., 2011a; Hoffmann et al., 2011b). While Hf contamination during amphibolite facies metamorphism of the SOISB peridotites is in principle possible, as demonstrated by Vezinet et al. (2021), the absence of a credible nearby contaminant with high εHf values, such as those observed in the SOISB peridotites, make this scenario unlikely. Additionally, such contamination by fluid infiltration from crustal lithologies would be expected to also introduce a scatter to the Lu–Hf isochrons (Vezinet et al., 2021), which however is not observed in the SOISB peridotites (van de Löcht et al., 2020). Hence, it is unlikely that contamination by metamorphic agents occurred. Finally, like other signs of melt metasomatism that modified the Group 2 more than the Group 1 peridotites, a trend is observed between $\Delta^{33}S$ and εHf (Figure 3.4), showing that both S and Hf isotopes preserve a signal left by the metasomatizing melt that was not erased by subsequent processes. This trend, along with the association between elevated εHf and melt mobile, fluid immobile elements in the Group 2 peridotites (Figure 3.4), argue against metamorphism and for melt metasomatism as the process that brought about the elevated εHf signature in the SOISB peridotites. Such a trend would not be expected if the elevated εHf was introduced by a fluid and not a melt.

3.6.3. Introduction of sediment-derived sulfur

Both groups of peridotites contain sulfur dominated by positive $\Delta^{33}S$, with the group 1 peridotites, which show the least evidence for melt metasomatism (Figure 3.3), having a characteristically narrow range in $\Delta^{33}S$ values of 0.14–0.21‰. This suggests the introduction of S with a high $\Delta^{33}S$ signature affecting both peridotite groups, a process which, however, must have been unrelated to melt metasomatism, because melt metasomatism affected Group 2 peridotites more extensively than Group 1 peridotites (van de Löcht et al., 2018; van de Löcht et al., 2020). A potential source of S with high $\Delta^{33}S$ values is sedimentary material. Sedimentary material of Eoarchean age with high $\Delta^{33}S$ values and $\delta^{34}S$ values around 1–3‰ has been found in the ISB (e.g., Mojzsis et al., 2003; Papineau and Mojzsis, 2006; Whitehouse et al., 2005 Figure 3.5). Sedimentary material such as this, mixed with magmatic sulfur from the primitive mantle with $\Delta^{33}S = \Delta^{36}S = 0‰$ (e.g., Dottin III et al., 2020 and citations therein), could explain the measured isotopic compositions of the least metasomatized peridotites (Figures 3.5, 3.6). The fact that this sedimentary endmember is present in both groups of peridotites and the fact that its isotopic signature is most dominant in the least metasomatized samples suggests that its introduction is not only unrelated to melt metasomatism but predates it. Furthermore, it suggests the introduction of a MIF-S signature at a relatively uniform $\Delta^{33}S$ value of around 0.14–0.21‰ (as preserved in the group 1 peridotites) over a large area.

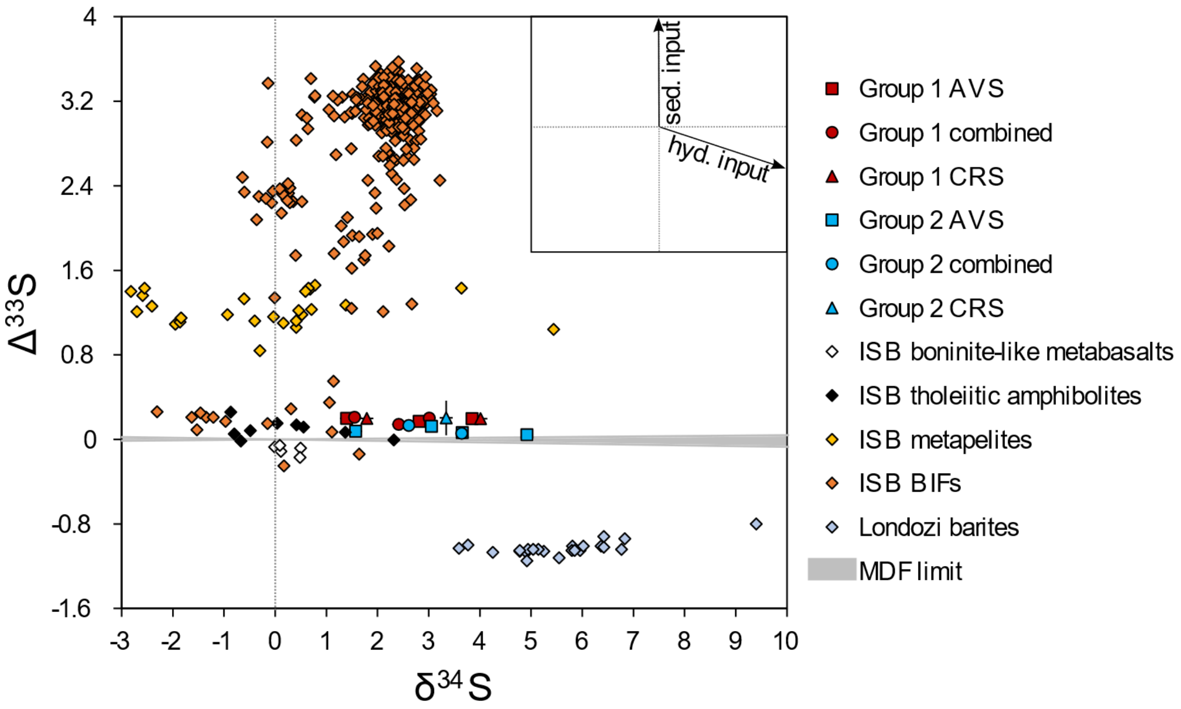

Figure 3.5. Comparison of $\delta^{34}S$ versus $\Delta^{33}S$ values as shown in Figure 3.2 with S isotope data for metabasalts from the ISB with boninite-like compositions (Siedenberg et al., 2016), tholeiitic amphibolites (Lewis et al., 2021; Siedenberg et al., 2016), and sediments from the ISB including metapelites (Mojzsis et al., 2003; Papineau and Mojzsis, 2006), BIFs (Baublys et al., 2004; Mojzsis et al., 2003; Papineau and Mojzsis, 2006; Whitehouse, 2013; Whitehouse et al., 2005), and barites of Paleoarchean age from the Londozi deposit (Roerdink et al., 2012). Errors from literature data are not displayed and are available in the relevant cited papers. Note that Group 2 peridotites fall between Group 1 peridotites and Londozi barites, suggesting that the melt overprinting these peridotites carried sulfur similar to this hydrothermally-derived material. Arrows in the inset show the expected approximate directions input from sedimentary and hydrothermally-derived sulfur would move primary mantle sulfur from the origin at $\delta^{34}S = \Delta^{33}S = 0$.

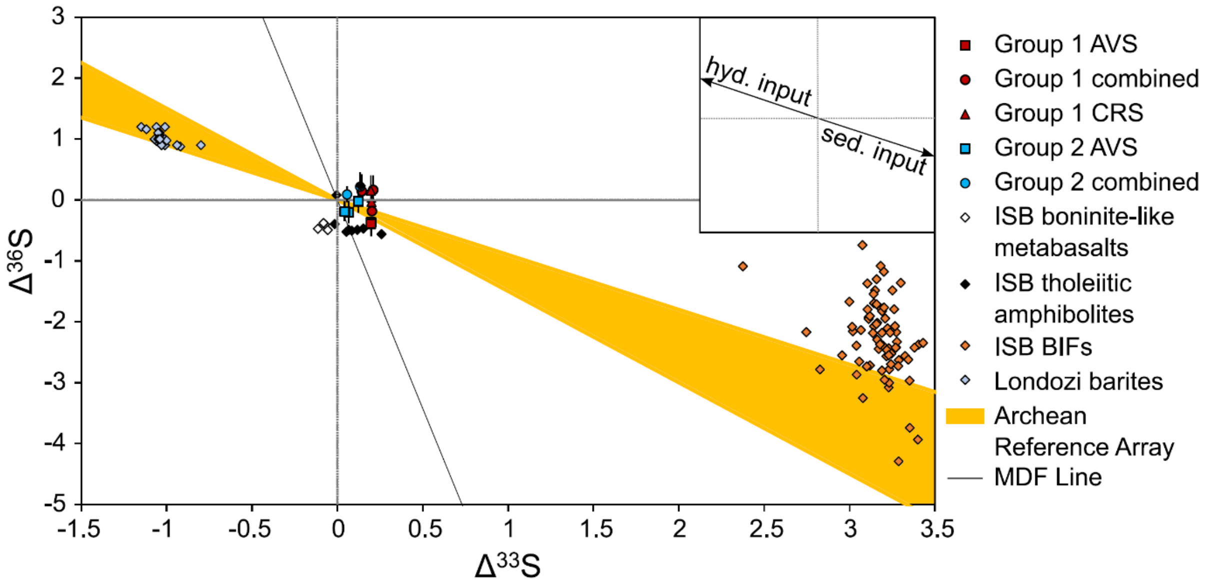

Figure 3.6. Comparison of $\Delta^{33}S$ versus $\Delta^{36}S$ values as in Figure 3.3 to S data for metabasalts from the ISB with boninite-like compositions (Siedenberg et al., 2016), tholeiitic amphibolites (Lewis et al., 2021; Siedenberg et al., 2016), banded iron formations (BIFs) from the ISB (Whitehouse, 2013), and Paleoarchean Londozi barites (Roerdink et al., 2012). Note that a systematic positive $\Delta^{36}S$ offset of 0.8‰ in data from Montinaro et al. (2015), detected subsequent to its original publication, has been corrected in this figure. The Archean reference array is shown in yellow covering typical values of MIF-S (Farquhar et al., 2000; Ono, 2017; Zerkle et al., 2012). The expected array of values produced by mass dependent fractionation (MDF) from microbial sulfate reduction (Ono et al., 2006) is shown as a line. Errors from literature data are not displayed and are available in the relevant cited papers. Group 1 peridotites are offset from the origin in the direction of sedimentary sulfides, Group 2 peridotites are offset from the Group 1 peridotites in the direction of the hydrothermal barites.

If the SOISB peridotites are crustal cumulates, it might be argued that this surface-derived sulfur was incorporated into the rocks via assimilation of crustal material during ascent and emplacement. The Hf isotope compositions of these rocks (van de Löcht et al., 2020), however, argues against significant incorporation of crustal material (such as sedimentary material) on ascent and emplacement if indeed these rocks are crustal cumulates. Furthermore, metasediments capable of significantly contributing to the sulfur inventory of the SOISB peridotites are only very rarely found in the SOISB (Nutman and Friend, 2009). Finally, the olivine-rich compositions of these rocks mean that if they are indeed cumulates, they must have formed at temperatures too high for sulfides to crystallize along with them, even if the melt they formed from contained sulfur. This is because the melting temperature for olivine is much higher than that of sulfide minerals such as the pentlandite and pyrrhotite found in the SOISB peridotites. An injection of evolved melt or fluid would be needed to explain the observed sulfur concentrations, or an early metasomatic event that uniformly affected both groups of rocks, subsequent to initial formation. This injection would have had to predate the melt metasomatic event that preferentially affected the Group 2 peridotites, as well as any subsequent metamorphism we have evidence for. An evolved remnant of the melt that initially formed the cumulate is one possible source for such an injection. However, the lack of compositional or textural evidence for this, particularly in the Group 1 peridotites, favors a mantle origin for these rocks.

Incorporation of sediment-derived material in a mantle setting is furthermore consistent with existing interpretations arguing for a mantle origin of the SOISB peridotites (van de Löcht et al., 2020; van de Löcht et al., 2018). SOISB peridotites all display trace element depletion patterns consistent with mantle rocks subject to high initial degrees of melt extraction of up to 30% or more in the spinel stability field, followed later by melt re-fertilization (van de Löcht et al., 2020). According to this interpretation, the initial depletion of the SOISB peridotites may have occurred through hydrous melting, as van de Löcht et al. (2020) demonstrated using hydrous batch melting models that are consistent with the Th-REE and HFSE systematics of the SOISB peridotites. This melt depletion must have taken place prior to 3.81 Ga, the maximum age of zircon-dated tonalites that are intrusive into the peridotite bodies in the study area (Nutman et al., 2007b), and Re-depletion ages of the peridotites (Bennett et al., 2002; van de Löcht et al., 2018), and therefore the minimum age of the peridotites. Sulfur is expected to behave incompatibly in such a melt depletion event, reducing S to below primitive mantle concentrations (e.g., Fonseca et al., 2011), but variable concentrations between 95 µg/g and 800 µg/g were measured. Therefore, a refertilization event, consistent with this interpretation, is necessary to explain the sulfur concentrations in the studied peridotites alongside their REE and HFSE inventories.

Non-uniformitarian vertical tectonic processes as suggested e.g., by Johnson et al. (2017), Rollinson (2021) and Webb et al. (2020) are not generally expected to bring crustal material containing significant concentrations of surface-derived sulfur or volatiles into the mantle. In contrast, a horizontal tectonic process in which pieces of crust override each other and trap pieces of the mantle in between them would be capable of delivering sulfur from Earth’s surface into the mantle (e.g., Lewis et al., 2021). In modern subduction settings, such a process can release up to 20% of subducted sulfur to the overlying mantle wedge through fluid release (Li et al., 2020).

Importantly though, the Group 1 and Group 2 peridotites are offset from one another along all axes shown in Figures 3.2 and 3.3. This implies that while both groups of peridotites have incorporated surface-derived sulfur, one has incorporated a source of sulfur that the other group has not incorporated to the same extent or at all. This requires a second, different source of sulfur that was preferentially introduced to the Group 2 peridotites.

3.6.4. Melt metasomatism delivering a distinct, second source of likely hydrothermally-derived sulfur

Following depletion (assuming the rocks are mantle peridotites) and initial metasomatism introducing sediment-derived sulfur as evidenced by the peridotites' consistently positive $\Delta^{33}S$ signatures, the textural and compositional properties of the peridotites indicate that they were variably re-enriched by a second metasomatizing agent, specifically in this case a melt (van de Löcht et al., 2020; van de Löcht et al., 2018). Melt metasomatism is typically reflected by an increase in melt mobile, fluid immobile element concentrations such as Al, Ti, and Sc, as well as modification of PGE ratios such as increasing Pt/Ir ratios (e.g., van de Löcht et al., 2018; van de Löcht et al., 2020). Based on these proxies, melt overprint affected the Group 2 peridotites to a greater extent than the Group 1 peridotites (Figure 3.4), and this has been further confirmed by their trace element patterns (van de Löcht et al., 2020). Additionally, melt depletion of mantle rocks tends to increase their Fo#, whereas reenrichment with melts high in incompatible elements tends to decrease it (Friend et al., 2002; van de Löcht et al., 2018). Of the selected SOISB peridotites with Fo#s falling within the typical mantle range, whose olivine compositions appear unaffected by metamorphic reequilibration with other minerals, Group 2 peridotites have lower Fo#s than Group 1 peridotites (van de Löcht et al., 2018). This melt percolation is also documented on an outcrop scale by dunite veining in harzburgite (Supplementary Figure 3.10.A.4; van de Löcht et al., 2020).

Negative trends are observed between $\Delta^{33}S$ values and various proxies for melt metasomatism (i.e., Al_2O_3, TiO_2, Sc contents, and Pt/Ir ratios), as well as a trend between olivine Fo# and $\Delta^{33}S$ values in peridotites with typical mantle Fo#s (Figure 3.4). Melt proxies in the peridotites also display positive correlations with $\delta^{34}S$ values (supplementary Figure 3.10.A.5), indicating that the metasomatizing melt delivered sulfur with relatively high $\delta^{34}S$. Note that some samples show evidence for metamorphic equilibration between olivine and other minerals within the rock as reflected by Fo# lower than typical mantle values, and these do not fall on the same trend (van de Löcht et al., 2018; see also Figure 3.4). These trends point in the direction of a mantle origin for the SOISB peridotites. However, an interpretation positing that the rocks are ultramafic cumulates with initial compositions similar to depleted mantle rocks, which were subject first to a metasomatizing agent that brought in sulfur with high Δ^{33}S, and subsequently were subject to variable melt metasomatism delivering sulfur with lower Δ^{33}S, cannot be excluded.

The correlations between melt proxies with elevated δ^{34}S and lower Δ^{33}S indicate that the refertilizing melt contained sulfur with elevated δ^{34}S and near-zero to negative Δ^{33}S values. Hydrothermal deposits found in Archean deposits younger than the IGC contain such sulfur isotopic signatures (e.g., Bao et al., 2007; Farquhar et al., 2000; Montinaro et al., 2015; Roerdink et al., 2012). While no similar hydrothermally derived material has yet been found in the IGC, evidence for the existence of such a hydrothermally derived input has been observed in the sulfur isotopic composition of TTGs from the IGC (Lewis et al., 2021). δ^{34}S values as high as those measured in the most ^{34}S-enriched SOISB peridotites are rarely observed in sedimentary deposits in the IGC, and when they are, they have elevated Δ^{33}S values. The inclusion of such sedimentary material in a percolating melt therefore cannot be a complete explanation for the offset observed between the Groups 1 and 2 peridotites (Figures 3.2, 3.4). Melting processes within the magmatic system do not produce substantial offsets in δ^{34}S, and while metamorphic desulfidation can increase δ^{34}S in rocks containing disulfides such as pyrite (e.g., Bucholz et al., 2020), it should be noted that the SOISB peridotites are dominated by monosulfides (e.g., pyrrhotite), and there does not appear to be a difference in metamorphic grade experienced by the Groups 1 and 2 peridotites. While late fluid alteration could also provide an explanation for elevated δ^{34}S in the SOISB peridotites, there is little petrographic evidence for this as discussed previously. Additionally, if both groups of peridotites were equally subject to such late alteration, it would not explain the systematic offset observed between the Group 1 and 2 peridotites. Hence, the addition of hydrothermally derived sulfur in the metasomatizing melt is our preferred explanation for the shift towards lower Δ^{33}S and higher δ^{34}S values of the Group 2 peridotites relative to the Group 1 peridotites (Figures 3.5, 3.6).

These observations are consistent with the interpretations of past studies arguing for a mantle origin (Bennett et al., 2002; Friend et al., 2002; van de Löcht et al., 2018; van de Löcht et al., 2020) and a history of depletion and melt refertilization for the studied peridotites (van de Löcht et al., 2018; van de Löcht et al., 2020). While similar PGE patterns to those in the SOISB peridotites have been observed elsewhere in komatiites and chromite cumulates, no komatiites are found in the SOISB and the studied peridotites are not chromite cumulates (van de Löcht et al., 2018), highlighting the distinction and potential genetic difference between the studied peridotites and known cumulate rocks. A melt metasomatizing event is, however, also conceivable in the case of a crustal cumulate origin for the SOISB peridotites. In this case, the metasomatizing melt would need to have been introduced to the cumulate via a secondary injection following emplacement in the crust. The mantle source of this metasomatizing melt would also need to have incorporated sulfur from a different source than the one that dominates the isotopic signatures of the Group 1 peridotites.

3.6.5. Constraints on the source and chemical composition of the metasomatizing melt

Characterization of the depletion and re-enrichment history of the SOISB peridotites provides constraints on the geodynamic context in which these processes operated. Van de Löcht et al. (2020) proposed, based on consistent trace element modeling, that the SOISB peridotites had initial compositions consistent with the depleted mantle and were overprinted to a minor, variable degree by an adakite-like slab melt. A combined evaluation of sulfur isotope compositions, initial Hf isotope compositions, and major and trace elements is used here to place tighter constraints on the source and composition of the overprinting melt, assuming the peridotites have an origin in the depleted mantle, and to evaluate the depletion history of the SOISB peridotites. Previous investigations have shown that the most depleted Group 1 peridotites have near to chondritic initial εHf values (εHf(t) = +0.6 (van de Löcht et al., 2020); Figure 3.4C). This limits the timing of mantle depletion of these peridotites (or, if they are cumulates, depletion of their mantle sources) to shortly before their inferred minimum age of ca. 3.81 Ga (van de Löcht et al., 2020).

In contrast to Group 1 peridotites, Group 2 peridotites include highly depleted initial εHf values of up to +7.2 (van de Löcht et al., 2020; Figure 3.4C). The negative correlation between initial εHf with $\Delta^{33}S$ values in both groups of peridotites is in line with the introduction of an overprinting, metasomatizing melt with a highly depleted Hf isotope composition (Figure 3.4C). Of the igneous rocks outcropping in the IGC, the only ones found to possess sufficiently high εHf values to form a potential endmember composition to explain this trend are 3.7 Ga, SiO_2-poor, boninite-like metabasalts found in the ISB (Hoffmann et al., 2010). These are also the only igneous rocks in the IGC found to possess a MIF-S signature consistent with an endmember dominated by negative $\Delta^{33}S$, likely hydrothermally-derived, material (Siedenberg et al., 2016). These boninite-like metabasalts were interpreted to have formed in a subduction zone analogous to modern boninite formation (Polat et al., 2002). Compositionally and isotopically, melts similar to these boninite-like metabasalts may fit as potential endmembers as exemplified by negative correlations between $\Delta^{33}S$ values and Al_2O_3, Sc, and TiO_2 contents (Figure 3.4 D, E, F) (Hoffmann et al., 2010; Polat et al., 2002; Szilas et al., 2015) as well as their Pd/Ir ratios of ca. 50 (Szilas et al., 2015). Only the least differentiated boninite-like metabasalts have suitable mixing endmember compositions opposite the least altered Group 1 peridotites that can explain the compositions of Group 2 peridotites (Polat et al., 2002; Szilas et al., 2015) (Figure 3.4 D, E, F), with the least differentiated boninite-like metabasalts yielding MgO contents of ca. 15–18 wt% (Polat et al., 2002; Szilas et al., 2015). Correlations in existing data between initial εHf values and Pt/Ir ratios, as well as Al, Sc, and Ti concentrations, reinforce the link between εHf and $\Delta^{33}S$ values and further demonstrate the connection between these isotope signals and melt processes (Supplementary Figure 3.10.A.6). These correlations further underscore the probable absence of post-emplacement metamorphic processes disrupting the εHf and $\Delta^{33}S$ values in the Group 1 and Group 2 peridotites. However, the age of the existing ISB boninite-like metabasalts is >100 million years younger than the peridotites analyzed here (Frei et al., 2004; Hoffmann et al., 2011b; Nutman et al., 2007b). While the existing ISB boninite-like metabasalts cannot directly represent the melt that percolated into the SOISB peridotites, these metabasalts may share a depleted mantle source with this melt or at least have a very similar geodynamic origin.

The sulfur isotope composition of the metasomatizing melt implied by the offset between the Group 1 and Group 2 peridotites is not identical to that of the younger ISB boninite-like amphibolites (Figure 3.5). The Group 2 peridotites are offset from the Group 1 peridotites towards elevated $\delta^{34}S$ values and lower $\Delta^{33}S$ values in the direction of Archean hydrothermal sulfur such as that contained in the Londozi barites. Hence, they cannot have been offset in the direction of the sulfur isotope compositions of the ISB 3.72 Ga boninite-like amphibolites that have $\delta^{34}S$ values around 0–0.5‰ (Figure 3.5). If the boninite-like metabasalts were directly representative of the overprinting melt, the Group 2 peridotites would be expected to have lower, not higher average $\delta^{34}S$ values as compared to the Group 1 peridotites. This suggests that the overprinting melt primarily modifying the Group 2 peridotites had a sulfur isotope composition with elevated $\delta^{34}S$ as compared to the boninite-like metabasalts, more closely resembling the composition of the Londozi barites, comparatively unattenuated by magmatic sulfur with $\delta^{34}S = \Delta^{33}S = 0$. This likely hydrothermally-derived material must have been brought into the mantle source of the melt by dehydration of oceanic crust and possibly associated supracrustal material into an overlying mantle domain. Older analogous melts to the ISB boninite-like rocks tapping a sulfur source similar to, e.g., the Mesoarchean Londozi barites would therefore represent a viable endmember that interacted with the Group 1 peridotites to form the Group 2 peridotites. The existing ISB boninite-like metabasalts appear to contain $\delta^{34}S$ and $\Delta^{33}S$ values in which this hypothetical endmember composition has been attenuated by mixing with primitive mantle-derived ($\delta^{34}S = \Delta^{33}S = 0$) sulfur during ascent.

To demonstrate the feasibility of mixing depleted mantle with a metasomatizing melt compositionally analogous to the ISB boninite-like metabasalts to produce the SOISB peridotites, we developed a melt-refertilization model of trace element compositions of a strongly depleted mantle source that was variably overprinted by a melt with the trace element inventory of a representative sample of the ISB boninite-like metabasalts (Figure 3.7). For this model, an initial depleted mantle composition was produced by subjecting a primitive mantle reservoir to 40% batch partial melting at 2 GPa. This primitive mantle reservoir had a trace element composition following Palme and O'Neill (2014), an initial mineral composition of 53% olivine, 29% orthopyroxene, and 18% clinopyroxene following (van de Löcht et al., 2020), and partition coefficients for the partial melt were employed following Salters and Stracke (2004); Stracke and Bourdon (2009); van de Löcht et al. (2020) and references therein; Figure 3.7. The partition coefficients employed in the model are based on the compilation by Tusch et al. (2022) and are shown in supplementary Table 3.10.D. Re-enrichment of the depleted mantle to varying degrees by a melt with a trace element composition of a representative ISB boninite-like metabasalt was calculated by simple two component mixing. It is demonstrated that a relatively low degree of melt refertilization on the order of 5% produces a trace element pattern similar to that of a representative Group 1 peridotite, and a higher degree of re-fertilization up to 30% produces a trace element pattern resembling that of a representative Group 2 peridotite. Such a melt refertilization event would therefore explain the trace element patterns of Group 1 and 2 peridotites.

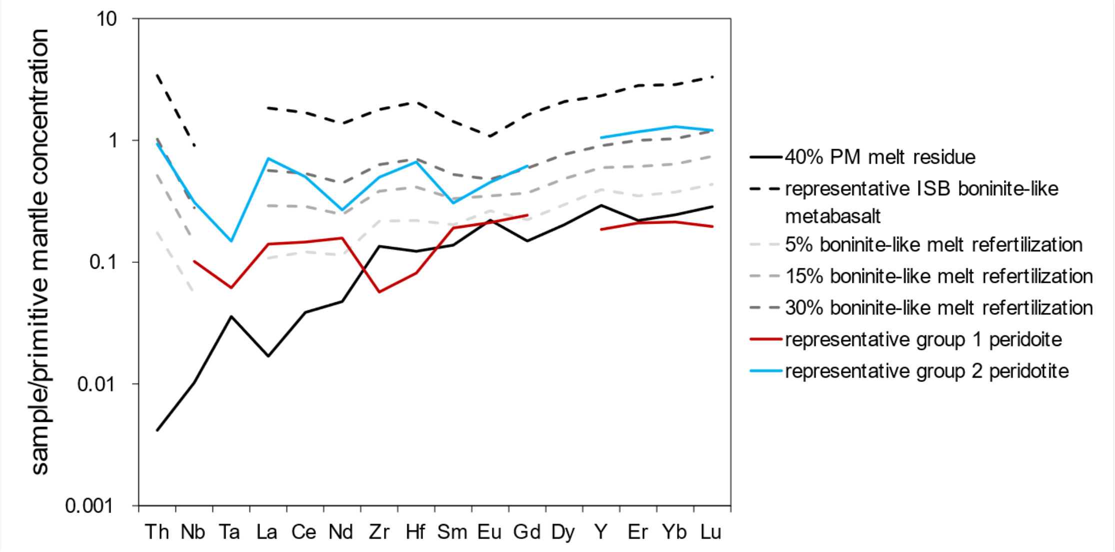

Figure 3.7. Primitive mantle normalized trace element patterns showing the composition of primitive mantle subject to 40% partial melting (Palme and O'Neill, 2014) employing a melting-refertilization model modified from van de Löcht et al. (2020). Further employing this melting-refertilization model, the depleted mantle residue is re-fertilized by 5%, 15%, and 30% with a melt with a trace element composition of a representative ISB boninite-like metabasalt. The resulting composition subject to a low degree (5%) of refertilization resembles that of a representative ISB Group 1 peridotite, whereas the composition subject to a higher degree of refertilization (30%) resembles that of a representative ISB Group 2 peridotite.

3.6.6. Combined S and Hf isotope constraints on depleted mantle reservoirs and timing of mantle depletion

The presence of a boninite-like metasomatizing melt with relatively low $\Delta^{33}S$ and high $\delta^{34}S$ infiltrating the SOISB peridotites provides further evidence for highly depleted mantle reservoirs in the Eoarchean and earlier. Previously, the anomalous Hf isotope record found in mafic and ultramafic IGC rocks has been called into question in light of the fact that other rocks in the IGC, notably tholeiitic metabasalts and TTGs, display bulk rock and zircon Hf isotope systematics indicative of a chondritic, and not a depleted, mantle source (e.g., Fisher and Vervoort, 2018; Hiess et al., 2008; Polat et al., 2003). However, in contrast to the boninite-like metabasalts, IGC TTGs and tholeiite-like metabasalts both have sulfur isotope signatures with elevated $\Delta^{33}S$ (Lewis et al., 2021; Siedenberg et al., 2016). It is therefore tholeiitic, not boninite-like rocks that are thought to be the source rocks of Eoarchean TTGs (e.g., Hoffmann et al., 2014; Lewis et al., 2021). Evidence for a melt with a source similar to that of the boninite-like metabasalts found in the ISB modifying the SOISB peridotites reinforces the interpretation that the former also have their source in the depleted mantle (Hoffmann et al., 2010).

Superchondritic εHf(t) values found in both the ISB peridotites and the ISB boninite-like metabasalts are consistent with the formation of depleted mantle domains as early as 4.1 Ga that contributed to both the ISB boninite-like metabasalts and the melt that refertilized the peridotites. Based on our model for this depleted endmember, a 40% melt depletion of primitive mantle as modelled in Figure 3.7 is consistent with a melt depletion age of 4.1 Ga, reproducing ^{176}Lu/^{177}Hf ratios consistent with those of the most radiogenic Group 2 peridotites and boninite-like metabasalts (Figure 3.8). This suggests that both the ISB boninite-like metabasalts and the melt metasomatizing the peridotites could have tapped the same mantle source. Note that the near-chondritic, lowest εHf (3.81Ga) values of the Group 1 peridotites correlate strongly with the highest Δ^{33}S values observed in these rocks (Figure 3.4 C). This implies that the melting event that initially depleted the mantle domain represented by the Group 1 peridotites (or, in the case of a cumulate origin, their source rocks) occurred very close in time to the process that introduced sediment-derived sulfur and that variable melt refertilization at ca. 3.81 Ga occurred (Figure 3.8). However, a single depletion scenario for the mantle source of the boninite-like and refertilizing melt is not the only option, and it remains possible that the ISB boninite-like rocks and the melt metasomatizing the SOISB peridotites could have tapped different mantle sources carrying similar sulfur isotopic signatures at different times.

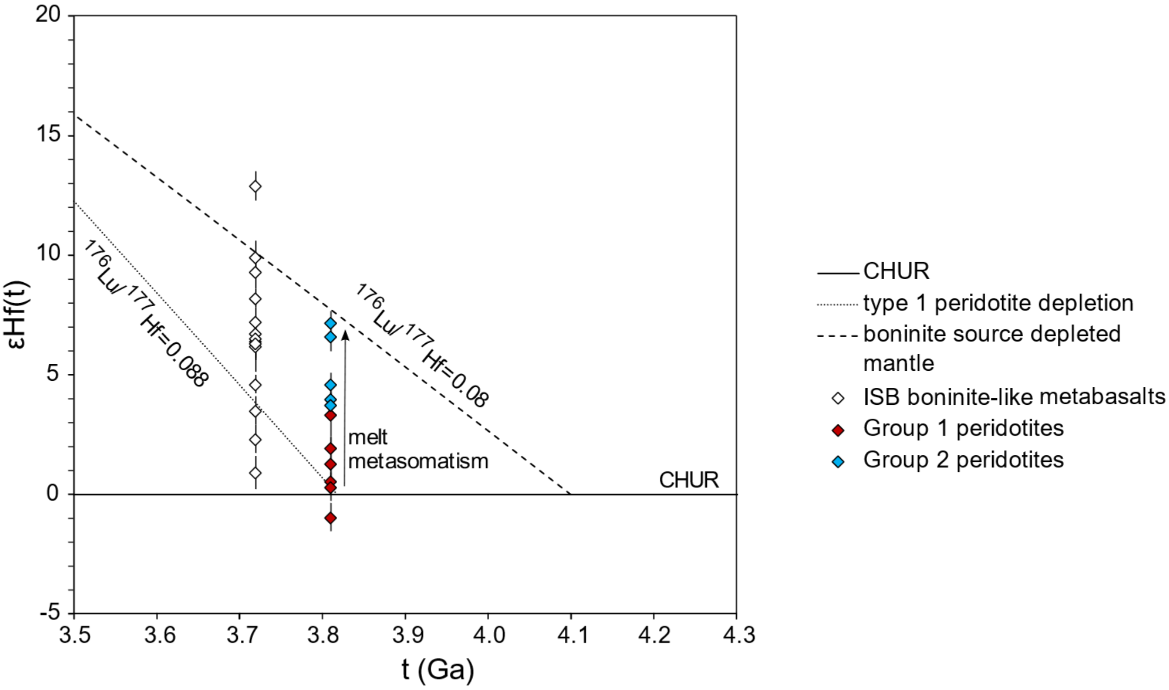

Figure 3.8. Plot illustrating εHf evolution of hypothetical mantle domains over time along with the εHf compositions and minimum ages of SOISB peridotites and ISB boninite-like metabasalts. A 40% depletion of a hypothetical primitive mantle source for both the SOISB peridotites and the ISB boninite-like metabasalts at 4.1Ga agrees well with the maximum εHf (3.81Ga) of +7.1 of the peridotites (van de Löcht et al., 2020) and (barring one outlier of +12.9) the highest εHf(3.72Ga) of +9.9 of the boninite-like rocks. Note that the near-zero minimum εHf(3.81Ga) of the peridotites and the correlation between low εHf (3.81Ga) and elevated $\Delta^{33}S$ in the peridotites strongly imply that the initial hydrous melt depletion of the peridotites (or their mantle source rocks) and the introduction of sediment-derived sulfur to these rocks occurred only shortly before melt re-enrichment. CHUR and εHf values are calculated using modern Lu-Hf systematics from Bouvier et al. (2008) and $\lambda^{176}Lu = 1.867*10^{-11}$ from Scherer et al. (2001); Söderlund et al. (2004).

3.6.7. Geodynamic implications and the case for early crustal recycling

A mantle origin for MIF-S in the SOISB peridotites may be required regardless of whether the SOISB peridotites have their origin in the mantle or as crustal cumulates. In the latter case, the cumulate may have originated from melting of a depleted mantle source that had already incorporated sediment-derived sulfur, and, shortly after formation, experienced an injection of melt or fluid from the remaining liquid, explaining the elevated $\Delta^{33}S$ values found in the least melt overprinted peridotites. A second melt injection carrying sulfur with lower $\Delta^{33}S$ (as well as elevated $\delta^{34}S$), influencing the composition of the Group 2 peridotites to a greater extent than the Group 1 peridotites, is therefore needed to produce the trends observed in Figure 3.4 (and Figure 3.10.A.6 in the supplementary material).

While a cumulate origin for the SOISB peridotites cannot be completely ruled out, the PGE systematics of known IGC cumulates are not identical to those of the SOISB peridotites. The IGC ultramafic cumulate rocks identified by Waterton et al. (2022) as similar to those of the SOISB peridotites and reported by McIntyre et al. (2019) all have higher Ru concentrations than the primitive mantle, unlike the SOISB peridotites. In the case of the Group 1 peridotites, positive Ru anomalies are observed, but they are smaller. As discussed in the GSA data repository of van de Löcht et al. (2018), PGE patterns similar to those of the SOISB Group 1 peridotites have been identified in chromite-bearing cumulates and komatiites (Coggon et al., 2015; Puchtel et al., 2009). However, no komatiites have been identified in the IGC and the studied SOISB peridotites are not associated with chromite cumulates (van de Löcht et al., 2018). Therefore, a mantle source for the SOISB peridotites remains our preferred model.

In summary and as shown in Figure 3.9, our preferred model posits that two distinct mantle domains were involved in the formation of the SOISB peridotites. At ~3.81 Ga, a portion of the mantle was depleted by partial melting and metasomatized with introduction of sediment-derived sulfur, forming the high $\Delta^{33}S$ endmember. This portion of metasomatized mantle would become the ISB peridotites analyzed in this study. A second portion of the mantle first underwent partial melting earlier, at ~4.1 Ga, to produce highly depleted mantle material. This depleted mantle was subsequently metasomatized with introduction of hydrothermally-derived sulfur, forming a high $\delta^{34}S$, low $\Delta^{33}S$ endmember. After metasomatism of the first mantle domain, this second domain partially melted, and the resulting melt overprinted the first mantle domain, as evidenced by the negative correlation between initial εHf and $\Delta^{33}S$ values. This hydrothermal sulfur bearing endmember has as yet not been directly sampled, but its contribution is strongly indicated by the direction of the offset between the two groups of peridotites and Hf isotope data. The degree of melt overprint of the first mantle domain was variable. The less overprinted material is recorded in Group 1 peridotites, whereas the more overprinted material is recorded in Group 2 peridotites. Part of the metasomatized mantle bearing hydrothermally-derived sulfur may also have provided the source of sulfur in the ISB boninite-like metabasalts that contain a hydrothermally-derived sulfur signature (Siedenberg et al., 2016) (lightest gray field in Figure 3.9). Note that the boninite-like rocks and the melt metasomatizing the peridotites do not necessarily share a common source in the mantle, but the isotopic evidence is consistent with this possibility. This possible genetic link is depicted by the dotted line in Figure 3.9. The hydrothermally-derived signal in the ISB boninite-like rocks was attenuated compared to its probable value in the metasomatized mantle as a result of mixing with magmatic sulfur during ascent.

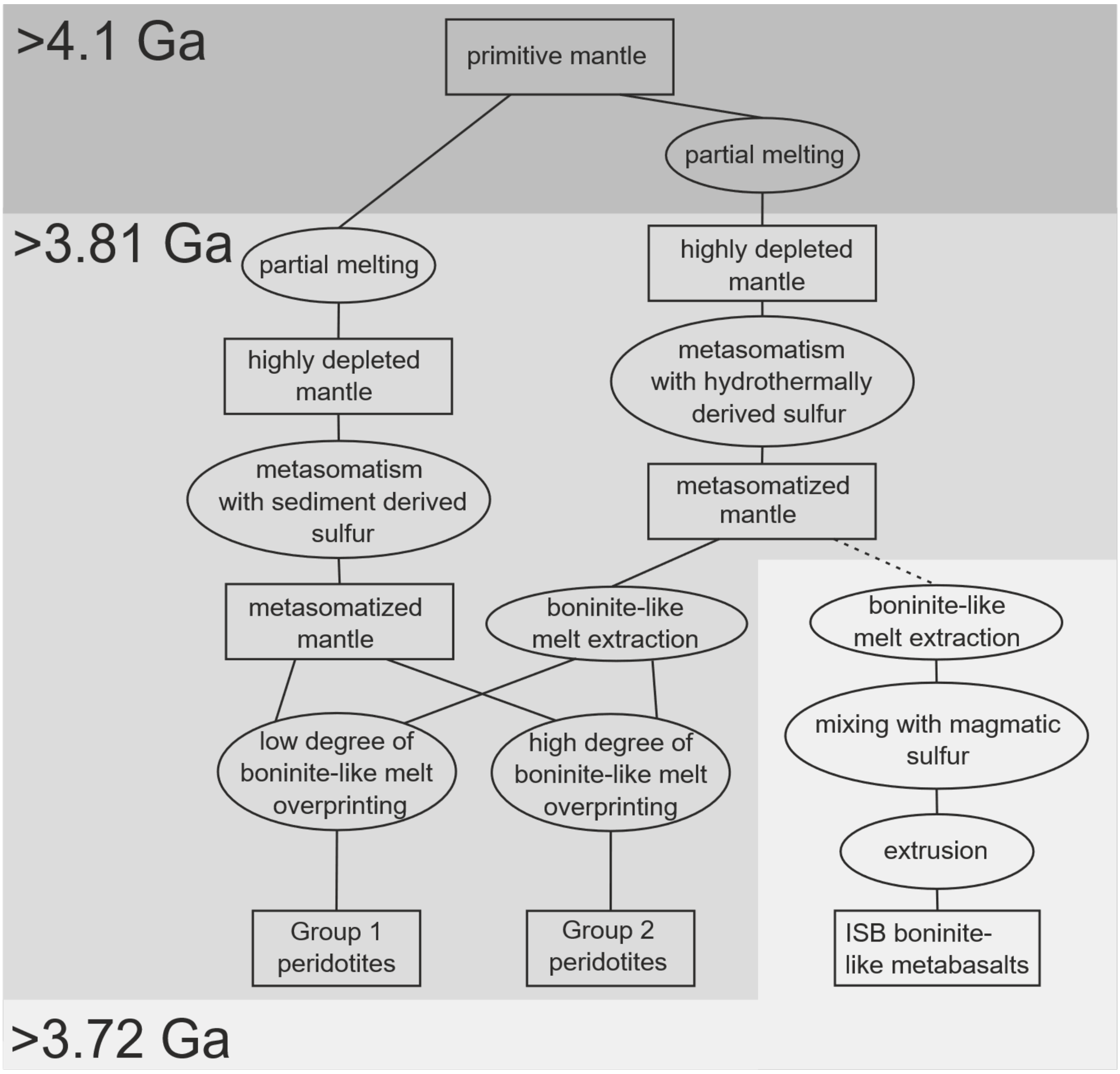

Figure 3.9. Summary of the processes involved in our preferred model of the formation of the ISB peridotites and related rocks. See text for discussion.

3.7. Conclusions

The sulfur isotope compositions of the SOISB peridotites indicate that they have incorporated surface-derived material of Archean age. Specifically, the least metasomatized (Group 1) peridotites are dominated by sulfur with high $\Delta^{33}S$ values characteristic of sedimentary input, and peridotites subject to more melt metasomatism (Group 2) appear to have incorporated additional sulfur with low $\Delta^{33}S$ and high $\delta^{34}S$, characteristic of hydrothermally derived S input. When combined with major and trace element bulk rock chemistry and Hf isotope systematics from previous studies, correlations are observed corroborating previous interpretations that many SOISB peridotites have been subject to a two-stage process of hydrous melt depletion and melt refertilization. Therefore, two distinct mantle domains must have formed in the Hadean and Eoarchean prior to the formation of the ISB. Different surface-derived sulfur sources, one dominated by sediment and the other likely by hydrothermally deposited material, were then incorporated in these mantle domains to different degrees. These two mantle domains would respectively represent the sources for the melt that formed the initial cumulate and the overprinting melt in the case of a cumulate origin for these rocks. In our preferred mantle origin interpretation, the first mantle domain is represented by the Group 1 peridotites, with the melt that percolated through them sourced in the second mantle domain (Figure 3.9).

Boninite-like metabasalts that have been linked to subduction-modified mantle (Hoffmann et al., 2010; Polat et al., 2002) found in the ISB may but do not necessarily share a common mantle source with the metasomatizing melt that intruded the SOISB peridotites. The correlations between the sulfur isotope compositions of the SOISB peridotites and various melt proxies reinforce existing interpretations that these rocks were subject to depletion and re-enrichment. Collectively, the SOISB peridotites document the presence of depleted mantle domains and recycling of material from the Earth's surface in a heterogeneous Eoarchean mantle.

3.8. Declaration of Competing Interest

The authors declare that they have no known competing financial interests or personal relationships that could have appeared to influence the work reported in this paper.

3.9. Acknowledgements

The authors thank the German Science Foundation (DFG) for supporting project HO4794/3-1 and SCHW1889/2-1 within the DFG priority program SPP1833 ‘Building a Habitable Earth,’ as well as DFG grant Mu 1406/8-2. We thank Sonja Aulbach for patient editorial handling of the manuscript and helpful comments, as well as Pedro Waterton and an anonymous reviewer for constructive comments that helped to improve the manuscript. The authors also wish to thank the National Natural Science Foundation of China for NSFC 41703019 in support of the acquisition of sulfur concentration data. We thank the Danish National Research Fund for grants to NordCEE. The authors also thank Andreas Lutter for

technical assistance. We thank Julia van de Löcht for valuable descriptions and information about the peridotite samples.

3.10. Supplementary material for the third chapter

3.10.A. Supplementary figures and captions

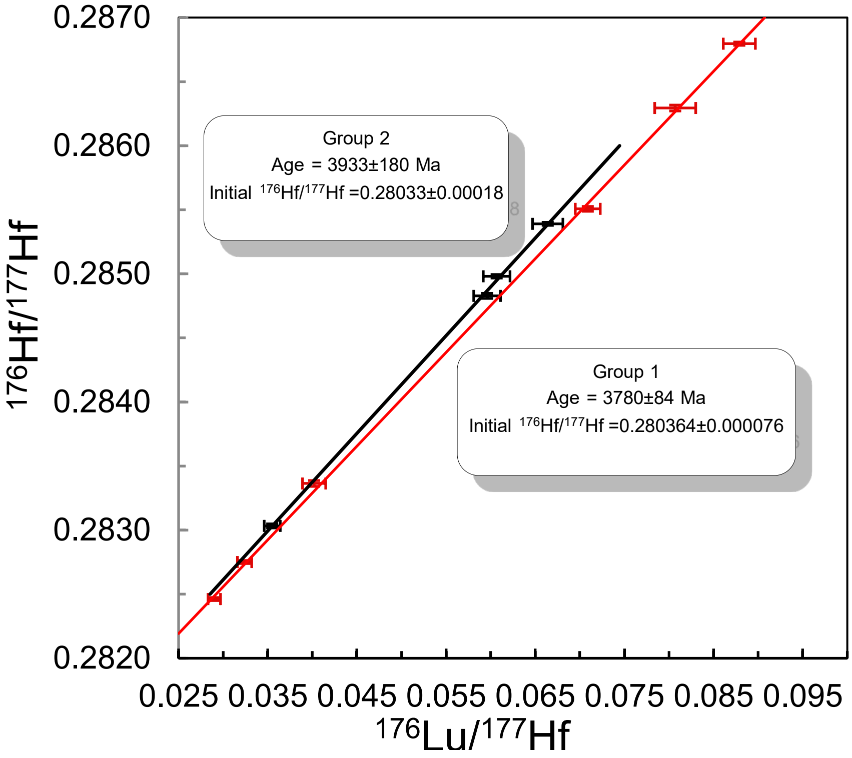

Supplementary Figure 3.10.A.1: Separate Lu-Hf age regressions for Group 1 and 2 peridotites. Data from van de Löcht et al. (2020).

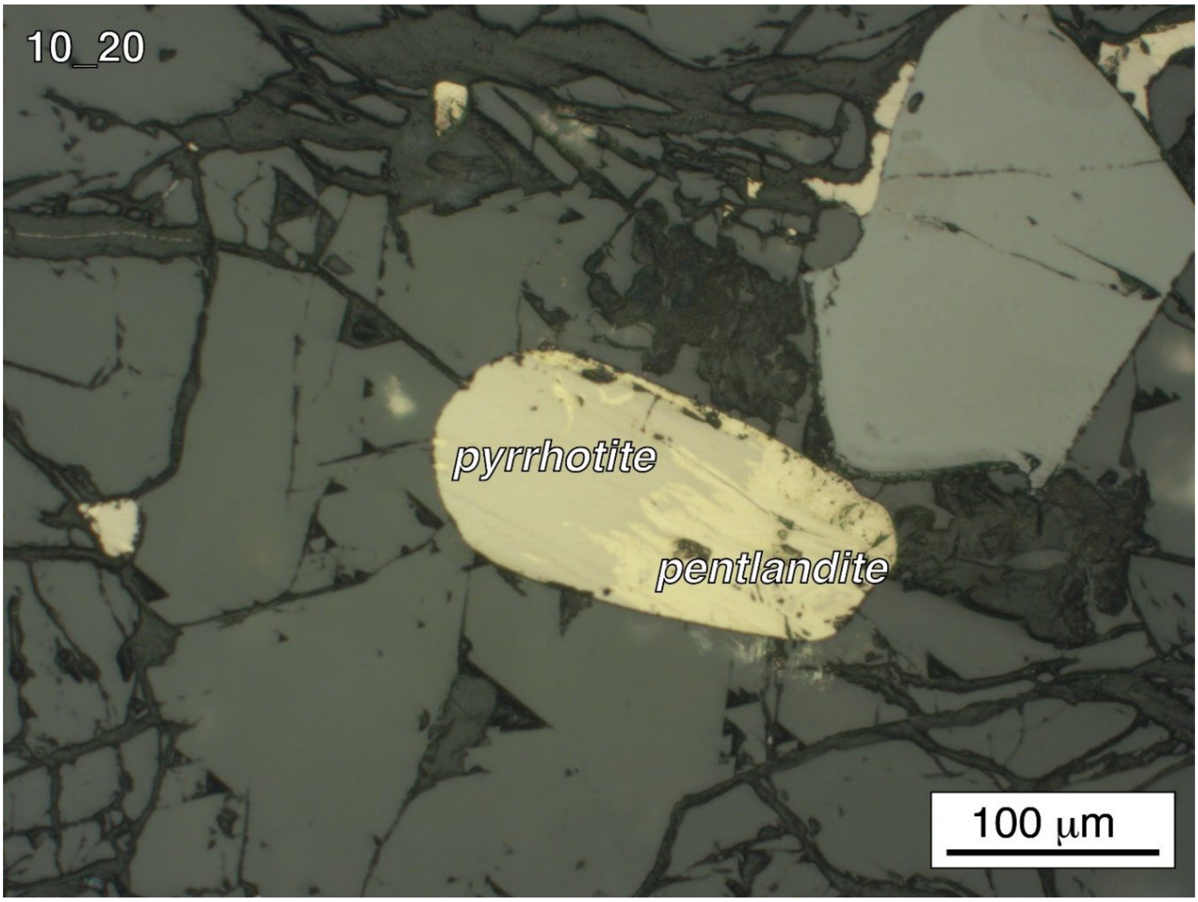

Supplementary Figure 3.10.A.2: Representative photomicrograph of intergrown pentlandite and pyrrhotite in the SOISB peridotites

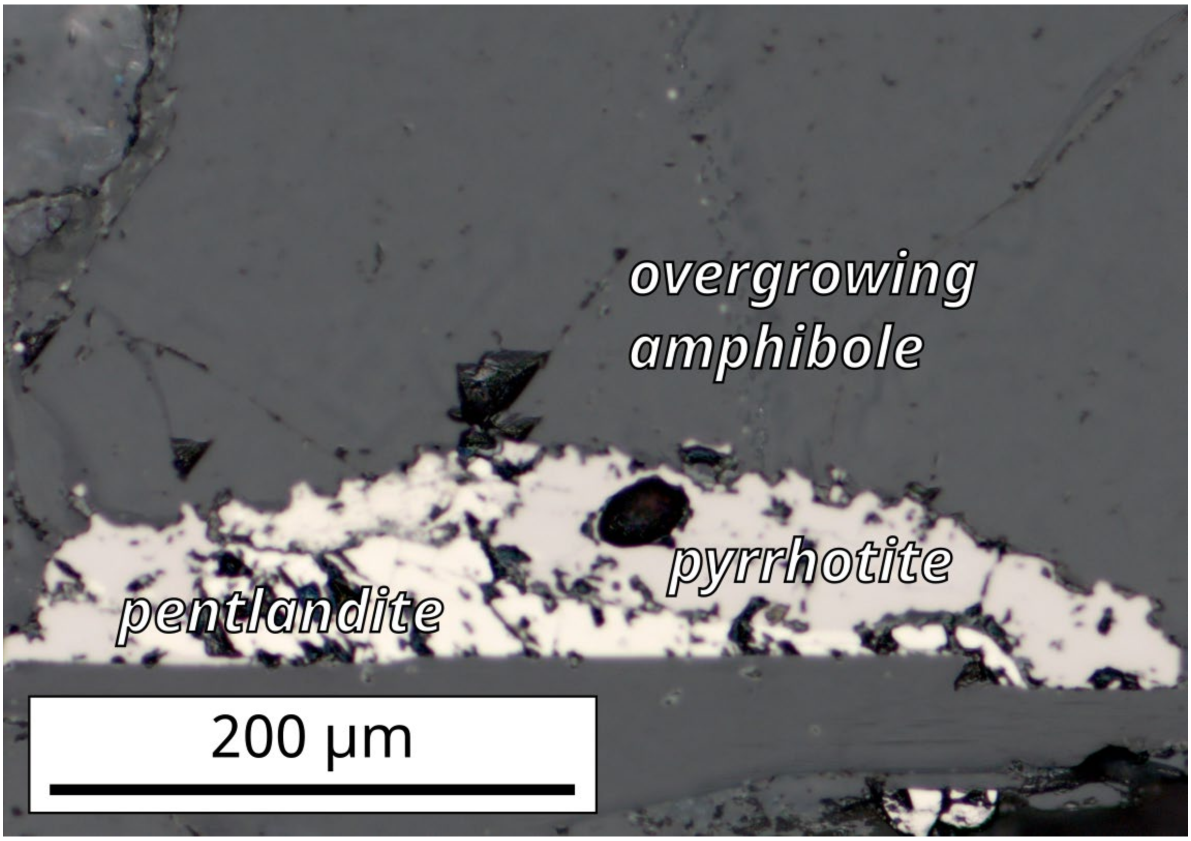

Supplementary Figure 3.10.A.3: Amphibole overgrowing a sulfide in a SOISB peridotite. Note the scalloped texture of the overgrowing crystal.

Supplementary Figure 3.10.A.4, originally published in (van de Löcht et al., 2020): Dunite veining visible on outcrop scale in SOISB peridotite.

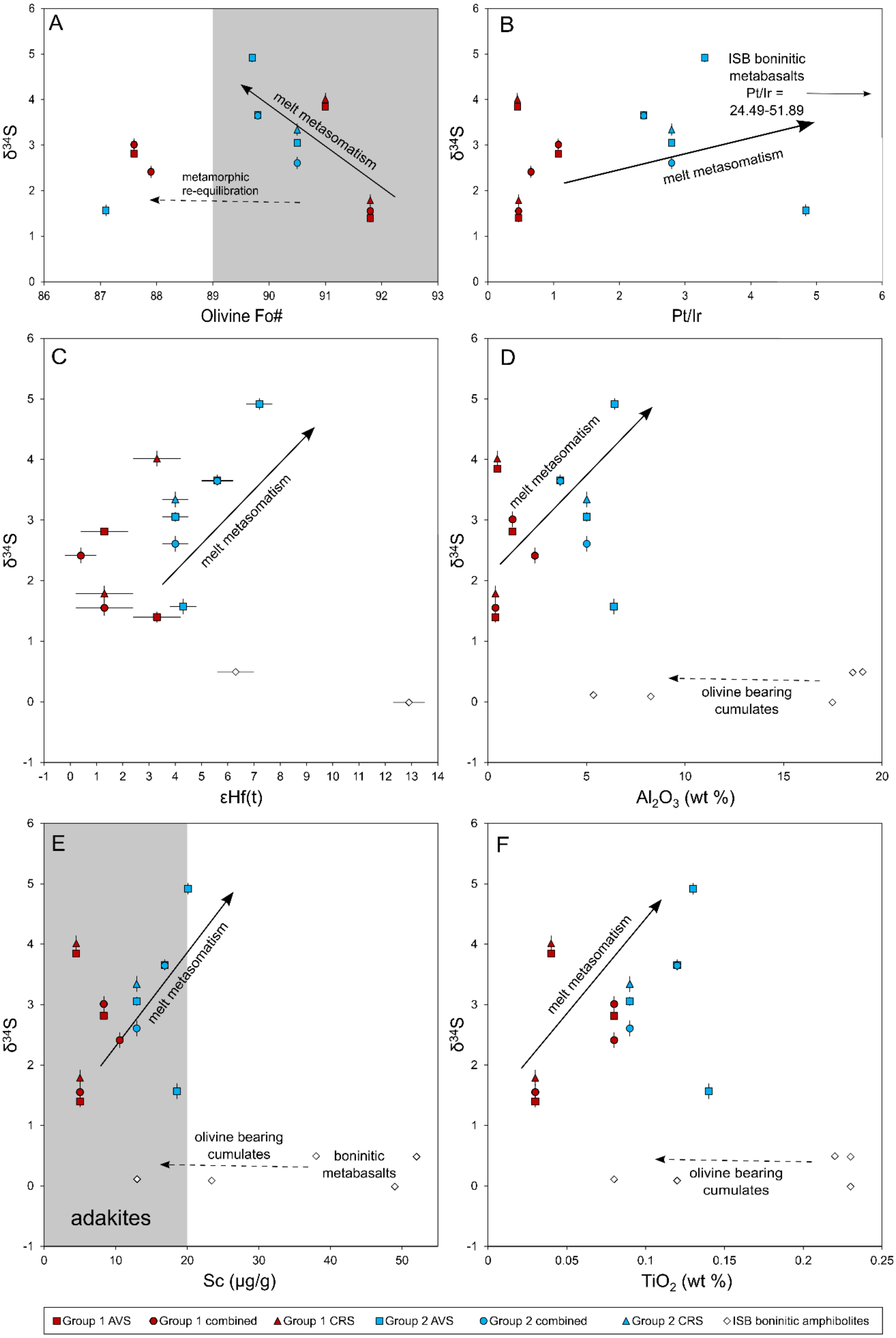

Supplementary Figure 3.10.A.5: $\delta^{34}S$ values of Group 1 and Group 2 peridotites shown against previously published data as in Figure 6 of the main text, including A) olivine Fo# (van de Löcht et al., 2018b; van de Löcht et al., 2020), B) Pt/Ir (van de Löcht et al., 2018b), C) εHf values (van de Löcht et al., 2018b; van de Löcht et al., 2020), D) Al_2O_3 (van de Löcht et al., 2018b; van de Löcht et al., 2020), E) Sc (van de Löcht et al., 2018b; van de Löcht et al., 2020), and F) TiO_2 (van de Löcht et al., 2018b; van de Löcht et al., 2020). B includes Pt/Ir inferred from (Szilas et al., 2015), C, D, E, and F also include data for ISB boninite-like metabasalts from (Polat and Hofmann, 2003; Polat et al., 2002; Siedenberg et al., 2016).

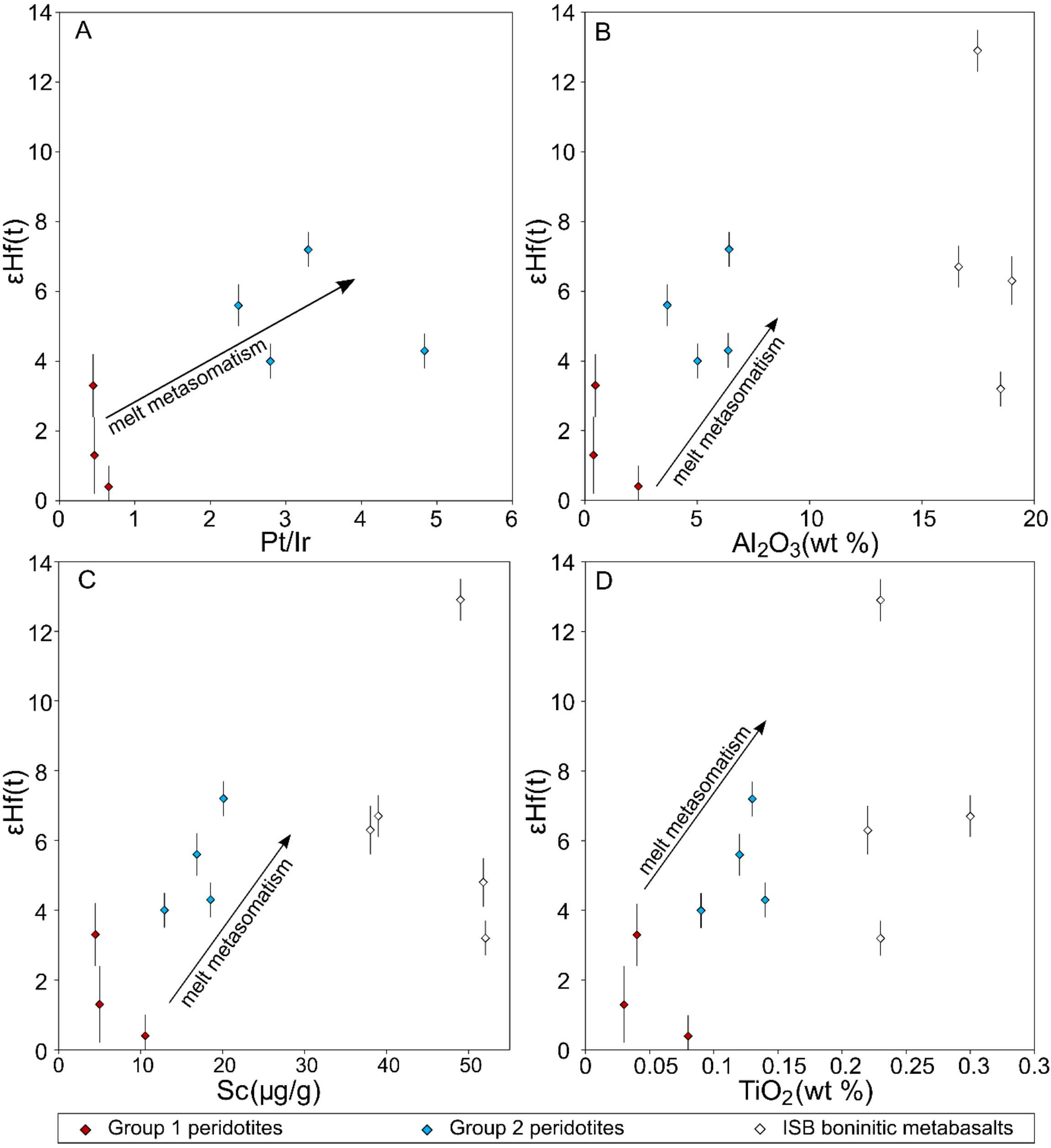

Supplementary Figure 3.10.A.6: initial εHf values of Group 1 and Group 2 peridotites shown against A) Pt/Ir ratios (Szilas et al., 2015; van de Löcht et al., 2018b; van de Löcht et al., 2020), B) Al_2O_3 contents (van de Löcht et al., 2018b; van de Löcht et al., 2020), C) Sc contents (van de Löcht et al., 2018b; van de Löcht et al., 2020), and D) TiO_2 contents (van de Löcht et al., 2018b; van de Löcht et al., 2020). B, C, and D also show data from ISB boninite-like metabasalts (Polat and Hofmann, 2003; Polat et al., 2002) for comparison.

3.10.B. Sample locations

Supplementary Table 3.10.B: Sample locations

Sample Name	Sample Type	Rock Type	Latitude (N)	Longtitude (W)
010-020C	SOISB Group 1	Harzburgite	65°00.740'	50°14.977'
010-022	SOISB Group 1	Dunite	65°00.896'	50°15.007'
010-023	SOISB Group 1	Dunite	65°00.921'	50°14.992'
010-034	SOISB Group 1	Harzburgite	65°00.746'	50°11.965'
010-029A	SOISB Group 2	Harzburgite	65°00.997'	50°12.580'
010-029B	SOISB Group 2	Harzburgite	65°00.997'	50°12.580'
010-030	SOISB Group 2	Harzburgite	65°01.007'	50°12.468'
010-031	SOISB Group 2	Harzburgite	65°00.956'	50°14.498'

Data first reported in van de Löcht et al., (2018)

3.10.C. Standard results

Table 3.10.C: Standard Results

sample name	$\delta^{34}S$ vs CDT [‰]	$2\sigma(\delta^{34}S)$ [‰]	$\Delta^{33}S$ [‰]	$2\sigma(\Delta^{33}S)$ [‰]	$\Delta^{36}S$ [‰]	$2\sigma(\Delta^{36}S)$ [‰]
IAEA-S1	-0.366	0.01	0.083	0.019	-1.02	0.145
IAEA-S1	-0.372	0.01	0.068	0.044	-0.768	0.11
IAEA-S1	-0.367	0.014	0.078	0.023	-0.976	0.168
IAEA-S1	-0.399	0.012	0.081	0.031	-0.918	0.209
IAEA-S1	-0.391	0.016	0.063	0.029	-0.574	0.177
IAEA-S1	-0.407	0.01	0.074	0.034	-0.758	0.207
IAEA-S1	-0.279	0.008	0.068	0.038	-0.943	0.242
IAEA-S1	-0.282	0.018	0.078	0.02	-0.882	0.229
IAEA-S1	-0.28	0.006	0.064	0.03	-0.655	0.134
IAEA-S1	-0.291	0.016	0.082	0.033	-0.656	0.145

3.10.D. Partition coefficients

Supplementary Table 3.10.D: Partition Coefficients

$D^{\text{melt-silicate}}$	W	Th	Nb	Ta	La
Ol [1 & 2 (Ta)]	8.82353E-05	0.00005	0.0005	0.003	0.0005
Opx [1 & 2 (Ta)]	0.0008	0.002	0.004	0.017818	0.004
Cpx [1 & 2 (Ta)]	0.000122917	0.0059	0.015	0.04375	0.03

$D^{\text{melt-silicate}}$	Ce	Nd	Zr	Hf	Sm
Ol [1 & 2 (Zr, Hf)]	0.0005	0.00042	0.0011	0.0011	0.0011
Opx [1 & 2 (Zr, Hf)]	0.004	0.012	0.024	0.0044	0.02
Cpx [1 & 2 (Zr, Hf)]	0.08	0.088	0.284	0.284	0.299

$D^{\text{melt-silicate}}$	Eu	Gd	Dy	Y	Er
Ol [1 & 2 (Eu, Y)]	0.0005	0.0011	0.0027	0.0082	0.013
Opx [1 & 2 (Eu, Y)]	0.009	0.0065	0.065	0.015	0.065
Cpx [1 & 2 (Eu, Y)]	0.55	0.35	0.4	0.74	0.42

$D^{\text{melt-silicate}}$	Yb	Lu
Ol	0.02	0.02
Opx	0.08	0.12
Cpx	0.45	0.511

[1] Salters and Stracke (2004)

[2] Stracke and Bourdon (2009)

Other D values calculated per van de Löcht et al. (2020)

Chapter 4

Evidence for Eoarchean crustal recycling from In-situ sulfur and lead isotope analyses of peridotite enclaves (southern West Greenland)

This chapter is in preparation for submission to a peer-reviewed journal.

by

Lewis, J.A.[1], Schwarzenbach, E.M.[1,2], Liesegang, M. [1], van de Löcht, J. [1], Schwarz, A. [1], Strauss, H.[3], Münker, C.[4], Rosing, M.T.[5], Whitehouse, M. J. [6], Jeon, H. [6], Hoffmann, J.E.[1]

[1]Institut für Geologische Wissenschaften, Freie Universität Berlin, Malteserstr. 74-100, 12249 Berlin, Germany

[2]Department of Geosciences, University of Fribourg, Chemin du Musée 6, 1700 Fribourg, Switzerland

[3]Institut für Geologie und Paläontologie, Westfälische Wilhelms-Universität Münster, Corrensstr. 24, 48149 Münster, Germany

[4]Institut für Geologie und Mineralogie, Universität zu Köln, Zülpicher Str. 49b, 50674 Köln, Germany

[5]GLOBE Institute, University of Copenhagen, Øster Voldgade 5, DK-1350 Copenhagen, Denmark

[6]Naturhistorika riksmuseet, P.O. Box 50007, SE-104 05 Stockholm, Sweden

4.1. Abstract

The timing of the onset of crustal recycling on Earth remains controversial. Competing models of Eoarchean geodynamics have been presented in recent years. Some include a mechanism for recycling crustal material into Earth's mantle, others do not. Peridotite enclaves located within the Eoarchean Itsaq Gneiss Complex (IGC), south of the Isua Supracrustal Belt in southern West Greenland (SOISB), have been found to contain well-preserved dunites and harzburgites with bulk sulfur isotope compositions indicating incorporation of surface-derived, mass-independently fractionated sulfur (MIF-S). According to recent interpretations, MIF-S identified via bulk analyses of these rocks represents evidence for crustal recycling in the Eoarchean. However, the Eoarchean origin of sulfur within these peridotites remains unconfirmed. Here, we present new in-situ multiple sulfur and lead isotope analyses of sulfides found in these peridotites, along with mineralogical and petrographic observations of the SOISB peridotites. Petrographic and mineralogical evidence point to an early origin to the sulfides prior to ca. 2.6-2.7 Ga metamorphism, and the sulfide minerals observed are consistent with previous interpretations that the SOISB peridotites have their origin and were overprinted by surface-derived sulfur in the Earth's mantle. Average in-situ sulfur isotope compositions of sulfides in the peridotites are in good agreement with previous bulk measurements of sulfur isotope compositions of these rocks, confirming the presence of surface-derived, mass independently fractionated sulfur. Lead isotope results overlap with those of highly unradiogenic galena of Eoarchean origin, though they also record later metamorphic re-equilibration. These results support previous interpretations that the SOISB peridotites preserve an isotopic record of crustal recycling in the Eoarchean.

4.2. Introduction

The mechanisms that formed the Earth's first cratons are controversial. Geodynamic processes active in the Eoarchean have been described by various models. Some of these include processes of crustal recycling and horizontal tectonics similar to modern subduction (e.g., Hastie et al., 2023; Jenner et al., 2009; Nutman, 2023; Nutman et al., 1996). Other models exclude significant horizontal movement of plates or other modern-like tectonic processes, favoring e.g., heat pipe driven vertical stacking of igneous lithologies followed by reworking of these lithologies within the crust to form evolved rocks such as TTGs (e.g., Johnson et al., 2017; Rollinson, 2021; Webb et al., 2020). These models have been informed by the geology of Eoarchean cratons that remain preserved in the rock record, notably including southern West Greenland's IGC (e.g., Jenner et al., 2009; Lewis et al., 2023; Lewis et al., 2021; Nutman et al., 1996).

Peridotite enclaves found in an area south of the ISB (SOISB) in the IGC have unique potential to resolve debates about the origins of Earth's earliest cratons. Several lines of evidence suggest that these rocks have been subject to modification by processes similar to those in a mantle wedge. On an outcrop scale, these rocks display dunite veining in harzburgite similar to that caused by melt percolation in modern ophiolites (Lewis et al., 2023; van de Löcht et al., 2020). The bulk composition of these peridotites is consistent with an origin in Earth's mantle (Friend et al., 2002; van de Löcht et al., 2018), and the low sodium and potassium concentrations in these rocks strongly suggest that their bulk chemistry was not significantly modified by hydrous alteration (Friend et al., 2002). The overall low rare earth element (REE) abundances in these rocks provide further evidence that they have not been subject to significant serpentinization and subsequent dehydration (Friend et al., 2002). The chondritic $^{187}Os/^{188}Os$ isotopic compositions of these rocks further point to a source in the Earth's mantle (Bennett et al., 2002). REE patterns in these rocks hint that they have been subject to melt depletion and refertilization (Friend et al., 2002), and this interpretation is borne out by platinum group element abundances and Re-Os isotope compositions (van de Löcht et al., 2018). Platinum group element (PGE) and Re abundances in these peridotites reveal that they fall into two distinct groups identified by van de Löcht et al. (2018b). Group 1 peridotites include dunites and harzburgites that have distinctly lower primitive mantle normalized PPGE (Pt and Pd) and Re concentrations than primitive mantle normalized IPGE (Os, Ir, and Ru) concentrations, indicating depletion in melt-mobile elements (van de Löcht et al., 2018). Group 2 peridotites are harzburgites with higher PPGE concentrations than Group 1 peridotites, suggesting they experienced a relatively high degree of re-enrichment with melt mobile elements subsequent to their depletion (van de Löcht et al., 2018). The Eoarchean Re depletion ages of the Group 1 peridotites suggest that the initial depletion took place early in the rocks' histories, though younger Re depletion ages of the Group 2 peridotites appear to reflect subsequent metamorphic resetting (van de Löcht et al., 2018). This interpretation is further corroborated by microstructural differences between the two groups of peridotites. Group 1 peridotites are coarse grained, while Group 2 peridotites contain grains of heterogeneous sizes indicative of recrystallization (van de Löcht et al., 2020). A whole rock ^{176}Lu-^{177}Hf regression line of the best preserved SOISB peridotites yields an age of 3908±50 Ma, interpreted to represent the age of a melt refertilization event that affected both groups of peridotites, but Group 2 to a greater extent than Group 1 (van de Löcht et al., 2020).

The Hf isotope compositions of the SOISB peridotites also offer compelling evidence that these rocks have their origins in the Eoarchean depleted mantle. All but two of the 12 Group 1 and 2 SOISB peridotites measured by van de Löcht et al. (2020) have significant, positive εHf(3.81Ga) values up to +7.2 consistent with a mantle depletion event before this time, though notably, the Group 2 SOISB peridotites have generally higher εHf values than the Group 1 SOISB peridotites. The only other rocks from the IGC that have comparably elevated initial εHf values are 3.72 Ga boninite-like metabasalts found in the ISB (Hoffmann et al., 2010; Polat and Hofmann, 2003). These metabasalts have εHf(3.72 Ga) values up to +12.9, pointing to a mantle source that was subject to a high degree of depletion as early as the Hadean (Hoffmann et al., 2010). The Hf isotope evidence suggests that the melt that preferentially overprinted the Group 2 peridotites tapped a mantle domain similar to the one tapped by these boninite-like metabasalts (Hoffmann et al., 2010; Lewis et al., 2023).

A direct mantle origin for SOISB peridotites is not universally accepted, however, and remains controversial. For example, Waterton et al. (2022) performed major, trace element, PGE, and Re-Os isotope analyses on a different suite of peridotites found within the ISB and concluded that these ISB peridotites have a cumulate origin, and not a mantle origin as others have suggested (e.g., Friend and Nutman, 2011). Based on their interpretations of these findings, notably the ISB peridotites' Ni and Cr systematics, low Ti contents, and flat REE patterns, Waterton et al. (2022) argue that all peridotites in the IGC with similarly mantle-like Al/Si and Mg/Si systematics, including the studied SOISB peridotites, have cumulate origins. However, the PGE patterns of the SOISB peridotites (van de Löcht et al., 2018) are not the same as the results of Waterton et al. (2022), suggesting that the ISB and SOISB peridotites formed through different processes, leaving open the possibility of a mantle origin for the latter.

The interpretation that the SOISB peridotites have their origin in the mantle and were subject to variable re-enrichment by a boninite-like melt in a modern subduction-like setting is corroborated by recent work measuring the bulk multiple sulfur isotope compositions of these rocks (Lewis et al., 2023). Multiple sulfur isotopes have the unique potential to trace material recycled from the Earth's surface in the Archean because they can preserve signatures of mass independently fractionated sulfur (MIF-S) that took place as a result of photolytic processes in the Earth's reducing atmosphere at this time (Farquhar et al., 2000). Mass independent differences in the abundance of ^{33}S vs. ^{32}S and ^{34}S are expressed as $\Delta^{33}S$ values, which are generally positive in Archean sediments bearing reduced sulfur species produced by photolytic processes, and negative in Archean hydrothermal deposits that preserve complimentary oxidized species (Farquhar et al., 2000; Farquhar et al., 2002). Small $\Delta^{33}S$ values within 0 ±0.2‰ were until recently not regarded as indicative of MIF-S (e.g., Farquhar and Wing, 2003). However, recent research has shown that small nonzero $\Delta^{33}S$ values in combination with sufficiently low $\delta^{34}S$ values in Archean rocks are unlikely to be the result of mass dependent processes, and are therefore very likely to be a result of MIF-S (LaFlamme et al., 2018b). This insight has led to a growing body of published work finding evidence for MIF-S in igneous lithologies, including cases in which nonzero $\Delta^{33}S$ values are small as a result of mixing with magmatic sulfur with $\Delta^{33}S=0$ (e.g., Cabral et al., 2013; Caruso et al., 2022a; Delavault et al., 2016; Dottin III et al., 2021; Dottin III et al., 2020a; Dottin III et al., 2020b; Farquhar et al., 2002; Kubota et al., 2022; Labidi et al., 2015; Labidi et al., 2022; LaFlamme et al., 2018a; Lewis et al., 2021; Ranta et al., 2022). These results show that MIF-S can survive incorporation into magmatic rocks and carry a record of surface-derived input through the rock cycle, preserving evidence for crustal recycling for billions of years.

All analyzed SOISB peridotites were found to have positive bulk rock $\Delta^{33}S$ values, indicating incorporation of sediment-derived sulfur (Lewis et al., 2023). Group 1 peridotites have the most positive $\Delta^{33}S$ values of up to 0.21 ±0.02‰, while lower $\Delta^{33}S$ values and elevated $\delta^{34}S$ values up to 4.94 ±0.01‰ in the Group 2 peridotites point to hydrothermally derived input delivered by the percolating melt that preferentially influenced these rocks (Lewis et al., 2023). The only igneous rocks in the IGC ever found to contain sulfur dominated by seawater-sulfate derived, negative $\Delta^{33}S$ values are the boninite-like metabasalts, with $\Delta^{33}S$ values as low as -0.171 (Siedenberg et al., 2016). Notably, lower $\Delta^{33}S$ values were found to correlate with higher εHf(3.81Ga) values in the SOISB peridotites along with other melt mobile elements, strongly suggesting that the percolating melt derived from the depleted mantle also carried hydrothermally-derived sulfur from the Earth's surface, and that this percolating melt was distinct from and was introduced after the metasomatizing agent that first introduced the sediment-derived sulfur (Lewis et al., 2023). Furthermore, a model of the trace element composition of the depleted mantle subject to refertilization with a melt with the composition of a representative ISB boninitic metabasalt produces results comparable to the compositions of the Groups 1 and 2 peridotites, depending on the degree of refertilization (Lewis et al., 2023). The explanation for the history of melting and refertilization of the SOISB peridotites considered most probable by Lewis et al. (2023) is for these rocks to have their origins in the Eoarchean mantle prior to emplacement in the crust. These recent findings supply further evidence for a direct mantle origin for the SOISB peridotites, as a cumulate origin would require the peridotites to have experienced two distinct overprinting events with different mantle sources following emplacement in the crust within a very short time (Lewis et al., 2023). Overprinting one metasomatized mantle domain with melt extracted from another in a setting resembling a modern mantle wedge offers a simpler explanation for the observed trends (Lewis et al., 2023), and remains our preferred model for the origin of the studied rocks.

While robust evidence for the mantle origin and history of depletion and refertilization of the SOISB peridotites has been found by previous studies (Friend et al., 2002; Lewis et al., 2023; van de Löcht et al., 2018; van de Löcht et al., 2020), an Eoarchean origin of the sulfides within these rocks has still yet to be demonstrated directly. In this study, we present new, in-situ S and Pb isotopic measurements and petrographic observations of sulfides in the SOISB peridotites in order to verify and reinforce previous interpretations of processes that formed these rocks. While reactive transport has been found to play a limited role in moving sulfur between lithologies under the relatively dry (as compared to e.g., suprasubduction settings) conditions of metamorphism within the Earth's crust, even in metamorphosed rocks of Eoarchean and even Hadean age (Thomassot et al., 2015), direct dating of sulfides in SOISB peridotites would further confirm the Eoarchean origins of the MIF-S they carry. Furthermore, in-situ measurement of the S isotope compositions of individual sulfides in the SOISB peridotites would provide confirmation of the results reported in (Lewis et al., 2023). Petrographic observations of the sulfides may also help to further elucidate the histories of the SOISB peridotites and determine whether one or multiple sulfide generations are present. Further observations of the silicate petrography of the SOISB peridotites may also reveal insights into the history of these rocks.

4.3. Analytical methods

Selected samples of Group 1 and Group 2 peridotites were prepared as thin and thick sections for subsequent optical microscopy followed by electron microprobe analyses and scanning electron microscopy. Additionally, separated sulfide grains from three samples (010-020C, 010-022, and 010-029B) were mounted in epoxy and polished.

Electron microprobe (EMP) analyses of silicate mineral compositions of polished thin sections were conducted with a JEOL JXA 8200 Superprobe at Freie Universität Berlin at 20 kV accelerating potential and 20 nA current. Sulfides on thick sections were initially identified by reflected light and scanning electron microscopy (SEM), and flagged for Secondary ion mass spectrometry (SIMS) and EMP analysis.

As part of the initial electron microscope analysis, the thick sections were subject to a scanning electron microscope mapping procedure with a Zeiss Sigma 300 VP Field-Emission Scanning Electron Microscope and Zeiss' ATLAS software at Freie Universität Berlin. Backscattered electron (BSE) maps of the thick sections were produced at various magnifications including 47-89x, as well as more detailed, high-resolution images of selected sulfide grains. Additionally, the centroids of especially electron-reflective spots larger than 15 μm (including sulfides, certain oxides such as magnetite, and spinels) were subject to elemental analysis with a dual Bruker Quantax Xflash 60mm^2 silicon drift detector (SDD) energy dispersive spectroscopy (EDS) detectors. These composition data points allowed grains of sulfide minerals such as pentlandite to be identified and distinguished from other electron-bright phases. The resulting maps of electron-bright phases, color coded by composition and interpreted mineralogy, were exported into navigable maps viewable in a web browser, which could be displayed side-by-side with reflected electron maps generated at lower brightness sensitivities, as well as map layers with detailed electron images of sulfide grains appropriately scaled and positioned. These maps were used as navigation aids during SIMS analysis.

A separate set of thin sections of the same peridotite samples were also analyzed, with sulfides identified by light microscopy initially and then subject to EMP analysis.

SIMS analysis was conducted using a CAMECA IMS 1280 instrument at the NordSIMS facility at the Swedish Museum of Natural History, Stockholm. Individual sulfides in thick section samples (cut to 1-inch round blocks) and mounted sulfide separates from selected SOISB peridotites were coated with gold and measured for triple sulfur isotopes (^{32}S, ^{33}S, and ^{34}S) and subsequently for lead isotopes (^{204}Pb, ^{206}Pb, ^{207}Pb, and ^{208}Pb) following the method of Whitehouse et al. (2005). Spots excavated by individual SIMS measurements were approximately 30 μm across (see Figure 1a).

Known Pyrite and pyrrhotite standards including Ruttan pyrite, Balmat pyrite, Isua pyrite, and MV pyrrhotite reported in Whitehouse (2013) for S isotope measurements by SIMS, as well as pyrite standard S302A (Liseroudi et al., 2021) and pyrrhotite standard YP136 (Li et al., 2019), were measured prior to each of three measurement sessions and intermittently between unknown measurements during each session, and linear δ^{34}S (-0.08‰) and δ^{33}S (-0.0412‰) corrections were made to account for instrumental mass fractionation in measured pentlandite against pyrrhotite standards (LaFlamme et al., 2016). Note that this correction has no influence on Δ^{33}S. The average 2σ standard measurement errors were 0.25‰ for δ^{34}S and 0.23‰ for Δ^{33}S. The average 2σ measurement errors for all SOISB peridotite sulfides were 0.23‰ for δ^{34}S and 0.27‰ for Δ^{33}S. S isotope results are reported relative to the standard Vienna-Canyon Diablo Troilite (V-CDT).

A known Pb standard (BCR-2G (Woodhead and Hergt, 2000)) was measured prior to each of two measurement sessions and at least once after every eight sequential unknown measurements. ^{208}Pb counts per second (cps) ranged between 31.39 and 1783.07 for all standards. ^{208}Pb counts per second (cps) ranged between 0.01 and 64053 for all SOISB peridotite samples.

Additional SEM imagining was done in Stockholm prior to gold coating to confirm the sulfide mineralogy of measured sulfide grains, including the separates. The thick section and separated sulfides that were measured by SIMS were subsequently subject to EMP analysis. Microprobe measurements of sulfides were conducted with a JEOL JXA 8200 Superprobe at Freie Universität Berlin at 15-20 kV accelerating potential, 20 nA current, and 1 μm beam diameter. Backscattered electron images were also taken of analyzed sulfides, and selected sulfides in thin section specimens were also subject to high-resolution compositional mapping with the microprobe in order to identify any unusual sulfide phases.

4.4. Results

4.4.1. Sulfide and associated silicate phase mineralogy and petrography

Sulfide mineralogy in each peridotite sample is summarized in Table 4.1 and detailed electron microprobe results are shown in supplementary Table S1. Sulfide grains identified in the Group 1 peridotites range in size from μm-scale to 2000μm along their long axes. They typically range from subangular to subrounded in shape, with occasionally elongate and amoeboid forms, and occur between silicate mineral grains comprising typical peridotite minerals such as olivine and orthopyroxene. Hydrous silicate minerals, including amphibole, serpentine, and chlorite, as well as magnetite, were in some cases observed overgrowing and crosscutting the sulfides (Figure 4.1). Sulfide mineral compositions include phases typical of mantle peridotites, primarily pentlandite in all analyzed peridotite samples, as well as pyrrhotite in two of the four Group 1 peridotite samples analyzed (010-020 and 010-020C). Pyrrhotite was typically observed intergrown with pentlandite in sulfide grains (Figure 4.1).

Table 4.1: sulfide minerals identified in each sample

group	sample	pentlandite	pyrrhotite	heazlewoodite	chalcopyrite	As-rich phase
1	010-020	x	x			
1	010-020C	x	x			
1	010-022	x				
1	010-023	x				
2	010-029B	x	x		x	
2	010-030	x		x		x

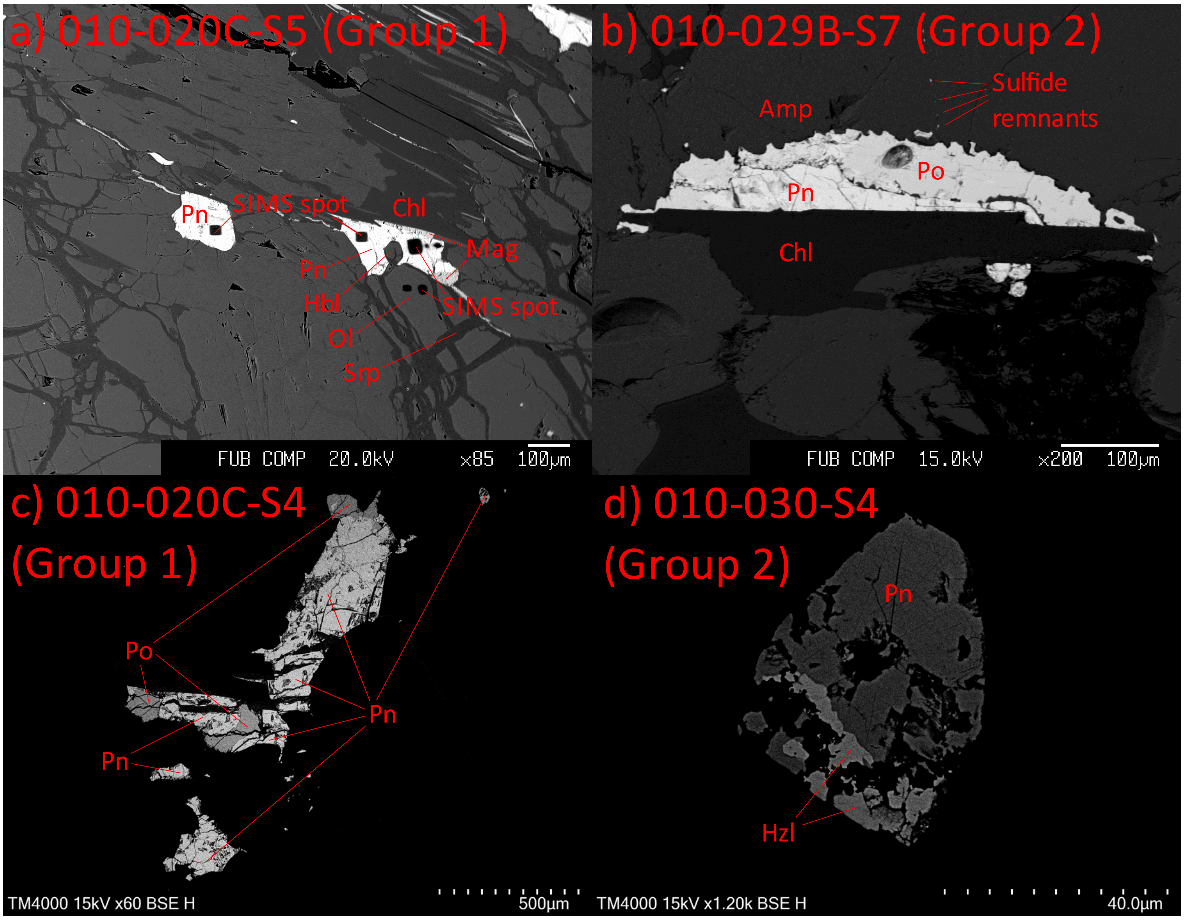

Figure 4.1: Backscattered electron images of representative sulfides from Groups 1 (a) and 2 (b) overgrown by hydrous phases during metamorphism. Note that the hornblende grain crosscutting the larger sulfide in (a) is crosscut by serpentine, indicating the serpentine formed after amphibolite facies metamorphism. Also note that craters excavated by SIMS are visible in (a); (b) shows a grain on a thin section that was not subject to SIMS analysis. Overgrowing and other nonsulfide minerals in (a) and (b) determined by light microscopy, EDS, and/or microprobe analyses. Note also the intergrown pentlandite and pyrrhotite in the (b). Intergrown sulfides are shown more clearly in Group 1 (c) and 2 (d) peridotites. Intergrown pentlandite and pyrrhotite in a Group 1 peridotite sulfide is shown in (c), intergrown pentlandite and heazlewoodite in a Group 2 peridotite is shown in (d). Abbreviations for minerals in this and following figures are after Whitney and Evans (2010) where applicable (Amp = amphibole, Chl = chlorite, Hbl = hornblende, Hzl = heazlewoodite, Srp = serpentine, Mag = magnetite, Pn = pentlandite, Po = pyrrhotite).

Sulfide grains identified in the Group 2 peridotites measure up to 300μm along their long axes with subrounded to subangular shapes. Group 2 peridotite sulfides were found between silicate grains, with very small μm-scale intragranular exceptions representing remnants of intergranular sulfides that were partially overgrown (Figure 4.1). Hydrous phases including amphibole could occasionally be observed overgrowing sulfide minerals (Figure 4.1). Group 2 peridotite sulfide minerals are also predominantly pentlandite, with pyrrhotite also representing a major sulfide phase in one of the two analyzed Group 2 peridotite samples and typically intergrown with pentlandite (Figure 4.1). Minor heazlewoodite was also observed, forming anhedral and irregularly shaped overgrowths in pentlandite grains observed in peridotite sample 010-030 (Figure 4.1). Minor chalcopyrite was observed replacing parts of the margins of three sulfide grains in sample 010-029B (Figure 4.2).

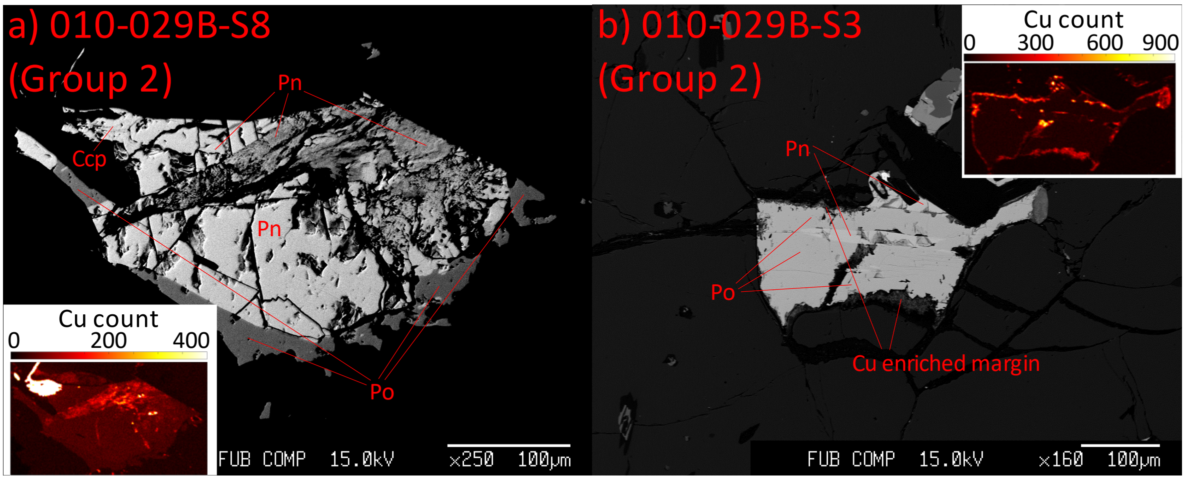

Figure 4.2: a) Backscattered electron image of an intergrown pentlandite and pyrrhotite grain in a Group 2 peridotite, with minor chalcopyrite replacement in one corner. Note the elevated Cu concentration in the upper left corner of the Cu WDS count map of the grain in the inset. B) Intergrown pentlandite and pyrrhotite grain in a Group 2 peridotite with Cu enriched rim. Inset map of Cu WDS as in (a). Ccp = chalcopyrite, Pn = pentlandite, Po = pyrrhotite.

4.4.2. Sulfide mineral chemistry

Major element chemistry of the sulfides analyzed in supplementary Table S1 is plotted in Figure 4.3. Group 1 peridotite pentlandites range in composition from 28.5 to 45.0 wt% Fe and 19.8 to 36.3 wt% Ni. Cu concentrations do not exceed 0.54 wt% in Group 1 peridotite pentlandites and are under 0.01 wt% Cu in the majority of measured grains. Co contents in Group 1 peridotite pentlandite grains range primarily from 0.37 to 2.13 wt.% and locally up to 8.30 wt%. As did not exceed 0.13 wt% in Group 1 peridotite pentlandites and was undetectable in the vast majority of measured grains. Similarly, Zn did not exceed 0.11 wt% in Group 1 peridotite pentlandites and was in most cases below the detection limit.

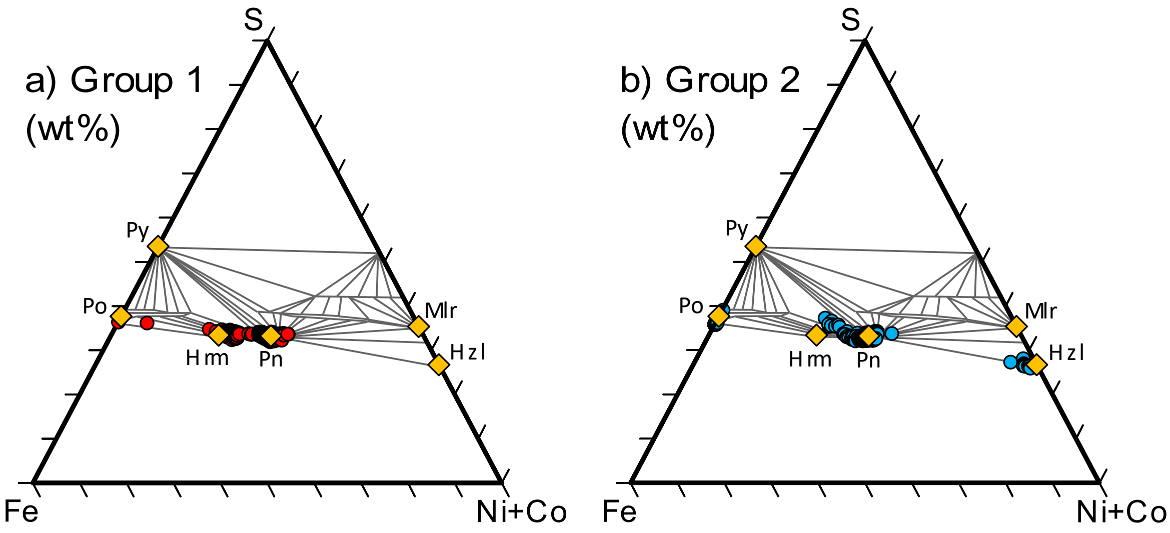

Figure 4.3: Major element compositions of (a) Group 1 and (b) Group 2 peridotite sulfides with reference mineral compositions (Hrm = horomanite, Hzl = heazlewoodite, Mlr = millerite, Pn = pentlandite, Po = pyrrhotite, Py = pyrite) for comparison. Note that chalcopyrite and one pentlandite-like measurement with >1% Cu are omitted. While more Fe-rich pentlandite measurements may represent Fe-rich pentlandite or admixture with pyrrhotite, note that they are also consistent with horomanite, a sulfide phase that is crystolographically distinct from pentlandite and is also found in mantle peridotites (Kitakaze et al., 2011; Ozawa, 2004). Tie lines for phase relations at 200°C from Craig (1973) are shown in the background; note that direct lines between pentlandite and pyrite compositions are disrupted at temperatures as low as 250°C (Craig, 1973).

Group 1 peridotite pyrrhotites range in composition from 62.2 to 63.7 wt% Fe and contain up to 0.4 wt% Ni. Contents of Co were below 0.09 wt%, Cu is ≤ 0.16 wt%, As is ≤ 0.07 wt% and Zn ≤ 0.08 wt%.

Group 2 peridotite pentlandites range in composition from 27.4 to 40.0 wt% Fe and from 15.9 to 38.4 wt% Ni. Cu was undetectable in most measured Group 2 peridotite pentlandite grains, and locally up to 1.16 wt% Cu on grain margins. Co is 0.44 to 1.29 wt%. As was generally below the detection limit and locally up to 0.1 wt%. Zn was detected in a minority of Group 2 peridotite pentlandite grains at concentrations up to 0.13 wt%. A few relatively iron-rich, pentlandite-like sulfide compositions in the Group 2 peridotites are also enriched in S, with the most extreme composition 42.0 wt% S. Plotted on a ternary diagram, these Fe and S-rich pentlandite compositions appear to reflect admixture with a small amount of pyrite (Figure 4.3).

Group 2 peridotite pyrrhotites range in composition from 60.8 to 64.2 wt% Fe and up to 0.43 wt% Ni. Cu concentrations range up to 0.16 wt%, Co contents are ≤ 0.07 wt%, As is ≤ 0.17 wt% and Zn ≤ 0.11 wt%.

Heazlewoodite in the Group 2 peridotites range in composition from 1.75 to 5.19 wt% Fe and 63.4 to 72.3 wt% Ni. Co contents are ≤ 0.09 wt.%, As is ≤ 0.07 wt.%, Zn ≤ 0.09 wt.% and, Cu was in all measurements below detection limit.

Chalcopyrite in the Group 2 peridotites has a close to stoichiometric composition with traces of Ni (0.06 to 0.25 wt.%), and Co (0.05 to 0.07 wt%). As and Zn were not detected in this phase.

Pb concentration measurements were attempted with the microprobe, but measurable Pb was never detected.

Compositional mapping of selected sulfide grains in both groups of peridotites are consistent with quantitative observations, with limited evidence for incorporation of material enriched in Cu around the margins of some Group 2 peridotites (Figure 4.2).

4.4.3. In-Situ S isotope compositions

In-situ multiple sulfur isotope analysis results are plotted in Figure 4.4 and shown in detail in supplementary Table S2. Analysis of sulfides in the Group 1 peridotites yielded $\delta^{34}S$ values ranging from -1.23‰ to 3.68‰. The least squares measurement error weighted $\delta^{34}S$ value was 0.59±0.10‰ (2σ). The $\Delta^{33}S$ values in Group 1 peridotites range from -0.29‰ to 1.00‰. The error weighted average $\Delta^{33}S$ value was 0.20±0.02‰ (2σ). Analysis of sulfides in the Group 2 peridotites yielded $\delta^{34}S$ values ranging from -2.54‰ to 4.77‰. The average error weighted $\delta^{34}S$ value was 3.63±0.23‰ (2σ). The $\Delta^{33}S$ values in Group 2 peridotites range from -0.19‰ to 0.60‰. The average error weighted $\Delta^{33}S$ value was 0.09±0.03‰ (2σ).

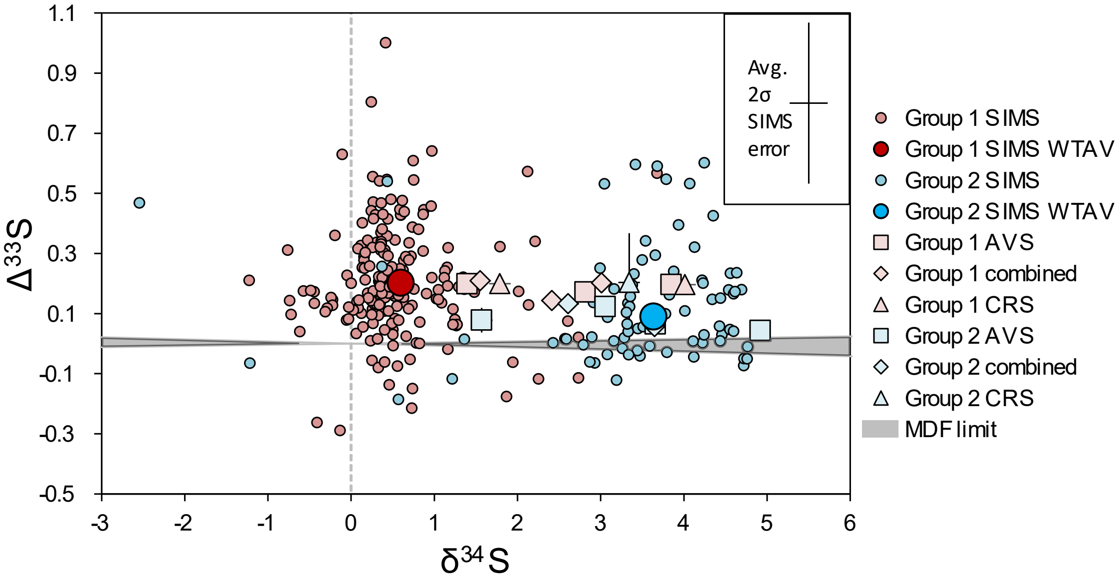

Figure 4.4: In-situ sulfur isotope results. Large circles in bold colors represent the least squares error weighted average (WTAV) results for each group of peridotites. Acid volatile sulfur (AVS), chromium reducible sulfur (CRS), and combined AVS+CRS bulk isotope results for representative samples of both groups of peridotites from Lewis et al. (2023) are also shown. Additionally, the range of values typically attributable to mass dependent fractionation (MDF) processes, from LaFlamme et al. (2018b), is shown in gray.

4.4.4. In-Situ Pb isotope compositions

^{207}Pb/^{206}Pb ratios measured in Group 1 peridotites range from 0.839 to 1.128 and in Group 2 peridotites from 1.05 to 1.15. ^{208}Pb/^{206}Pb ratios measured in Group 1 peridotites range from 2.21 to 2.66 and in Group 2 peridotites from 2.46 to 2.69. ^{206}Pb/^{204}Pb ratios measured in Group 1 peridotites range from 11.91 to 15.19 and in Group 2 peridotites from 11.85 to 15.94. ^{207}Pb/^{204}Pb ratios measured in Group 1 peridotites range from 13.08 to 14.97 and in Group 2 peridotites from 13.27 to 16.43. ^{208}Pb/^{204}Pb ratios measured in Group 1 peridotites range from 29.82 to 34.67 and in Group 2 peridotites from 31.43 to 40.19. Pb isotope results are shown in terms of ^{206}Pb/^{204}Pb vs. ^{207}Pb/^{204}Pb, ^{207}Pb/^{206}Pb vs. ^{208}Pb/^{206}Pb, and ^{206}Pb/^{204}Pb vs. ^{208}Pb/^{204}Pb in Figure 4.5 and are shown in detail in supplementary Table S3. Only results with ^{206}Pb detected at or above 50 cps (or 10 cps in the case of relatively robust ^{207}Pb/^{206}Pb and ^{208}Pb/^{206}Pb ratios) are displayed in Figure 4.5. Pb isotope results from the two groups of peridotites largely overlap.

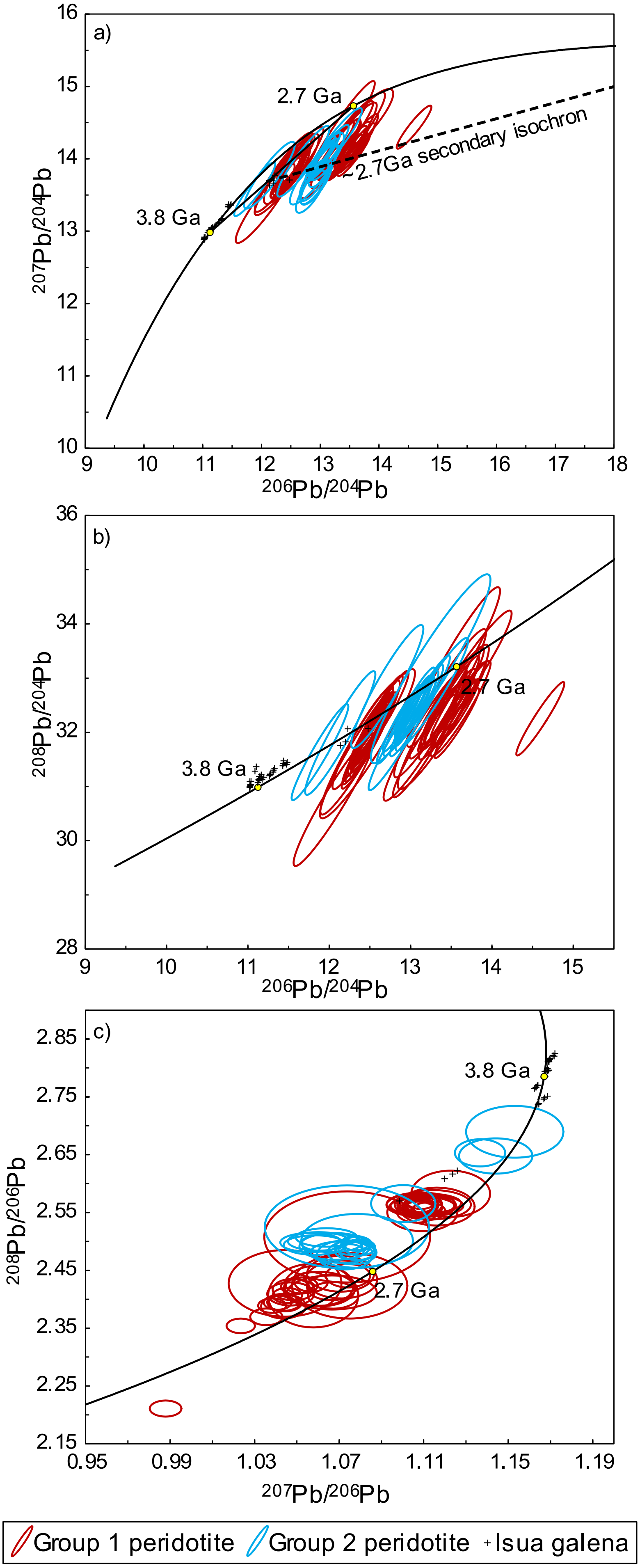
a)
2.7 Ga
3.8 Ga
~2.7Ga secondary isochron
$^{207}Pb/^{204}Pb$
$^{206}Pb/^{204}Pb$
16
15
14
13
12
11
10
9
10
11
12
13
14
15
16
17
18
b)
2.7 Ga
3.8 Ga
$^{208}Pb/^{204}Pb$
$^{206}Pb/^{204}Pb$
36
34
32
30
28
9
10
11
12
13
14
15
c)
3.8 Ga
2.7 Ga
$^{208}Pb/^{206}Pb$
$^{207}Pb/^{206}Pb$
2.85
2.75
2.65
2.55
2.45
2.35
2.25
2.15
0.95
0.99
1.03
1.07
1.11
1.15
1.19
Group 1 peridotite
Group 2 peridotite
+ Isua galena

Figure 4.5: Pb isotope results, shown in terms of a) ^{206}Pb/^{204}Pb vs. ^{207}Pb/^{204}Pb, b) ^{206}Pb/^{204}Pb vs. ^{208}Pb/^{204}Pb, and c) ^{207}Pb/^{206}Pb vs. ^{208}Pb/^{206}Pb (bottom). Error ellipses representing individual sulfide measurements are 2σ. Our data overlap with previously studied unradiogenic galenas from the ISB (Appel et al., 1978; Frei and Rosing, 2001; Kamber et al., 2003; Richards and Appel, 1987). An Earth Pb isotope evolution curve based on Maltese and Mezger (2020) is also plotted for comparison, along with points representing 2.7 and 3.8 Ga ages. In (a), a mixing line between the two is also plotted, along with a dotted line representing a potential secondary isochron associated with partial re-equilibration associated with metamorphism at ca. 2.7 Ga.

4.5. Discussion

4.5.1. Sulfide mineralogy and petrography consistent with Eoarchean mantle origin

The textures and mineralogy of the sulfides are consistent with previous interpretations that the peridotites that host them have an Eoarchean mantle origin, and have been subject only to minor subsequent alteration (Lewis et al., 2023; van de Löcht et al., 2018b; van de Löcht et al., 2020), though they cannot by themselves rule out a cumulate origin. The dominant phases of pentlandite and pyrrhotite are typical of mantle peridotite sulfides, which form through re-equilibration below 300°C of monosulfide solid solution and melt phases that are stable under thermal conditions typical of the mantle (e.g., Kiseeva et al., 2017; Lorand, 1989). Some measured pentlandite-like compositions are relatively high in Fe and may represent horomanite (Figure 4.4), a sulfide mineral first identified in the Horoman Peridotite Complex in Japan (Kitakaze et al., 2011), an obducted mantle section (Ozawa, 2004). However, the crystallography of individual sulfide grains could not be determined with the methods employed in this study. Hence, these measured compositions may also reflect Fe-rich pentlandite or mixtures of pentlandite and pyrrhotite. Future studies may show whether or not horomanite is present in the SOISB peridotites.

Heazlewoodite, an accessory phase found in one Group 2 peridotite sample (010-030; Figure 4.2), is also found in mantle peridotites (Kitakaze, 1998). It may represent late hydrous alteration, as the occurrence of heazlewoodite is typically associated with serpentinization processes in peridotites (e.g., Klein and Bach, 2009). Additionally, chalcopyrite was observed as a minor accessory phase, typically along the margins of grains (e.g., Figure 4.3a) and interpreted to represent replacement of the dominant sulfide phases, possibly in association with the melt percolation that preferentially affected the Group 2 peridotites (Lewis et al., 2023; van de Löcht et al., 2018b; van de Löcht et al., 2020), or during later alteration processes. This is also consistent with the enrichment in copper (e.g., Lorand et al., 1993) observed around the margin of one sulfide grain in sample 010-029B (Figure 4.3b). While pyrite was never directly observed, a few group 2 peridotite compositions appear to represent admixture between pentlandite and pyrite (Figure 4.4). This may also be a result of a late alteration process, as the measurements forming the trend away from pentlandite compositions towards pyrite compositions in the ternary sulfide diagram (Figure 4.4) appear to follow a tie line between pentlandite and pyrite compositions at 200°C (Craig, 1973). It is important to emphasize that phases potentially attributable to late alteration are minor accessories and do not represent the majority of the sulfides, and that points selected for measurement by SIMS were identified as either pentlandite or pyrrhotite. It is also worth noting that while the sulfide minerals observed are consistent with an origin in the mantle, these minerals are not exclusively found in mantle peridotites (e.g., Augustin et al., 2022), and cannot by themselves rule out the possibility that the SOISB peridotites have a cumulate origin, as suggested by Waterton et al. (2022).

Amphibole (hornblende) that overgrows sulfide grains (Figure 4.1) demonstrates that the sulfides predate upper amphibolite- to granulite-facies metamorphism, which took place locally at ca. 2.6-2.7 Ga (e.g., Eskesen et al., 2023; Nutman and Bennett, 2019). Metamorphism appears unlikely to have significantly mobilized sulfur, as relatively dry metamorphic conditions within the Earth's crust tend not to mobilize sulfur, and pre-metamorphic sulfur isotope compositions within metamorphic lithologies that have been subject to such conditions are generally retained (e.g., Corriveau and Spry, 2014 and citations therein). It has been demonstrated that in the Nuvvuagittuq Greenstone Belt, which has a comparable age and metamorphic history to the IGC, sulfur and its associated isotopic signatures was not subject to metamorphism-related reactive transport between lithologies over more than a few meters (Thomassot et al., 2015). The studied SOISB peridotites are found in enclaves much further away from any source of sedimentary rock that could have introduced nonzero $\Delta^{33}S$ during metamorphism (Lewis et al., 2023). Additionally, the chondritic initial $^{187}Os/^{188}Os$ isotope compositions of the Group 1 peridotites, which have the highest $\Delta^{33}S$ values, preclude contamination from felsic lithologies such as the surrounding TTGs (Bennett et al., 2002; van de Löcht et al., 2018b). Furthermore, the observed relationships between melt-mobile, fluid-immobile elements and $\Delta^{33}S$ values of the peridotites measured in a previous bulk study by Lewis et al. (2023) would be difficult to explain if fluid-related introduction of sulfur to these rocks occurred after, and not before, melt metasomatic processes that must have occurred early in the peridotites' history, in the Eoarchean (Lewis et al., 2023). Because the most positive $\Delta^{33}S$ values measured in this previous study are found in SOISB peridotites with the least evidence for melt overprint (Lewis et al., 2023), it is very likely that a metasomatizing fluid, not a melt, introduced sulfur with positive Δ^{33}S into these rocks in the Eoarchean.

4.5.2. In-situ sulfur isotope measurements confirm previous bulk analyses

The weighted average results of both groups of peridotites fall outside the range in δ^{34}S-Δ^{33}S space generally attributable to mass-dependent processes (LaFlamme et al., 2018b) and, significantly, are consistent with previously published bulk results on the Δ^{33}S axis (Figure 4.4). The relative enrichment of the Group 2 peridotites in ^{34}S as compared to the Group 1 peridotites is also consistent with previously published results. These findings confirm the validity of previous results and also demonstrate that the bulk sulfur is hosted in the sulfides.

However, in both groups of peridotites, average SIMS results are lower in δ^{34}S than bulk results (Lewis et al., 2023) by ca. 1-3‰. A comparison of SIMS and bulk results for 010-020C, a Group 1 peridotite and the rock for which the largest SIMS S isotope dataset was collected, is shown in Figure 4.6. The observed δ^{34}S offsets between bulk and in-situ results may be a result of measurement bias towards the centers of larger grains that have not been influenced by low degrees of alteration that these rocks have experienced subsequent to peak metamorphism (e.g., van de Löcht et al., 2020). The presence of sulfide minerals other than pentlandite such as horomanite is another potential reason for apparent mass-dependent offset in SIMS results, as matrix effects can problematize S isotope measurements by SIMS in the absence of a matrix-matched standard (e.g., LaFlamme et al., 2016). However, because any potential instrumental mass fractionation as a result of imperfect standardization is mass-dependent, it should be noted that it is not expected to influence Δ^{33}S results. The significant difference of ca. 3‰ in δ^{34}S between the weighted average in-situ results of the two peridotite groups is larger than that between the bulk results of the two groups, which is approximately 0.7‰ (Lewis et al., 2023, Figure 4.4). This reinforces the interpretation that the melt preferentially overprinting the Group 2 peridotites had a substantially positive δ^{34}S value in addition to a near-zero or negative Δ^{33}S value, consistent with Archean seawater sulfate that tends to be deposited in hydrothermally-derived material (Farquhar et al., 2002; Lewis et al., 2023). As noted in Lewis et al. (2023), hydrothermal deposits with sulfur isotope compositions consistent with an endmember along the vector defined in δ^{34}S-Δ^{33}S space (that is, positive δ^{34}S and low to negative Δ^{33}S) by the two groups of peridotites have not been found in the IGC or other Eoarchean terranes. Such deposits have been found in terranes as old as Paleoarchean in age, such as the Londozi barites from the Barberton Greenstone Belt (Roerdink et al., 2012). Additionally, while they are not in well preserved primary context (they occur in a biotite gneiss), a few in-situ measurements with positive $\delta^{34}S$ and negative $\Delta^{33}S$ have been made of Eoarchean ISB lithologies (Hu et al., 2003), consistent with a seawater sulfate origin (Siedenberg et al., 2016).

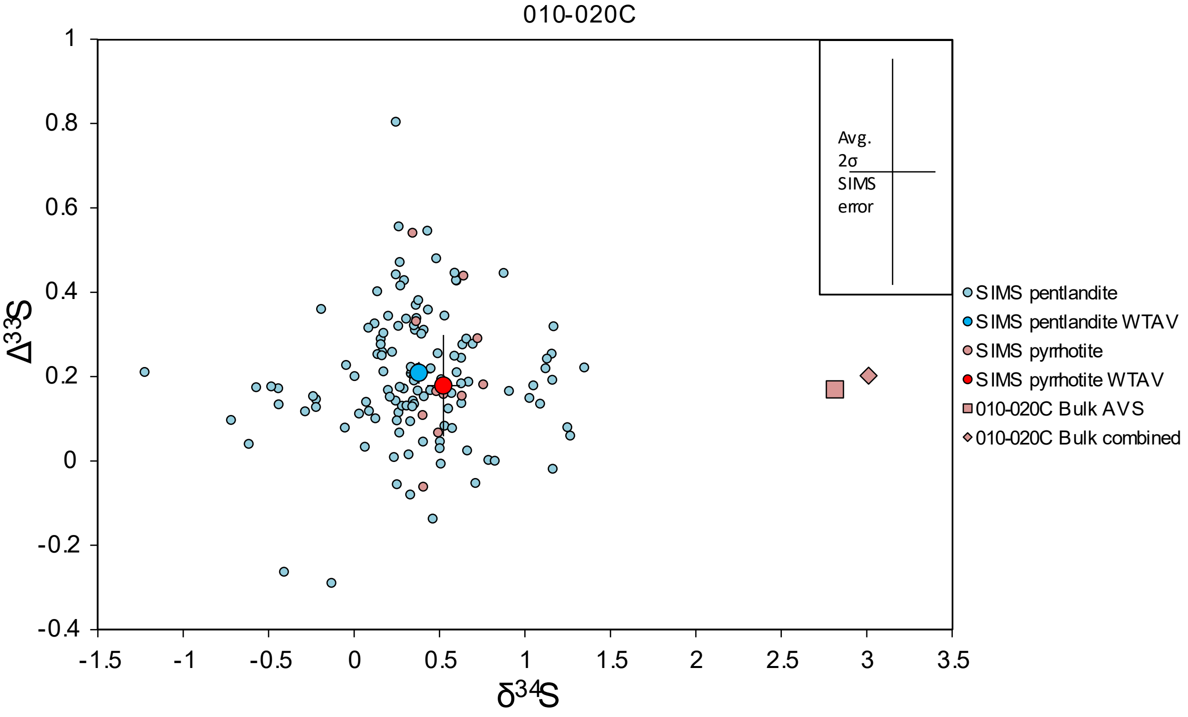

Figure 4.6: Group 1 peridotite sample 010-020C SIMS pentlandite and pyrrhotite results compared. Note the δ34S offset between the bulk and SIMS results, as well as the smaller δ34S offset between average pentlandite and pyrrhotite in-situ measurements of ca. 0.2‰. Note that the 95% error weighted average (WTAV) error bars between the pentlandite and pyrrhotite results slightly overlap on the δ34S axis (and completely overlap on the Δ33S axis). Though it does not rise to 95% significance, the slight offset observed between phases on the δ34S axis may be attributed to equilibrium fractionation.

Pyrrhotite results, where available, were slightly higher in $\delta^{34}S$ than pentlandite results in the same rock sample by ca. 0.2‰ (though note that this offset is not significant at the 95% confidence level), with no significant offset in $\Delta^{33}S$ (see Figure 4.6). The small offset between the pentlandite and pyrrhotite results is consistent with the range of equilibrium fractionation between pentlandite and pyrrhotite of 0.2-1.5‰ estimated by LaFlamme et al. (2016). No systematic relationships were observed between chemical compositions measured by microprobe and in-situ sulfur isotope compositions where comparison was possible. Generally, in-situ S isotope results for each sample (e.g. Figure 4.6) and each peridotite group

(Figure 4.4) formed clouds and did not appear to reflect distinct populations representing potentially different sulfide generations.

4.5.3. Lead isotopes preserve a highly unradiogenic, partially metamorphic-reequilibrated Eoarchean signature

The lead isotope results (Figure 4.5) appear to reflect a mixture of Eoarchean lead, with likely origins in the two Eoarchean metasomatic events that introduced surface derived sulfur to the SOISB peridotites (Lewis et al., 2023), as well as lead introduced by metamorphic resetting, represented in Figure 4.5 at 2.7 Ga (in agreement with e.g., Eskesen et al., 2023; Nutman and Bennett, 2019), and common lead introduced as this time following a secondary isochron. There is no clear difference between the Group 1 and Group 2 peridotite lead isotope compositions, and any observable average difference may be an artifact due to the small number of rock samples analyzed and consequent low statistical repres4entation. The fact that there does not appear to be significant variation between measurements along the $^{208}Pb/^{204}Pb$ axis suggests that the metamorphism the SOISB peridotites experienced at ca. 2.7 Ga did not mobilize thorium (Figure 4.5). Furthermore, the close overlap between the Group 1 and Group 2 peridotite lead isotope compositions underscores the fact that both groups of peridotites originally contained highly unradiogenic lead, and that metamorphic disturbance of lead in these rocks is unrelated to the process that differentiated the Group 1 peridotites from the Group 2 peridotites.

As there are unfortunately no bulk lead isotope data available for the studied peridotites, it is not possible to further evaluate whether the lead introduced to the sulfides during metamorphism came from the host rock or elsewhere. However, because of the highly depleted nature of the peridotites, it appears likely that the TTGs surrounding the peridotite enclaves are the most likely lead source during metamorphism. This is not necessarily the case for other constituents of the studied sulfides, however, as indicated by correlations between multiple sulfur isotope signatures in the SOISB peridotites and melt-mobile, fluid immobile elements associated with an Eoarchean melt overprinting event (Hoffmann et al., 2014; Lewis et al., 2023). Notably, the fact that this overprinting melt signature is associated with a high εHf(t) value inconsistent with the surrounding TTGs (Hoffmann et al., 2014; Lewis et al., 2023) indicates that the surrounding TTGs cannot also be a significant source of sulfur input associated with this event, and that the sulfur in the SOISB peridotites is strongly dominated by metasomatic events that predate amphibolite facies metamorphism at ca. 2.7 Ga. The fact that the lead isotope compositions overlap with some of the least radiogenic lead ever measured in galenas from the ISB (Appel et al., 1978; Frei and Rosing, 2001; Kamber et al., 2003; Richards and Appel, 1987; Figure 4.5) suggests that the lead found in these galenas and the lead found in the SOISB peridotites may share a common source. While lead represents only a trace component of the studied sulfides (Pb concentration measurements were attempted but Pb was always below detection), sulfur is a major component, and therefore a very small amount of fluid interacting with these highly depleted rocks during metamorphism may well be expected to partially reset their lead, but not sulfur, isotopic compositions.

4.6. Conclusions

New in-situ chemical and isotopic analyses of sulfides in the SOISB peridotites reinforce conclusions drawn by previous work (Lewis et al., 2023) that these rocks have incorporated surface-derived sulfur in the Eoarchean. Our results are also consistent with interpretations that the studied SOISB peridotites are depleted and refertilized mantle rocks (Bennett et al., 2002; Friend et al., 2002; van de Löcht et al., 2018b; van de Löcht et al., 2020), specifically from mantle domains modified by metasomatism in which material recycled from Earth's surface was introduced to the peridotites (Lewis et al., 2023). This is the most parsimonious explanation for the chemical and isotopic evidence of multiple overprinting events carrying surface derived sulfur from distinct surface-derived sources to the peridotites in the Eoarchean, with one of these overprints sourced in a distinct, highly depleted mantle domain (Lewis et al., 2023; van de Löcht et al., 2018b; van de Löcht et al., 2020). However, the evidence presented here cannot entirely rule out the possibility that the studied SOISB peridotites are crustal cumulates (Waterton et al., 2022) and that the various overprinting events took place after emplacement.

The mineralogy found in the sulfides, as well as textural evidence in the form of crosscutting silicate grains, strongly suggests that the sulfides predate the peak metamorphic event their host rocks experienced in the Neoarchean. In-situ multiple sulfur isotope analyses of the sulfides by SIMS confirm the positive $\Delta^{33}S$ values concurrent with low $\delta^{34}S$ values best explained by the incorporation of MIF-S dominated by sediment-derived sulfur. The lower $\Delta^{33}S$ and higher $\delta^{34}S$ values measured in Group 2 peridotites as compared to Group 1 peridotites reinforces interpretations that the melt that variably overprinted the peridotites in the Eoarchean delivered a distinct source of surface-derived sulfur with an isotopic composition consistent with that of seawater sulfate similar to what is found in Paleoarchean hydrothermal deposits, pointing to the possibility that such deposits may also be found in

Eoarchean terranes. Furthermore, in-situ Pb isotope analyses demonstrate the Eoarchean origin of the sulfides and their constituent sulfur. These results are best explained by the SOISB peridotites' incorporation of sedimentary and hydrothermally-derived sulfur in the Earth's mantle in the Eoarchean, supporting the case for an onset to crustal recycling processes no later than this time.

4.7. Acknowledgements

The authors express gratitude to the German Science Foundation (DFG) for funding project HO4794/3-1 and SCHW1889/2-1 within the SPP1833 'Building a Habitable Earth' priority program, and DFG grant Mu 1406/8-2. We also thank the Danish National Research Fund for funding NordCEE. We thank Johannes C. Vrijmoed for his help with electron microscopy and mapping the locations of sulfides on the thick sections. We thank Konstantin Huber for his help generating a script to visualize the microprobe element mapping results. We would also like to thank Daniel Dunkley for a valuable discussion about the tectonic context of SIOISB rocks.

4.8. Supplementary material for the fourth chapter

4.8.A. Sulfide mineral chemistry

Supplementary table 4.8.A: sulfide mineral chemistry

Ni wt%	S wt%	As wt%	Fe wt%	Cu wt%	Pb wt%	Co wt%	Zn wt%	Total wt%	measuement number	sample	group	kv	mineral
25.48	34.31	bdl	39.78	bdl	bdl	0.75	bdl	100.32	10_20_S1_P2	010-020	1	15	pentlandite
25.74	33.67	0.06	39.91	0.09	bdl	0.98	bdl	100.44	10_20_S1_P2	010-020	1	15	pentlandite
25.81	33.66	bdl	40.25	bdl	bdl	0.76	0.05	100.52	10_20_S1_P3	010-020	1	15	pentlandite
23.63	34.61	bdl	41.85	bdl	bdl	0.85	bdl	100.95	10_20_S11_P10	010-020	1	15	pentlandite
25.03	33.86	bdl	40.77	bdl	bdl	0.79	bdl	100.44	10_20_S11_P2	010-020	1	15	pentlandite
22.31	34.72	0.13	42.20	0.07	bdl	0.82	bdl	100.24	10_20_S11_P3	010-020	1	15	pentlandite
24.76	34.02	bdl	41.14	0.16	bdl	0.67	bdl	100.75	10_20_S11_P6	010-020	1	15	pentlandite
25.09	34.29	bdl	40.50	0.04	bdl	0.92	0.06	100.91	10_20_S11_P8	010-020	1	15	pentlandite
25.87	33.71	bdl	38.65	0.06	bdl	0.88	0.06	99.24	10_20_S12_P1	010-020	1	15	pentlandite
25.57	33.78	bdl	39.45	0.55	bdl	0.94	bdl	100.30	10_20_S12_P2	010-020	1	15	pentlandite
24.31	33.50	bdl	40.53	0.33	bdl	0.81	bdl	99.47	10_20_S12_P4	010-020	1	15	pentlandite
bdl	36.89	bdl	62.69	0.03	bdl	bdl	bdl	99.61	10_20_S13_P1	010-020	1	15	pyrrhotite
25.24	33.63	bdl	39.25	0.38	bdl	0.91	0.06	99.46	10_20_S13_P2	010-020	1	15	pentlandite
23.08	34.54	bdl	42.14	0.08	bdl	0.79	0.12	100.73	10_20_S14_P2	010-020	1	15	pentlandite
25.40	34.00	0.05	40.27	0.04	bdl	1.05	0.07	100.89	10_20_S14_P5	010-020	1	15	pentlandite
24.60	34.56	0.06	41.01	0.06	bdl	0.61	bdl	100.90	10_20_S15_P1	010-020	1	15	pentlandite
bdl	37.19	bdl	61.94	0.07	bdl	bdl	bdl	99.20	10_20_S15_P3	010-020	1	15	pyrrhotite
26.59	33.85	bdl	38.88	bdl	bdl	0.82	bdl	100.14	10_20_S3_P1	010-020	1	15	pentlandite
25.71	34.27	bdl	39.92	bdl	bdl	0.90	0.05	100.85	10_20_S3_P4	010-020	1	15	pentlandite
0.20	36.89	0.07	61.97	0.04	bdl	bdl	bdl	99.16	10_20_S3_P5	010-020	1	15	pyrrhotite
0.03	36.66	bdl	62.20	0.16	bdl	bdl	bdl	99.04	10_20_S3_P6	010-020	1	15	pyrrhotite
26.11	34.18	bdl	39.56	bdl	bdl	0.84	0.08	100.78	10_20_S4_P1	010-020	1	15	pentlandite
24.71	33.79	0.07	40.83	0.06	bdl	0.66	0.10	100.23	10_20_S4_P10	010-020	1	15	pentlandite
24.82	34.12	bdl	40.91	0.05	bdl	0.72	bdl	100.62	10_20_S4_P11	010-020	1	15	pentlandite
24.82	34.02	bdl	40.66	bdl	bdl	0.57	bdl	100.06	10_20_S4_P13	010-020	1	15	pentlandite
25.19	33.89	bdl	40.03	0.04	bdl	0.53	bdl	99.67	10_20_S4_P18	010-020	1	15	pentlandite
0.37	36.85	0.12	62.04	bdl	bdl	bdl	bdl	99.38	10_20_S4_P2	010-020	1	15	pyrrhotite
24.42	34.78	bdl	40.85	bdl	bdl	0.54	bdl	100.58	10_20_S4_P3	010-020	1	15	pentlandite
0.08	37.24	bdl	61.70	0.11	bdl	bdl	bdl	99.13	10_20_S4_P5	010-020	1	15	pyrrhotite

Supplementary table 4.8.A: sulfide mineral chemistry

Ni wt%	S wt%	As wt%	Fe wt%	Cu wt%	Pb wt%	Co wt%	Zn wt%	Total wt%	measuement number	sample	group	kv	mineral
0.06	37.03	bdl	61.94	0.09	bdl	bdl	bdl	99.12	10_20_S4_P8	010-020	1	15	pyrrhotite
25.34	34.03	bdl	40.31	0.04	bdl	0.87	bdl	100.59	10_20_S4_P9	010-020	1	15	pentlandite
0.10	36.82	bdl	62.34	0.08	bdl	bdl	bdl	99.35	10_20_S5_P2	010-020	1	15	pyrrhotite
31.46	34.06	bdl	34.30	bdl	bdl	0.75	0.03	100.61	10_20_S5_P4	010-020	1	15	pentlandite
24.94	33.70	bdl	40.42	0.04	bdl	0.73	bdl	99.82	10_20_S5_P5	010-020	1	15	pentlandite
24.46	34.20	0.08	40.94	0.14	bdl	0.81	0.06	100.70	10_20_S5_P6	010-020	1	15	pentlandite
24.91	33.99	bdl	40.68	bdl	bdl	0.71	0.11	100.40	10_20_S5_P7	010-020	1	15	pentlandite
bdl	37.38	bdl	62.14	0.10	bdl	bdl	bdl	99.62	10_20_S6_P1	010-020	1	15	pyrrhotite
19.66	34.58	bdl	44.76	bdl	bdl	0.49	bdl	99.48	10_20_S6_P10	010-020	1	15	pentlandite
24.87	34.32	0.06	40.27	0.04	bdl	0.77	bdl	100.33	10_20_S6_P11	010-020	1	15	pentlandite
25.26	33.83	bdl	40.11	bdl	bdl	0.58	bdl	99.77	10_20_S6_P12	010-020	1	15	pentlandite
25.62	34.11	bdl	39.68	bdl	bdl	0.79	0.08	100.28	10_20_S6_P13	010-020	1	15	pentlandite
25.16	33.99	bdl	40.30	0.05	bdl	0.62	bdl	100.11	10_20_S6_P3	010-020	1	15	pentlandite
25.60	34.19	bdl	39.80	bdl	bdl	0.76	bdl	100.35	10_20_S6_P4	010-020	1	15	pentlandite
25.50	34.16	bdl	39.71	bdl	bdl	0.86	0.06	100.28	10_20_S6_P7	010-020	1	15	pentlandite
25.33	34.20	bdl	39.60	bdl	bdl	0.81	bdl	99.94	10_20_S6_P8	010-020	1	15	pentlandite
25.77	33.84	bdl	39.98	0.03	bdl	0.91	0.04	100.56	10_20_S7_P1	010-020	1	15	pentlandite
25.29	33.95	bdl	40.26	0.04	bdl	1.03	bdl	100.57	10_20_S7_P4	010-020	1	15	pentlandite
25.58	33.97	bdl	39.84	0.03	bdl	1.05	0.04	100.51	10_20_S7_P5	010-020	1	15	pentlandite
25.55	33.78	bdl	39.95	0.06	bdl	1.06	bdl	100.39	10_20_S7_P6	010-020	1	15	pentlandite
25.96	33.99	bdl	39.73	0.03	bdl	1.16	0.02	100.88	10_20_S7_P7	010-020	1	15	pentlandite
6.27	35.97	bdl	57.06	0.06	bdl	bdl	bdl	99.35	10_20_S7_P8	010-020	1	15	pentlandite
25.66	33.67	bdl	39.07	bdl	bdl	0.83	bdl	99.24	10_20_S8_P1	010-020	1	15	pentlandite
bdl	36.83	0.07	62.17	0.05	bdl	bdl	bdl	99.11	10_20_S9_P1	010-020	1	15	pyrrhotite
25.93	33.56	0.08	39.94	0.05	bdl	0.61	bdl	100.17	10_20_S9_P4	010-020	1	15	pentlandite
24.74	34.13	bdl	40.56	0.12	bdl	0.99	bdl	100.53	10_20_S9_P5	010-020	1	15	pentlandite
22.96	33.89	bdl	41.60	0.30	bdl	0.87	bdl	99.63	10_20_S9_P6	010-020	1	15	pentlandite
bdl	36.88	bdl	62.30	0.05	bdl	bdl	bdl	99.23	10_20_S9_P7	010-020	1	15	pyrrhotite
25.48	34.11	bdl	40.48	0.10	bdl	0.61	0.10	100.87	10_20C_S01_P1	010-020	1	15	pentlandite

Supplementary table 4.8.A: sulfide mineral chemistry

Ni wt%	S wt%	As wt%	Fe wt%	Cu wt%	Pb wt%	Co wt%	Zn wt%	Total wt%	measuement number	sample	group	kv	mineral
31.52	33.85	bdl	34.43	bdl	bdl	0.88	bdl	100.67	10_20C_S02_P1	010-020	1	15	pentlandite
30.99	33.58	bdl	34.89	0.09	bdl	0.73	bdl	100.30	10_20C_S02_P2	010-020	1	15	pentlandite
25.17	33.92	bdl	40.85	0.03	bdl	0.59	bdl	100.56	10_20C_S03_P1	010-020	1	15	pentlandite
25.02	34.01	bdl	41.11	0.08	bdl	0.59	0.03	100.83	10_20C_S03_P2	010-020	1	15	pentlandite
25.63	33.79	bdl	40.49	0.12	bdl	0.69	bdl	100.72	10_20C_S03_P3	010-020	1	15	pentlandite
24.74	33.90	0.05	41.33	0.05	bdl	0.48	0.04	100.59	10_20C_S03_P4	010-020	1	15	pentlandite
24.11	33.88	bdl	41.19	0.15	bdl	0.61	bdl	99.94	10_20C_S03_P5	010-020	1	15	pentlandite
24.85	33.61	bdl	40.52	0.06	bdl	0.74	0.05	99.82	10_20C_S04_P1	010-020	1	15	pentlandite
25.31	33.91	bdl	40.40	0.03	bdl	0.68	bdl	100.33	10_20C_S04_P2	010-020	1	15	pentlandite
25.40	33.98	bdl	40.70	0.10	bdl	0.69	bdl	100.86	10_20C_S04_P3	010-020	1	15	pentlandite
0.07	36.96	bdl	63.21	bdl	bdl	bdl	0.08	100.31	10_20C_S04_P4	010-020	1	15	pyrrhotite
24.47	34.00	bdl	41.04	0.13	bdl	0.54	bdl	100.17	10_20C_S04_P5	010-020	1	15	pentlandite
29.28	33.49	0.12	28.34	bdl	bdl	8.24	0.08	99.55	10_20C_S05_P1	010-020	1	15	pentlandite
28.28	33.60	0.12	36.48	0.03	bdl	1.53	bdl	100.04	10_20C_S06_P1	010-020	1	15	pentlandite
27.89	33.88	bdl	37.22	bdl	bdl	1.39	0.04	100.41	10_20C_S06_P2	010-020	1	15	pentlandite
28.27	33.58	bdl	36.12	0.07	bdl	1.54	bdl	99.57	10_20C_S06_P3	010-020	1	15	pentlandite
0.12	36.52	bdl	63.32	bdl	bdl	bdl	bdl	99.95	10_20C_S07_P1	010-020	1	15	pyrrhotite
25.27	34.03	bdl	41.02	0.07	bdl	0.61	bdl	100.99	10_20C_S07_P2	010-020	1	15	pentlandite
25.63	33.94	bdl	39.93	0.08	bdl	0.59	0.07	100.23	10_20C_S07_P4	010-020	1	15	pentlandite
25.12	33.95	bdl	40.68	0.17	bdl	0.70	0.04	100.64	10_20C_S07_P5	010-020	1	15	pentlandite
25.68	33.98	bdl	40.28	0.07	bdl	0.64	bdl	100.65	10_20C_S07_P6	010-020	1	15	pentlandite
26.46	33.37	bdl	39.53	0.16	bdl	0.49	bdl	100.02	10_20C_S08_P1	010-020	1	15	pentlandite
26.16	33.70	bdl	39.69	0.07	bdl	0.62	bdl	100.24	10_20C_S08_P2	010-020	1	15	pentlandite
26.53	33.83	bdl	39.32	0.06	bdl	0.69	0.11	100.54	10_20C_S08_P3	010-020	1	15	pentlandite
26.58	33.95	bdl	39.49	0.04	bdl	0.67	bdl	100.74	10_20C_S08_P4	010-020	1	15	pentlandite
24.27	33.76	bdl	41.20	0.11	bdl	0.99	bdl	100.33	10_20C_S08_P5	010-020	1	15	pentlandite
24.76	33.80	bdl	40.34	0.04	bdl	1.07	bdl	100.01	10_20C_S08_P6	010-020	1	15	pentlandite
24.98	33.82	bdl	40.81	0.02	bdl	0.72	0.07	100.42	10_20C_S08_P7	010-020	1	15	pentlandite
24.80	33.83	bdl	40.83	0.06	bdl	0.57	0.03	100.12	10_20C_S08_P8	010-020	1	15	pentlandite

Supplementary table 4.8.A: sulfide mineral chemistry

Ni wt%	S wt%	As wt%	Fe wt%	Cu wt%	Pb wt%	Co wt%	Zn wt%	Total wt%	measuement number	sample	group	kv	mineral
24.90	33.56	bdl	41.25	0.07	bdl	0.44	0.06	100.29	10_20C_S09_P1	010-020	1	15	pentlandite
25.09	33.67	bdl	41.24	0.15	bdl	0.54	bdl	100.70	10_20C_S09_P2	010-020	1	15	pentlandite
25.18	33.66	bdl	41.05	0.11	bdl	0.57	0.11	100.68	10_20C_S10_P1	010-020	1	15	pentlandite
25.27	33.69	bdl	40.81	0.03	bdl	0.63	bdl	100.42	10_20C_S10_P2	010-020	1	15	pentlandite
0.21	36.81	bdl	63.09	0.10	bdl	bdl	0.04	100.25	10_20C_S10_P3	010-020	1	15	pyrrhotite
25.10	34.31	bdl	40.66	bdl	bdl	0.77	bdl	100.84	10_20C_S10_P4	010-020	1	15	pentlandite
24.88	33.76	bdl	40.88	0.05	bdl	0.49	bdl	100.07	10_20C_S11_P1	010-020	1	15	pentlandite
25.17	33.60	bdl	41.09	0.05	bdl	0.67	bdl	100.58	10_20C_S11_P2	010-020	1	15	pentlandite
24.95	34.00	0.10	40.86	0.12	bdl	0.65	0.11	100.79	10_20C_S11_P3	010-020	1	15	pentlandite
25.54	33.61	0.07	40.29	0.07	bdl	0.62	bdl	100.20	10_20C_S11_P4	010-020	1	15	pentlandite
0.18	36.58	bdl	63.16	bdl	bdl	bdl	bdl	99.93	10_20C_S11_P5	010-020	1	15	pyrrhotite
24.77	33.93	bdl	41.53	0.04	bdl	0.47	bdl	100.73	10_20C_S12_P3	010-020	1	15	pentlandite
26.03	33.58	bdl	40.18	0.06	bdl	0.59	bdl	100.44	10_20C_S12_P4	010-020	1	15	pentlandite
25.37	33.63	bdl	40.02	0.11	bdl	0.57	0.07	99.78	10_20C_S12_P5	010-020	1	15	pentlandite
25.69	33.43	bdl	40.36	0.06	bdl	0.59	bdl	100.12	10_20C_S12_P6	010-020	1	15	pentlandite
25.83	33.64	0.09	39.91	bdl	bdl	0.70	bdl	100.18	10_20C_S12_P8	010-020	1	15	pentlandite
26.63	33.57	bdl	38.79	0.09	bdl	0.53	bdl	99.62	10_20C_S12_P9	010-020	1	15	pentlandite
21.53	34.23	bdl	43.56	0.10	bdl	0.37	bdl	99.78	10_20C_S13_P2	010-020	1	15	pentlandite
25.63	32.81	0.05	40.56	bdl	bdl	0.70	bdl	99.77	010-020C-thick-2-sul-1	010-020C	1	20	pentlandite
25.50	32.80	bdl	40.75	bdl	bdl	0.67	bdl	99.73	010-020C-thick-2-sul-2	010-020C	1	20	pentlandite
25.41	33.00	bdl	40.87	bdl	bdl	0.68	bdl	99.96	010-020C-thick-2-sul-3	010-020C	1	20	pentlandite
25.56	32.90	bdl	40.59	bdl	bdl	0.70	bdl	99.75	010-020C-thick-2-sul-4	010-020C	1	20	pentlandite
26.00	33.01	bdl	39.86	0.03	bdl	0.94	bdl	99.84	010-020C-thick-3-sul-1	010-020C	1	20	pentlandite
25.89	32.91	bdl	40.14	bdl	bdl	0.89	bdl	99.82	010-020C-thick-3-sul-2	010-020C	1	20	pentlandite
25.78	32.68	bdl	40.37	bdl	bdl	0.86	bdl	99.70	010-020C-thick-3-sul-3	010-020C	1	20	pentlandite
25.86	32.36	bdl	40.10	bdl	bdl	0.92	bdl	99.24	010-020C-thick-3-sul-4	010-020C	1	20	pentlandite
25.72	32.90	bdl	40.47	bdl	bdl	0.93	bdl	100.02	010-020C-thick-3-sul-5	010-020C	1	20	pentlandite
26.12	32.70	bdl	39.82	bdl	bdl	1.04	bdl	99.67	010-020C-thick-3-sul-6	010-020C	1	20	pentlandite
25.80	32.58	bdl	40.41	bdl	bdl	0.91	bdl	99.69	010-020C-thick-3-sul-7	010-020C	1	20	pentlandite

Supplementary table 4.8.A: sulfide mineral chemistry

Ni wt%	S wt%	As wt%	Fe wt%	Cu wt%	Pb wt%	Co wt%	Zn wt%	Total wt%	measuement number	sample	group	kv	mineral
25.79	32.68	bdl	40.28	bdl	bdl	0.91	bdl	99.66	010-020C-thick-3-sul-8	010-020C	1	20	pentlandite
25.39	32.71	bdl	40.82	bdl	bdl	0.86	bdl	99.78	010-020C-thick-4-sul-11	010-020C	1	20	pentlandite
24.76	32.69	bdl	41.40	bdl	bdl	0.74	bdl	99.58	010-020C-thick-4-sul-12	010-020C	1	20	pentlandite
bdl	36.04	bdl	63.04	bdl	bdl	0.09	bdl	99.17	010-020C-thick-4-sul-13	010-020C	1	20	pyrrhotite
0.02	36.16	bdl	62.86	bdl	bdl	0.06	bdl	99.10	010-020C-thick-4-sul-14	010-020C	1	20	pyrrhotite
25.32	32.82	bdl	40.90	bdl	bdl	0.72	bdl	99.76	010-020C-thick-4-sul-15	010-020C	1	20	pentlandite
24.99	32.59	bdl	41.18	bdl	bdl	0.68	bdl	99.43	010-020C-thick-4-sul-16	010-020C	1	20	pentlandite
25.38	32.75	bdl	40.99	bdl	bdl	0.72	bdl	99.82	010-020C-thick-4-sul-17	010-020C	1	20	pentlandite
25.21	32.79	bdl	41.02	bdl	bdl	0.73	bdl	99.74	010-020C-thick-4-sul-18	010-020C	1	20	pentlandite
24.21	32.94	bdl	41.97	bdl	bdl	0.76	bdl	99.88	010-020C-thick-4-sul-3	010-020C	1	20	pentlandite
24.81	32.98	bdl	41.44	bdl	bdl	0.72	bdl	99.94	010-020C-thick-4-sul-4	010-020C	1	20	pentlandite
22.55	33.12	bdl	43.27	0.04	bdl	0.73	bdl	99.71	010-020C-thick-4-sul-5	010-020C	1	20	pentlandite
25.24	32.18	bdl	41.04	bdl	bdl	0.79	bdl	99.25	010-020C-thick-4-sul-6	010-020C	1	20	pentlandite
25.04	32.90	bdl	41.15	bdl	bdl	0.76	bdl	99.84	010-020C-thick-4-sul-7	010-020C	1	20	pentlandite
bdl	36.04	bdl	63.28	bdl	bdl	0.08	bdl	99.41	010-020C-thick-4-sul-8	010-020C	1	20	pyrrhotite
25.13	32.88	bdl	40.50	0.09	bdl	0.75	bdl	99.34	010-020C-thick-5-sul-1	010-020C	1	20	pentlandite
25.71	32.91	bdl	40.25	bdl	bdl	1.05	bdl	99.92	010-020C-thick-5-sul-10	010-020C	1	20	pentlandite
25.26	32.89	0.06	40.46	0.11	bdl	0.67	bdl	99.45	010-020C-thick-5-sul-2	010-020C	1	20	pentlandite
26.11	32.71	0.06	39.89	bdl	bdl	0.80	bdl	99.56	010-020C-thick-5-sul-3	010-020C	1	20	pentlandite
26.03	32.79	bdl	40.18	bdl	bdl	0.80	bdl	99.81	010-020C-thick-5-sul-4	010-020C	1	20	pentlandite
25.90	32.96	bdl	40.20	bdl	bdl	0.73	bdl	99.80	010-020C-thick-5-sul-5	010-020C	1	20	pentlandite
25.22	32.69	bdl	40.82	bdl	bdl	0.69	bdl	99.42	010-020C-thick-5-sul-6	010-020C	1	20	pentlandite
25.47	32.80	bdl	40.49	bdl	bdl	0.73	bdl	99.49	010-020C-thick-5-sul-7	010-020C	1	20	pentlandite
25.73	32.72	bdl	40.64	bdl	bdl	0.81	bdl	99.89	010-020C-thick-5-sul-8	010-020C	1	20	pentlandite
25.51	32.91	bdl	40.75	bdl	bdl	0.82	bdl	99.99	010-020C-thick-5-sul-9	010-020C	1	20	pentlandite
32.57	31.90	bdl	33.29	bdl	bdl	1.24	bdl	99.00	010-022-thick-1-sul-6	010-022	1	20	pentlandite
32.71	31.96	0.06	33.28	bdl	bdl	1.16	bdl	99.16	010-022-thick-1-sul-7	010-022	1	20	pentlandite
34.39	31.96	bdl	31.57	bdl	bdl	1.18	bdl	99.10	010-022-thick-2-sul-3	010-022	1	20	pentlandite
33.99	32.20	bdl	31.35	bdl	bdl	1.57	bdl	99.11	010-022-thick-2-sul-5	010-022	1	20	pentlandite

Supplementary table 4.8.A: sulfide mineral chemistry

Ni wt%	S wt%	As wt%	Fe wt%	Cu wt%	Pb wt%	Co wt%	Zn wt%	Total wt%	measuement number	sample	group	kv	mineral
33.33	32.12	bdl	32.77	bdl	bdl	0.90	bdl	99.12	010-022-thick-2-sul-7	010-022	1	20	pentlandite
33.48	31.88	bdl	32.73	bdl	bdl	0.94	bdl	99.03	010-022-thick-2-sul-8	010-022	1	20	pentlandite
33.39	32.16	0.05	32.79	bdl	bdl	0.77	bdl	99.15	010-022-thick-2-sul-9	010-022	1	20	pentlandite
35.31	32.08	bdl	30.60	bdl	bdl	1.40	bdl	99.39	010-022-thick-5-sul-1	010-022	1	20	pentlandite
33.08	31.67	bdl	33.12	bdl	bdl	1.27	bdl	99.13	010-022-thick-6-sul-1	010-022	1	20	pentlandite
33.09	32.06	bdl	33.14	bdl	bdl	1.30	bdl	99.59	010-022-thick-6-sul-2	010-022	1	20	pentlandite
33.08	31.99	bdl	33.16	bdl	bdl	1.26	bdl	99.49	010-022-thick-6-sul-4	010-022	1	20	pentlandite
32.84	31.90	bdl	33.18	bdl	bdl	1.22	bdl	99.15	010-022-thick-6-sul-5	010-022	1	20	pentlandite
33.18	31.98	bdl	33.04	bdl	bdl	1.25	bdl	99.45	010-022-thick-6-sul-7	010-022	1	20	pentlandite
33.46	32.01	bdl	32.61	bdl	bdl	1.05	bdl	99.14	010-022-thick-7-sul-12	010-022	1	20	pentlandite
34.94	32.22	bdl	30.94	bdl	bdl	1.26	bdl	99.35	010-022-thick-7-sul-2	010-022	1	20	pentlandite
33.89	32.02	bdl	32.60	bdl	bdl	0.76	bdl	99.27	010-022-thick-7-sul-3	010-022	1	20	pentlandite
33.72	31.96	bdl	32.73	bdl	bdl	0.67	bdl	99.09	010-022-thick-7-sul-4	010-022	1	20	pentlandite
33.04	31.87	bdl	32.11	bdl	bdl	2.11	bdl	99.13	010-022-thick-7-sul-6	010-022	1	20	pentlandite
33.08	31.82	0.05	32.17	bdl	bdl	2.10	bdl	99.21	010-022-thick-7-sul-7	010-022	1	20	pentlandite
33.65	32.11	0.06	32.65	bdl	bdl	0.97	bdl	99.45	010-022-thick-7-sul-9	010-022	1	20	pentlandite
35.85	33.87	bdl	29.57	0.06	bdl	1.50	bdl	100.84	10_22_S1_P4	010-022	1	15	pentlandite
34.76	33.52	bdl	30.57	0.05	bdl	1.02	bdl	99.92	10_22_S10_P2	010-022	1	15	pentlandite
34.96	34.02	bdl	30.90	bdl	bdl	1.07	bdl	100.94	10_22_S10_P3	010-022	1	15	pentlandite
34.78	33.91	bdl	31.19	bdl	bdl	0.99	bdl	100.87	10_22_S10_P4	010-022	1	15	pentlandite
34.17	33.34	bdl	30.24	bdl	bdl	1.31	bdl	99.07	10_22_S10_P5	010-022	1	15	pentlandite
35.09	33.90	bdl	30.33	0.02	bdl	1.04	bdl	100.38	10_22_S10_P6	010-022	1	15	pentlandite
35.48	33.83	bdl	30.26	bdl	bdl	1.14	bdl	100.72	10_22_S2_P1	010-022	1	15	pentlandite
35.48	33.86	bdl	29.51	0.14	bdl	1.21	bdl	100.21	10_22_S2_P3	010-022	1	15	pentlandite
32.44	34.27	bdl	32.84	bdl	bdl	1.36	bdl	100.90	10_22_S3_P1	010-022	1	15	pentlandite
33.27	33.49	bdl	32.53	0.11	bdl	0.83	bdl	100.22	10_22_S3_P5	010-022	1	15	pentlandite
32.75	32.66	bdl	31.36	0.09	bdl	2.11	0.07	99.03	10_22_S4_P1	010-022	1	15	pentlandite
33.18	33.68	bdl	32.08	0.06	bdl	1.49	bdl	100.48	10_22_S4_P2	010-022	1	15	pentlandite
33.15	34.22	bdl	32.00	0.07	bdl	0.95	bdl	100.39	10_22_S4_P4	010-022	1	15	pentlandite

Supplementary table 4.8.A: sulfide mineral chemistry

Ni wt%	S wt%	As wt%	Fe wt%	Cu wt%	Pb wt%	Co wt%	Zn wt%	Total wt%	measuement number	sample	group	kv	mineral
33.02	34.02	bdl	32.60	0.05	bdl	0.87	0.04	100.60	10_22_S4_P5	010-022	1	15	pentlandite
33.84	33.90	bdl	32.07	0.05	bdl	1.04	0.03	100.92	10_22_S5_P1	010-022	1	15	pentlandite
33.89	33.98	bdl	31.96	0.04	bdl	1.05	bdl	100.91	10_22_S5_P2	010-022	1	15	pentlandite
31.55	34.05	bdl	34.22	0.02	bdl	0.85	bdl	100.68	10_22_S6_P1	010-022	1	15	pentlandite
30.67	33.86	bdl	35.00	0.04	bdl	0.75	0.04	100.36	10_22_S6_P3	010-022	1	15	pentlandite
35.62	33.29	bdl	29.57	0.07	bdl	1.10	bdl	99.64	10_22_S7_P1	010-022	1	15	pentlandite
32.85	33.86	bdl	32.79	0.03	bdl	0.75	bdl	100.28	10_22_S8_P2	010-022	1	15	pentlandite
36.65	33.97	bdl	29.01	0.06	bdl	1.24	bdl	100.93	10_22_S9_P2	010-022	1	15	pentlandite
31.59	33.25	bdl	34.57	bdl	bdl	1.11	0.03	100.55	010-023-S10-P1	010-023	1	15	pentlandite
30.72	33.33	bdl	34.40	0.03	bdl	1.77	bdl	100.24	010-023-S10-P2	010-023	1	15	pentlandite
31.62	33.43	bdl	34.45	bdl	bdl	1.23	0.05	100.78	010-023-S10-P3	010-023	1	15	pentlandite
31.50	33.16	bdl	34.82	bdl	bdl	1.05	bdl	100.52	010-023-S10-P4	010-023	1	15	pentlandite
31.67	32.87	bdl	34.07	bdl	bdl	1.20	bdl	99.81	010-023-S10-P5	010-023	1	15	pentlandite
30.68	34.11	bdl	33.98	bdl	bdl	1.21	bdl	99.98	010-023-S3-test	010-023	1	20	pentlandite
32.63	33.06	bdl	33.61	bdl	bdl	1.27	bdl	100.57	010-023-S4-P1	010-023	1	15	pentlandite
32.53	33.04	bdl	33.44	bdl	bdl	1.21	bdl	100.21	010-023-S4-P2	010-023	1	15	pentlandite
31.94	32.83	bdl	33.27	bdl	bdl	1.81	0.03	99.87	010-023-S4-P3	010-023	1	15	pentlandite
32.40	33.11	bdl	33.57	bdl	bdl	1.22	bdl	100.30	010-023-S4-P4	010-023	1	15	pentlandite
32.16	32.87	bdl	32.97	bdl	bdl	1.08	bdl	99.08	010-023-S4-P5	010-023	1	15	pentlandite
31.97	33.32	bdl	34.24	bdl	bdl	1.08	bdl	100.61	010-023-S5-P1	010-023	1	15	pentlandite
31.02	33.54	bdl	34.55	bdl	bdl	1.10	bdl	100.22	010-023-S5-P2	010-023	1	15	pentlandite
31.86	33.18	bdl	33.68	bdl	bdl	1.14	bdl	99.86	010-023-S5-P3	010-023	1	15	pentlandite
30.38	33.68	bdl	34.14	bdl	bdl	1.25	0.03	99.47	010-023-S5-P4	010-023	1	15	pentlandite
31.83	33.25	bdl	34.26	bdl	bdl	1.11	bdl	100.45	010-023-S6-P1	010-023	1	15	pentlandite
31.62	33.13	bdl	34.29	bdl	bdl	1.08	bdl	100.12	010-023-S6-P2	010-023	1	15	pentlandite
31.65	33.21	bdl	34.33	bdl	bdl	1.11	0.03	100.35	010-023-S7-P3	010-023	1	15	pentlandite
31.12	33.06	bdl	34.15	bdl	bdl	1.43	bdl	99.76	010-023-S7-P5	010-023	1	15	pentlandite
31.93	32.79	bdl	33.58	bdl	bdl	1.34	bdl	99.65	010-023-thick-1A-sul-2	010-023	1	20	pentlandite
31.74	33.10	bdl	33.25	bdl	bdl	1.39	bdl	99.48	010-023-thick-1A-sul-4	010-023	1	20	pentlandite

Supplementary table 4.8.A: sulfide mineral chemistry

Ni wt%	S wt%	As wt%	Fe wt%	Cu wt%	Pb wt%	Co wt%	Zn wt%	Total wt%	measuement number	sample	group	kv	mineral
31.88	32.66	bdl	33.76	bdl	bdl	1.21	bdl	99.52	010-023-thick-1A-sul-5	010-023	1	20	pentlandite
31.40	32.77	0.07	34.29	bdl	bdl	1.26	bdl	99.80	010-023-thick-2A-sul-1	010-023	1	20	pentlandite
31.41	32.70	bdl	34.07	bdl	bdl	1.28	bdl	99.46	010-023-thick-2A-sul-2	010-023	1	20	pentlandite
31.71	32.48	bdl	33.80	bdl	bdl	1.15	bdl	99.14	010-023-thick-4-sul-1	010-023	1	20	pentlandite
32.08	32.56	bdl	33.60	bdl	bdl	1.12	bdl	99.36	010-023-thick-4-sul-3	010-023	1	20	pentlandite
31.47	32.56	bdl	34.16	bdl	bdl	1.32	bdl	99.51	010-023-thick-4-sul-4	010-023	1	20	pentlandite
31.63	32.78	bdl	34.13	bdl	bdl	1.11	bdl	99.65	010-023-thick-4-sul-5	010-023	1	20	pentlandite
32.29	32.47	bdl	33.37	bdl	bdl	1.09	bdl	99.22	010-023-thick-7-sul-1	010-023	1	20	pentlandite
32.64	32.70	0.08	33.23	bdl	bdl	1.19	bdl	99.84	010-023-thick-7-sul-2	010-023	1	20	pentlandite
32.28	32.53	bdl	33.61	bdl	bdl	1.11	bdl	99.52	010-023-thick-7-sul-3	010-023	1	20	pentlandite
32.16	32.46	bdl	33.50	bdl	bdl	1.13	bdl	99.25	010-023-thick-7-sul-4	010-023	1	20	pentlandite
32.39	32.53	bdl	33.49	bdl	bdl	1.08	bdl	99.48	010-023-thick-7-sul-5	010-023	1	20	pentlandite
32.52	32.49	bdl	33.28	bdl	bdl	1.10	bdl	99.39	010-023-thick-7-sul-6	010-023	1	20	pentlandite
32.05	32.63	bdl	33.79	bdl	bdl	1.13	bdl	99.60	010-023-thick-8-sul-1	010-023	1	20	pentlandite
32.18	32.55	bdl	33.75	bdl	bdl	1.13	bdl	99.61	010-023-thick-8-sul-2	010-023	1	20	pentlandite
32.25	32.52	bdl	33.71	bdl	bdl	1.09	bdl	99.57	010-023-thick-8-sul-3	010-023	1	20	pentlandite
31.92	32.31	bdl	33.82	bdl	bdl	1.25	bdl	99.31	010-023-thick-8-sul-4	010-023	1	20	pentlandite
32.18	32.58	bdl	33.72	bdl	bdl	1.10	bdl	99.58	010-023-thick-8-sul-5	010-023	1	20	pentlandite
32.51	32.66	0.06	33.39	bdl	bdl	1.16	bdl	99.78	010-023-thick-9-sul-1	010-023	1	20	pentlandite
32.50	32.77	bdl	33.31	bdl	bdl	1.24	bdl	99.83	010-023-thick-9-sul-2	010-023	1	20	pentlandite
32.90	32.46	bdl	32.93	bdl	bdl	1.24	bdl	99.53	010-023-thick-9-sul-3	010-023	1	20	pentlandite
32.84	32.54	bdl	32.98	bdl	bdl	1.25	bdl	99.61	010-023-thick-9-sul-4	010-023	1	20	pentlandite
32.51	32.76	bdl	33.47	bdl	bdl	1.16	bdl	99.90	010-023-thick-9-sul-5	010-023	1	20	pentlandite
32.53	32.40	bdl	33.49	bdl	bdl	1.15	bdl	99.57	010-023-thick-9-sul-6	010-023	1	20	pentlandite
32.76	33.77	bdl	33.06	bdl	bdl	1.19	0.02	100.80	10_23_S01_P1	010-023	1	15	pentlandite
32.29	33.84	bdl	32.75	0.04	bdl	1.43	bdl	100.36	10_23_S01_P3	010-023	1	15	pentlandite
32.57	33.50	bdl	33.29	bdl	bdl	0.90	bdl	100.26	10_23_S01_P4	010-023	1	15	pentlandite
31.46	33.50	bdl	33.87	0.03	bdl	1.31	bdl	100.17	10_23_S02_P1	010-023	1	15	pentlandite
31.13	33.69	bdl	33.61	0.03	bdl	1.63	bdl	100.10	10_23_S02_P3	010-023	1	15	pentlandite

Supplementary table 4.8.A: sulfide mineral chemistry

Ni wt%	S wt%	As wt%	Fe wt%	Cu wt%	Pb wt%	Co wt%	Zn wt%	Total wt%	measuement number	sample	group	kv	mineral
31.37	33.61	bdl	34.10	bdl	bdl	1.14	bdl	100.23	10_23_S02_P4	010-023	1	15	pentlandite
31.24	33.21	bdl	34.57	0.09	bdl	1.20	0.06	100.37	10_23_S02_P5	010-023	1	15	pentlandite
30.74	33.75	0.12	34.78	0.03	bdl	1.23	bdl	100.65	10_23_S03_P1	010-023	1	15	pentlandite
30.96	33.83	bdl	35.07	bdl	bdl	0.95	0.07	100.88	10_23_S03_P2	010-023	1	15	pentlandite
31.05	33.41	bdl	34.95	0.09	bdl	1.05	bdl	100.55	10_23_S03_P3	010-023	1	15	pentlandite
30.54	33.60	bdl	35.35	bdl	bdl	1.09	bdl	100.57	10_23_S04_P2	010-023	1	15	pentlandite
32.66	33.83	bdl	33.06	0.08	bdl	1.03	bdl	100.65	10_23_S05_P1	010-023	1	15	pentlandite
32.34	33.68	bdl	33.66	bdl	bdl	0.93	0.09	100.71	10_23_S06_P2	010-023	1	15	pentlandite
32.18	33.71	bdl	33.76	bdl	bdl	1.10	bdl	100.75	10_23_S06_P4	010-023	1	15	pentlandite
30.40	34.11	bdl	34.60	0.16	bdl	0.72	bdl	100.00	10_23_S07_P2	010-023	1	15	pentlandite
32.21	33.31	bdl	34.09	bdl	bdl	0.93	0.09	100.64	10_23_S07_P3	010-023	1	15	pentlandite
32.28	33.58	bdl	33.77	bdl	bdl	1.07	0.05	100.75	10_23_S07_P4	010-023	1	15	pentlandite
31.25	33.99	bdl	33.92	bdl	bdl	1.76	bdl	100.91	10_23_S07_P5	010-023	1	15	pentlandite
31.51	33.49	bdl	33.63	0.05	bdl	1.36	0.05	100.10	10_23_S08_P1	010-023	1	15	pentlandite
31.45	34.04	0.07	33.99	0.06	bdl	1.20	bdl	100.80	10_23_S08_P2	010-023	1	15	pentlandite
31.97	33.72	bdl	34.31	bdl	bdl	0.81	bdl	100.79	10_23_S08_P3	010-023	1	15	pentlandite
32.94	33.60	bdl	32.20	0.07	bdl	1.20	bdl	99.99	10_23_S09_P3	010-023	1	15	pentlandite
32.90	33.64	bdl	31.69	0.03	bdl	1.13	bdl	99.39	10_23_S09_P4	010-023	1	15	pentlandite
31.82	33.65	bdl	33.36	0.02	bdl	2.10	bdl	100.94	10_23_S10_P1	010-023	1	15	pentlandite
32.15	33.63	bdl	33.95	0.06	bdl	1.10	0.03	100.91	10_23_S10_P2	010-023	1	15	pentlandite
32.15	33.57	bdl	33.73	bdl	bdl	0.97	0.05	100.46	10_23_S10_P3	010-023	1	15	pentlandite
31.83	33.56	bdl	33.60	bdl	bdl	1.11	0.10	100.20	10_23_S10_P4	010-023	1	15	pentlandite
31.22	33.48	bdl	33.62	0.16	bdl	0.97	0.04	99.48	10_23_S10_P5	010-023	1	15	pentlandite
32.26	33.47	bdl	33.90	0.15	bdl	1.01	0.05	100.83	10_23_S10_P7	010-023	1	15	pentlandite
30.59	33.72	bdl	34.86	0.08	bdl	1.16	0.06	100.48	10_23_S11_P1	010-023	1	15	pentlandite
31.00	33.65	bdl	34.76	bdl	bdl	1.11	bdl	100.52	10_23_S11_P2	010-023	1	15	pentlandite
31.30	33.59	0.08	34.75	0.02	bdl	1.05	0.03	100.83	10_23_S12_P1	010-023	1	15	pentlandite
31.06	33.74	bdl	34.79	0.23	bdl	0.99	bdl	100.81	10_23_S12_P2	010-023	1	15	pentlandite
32.35	33.74	bdl	33.57	0.06	bdl	1.05	bdl	100.76	10_23_S12_P3	010-023	1	15	pentlandite

Supplementary table 4.8.A: sulfide mineral chemistry

Ni wt%	S wt%	As wt%	Fe wt%	Cu wt%	Pb wt%	Co wt%	Zn wt%	Total wt%	measuement number	sample	group	kv	mineral
31.18	33.97	bdl	34.57	0.02	bdl	1.04	0.06	100.84	10_23_S12_P4	010-023	1	15	pentlandite
30.89	33.79	bdl	35.01	0.05	bdl	1.22	bdl	100.96	10_23_S12_P6	010-023	1	15	pentlandite
30.80	33.97	bdl	34.85	0.11	bdl	0.96	bdl	100.68	10_23_S12_P7	010-023	1	15	pentlandite
31.11	33.58	bdl	34.83	0.02	bdl	1.00	0.09	100.63	10_23_S13_P1	010-023	1	15	pentlandite
31.25	33.48	bdl	34.90	0.03	bdl	1.07	bdl	100.73	10_23_S13_P2	010-023	1	15	pentlandite
33.44	33.61	bdl	32.75	0.03	bdl	1.00	bdl	100.83	10_23_S13_P3	010-023	1	15	pentlandite
33.33	32.10	bdl	33.28	bdl	bdl	0.94	bdl	99.64	010-029B-250-180-1-sul-4	010-029B	2	20	pentlandite
33.27	32.38	bdl	33.26	bdl	bdl	0.98	bdl	99.88	010-029B-250-180-1-sul-5	010-029B	2	20	pentlandite
32.85	32.32	bdl	33.59	bdl	bdl	0.95	bdl	99.71	010-029B-250-180-1-sul-6	010-029B	2	20	pentlandite
33.10	32.33	bdl	33.31	bdl	bdl	0.91	bdl	99.65	010-029B-250-180-1-sul-7	010-029B	2	20	pentlandite
33.05	32.07	bdl	33.42	bdl	bdl	0.92	bdl	99.46	010-029B-250-180-1-sul-8	010-029B	2	20	pentlandite
31.70	32.25	bdl	34.42	bdl	bdl	1.20	bdl	99.57	010-029B-250-180-2-sul-15	010-029B	2	20	pentlandite
31.82	32.15	bdl	34.21	bdl	bdl	1.19	bdl	99.36	010-029B-250-180-2-sul-3	010-029B	2	20	pentlandite
32.44	32.10	bdl	33.90	bdl	bdl	1.09	bdl	99.53	010-029B-250-180-2-sul-4	010-029B	2	20	pentlandite
32.54	32.34	bdl	33.85	bdl	bdl	1.01	bdl	99.73	010-029B-250-180-2-sul-7	010-029B	2	20	pentlandite
32.84	32.25	bdl	33.44	bdl	bdl	1.16	bdl	99.68	010-029B-250-180-2-sul-9	010-029B	2	20	pentlandite
33.23	32.43	bdl	33.52	bdl	bdl	0.99	bdl	100.18	010-029B-250-180-3-sul-10	010-029B	2	20	pentlandite
33.14	32.21	bdl	33.39	bdl	bdl	0.98	bdl	99.72	010-029B-250-180-3-sul-4	010-029B	2	20	pentlandite
32.43	32.31	bdl	34.20	bdl	bdl	0.94	bdl	99.88	010-029B-250-180-3-sul-5	010-029B	2	20	pentlandite
33.17	32.05	bdl	33.50	bdl	bdl	0.98	bdl	99.68	010-029B-250-180-3-sul-6	010-029B	2	20	pentlandite
30.10	32.42	bdl	36.31	bdl	bdl	0.99	bdl	99.82	010-029B-250-180-3-sul-7	010-029B	2	20	pentlandite
32.76	32.10	bdl	33.40	bdl	bdl	1.04	bdl	99.28	010-029B-250-180-3-sul-9	010-029B	2	20	pentlandite
31.82	32.07	bdl	34.30	bdl	bdl	1.28	bdl	99.47	010-029B-250-180-4-sul-1	010-029B	2	20	pentlandite
29.66	32.29	bdl	36.40	bdl	bdl	1.21	bdl	99.56	010-029B-250-180-4-sul-10	010-029B	2	20	pentlandite
32.33	32.35	bdl	33.86	bdl	bdl	1.28	bdl	99.82	010-029B-250-180-4-sul-2	010-029B	2	20	pentlandite
32.00	32.14	bdl	34.15	bdl	bdl	1.29	bdl	99.58	010-029B-250-180-4-sul-3	010-029B	2	20	pentlandite
32.09	31.95	0.07	34.14	bdl	bdl	1.27	bdl	99.53	010-029B-250-180-4-sul-4	010-029B	2	20	pentlandite
32.68	32.35	bdl	33.73	bdl	bdl	0.98	bdl	99.74	010-029B-250-180-5-sul-10	010-029B	2	20	pentlandite
32.03	32.06	bdl	34.42	bdl	bdl	0.92	bdl	99.42	010-029B-250-180-5-sul-11	010-029B	2	20	pentlandite

Supplementary table 4.8.A: sulfide mineral chemistry

Ni wt%	S wt%	As wt%	Fe wt%	Cu wt%	Pb wt%	Co wt%	Zn wt%	Total wt%	measuement number	sample	group	kv	mineral
30.79	31.85	0.07	35.57	bdl	bdl	0.91	bdl	99.18	010-029B-250-180-5-sul-3	010-029B	2	20	pentlandite
30.49	32.28	bdl	35.86	bdl	bdl	0.88	bdl	99.52	010-029B-250-180-5-sul-4	010-029B	2	20	pentlandite
32.58	32.07	bdl	33.78	bdl	bdl	1.03	bdl	99.46	010-029B-250-180-5-sul-8	010-029B	2	20	pentlandite
32.77	32.17	0.06	33.42	bdl	bdl	1.00	bdl	99.41	010-029B-250-180-5-sul-9	010-029B	2	20	pentlandite
32.71	32.44	bdl	33.93	bdl	bdl	0.95	bdl	100.03	010-029B-250-180-6-sul-1	010-029B	2	20	pentlandite
32.87	32.28	bdl	33.58	bdl	bdl	0.97	bdl	99.70	010-029B-250-180-6-sul-3	010-029B	2	20	pentlandite
32.89	32.24	bdl	33.23	bdl	bdl	0.97	bdl	99.32	010-029B-250-180-6-sul-4	010-029B	2	20	pentlandite
30.66	32.23	bdl	35.68	bdl	bdl	0.93	bdl	99.49	010-029B-250-180-6-sul-5	010-029B	2	20	pentlandite
32.51	32.05	bdl	33.62	bdl	bdl	0.94	bdl	99.11	010-029B-250-180-6-sul-6	010-029B	2	20	pentlandite
29.65	32.25	0.06	36.19	bdl	bdl	1.05	bdl	99.21	010-029B-250-180-6-sul-7	010-029B	2	20	pentlandite
32.89	32.17	bdl	33.32	bdl	bdl	0.80	bdl	99.19	010-029B-250-180-7-sul-1	010-029B	2	20	pentlandite
31.73	32.00	bdl	34.59	bdl	bdl	1.00	bdl	99.31	010-029B-250-180-7-sul-11	010-029B	2	20	pentlandite
29.64	32.43	bdl	36.36	bdl	bdl	0.96	bdl	99.39	010-029B-250-180-7-sul-12	010-029B	2	20	pentlandite
31.52	32.01	0.06	34.70	bdl	bdl	0.83	bdl	99.12	010-029B-250-180-7-sul-2	010-029B	2	20	pentlandite
33.16	32.26	0.08	33.45	bdl	bdl	0.83	bdl	99.78	010-029B-250-180-7-sul-4	010-029B	2	20	pentlandite
32.76	32.13	bdl	33.58	bdl	bdl	0.86	bdl	99.32	010-029B-250-180-7-sul-7	010-029B	2	20	pentlandite
29.57	32.36	bdl	36.12	bdl	bdl	1.05	bdl	99.10	010-029B-250-180-8-sul-2	010-029B	2	20	pentlandite
33.48	32.15	bdl	32.93	bdl	bdl	0.95	bdl	99.52	010-029B-ii-iii-1-sul-1	010-029B	2	20	pentlandite
33.02	32.30	bdl	33.42	bdl	bdl	0.80	bdl	99.54	010-029B-ii-iii-1-sul-10	010-029B	2	20	pentlandite
32.75	32.03	bdl	33.52	bdl	bdl	0.92	bdl	99.21	010-029B-ii-iii-1-sul-11	010-029B	2	20	pentlandite
33.23	32.15	bdl	33.25	bdl	bdl	0.87	bdl	99.49	010-029B-ii-iii-1-sul-13	010-029B	2	20	pentlandite
32.83	32.44	bdl	33.55	bdl	bdl	0.88	bdl	99.70	010-029B-ii-iii-1-sul-14	010-029B	2	20	pentlandite
32.84	32.44	bdl	33.73	bdl	bdl	0.84	bdl	99.86	010-029B-ii-iii-1-sul-15	010-029B	2	20	pentlandite
33.71	32.00	bdl	32.75	bdl	bdl	0.96	bdl	99.42	010-029B-ii-iii-1-sul-17	010-029B	2	20	pentlandite
32.98	32.24	bdl	33.54	bdl	bdl	0.95	bdl	99.71	010-029B-ii-iii-1-sul-18	010-029B	2	20	pentlandite
33.68	32.24	bdl	32.71	bdl	bdl	0.98	bdl	99.61	010-029B-ii-iii-1-sul-2	010-029B	2	20	pentlandite
33.02	32.25	bdl	33.28	bdl	bdl	1.09	bdl	99.64	010-029B-ii-iii-1-sul-23	010-029B	2	20	pentlandite
32.67	32.26	bdl	33.41	bdl	bdl	1.12	bdl	99.45	010-029B-ii-iii-1-sul-24	010-029B	2	20	pentlandite
32.58	32.25	bdl	33.56	bdl	bdl	1.13	bdl	99.53	010-029B-ii-iii-1-sul-27	010-029B	2	20	pentlandite

Supplementary table 4.8.A: sulfide mineral chemistry

Ni wt%	S wt%	As wt%	Fe wt%	Cu wt%	Pb wt%	Co wt%	Zn wt%	Total wt%	measuement number	sample	group	kv	mineral
33.85	32.36	bdl	32.73	bdl	bdl	1.05	bdl	99.99	010-029B-ii-iii-1-sul-30	010-029B	2	20	pentlandite
33.63	32.23	bdl	32.79	bdl	bdl	1.03	bdl	99.68	010-029B-ii-iii-1-sul-31	010-029B	2	20	pentlandite
0.26	33.87	bdl	30.98	34.96	bdl	0.07	bdl	100.13	010-029B-ii-iii-1-sul-32	010-029B	2	20	chalcopyrite
33.15	32.03	bdl	33.24	bdl	bdl	1.05	bdl	99.46	010-029B-ii-iii-1-sul-35	010-029B	2	20	pentlandite
33.17	32.22	bdl	33.24	bdl	bdl	1.03	bdl	99.66	010-029B-ii-iii-1-sul-36	010-029B	2	20	pentlandite
32.86	32.04	bdl	33.40	bdl	bdl	1.04	bdl	99.34	010-029B-ii-iii-1-sul-37	010-029B	2	20	pentlandite
32.44	32.79	bdl	34.12	bdl	bdl	0.99	bdl	100.34	010-029B-ii-iii-1-sul-41	010-029B	2	20	pentlandite
32.87	32.39	bdl	33.74	bdl	bdl	1.01	bdl	100.01	010-029B-ii-iii-1-sul-5	010-029B	2	20	pentlandite
32.78	32.19	bdl	33.46	bdl	bdl	1.07	bdl	99.50	010-029B-ii-iii-1-sul-6	010-029B	2	20	pentlandite
32.87	32.14	bdl	33.57	bdl	bdl	0.96	bdl	99.54	010-029B-ii-iii-2-sul-1	010-029B	2	20	pentlandite
27.42	33.66	bdl	37.28	0.40	bdl	1.13	bdl	99.89	010-029B-ii-iii-2-sul-2	010-029B	2	20	pentlandite
0.02	36.08	bdl	64.17	bdl	bdl	bdl	bdl	100.26	010-029B-S10-P1	010-029B	2	15	pyrrhotite
29.35	32.69	bdl	36.78	bdl	bdl	0.70	bdl	99.51	010-029B-S10-P2	010-029B	2	15	pentlandite
0.14	36.02	bdl	63.89	bdl	bdl	bdl	bdl	100.04	010-029B-S10-P3	010-029B	2	15	pyrrhotite
32.44	33.06	bdl	33.76	bdl	bdl	0.77	bdl	100.03	010-029B-S10-P4	010-029B	2	15	pentlandite
32.56	33.09	0.09	34.20	bdl	bdl	0.72	0.07	100.72	010-029B-S10-P5	010-029B	2	15	pentlandite
0.02	36.24	bdl	63.57	bdl	bdl	bdl	bdl	99.83	010-029B-S10-P6	010-029B	2	15	pyrrhotite
31.85	32.50	bdl	33.89	bdl	bdl	0.94	bdl	99.17	010-029B-S1-P1	010-029B	2	15	pentlandite
0.05	36.09	bdl	64.22	bdl	bdl	bdl	bdl	100.36	010-029B-S1-P2	010-029B	2	15	pyrrhotite
0.03	36.37	bdl	64.33	bdl	bdl	bdl	bdl	100.73	010-029B-S1-P3	010-029B	2	15	pyrrhotite
30.71	33.00	bdl	35.39	bdl	bdl	0.86	0.04	99.99	010-029B-S1-P4	010-029B	2	15	pentlandite
23.59	35.40	bdl	40.06	bdl	bdl	1.11	bdl	100.16	010-029B-S1-P5	010-029B	2	15	pentlandite
0.30	36.06	bdl	64.24	bdl	bdl	0.07	bdl	100.68	010-029B-S1-P6	010-029B	2	15	pyrrhotite
31.89	32.85	bdl	34.10	bdl	bdl	0.90	0.06	99.79	010-029B-S1-P7	010-029B	2	15	pentlandite
0.07	36.13	bdl	64.18	bdl	bdl	bdl	bdl	100.38	010-029B-S1-P8	010-029B	2	15	pyrrhotite
0.12	36.30	bdl	64.47	bdl	bdl	bdl	bdl	100.89	010-029B-S2-P1	010-029B	2	15	pyrrhotite
31.79	33.07	bdl	34.25	bdl	bdl	0.87	bdl	99.99	010-029B-S2-P2	010-029B	2	15	pentlandite
31.60	32.99	bdl	34.35	bdl	bdl	0.82	bdl	99.76	010-029B-S2-P3	010-029B	2	15	pentlandite
0.21	35.76	bdl	63.98	bdl	bdl	0.02	bdl	99.97	010-029B-S2-P4	010-029B	2	15	pyrrhotite

Supplementary table 4.8.A: sulfide mineral chemistry

Ni wt%	S wt%	As wt%	Fe wt%	Cu wt%	Pb wt%	Co wt%	Zn wt%	Total wt%	measuement number	sample	group	kv	mineral
28.99	33.34	bdl	36.97	bdl	bdl	0.93	bdl	100.22	010-029B-S2-P5	010-029B	2	15	pentlandite
bdl	36.36	bdl	64.03	0.07	bdl	bdl	bdl	100.46	010-029B-S2-P6	010-029B	2	15	pyrrhotite
30.05	32.75	bdl	36.23	bdl	bdl	0.88	0.05	99.95	010-029B-S2-P7	010-029B	2	15	pentlandite
32.05	32.51	0.10	34.18	bdl	bdl	0.88	bdl	99.72	010-029B-S2-P8	010-029B	2	15	pentlandite
0.13	35.83	bdl	64.18	bdl	bdl	bdl	0.02	100.16	010-029B-S2-P9	010-029B	2	15	pyrrhotite
32.60	32.79	bdl	33.79	bdl	bdl	0.93	bdl	100.11	010-029B-S3-P1	010-029B	2	15	pentlandite
bdl	36.25	bdl	63.87	bdl	bdl	bdl	bdl	100.11	010-029B-S3-P2	010-029B	2	15	pyrrhotite
0.16	35.96	bdl	64.10	0.09	bdl	bdl	0.02	100.33	010-029B-S3-P3	010-029B	2	15	pyrrhotite
31.60	33.08	bdl	34.74	bdl	bdl	0.92	bdl	100.33	010-029B-S3-P4	010-029B	2	15	pentlandite
0.03	36.09	bdl	64.12	0.05	bdl	bdl	bdl	100.30	010-029B-S4-P1	010-029B	2	15	pyrrhotite
32.70	32.70	bdl	33.18	bdl	bdl	0.74	bdl	99.31	010-029B-S4-P2	010-029B	2	15	pentlandite
0.21	38.92	bdl	60.54	bdl	bdl	bdl	bdl	99.66	010-029B-S4-P3	010-029B	2	15	pyrrhotite
32.47	32.97	bdl	33.84	bdl	bdl	0.79	bdl	100.07	010-029B-S4-P4	010-029B	2	15	pentlandite
0.08	35.95	bdl	63.68	bdl	bdl	bdl	bdl	99.71	010-029B-S4-P5	010-029B	2	15	pyrrhotite
32.16	32.87	bdl	34.47	bdl	bdl	0.77	0.04	100.31	010-029B-S4-P6	010-029B	2	15	pentlandite
31.79	32.90	bdl	34.07	bdl	bdl	0.95	0.03	99.75	010-029B-S5-P1	010-029B	2	15	pentlandite
0.11	36.21	0.08	64.17	0.03	bdl	bdl	bdl	100.61	010-029B-S5-P10	010-029B	2	15	pyrrhotite
23.37	36.68	bdl	38.56	0.26	bdl	1.28	0.07	100.21	010-029B-S5-P11	010-029B	2	15	pentlandite
0.43	36.40	bdl	63.75	bdl	bdl	bdl	bdl	100.58	010-029B-S5-P12	010-029B	2	15	pyrrhotite
31.33	32.99	bdl	35.16	bdl	bdl	0.86	0.03	100.38	010-029B-S5-P2	010-029B	2	15	pentlandite
31.44	32.96	bdl	34.81	bdl	bdl	0.90	0.05	100.16	010-029B-S5-P3	010-029B	2	15	pentlandite
0.03	36.12	bdl	64.63	0.02	bdl	bdl	0.04	100.85	010-029B-S5-P5	010-029B	2	15	pyrrhotite
0.06	36.11	bdl	64.59	bdl	bdl	bdl	0.04	100.79	010-029B-S5-P6	010-029B	2	15	pyrrhotite
32.00	33.12	bdl	34.28	bdl	bdl	0.83	0.05	100.29	010-029B-S5-P7	010-029B	2	15	pentlandite
32.61	32.98	bdl	33.85	bdl	bdl	0.75	bdl	100.19	010-029B-S5-P8	010-029B	2	15	pentlandite
32.08	32.93	bdl	34.07	bdl	bdl	0.75	0.07	99.90	010-029B-S5-P9	010-029B	2	15	pentlandite
0.06	34.99	bdl	30.65	33.72	bdl	0.05	bdl	99.48	010-029B-S6-C1	010-029B	2	20	chalcopyrite
32.17	32.69	bdl	34.04	bdl	bdl	0.87	bdl	99.78	010-029B-S6-P1	010-029B	2	15	pentlandite
32.01	33.02	bdl	33.98	bdl	bdl	0.89	0.02	99.92	010-029B-S6-P2	010-029B	2	15	pentlandite

Supplementary table 4.8.A: sulfide mineral chemistry

Ni wt%	S wt%	As wt%	Fe wt%	Cu wt%	Pb wt%	Co wt%	Zn wt%	Total wt%	measuement number	sample	group	kv	mineral
0.03	36.06	bdl	64.65	bdl	bdl	bdl	bdl	100.73	010-029B-S6-P3	010-029B	2	15	pyrrhotite
31.96	32.84	bdl	34.54	bdl	bdl	0.76	bdl	100.10	010-029B-S6-P4	010-029B	2	15	pentlandite
0.08	35.92	bdl	64.37	bdl	bdl	bdl	0.04	100.41	010-029B-S6-P5	010-029B	2	15	pyrrhotite
32.44	33.01	bdl	34.01	bdl	bdl	0.81	0.06	100.33	010-029B-S6-P6	010-029B	2	15	pentlandite
23.55	35.84	bdl	39.64	0.09	bdl	0.70	bdl	99.81	010-029B-S6-P7	010-029B	2	15	pentlandite
0.06	36.15	bdl	64.40	bdl	bdl	bdl	0.05	100.66	010-029B-S6-P8	010-029B	2	15	pyrrhotite
31.62	32.66	bdl	34.53	bdl	bdl	0.71	0.03	99.55	010-029B-S6-P9	010-029B	2	15	pentlandite
32.45	33.21	bdl	33.74	bdl	bdl	0.93	bdl	100.34	010-029B-S7-P1	010-029B	2	15	pentlandite
0.06	36.02	bdl	63.98	bdl	bdl	0.03	0.02	100.11	010-029B-S7-P2	010-029B	2	15	pyrrhotite
32.20	33.20	0.07	33.69	bdl	bdl	0.80	bdl	99.96	010-029B-S7-P3	010-029B	2	15	pentlandite
0.05	36.21	bdl	64.03	bdl	bdl	bdl	bdl	100.29	010-029B-S7-P4	010-029B	2	15	pyrrhotite
29.54	32.92	0.08	35.70	bdl	bdl	0.86	bdl	99.10	010-029B-S7-P5	010-029B	2	15	pentlandite
0.18	34.64	bdl	30.53	33.73	bdl	0.06	bdl	99.14	010-029B-S8-C2	010-029B	2	20	chalcopyrite
32.66	32.96	bdl	33.10	bdl	bdl	0.81	0.02	99.55	010-029B-S8-P1	010-029B	2	15	pentlandite
0.07	36.28	bdl	63.89	bdl	bdl	0.04	bdl	100.29	010-029B-S8-P2	010-029B	2	15	pyrrhotite
32.70	33.06	bdl	33.97	bdl	bdl	0.85	bdl	100.58	010-029B-S8-P3	010-029B	2	15	pentlandite
0.10	36.15	0.07	63.80	bdl	bdl	bdl	bdl	100.12	010-029B-S8-P4	010-029B	2	15	pyrrhotite
32.57	32.97	bdl	33.79	bdl	bdl	0.87	bdl	100.20	010-029B-S8-P5	010-029B	2	15	pentlandite
24.25	35.52	bdl	38.82	0.54	bdl	0.79	0.03	99.94	010-029B-S8-P6	010-029B	2	15	pentlandite
25.03	35.47	bdl	38.69	bdl	bdl	0.99	bdl	100.18	010-029B-S8-P7	010-029B	2	15	pentlandite
32.07	33.30	bdl	34.57	bdl	bdl	0.84	0.04	100.81	010-029B-S8-P8	010-029B	2	15	pentlandite
bdl	36.29	bdl	63.96	0.02	bdl	bdl	bdl	100.27	010-029B-S9-P1	010-029B	2	15	pyrrhotite
28.79	33.11	bdl	37.37	bdl	bdl	0.86	0.03	100.16	010-029B-S9-P2	010-029B	2	15	pentlandite
bdl	36.31	bdl	64.27	bdl	bdl	bdl	0.05	100.62	010-029B-S9-P3	010-029B	2	15	pyrrhotite
32.22	33.00	bdl	34.19	bdl	bdl	0.87	0.03	100.32	010-029B-S9-P4	010-029B	2	15	pentlandite
0.09	35.99	bdl	64.08	bdl	bdl	bdl	bdl	100.16	010-029B-S9-P5	010-029B	2	15	pyrrhotite
30.34	33.15	bdl	35.87	bdl	bdl	0.59	bdl	99.94	010-029B-S9-P6	010-029B	2	15	pentlandite
32.12	33.05	bdl	34.00	bdl	bdl	0.85	0.02	100.04	010-029B-S9-P7	010-029B	2	15	pentlandite
0.25	36.15	0.06	63.75	0.03	bdl	bdl	bdl	100.23	010-029B-S9-P8	010-029B	2	15	pyrrhotite

Supplementary table 4.8.A: sulfide mineral chemistry

Ni wt%	S wt%	As wt%	Fe wt%	Cu wt%	Pb wt%	Co wt%	Zn wt%	Total wt%	measuement number	sample	group	kv	mineral
0.04	37.02	bdl	63.68	0.05	bdl	bdl	bdl	100.79	10_29B_S01_P2	010-029B	2	15	pyrrhotite
32.90	33.91	bdl	33.39	bdl	bdl	0.76	bdl	100.95	10_29B_S01_P3	010-029B	2	15	pentlandite
25.69	36.02	bdl	37.93	0.20	bdl	1.09	bdl	100.93	10_29B_S01_P4	010-029B	2	15	pentlandite
0.06	37.08	bdl	63.19	0.10	bdl	bdl	0.04	100.47	10_29B_S10_P1	010-029B	2	15	pyrrhotite
32.70	33.57	bdl	33.61	bdl	bdl	0.68	0.12	100.68	10_29B_S10_P2	010-029B	2	15	pentlandite
bdl	36.83	bdl	63.21	0.03	bdl	bdl	0.06	100.13	10_29B_S10_P3	010-029B	2	15	pyrrhotite
22.39	37.52	bdl	40.01	0.16	bdl	0.66	bdl	100.74	10_29B_S10_P4	010-029B	2	15	pentlandite
0.41	37.77	bdl	62.00	0.05	bdl	bdl	bdl	100.24	10_29B_S11_P2	010-029B	2	15	pyrrhotite
0.03	37.05	bdl	63.18	0.12	bdl	bdl	bdl	100.37	10_29B_S11_P3	010-029B	2	15	pyrrhotite
28.73	33.90	bdl	37.86	bdl	bdl	0.45	bdl	100.93	10_29B_S11_P4	010-029B	2	15	pentlandite
30.62	32.87	bdl	34.88	0.05	bdl	0.62	0.08	99.12	10_29B_S11_P5	010-029B	2	15	pentlandite
32.23	33.61	bdl	34.20	0.06	bdl	0.72	0.02	100.84	10_29B_S11_P6	010-029B	2	15	pentlandite
bdl	36.97	bdl	62.96	0.16	bdl	bdl	0.11	100.20	10_29B_S12_P1	010-029B	2	15	pyrrhotite
0.04	36.84	bdl	63.26	0.13	bdl	bdl	bdl	100.27	10_29B_S12_P2	010-029B	2	15	pyrrhotite
bdl	37.00	0.11	63.44	0.11	bdl	bdl	bdl	100.66	10_29B_S12_P3	010-029B	2	15	pyrrhotite
32.75	34.11	bdl	33.00	0.03	bdl	0.62	bdl	100.51	10_29B_S12_P4	010-029B	2	15	pentlandite
0.08	36.90	bdl	62.52	0.15	bdl	bdl	bdl	99.66	10_29B_S12_P5	010-029B	2	15	pyrrhotite
0.02	36.87	bdl	63.47	0.04	bdl	bdl	0.06	100.46	10_29B_S12_P6	010-029B	2	15	pyrrhotite
0.03	37.11	0.13	63.30	0.03	bdl	bdl	bdl	100.60	10_29B_S13_P1	010-029B	2	15	pyrrhotite
33.17	33.71	bdl	33.10	bdl	bdl	0.81	bdl	100.79	10_29B_S13_P2	010-029B	2	15	pentlandite
bdl	37.06	0.11	63.32	0.08	bdl	bdl	0.03	100.58	10_29B_S13_P3	010-029B	2	15	pyrrhotite
32.71	33.70	bdl	33.31	bdl	bdl	0.90	bdl	100.61	10_29B_S13_P4	010-029B	2	15	pentlandite
26.21	35.32	bdl	37.74	0.06	bdl	0.86	0.09	100.28	10_29B_S13_P6	010-029B	2	15	pentlandite
bdl	36.88	bdl	62.86	0.12	bdl	bdl	0.04	99.90	10_29B_S13_P7	010-029B	2	15	pyrrhotite
bdl	37.16	bdl	62.76	bdl	bdl	bdl	0.03	99.95	10_29B_S14_P1	010-029B	2	15	pyrrhotite
bdl	37.06	bdl	62.84	0.08	bdl	bdl	0.06	100.04	10_29B_S14_P5	010-029B	2	15	pyrrhotite
0.04	36.86	bdl	63.35	0.08	bdl	bdl	0.07	100.40	10_29B_S2_P1	010-029B	2	15	pyrrhotite
32.53	33.72	bdl	33.97	bdl	bdl	0.66	0.03	100.90	10_29B_S2_P2	010-029B	2	15	pentlandite
28.26	34.25	bdl	36.58	0.05	bdl	0.90	0.08	100.12	10_29B_S2_P4	010-029B	2	15	pentlandite

Supplementary table 4.8.A: sulfide mineral chemistry

Ni wt%	S wt%	As wt%	Fe wt%	Cu wt%	Pb wt%	Co wt%	Zn wt%	Total wt%	measuement number	sample	group	kv	mineral
0.11	36.84	0.07	62.99	0.12	bdl	bdl	bdl	100.13	10_29B_S3_P1	010-029B	2	15	pyrrhotite
30.67	33.78	bdl	34.51	0.08	bdl	0.69	bdl	99.72	10_29B_S3_P3	010-029B	2	15	pentlandite
0.11	36.91	bdl	62.30	0.15	bdl	bdl	bdl	99.47	10_29B_S4_P1	010-029B	2	15	pyrrhotite
32.66	33.59	bdl	33.94	0.04	bdl	0.72	bdl	100.96	10_29B_S4_P2	010-029B	2	15	pentlandite
0.12	36.70	0.17	63.18	0.04	bdl	bdl	bdl	100.22	10_29B_S4_P4	010-029B	2	15	pyrrhotite
24.06	35.66	bdl	38.16	0.70	bdl	1.08	bdl	99.65	10_29B_S4_P6	010-029B	2	15	pentlandite
bdl	36.89	bdl	63.29	0.10	bdl	bdl	0.07	100.35	10_29B_S5_P1	010-029B	2	15	pyrrhotite
bdl	36.69	bdl	62.70	0.06	bdl	bdl	bdl	99.45	10_29B_S5_P2	010-029B	2	15	pyrrhotite
27.73	33.84	bdl	37.33	0.12	bdl	0.93	0.13	100.10	10_29B_S5_P3	010-029B	2	15	pentlandite
0.04	36.70	bdl	62.95	0.06	bdl	bdl	0.02	99.78	10_29B_S5_P5	010-029B	2	15	pyrrhotite
32.98	33.80	bdl	33.58	0.05	bdl	0.54	bdl	100.96	10_29B_S6_P1	010-029B	2	15	pentlandite
0.09	36.72	bdl	63.18	bdl	bdl	bdl	0.03	100.01	10_29B_S6_P2	010-029B	2	15	pyrrhotite
0.09	36.79	0.06	62.99	bdl	bdl	bdl	0.07	99.99	10_29B_S7_P1	010-029B	2	15	pyrrhotite
32.72	33.69	bdl	33.59	0.05	bdl	0.75	bdl	100.81	10_29B_S7_P2	010-029B	2	15	pentlandite
0.07	36.82	bdl	63.06	0.10	bdl	bdl	bdl	100.05	10_29B_S7_P3	010-029B	2	15	pyrrhotite
bdl	36.73	bdl	63.07	bdl	bdl	bdl	bdl	99.80	10_29B_S7_P4	010-029B	2	15	pyrrhotite
0.11	36.43	0.06	63.23	0.07	bdl	bdl	0.07	99.97	10_29B_S8_P1	010-029B	2	15	pyrrhotite
bdl	36.36	bdl	63.07	0.13	bdl	bdl	bdl	99.56	10_29B_S8_P2	010-029B	2	15	pyrrhotite
0.09	36.56	bdl	63.53	0.12	bdl	bdl	bdl	100.30	10_29B_S8_P3	010-029B	2	15	pyrrhotite
33.08	33.64	bdl	33.29	0.06	bdl	0.83	0.03	100.93	10_29B_S9_P1	010-029B	2	15	pentlandite
16.03	42.25	bdl	40.14	1.16	bdl	1.12	bdl	100.70	10_29B_S9_P2	010-029B	2	15	pentlandite
71.34	26.30	bdl	1.88	bdl	bdl	bdl	bdl	99.52	010-030-S10-P2	010-030	2	15	heazlewoodite
32.79	32.89	bdl	32.59	bdl	bdl	0.71	0.03	99.00	010-030-S10-P4	010-030	2	15	pentlandite
68.02	27.53	0.07	5.24	bdl	bdl	0.09	bdl	100.96	010-030-S10-P5	010-030	2	15	heazlewoodite
33.27	33.15	bdl	32.72	bdl	bdl	0.68	0.03	99.86	010-030-S10-P6	010-030	2	15	pentlandite
70.97	26.36	bdl	2.63	bdl	bdl	bdl	0.05	100.01	010-030-S10-P7	010-030	2	15	heazlewoodite
33.39	33.01	bdl	32.40	bdl	bdl	0.73	bdl	99.53	010-030-S1-P1	010-030	2	15	pentlandite
70.57	27.01	bdl	2.62	bdl	bdl	bdl	bdl	100.19	010-030-S1-P2	010-030	2	15	heazlewoodite
32.92	32.98	0.10	32.63	bdl	bdl	0.71	bdl	99.35	010-030-S1-P4	010-030	2	15	pentlandite

Supplementary table 4.8.A: sulfide mineral chemistry

Ni wt%	S wt%	As wt%	Fe wt%	Cu wt%	Pb wt%	Co wt%	Zn wt%	Total wt%	measuement number	sample	group	kv	mineral
70.27	26.35	bdl	2.98	bdl	bdl	bdl	bdl	99.60	010-030-S1-P5	010-030	2	15	heazlewoodite
34.72	32.82	bdl	31.18	bdl	bdl	0.59	0.06	99.36	010-030-S3-P1	010-030	2	15	pentlandite
34.59	32.80	bdl	31.19	bdl	bdl	0.60	0.03	99.19	010-030-S3-P2	010-030	2	15	pentlandite
71.58	26.35	bdl	1.89	bdl	bdl	bdl	bdl	99.82	010-030-S3-P3	010-030	2	15	heazlewoodite
71.19	26.72	bdl	2.37	bdl	bdl	0.04	bdl	100.32	010-030-S3-P4	010-030	2	15	heazlewoodite
34.92	32.62	bdl	31.09	bdl	bdl	0.60	bdl	99.24	010-030-S3-P5	010-030	2	15	pentlandite
33.95	32.93	bdl	31.65	bdl	bdl	0.67	bdl	99.20	010-030-S4-P1	010-030	2	15	pentlandite
34.24	33.14	bdl	31.60	bdl	bdl	0.68	0.04	99.69	010-030-S4-P2	010-030	2	15	pentlandite
33.51	32.81	bdl	32.09	bdl	bdl	0.63	bdl	99.04	010-030-S6-P1	010-030	2	15	pentlandite
33.61	32.86	bdl	32.10	bdl	bdl	0.63	bdl	99.19	010-030-S6-P2	010-030	2	15	pentlandite
33.68	32.75	bdl	31.96	bdl	bdl	0.63	bdl	99.02	010-030-S6-P3	010-030	2	15	pentlandite
70.46	26.58	bdl	2.49	bdl	bdl	bdl	bdl	99.53	010-030-S9-P2	010-030	2	15	heazlewoodite
35.14	32.41	0.07	31.18	bdl	bdl	0.73	bdl	99.52	010-030-thick-1-sul-7	010-030	2	20	pentlandite
35.02	32.35	0.05	31.06	bdl	bdl	0.72	bdl	99.19	010-030-thick-1-sul-8	010-030	2	20	pentlandite
34.73	32.23	bdl	31.99	bdl	bdl	0.78	bdl	99.73	010-030-thick-2-sul-1	010-030	2	20	pentlandite
34.64	32.30	bdl	31.93	bdl	bdl	0.76	bdl	99.62	010-030-thick-2-sul-11	010-030	2	20	pentlandite
34.55	31.94	bdl	31.97	bdl	bdl	0.74	bdl	99.21	010-030-thick-2-sul-2	010-030	2	20	pentlandite
34.68	32.13	bdl	32.02	0.13	bdl	0.76	bdl	99.71	010-030-thick-2-sul-3	010-030	2	20	pentlandite
34.83	32.15	bdl	31.47	bdl	bdl	0.76	bdl	99.21	010-030-thick-2-sul-5	010-030	2	20	pentlandite
34.72	32.00	bdl	31.65	bdl	bdl	0.72	bdl	99.09	010-030-thick-2-sul-7	010-030	2	20	pentlandite
34.70	32.41	bdl	31.77	bdl	bdl	0.77	bdl	99.64	010-030-thick-2-sul-9	010-030	2	20	pentlandite
34.50	32.38	bdl	31.64	bdl	bdl	0.80	bdl	99.31	010-030-thick-4-sul-1	010-030	2	20	pentlandite
34.53	32.71	bdl	31.49	bdl	bdl	0.75	bdl	99.49	010-030-thick-4-sul-2	010-030	2	20	pentlandite
34.60	32.54	bdl	31.13	bdl	bdl	0.75	bdl	99.02	010-030-thick-4-sul-3	010-030	2	20	pentlandite
34.68	32.49	bdl	31.35	bdl	bdl	0.76	bdl	99.29	010-030-thick-4-sul-4	010-030	2	20	pentlandite
72.06	26.42	bdl	1.66	bdl	bdl	bdl	bdl	100.14	010-030-thick-4-sul-5	010-030	2	20	heazlewoodite
72.71	26.10	bdl	1.76	bdl	bdl	bdl	bdl	100.58	010-030-thick-4-sul-6	010-030	2	20	heazlewoodite
38.09	33.44	bdl	27.13	0.03	bdl	0.47	bdl	99.16	10_30_S1	010-030	2	15	pentlandite
34.97	33.30	bdl	30.21	0.06	bdl	0.54	bdl	99.09	10_30_S12	010-030	2	15	pentlandite

Supplementary table 4.8.A: sulfide mineral chemistry

Ni wt%	S wt%	As wt%	Fe wt%	Cu wt%	Pb wt%	Co wt%	Zn wt%	Total wt%	measuement number	sample	group	kv	mineral
34.64	33.64	bdl	30.12	0.07	bdl	0.56	0.03	99.05	10_30_S15	010-030	2	15	pentlandite
69.99	28.14	bdl	2.12	bdl	bdl	bdl	0.10	100.35	10_30_S2	010-030	2	15	heazlewoodite
35.09	33.49	bdl	30.39	bdl	bdl	0.60	bdl	99.58	10_30_S3	010-030	2	15	pentlandite
34.25	34.05	bdl	30.70	0.07	bdl	0.62	bdl	99.68	10_30_S4	010-030	2	15	pentlandite
34.68	33.45	bdl	30.22	0.07	bdl	0.62	bdl	99.03	10_30_S5	010-030	2	15	pentlandite
34.41	33.41	bdl	30.90	0.05	bdl	0.57	bdl	99.34	10_30_S6	010-030	2	15	pentlandite
35.12	33.44	bdl	30.37	0.09	bdl	0.54	0.05	99.60	10_30_S7_P1	010-030	2	15	pentlandite
34.85	33.41	bdl	30.60	0.10	bdl	0.54	bdl	99.49	10_30_S7_P2	010-030	2	15	pentlandite
34.05	33.90	bdl	30.24	0.13	bdl	0.59	0.12	99.04	10_30_S7_P3	010-030	2	15	pentlandite
34.51	33.93	bdl	29.89	0.12	bdl	0.63	bdl	99.08	10_30_S8	010-030	2	15	pentlandite
0.04	35.09	bdl	30.13	34.93	bdl	bdl	bdl	100.18	Chalcopyrite	standard	std	15	chalcopyrite
0.03	35.58	bdl	30.21	34.38	bdl	bdl	bdl	100.20	Chalcopyrite	standard	std	15	chalcopyrite
bdl	35.67	bdl	30.10	34.44	bdl	bdl	0.08	100.29	Chalcopyrite	standard	std	15	chalcopyrite
bdl	35.33	bdl	30.20	35.09	bdl	bdl	0.03	100.65	Chalcopyrite_3	standard	std	15	chalcopyrite
bdl	34.35	bdl	31.20	34.24	bdl	bdl	bdl	99.78	CHALCOPYRITE-STD-P1	standard	std	15	chalcopyrite
bdl	34.10	bdl	31.05	34.06	bdl	bdl	bdl	99.20	CHALCOPYRITE-STD-P2	standard	std	15	chalcopyrite
bdl	34.30	bdl	31.10	34.33	bdl	bdl	bdl	99.73	CHALCOPYRITE-STD-P3	standard	std	15	chalcopyrite

bdl = below detection limit

Supplementary table 4.8.B: S isotope results

Sample ID	group	phase	δ^{34}S V-CDT (‰)	±(2σ)	δ^{33}S V-CDT (‰)	±(2σ)	Δ^{33}S (‰)	±(2σ)
010-020C-iii-po-53	1	pyrrhotite	0.76	0.23	0.57	0.22	0.18	0.21
010-020C-iii-po-55	1	pyrrhotite	0.52	0.22	0.43	0.23	0.16	0.23
010-020C-iii-po-61	1	pyrrhotite	0.40	0.22	0.32	0.22	0.11	0.22
010-020C-iii-po-83	1	pyrrhotite	0.48	0.22	0.41	0.22	0.17	0.22
010-020C-iii-po-88	1	pyrrhotite	0.72	0.23	0.66	0.25	0.29	0.25
010-020C-iii-pt-52	1	pentlandite	0.14	0.23	0.47	0.24	0.40	0.24
010-020C-iii-pt-54	1	pentlandite	0.53	0.23	0.36	0.26	0.08	0.26
010-020C-iii-pt-56	1	pentlandite	0.25	0.24	0.07	0.24	-0.06	0.24
010-020C-iii-pt-57	1	pentlandite	1.17	0.23	0.92	0.31	0.32	0.31
010-020C-iii-pt-58	1	pentlandite	-0.22	0.24	0.03	0.28	0.15	0.28
010-020C-iii-pt-59	1	pentlandite	0.12	0.24	0.17	0.26	0.10	0.25
010-020C-iii-pt-60	1	pentlandite	-0.05	0.23	0.05	0.25	0.08	0.25
010-020C-iii-pt-62	1	pentlandite	0.33	0.23	0.38	0.23	0.21	0.22
010-020C-iii-pt-63	1	pentlandite	-0.41	0.97	-0.47	1.28	-0.26	1.37
010-020C-iii-pt-63a	1	pentlandite	0.46	0.23	0.10	0.23	-0.14	0.23
010-020C-iii-pt-63b	1	pentlandite	0.12	0.24	0.39	0.33	0.33	0.33
010-020C-iii-pt-64	1	pentlandite	0.39	0.24	0.40	0.25	0.20	0.25
010-020C-iii-pt-65	1	pentlandite	1.16	0.23	0.85	0.27	0.25	0.27
010-020C-iii-pt-66	1	pentlandite	0.51	0.23	0.25	0.21	-0.01	0.21
010-020C-iii-pt-67	1	pentlandite	0.36	0.24	0.56	0.21	0.37	0.21
010-020C-iii-pt-68	1	pentlandite	0.53	0.23	0.62	0.21	0.34	0.21
010-020C-iii-pt-69	1	pentlandite	0.30	0.24	0.49	0.23	0.34	0.23
010-020C-iii-pt-70	1	pentlandite	0.67	0.23	0.53	0.23	0.19	0.23
010-020C-iii-pt-71	1	pentlandite	1.13	0.23	0.82	0.28	0.24	0.28
010-020C-iii-pt-72	1	pentlandite	0.08	0.24	0.36	0.24	0.32	0.24
010-020C-iii-pt-73	1	pentlandite	0.50	0.24	0.30	0.34	0.05	0.34
010-020C-iii-pt-74	1	pentlandite	-0.72	0.25	-0.27	0.23	0.10	0.23
010-020C-iii-pt-75	1	pentlandite	0.20	0.23	0.45	0.30	0.34	0.30

Supplementary table 4.8.B: S isotope results

Sample ID	group	phase	δ^{34}S V-CDT (‰)	$\pm(2\sigma)$	δ^{33}S V-CDT (‰)	$\pm(2\sigma)$	Δ^{33}S (‰)	$\pm(2\sigma)$
010-020C-iii-pt-76	1	pentlandite	-0.57	0.25	-0.12	0.24	0.17	0.24
010-020C-iii-pt-77	1	pentlandite	0.60	0.24	0.74	0.24	0.43	0.24
010-020C-iii-pt-78	1	pentlandite	0.63	0.23	0.57	0.30	0.24	0.29
010-020C-iii-pt-79	1	pentlandite	0.20	0.24	0.27	0.24	0.17	0.25
010-020C-iii-pt-80	1	pentlandite	0.60	0.24	0.73	0.28	0.43	0.28
010-020C-iii-pt-81	1	pentlandite	0.63	0.23	0.60	0.21	0.28	0.21
010-020C-iii-pt-82	1	pentlandite	1.26	0.23	0.71	0.22	0.06	0.22
010-020C-iii-pt-84	1	pentlandite	-0.05	0.27	0.20	0.24	0.23	0.25
010-020C-iii-pt-85	1	pentlandite	0.63	0.23	0.46	0.25	0.14	0.24
010-020C-iii-pt-86	1	pentlandite	0.33	0.25	0.26	0.25	0.09	0.26
010-020C-iii-pt-87	1	pentlandite	1.12	0.23	0.80	0.23	0.22	0.23
010-020C-iii-pt-89	1	pentlandite	0.16	0.23	0.34	0.23	0.26	0.23
010-020C-iii-pt-90	1	pentlandite	-0.24	0.24	0.03	0.25	0.15	0.25
010-020C-iii-pt-91	1	pentlandite	0.16	0.23	0.37	0.25	0.29	0.24
010-020C-iii-pt-92	1	pentlandite	0.66	0.23	0.37	0.27	0.02	0.27
010-020C-iii-pt-93	1	pentlandite	0.26	0.24	0.25	0.23	0.12	0.23
010-020C-iii-pt-94	1	pentlandite	-0.44	0.23	-0.06	0.22	0.17	0.21
010-020C-iii-pt-95	1	pentlandite	0.36	0.23	0.49	0.26	0.31	0.26
010-020C-iii-pt-96	1	pentlandite	0.63	0.23	0.51	0.23	0.18	0.22
010-020C-iii-pt-97	1	pentlandite	0.50	0.24	0.29	0.25	0.03	0.25
010-020C-ii-po-127	1	pyrrhotite	0.63	0.23	0.48	0.28	0.15	0.27
010-020C-ii-po-130	1	pyrrhotite	0.49	0.23	0.32	0.22	0.07	0.21
010-020C-ii-pt-100	1	pentlandite	0.07	0.24	0.18	0.24	0.14	0.24
010-020C-ii-pt-101	1	pentlandite	0.41	0.23	0.52	0.22	0.31	0.22
010-020C-ii-pt-102	1	pentlandite	0.28	0.24	0.27	0.23	0.13	0.23
010-020C-ii-pt-103	1	pentlandite	1.35	0.24	0.91	0.29	0.22	0.29
010-020C-ii-pt-104	1	pentlandite	-0.13	1.14	-0.36	1.43	-0.29	1.55
010-020C-ii-pt-105	1	pentlandite	0.27	0.23	0.61	0.24	0.47	0.24

Supplementary table 4.8.B: S isotope results

Sample ID	group	phase	δ^{34}S V-CDT (‰)	±(2σ)	δ^{33}S V-CDT (‰)	±(2σ)	Δ^{33}S (‰)	±(2σ)
010-020C-ii-pt-106	1	pentlandite	0.60	0.23	0.52	0.23	0.21	0.22
010-020C-ii-pt-107	1	pentlandite	0.09	0.24	0.16	0.28	0.12	0.28
010-020C-ii-pt-108	1	pentlandite	0.57	0.23	0.45	0.22	0.16	0.22
010-020C-ii-pt-109	1	pentlandite	0.59	0.24	0.55	0.27	0.25	0.27
010-020C-ii-pt-110	1	pentlandite	1.09	0.24	0.70	0.27	0.14	0.27
010-020C-ii-pt-111	1	pentlandite	-1.23	0.26	-0.42	0.24	0.21	0.25
010-020C-ii-pt-112	1	pentlandite	0.31	0.23	0.29	0.23	0.13	0.23
010-020C-ii-pt-113	1	pentlandite	0.06	0.24	0.07	0.22	0.03	0.22
010-020C-ii-pt-114	1	pentlandite	0.34	0.25	0.32	0.24	0.14	0.24
010-020C-ii-pt-115	1	pentlandite	0.39	0.23	0.50	0.22	0.30	0.21
010-020C-ii-pt-116	1	pentlandite	0.57	0.23	0.37	0.29	0.08	0.29
010-020C-ii-pt-117	1	pentlandite	0.35	0.23	0.32	0.21	0.14	0.21
010-020C-ii-pt-118	1	pentlandite	0.91	0.24	0.63	0.27	0.17	0.27
010-020C-ii-pt-119	1	pentlandite	0.23	0.23	0.13	0.25	0.01	0.25
010-020C-ii-pt-120	1	pentlandite	0.26	0.24	0.20	0.29	0.07	0.29
010-020C-ii-pt-121	1	pentlandite	1.03	0.24	0.68	0.26	0.15	0.26
010-020C-ii-pt-122	1	pentlandite	0.26	0.23	0.45	0.28	0.32	0.28
010-020C-ii-pt-123	1	pentlandite	0.24	0.25	0.57	0.27	0.44	0.27
010-020C-ii-pt-124	1	pentlandite	0.87	0.24	0.90	0.22	0.45	0.23
010-020C-ii-pt-125	1	pentlandite	1.25	0.23	0.72	0.23	0.08	0.23
010-020C-ii-pt-126	1	pentlandite	0.00	0.24	0.20	0.28	0.20	0.28
010-020C-ii-pt-128	1	pentlandite	0.79	0.24	0.41	0.23	0.00	0.23
010-020C-ii-pt-129	1	pentlandite	0.43	0.23	0.58	0.30	0.36	0.30
010-020C-ii-pt-131	1	pentlandite	0.82	0.24	0.42	0.24	0.00	0.24
010-020C-ii-pt-132	1	pentlandite	0.29	0.23	0.58	0.31	0.43	0.30
010-020C-ii-pt-133	1	pentlandite	0.71	0.23	0.31	0.28	-0.05	0.28
010-020C-ii-pt-134	1	pentlandite	1.16	0.23	0.79	0.26	0.19	0.25
010-020C-ii-pt-135	1	pentlandite	0.27	0.23	0.55	0.23	0.42	0.23

Supplementary table 4.8.B: S isotope results

Sample ID	group	phase	δ^{34}S V-CDT (‰)	±(2σ)	δ^{33}S V-CDT (‰)	±(2σ)	Δ^{33}S (‰)	±(2σ)
010-020C-ii-pt-98	1	pentlandite	0.16	0.24	0.36	0.30	0.28	0.30
010-020C-ii-pt-99	1	pentlandite	0.29	0.24	0.32	0.26	0.17	0.26
010-020C-iv-pt-22	1	pentlandite	-0.22	0.28	0.01	0.28	0.13	0.29
010-020C-iv-pt-23	1	pentlandite	0.33	0.31	0.09	0.31	-0.08	0.33
010-020C-iv-pt-24	1	pentlandite	0.03	0.25	0.13	0.22	0.11	0.23
010-020C-iv-pt-25	1	pentlandite	0.17	0.25	0.30	0.24	0.21	0.25
010-020C-iv-pt-26	1	pentlandite	0.14	0.23	0.32	0.22	0.25	0.22
010-020C-iv-pt-27	1	pentlandite	0.27	0.24	0.31	0.25	0.18	0.25
010-020C-iv-pt-28	1	pentlandite	-0.62	0.30	-0.28	0.25	0.04	0.27
010-020C-iv-pt-29	1	pentlandite	-0.29	0.24	-0.03	0.21	0.12	0.21
010-020C-iv-pt-30	1	pentlandite	1.16	0.24	0.58	0.27	-0.02	0.27
010-020C-iv-pt-31	1	pentlandite	0.66	0.23	0.63	0.28	0.29	0.28
010-020C-iv-pt-32	1	pentlandite	0.38	0.25	0.57	0.22	0.38	0.22
010-020C-iv-pt-33	1	pentlandite	0.32	0.25	0.18	0.24	0.02	0.24
010-020C-iv-pt-34	1	pentlandite	0.41	0.26	0.36	0.29	0.15	0.30
010-020C-iv-pt-35	1	pentlandite	0.36	0.23	0.53	0.24	0.34	0.24
010-020C-iv-pt-36	1	pentlandite	0.40	0.25	0.25	0.23	0.05	0.23
010-020C-iv-pt-37	1	pentlandite	-0.19	0.26	0.26	0.26	0.36	0.27
010-020C-iv-pt-38	1	pentlandite	0.16	0.24	0.33	0.23	0.25	0.23
010-020C-iv-pt-39	1	pentlandite	0.24	0.26	0.27	0.25	0.14	0.25
010-020C-iv-pt-40	1	pentlandite	0.34	0.25	0.30	0.28	0.13	0.29
010-020C-iv-pt-41	1	pentlandite	0.35	0.24	0.38	0.23	0.20	0.23
010-020C-iv-pt-42	1	pentlandite	0.25	0.23	0.23	0.26	0.10	0.25
010-020C-iv-pt-43	1	pentlandite	0.69	0.25	0.64	0.25	0.28	0.26
010-020C-iv-pt-44	1	pentlandite	1.05	0.24	0.72	0.21	0.18	0.21
010-020C-iv-pt-45	1	pentlandite	0.45	0.23	0.40	0.25	0.17	0.24
010-020C-iv-pt-46	1	pentlandite	-0.48	0.24	-0.07	0.27	0.18	0.27
010-020C-iv-pt-47	1	pentlandite	0.49	0.24	0.51	0.23	0.26	0.24

Supplementary table 4.8.B: S isotope results

Sample ID	group	phase	δ^{34}S V-CDT (‰)	±(2σ)	δ^{33}S V-CDT (‰)	±(2σ)	Δ^{33}S (‰)	±(2σ)
010-020C-iv-pt-48	1	pentlandite	0.45	0.23	0.45	0.22	0.22	0.22
010-020C-iv-pt-49	1	pentlandite	0.21	0.23	0.26	0.21	0.15	0.21
010-020C-iv-pt-50	1	pentlandite	-0.44	0.28	-0.09	0.25	0.13	0.26
010-020C-iv-pt-51	1	pentlandite	0.17	0.25	0.39	0.21	0.30	0.22
010-020C-thick-2-po-1	1	pyrrhotite	0.36	0.24	0.52	0.32	0.33	0.26
010-020C-thick-2-pt-2	1	pentlandite	0.48	0.23	0.73	0.28	0.48	0.21
010-020C-thick-2-pt-3	1	pentlandite	0.26	0.24	0.69	0.28	0.56	0.21
010-020C-thick-2-pt-4	1	pentlandite	0.43	0.23	0.77	0.39	0.55	0.34
010-020C-thick-3-pt-5	1	pentlandite	0.55	0.25	0.41	0.28	0.12	0.22
010-020C-thick-3-pt-6	1	pentlandite	0.59	0.24	0.75	0.28	0.45	0.21
010-020C-thick-3-pt-7	1	pentlandite	0.37	0.24	0.36	0.34	0.17	0.29
010-020C-thick-4-po-11	1	pyrrhotite	0.40	0.23	0.15	0.24	-0.06	0.18
010-020C-thick-4-po-13	1	pyrrhotite	0.34	0.24	0.72	0.30	0.54	0.24
010-020C-thick-4-po-8	1	pyrrhotite	0.64	0.24	0.77	0.39	0.44	0.35
010-020C-thick-4-pt-10	1	pentlandite	0.51	0.24	0.46	0.29	0.19	0.22
010-020C-thick-4-pt-12	1	pentlandite	0.22	0.24	0.37	0.23	0.26	0.18
010-020C-thick-4-pt-14	1	pentlandite	0.33	0.23	0.40	0.35	0.22	0.30
010-020C-thick-4-pt-9	1	pentlandite	0.38	0.23	0.41	0.35	0.22	0.30
010-020C-thick-5-pt-15	1	pentlandite	0.24	0.24	0.93	0.29	0.80	0.23
010-020C-thick-pt-16	1	pentlandite	0.35	0.24	0.37	0.35	0.19	0.30
010-020C-thick-pt-17	1	pentlandite	0.35	0.23	0.50	0.31	0.32	0.25
010-022-thick-1-pt-6	1	pentlandite	0.73	0.23	0.50	0.37	0.13	0.37
010-022-thick-1-pt-7	1	pentlandite	1.05	0.23	0.69	0.36	0.15	0.36
010-022-thick-1-pt-8	1	pentlandite	0.87	0.23	0.87	0.31	0.43	0.31
010-022-thick-2-pt-10	1	pentlandite	0.74	0.25	0.77	0.36	0.39	0.37
010-022-thick-2-pt-11	1	pentlandite	-0.11	0.23	0.58	0.42	0.63	0.42
010-022-thick-2-pt-12	1	pentlandite	0.44	0.24	0.64	0.37	0.42	0.37
010-022-thick-2-pt-9	1	pentlandite	0.44	0.24	0.52	0.30	0.29	0.30

Supplementary table 4.8.B: S isotope results

Sample ID	group	phase	δ^{34}S V-CDT (‰)	±(2σ)	δ^{33}S V-CDT (‰)	±(2σ)	Δ^{33}S (‰)	±(2σ)
010-022-thick-3-pt-4	1	pentlandite	0.42	0.23	1.21	0.38	1.00	0.38
010-022-thick-5-pt-1	1	pentlandite	0.97	0.24	0.72	0.30	0.22	0.30
010-022-thick-6-pt-13	1	pentlandite	0.73	0.25	0.16	0.29	-0.21	0.29
010-022-thick-6-pt-14	1	pentlandite	0.74	0.24	0.23	0.28	-0.15	0.28
010-022-thick-7-pt-15	1	pentlandite	0.97	0.23	1.14	0.40	0.64	0.39
010-022-thick-7-pt-16	1	pentlandite	0.75	0.24	0.93	0.39	0.54	0.39
010-022-thick-7-pt-17	1	pentlandite	0.75	0.23	0.99	0.37	0.61	0.37
010-022-thick-7-pt-18	1	pentlandite	0.70	0.24	0.69	0.39	0.34	0.39
010-022-thick-7-pt-19	1	pentlandite	0.36	0.24	0.65	0.39	0.47	0.39
010-022-thick-7-pt-20	1	pentlandite	0.62	0.24	0.79	0.38	0.48	0.38
010-022-thick-7-pt-21	1	pentlandite	0.96	0.23	0.95	0.39	0.46	0.39
010-022-v-pt-1	1	pentlandite	-0.76	0.33	-0.08	0.23	0.31	0.26
010-022-v-pt-10	1	pentlandite	1.29	0.24	0.85	0.25	0.19	0.25
010-022-v-pt-11	1	pentlandite	1.27	0.26	0.72	0.22	0.06	0.23
010-022-v-pt-12	1	pentlandite	0.14	0.23	0.13	0.25	0.06	0.25
010-022-v-pt-13	1	pentlandite	1.22	0.24	0.69	0.20	0.06	0.21
010-022-v-pt-14	1	pentlandite	0.69	0.24	0.47	0.24	0.12	0.25
010-022-v-pt-15	1	pentlandite	1.23	0.25	0.75	0.23	0.12	0.24
010-022-v-pt-16	1	pentlandite	0.45	0.27	0.34	0.27	0.11	0.27
010-022-v-pt-17	1	pentlandite	0.87	0.24	0.75	0.26	0.31	0.26
010-022-v-pt-18	1	pentlandite	0.44	0.24	0.47	0.23	0.24	0.23
010-022-v-pt-19	1	pentlandite	0.38	0.24	0.63	0.23	0.43	0.23
010-022-v-pt-2	1	pentlandite	0.46	0.27	0.43	0.25	0.19	0.26
010-022-v-pt-20	1	pentlandite	0.81	0.25	0.80	0.20	0.38	0.21
010-022-v-pt-3	1	pentlandite	-0.74	0.33	-0.24	0.22	0.14	0.25
010-022-v-pt-4	1	pentlandite	0.82	0.28	0.50	0.21	0.07	0.23
010-022-v-pt-5	1	pentlandite	-0.31	0.29	-0.05	0.28	0.11	0.30
010-022-v-pt-6	1	pentlandite	-0.03	0.24	0.11	0.23	0.12	0.23

Supplementary table 4.8.B: S isotope results

Sample ID	group	phase	δ^{34}S V-CDT (‰)	±(2σ)	δ^{33}S V-CDT (‰)	±(2σ)	Δ^{33}S (‰)	±(2σ)
010-022-v-pt-7	1	pentlandite	0.09	0.23	0.19	0.26	0.14	0.25
010-022-v-pt-8	1	pentlandite	-0.03	0.29	0.07	0.21	0.08	0.23
010-022-v-pt-9	1	pentlandite	0.56	0.27	0.21	0.22	-0.07	0.23
010-023-thick-1A-pt-2	1	pentlandite	2.61	0.21	1.42	0.34	0.07	0.28
010-023-thick-1A-pt-3	1	pentlandite	2.01	0.21	1.22	0.31	0.17	0.24
010-023-thick-2A-pt-1	1	pentlandite	1.48	0.23	0.94	0.35	0.17	0.29
010-023-thick-3A-pt-6	1	pentlandite	1.36	0.24	0.89	0.25	0.18	0.20
010-023-thick-4-pt-4	1	pentlandite	2.25	0.22	1.05	0.41	-0.12	0.36
010-023-thick-4-pt-5	1	pentlandite	1.94	0.21	0.94	0.36	-0.06	0.31
010-023-thick-7-pt-7	1	pentlandite	1.79	0.21	1.25	0.32	0.32	0.25
010-023-thick-7-pt-8	1	pentlandite	2.73	0.22	1.30	0.28	-0.11	0.20
010-023-thick-8-pt-10	1	pentlandite	1.87	0.22	0.79	0.33	-0.18	0.26
010-023-thick-8-pt-11	1	pentlandite	2.21	0.21	1.48	0.37	0.34	0.31
010-023-thick-8-pt-9	1	pentlandite	2.13	0.23	1.23	0.37	0.13	0.32
010-023-thick-9-pt-12	1	pentlandite	2.12	0.23	1.67	0.37	0.57	0.31
010-023-thick-9-pt-13	1	pentlandite	3.68	0.21	2.47	0.31	0.57	0.24
010-023-thick-9-pt-14	1	pentlandite	2.73	0.22	1.44	0.40	0.02	0.34
010-029B-250-180-po-44	2	pyrrhotite	3.19	0.15	1.51	0.19	-0.12	0.16
010-029B-250-180-po-46	2	pyrrhotite	3.38	0.13	1.92	0.22	0.19	0.17
010-029B-250-180-po-47	2	pyrrhotite	3.33	0.11	1.83	0.17	0.13	0.16
010-029B-250-180-po-52	2	pyrrhotite	3.28	0.23	1.71	0.32	0.02	0.32
010-029B-250-180-po-54	2	pyrrhotite	3.45	0.23	1.82	0.35	0.05	0.35
010-029B-250-180-po-56	2	pyrrhotite	3.50	0.23	2.08	0.30	0.28	0.30
010-029B-250-180-po-58	2	pyrrhotite	3.54	0.23	2.16	0.31	0.34	0.31
010-029B-250-180-po-59	2	pyrrhotite	3.05	0.23	2.10	0.34	0.53	0.34
010-029B-250-180-po-65	2	pyrrhotite	3.88	0.23	2.23	0.24	0.24	0.23
010-029B-250-180-po-67	2	pyrrhotite	3.79	0.24	2.49	0.24	0.55	0.23
010-029B-250-180-po-76	2	pyrrhotite	3.66	0.24	2.17	0.53	0.29	0.53

Supplementary table 4.8.B: S isotope results

Sample ID	group	phase	δ^{34}S V-CDT (‰)	±(2σ)	δ^{33}S V-CDT (‰)	±(2σ)	Δ^{33}S (‰)	±(2σ)
010-029B-250-180-pt-41	2	pentlandite	4.46	0.11	2.31	0.21	0.03	0.17
010-029B-250-180-pt-42	2	pentlandite	2.93	0.22	1.43	0.22	-0.06	0.20
010-029B-250-180-pt-43	2	pentlandite	3.83	0.18	2.12	0.25	0.16	0.22
010-029B-250-180-pt-48	2	pentlandite	4.22	0.12	2.37	0.26	0.21	0.23
010-029B-250-180-pt-49	2	pentlandite	3.16	0.19	1.62	0.21	0.01	0.19
010-029B-250-180-pt-50	2	pentlandite	3.16	0.28	1.81	0.38	0.18	0.39
010-029B-250-180-pt-51	2	pentlandite	4.34	0.23	2.38	0.31	0.15	0.31
010-029B-250-180-pt-53	2	pentlandite	2.91	0.25	1.63	0.27	0.14	0.27
010-029B-250-180-pt-55	2	pentlandite	4.13	0.23	2.44	0.39	0.32	0.38
010-029B-250-180-pt-57	2	pentlandite	4.25	0.24	2.78	0.39	0.60	0.39
010-029B-250-180-pt-60	2	pentlandite	4.72	0.23	2.35	0.37	-0.07	0.37
010-029B-250-180-pt-61	2	pentlandite	4.56	0.23	2.58	0.31	0.23	0.31
010-029B-250-180-pt-63	2	pentlandite	4.07	0.24	2.63	0.32	0.53	0.32
010-029B-250-180-pt-64	2	pentlandite	3.80	0.23	1.92	0.29	-0.03	0.29
010-029B-250-180-pt-66	2	pentlandite	3.59	0.24	1.84	0.43	-0.01	0.43
010-029B-250-180-pt-68	2	pentlandite	3.68	0.24	2.48	0.41	0.59	0.41
010-029B-250-180-pt-69	2	pentlandite	4.22	0.25	2.17	0.48	0.00	0.48
010-029B-250-180-pt-70	2	pentlandite	4.35	0.23	2.66	0.51	0.43	0.51
010-029B-250-180-pt-71	2	pentlandite	4.12	0.24	2.07	0.33	-0.04	0.33
010-029B-250-180-pt-72	2	pentlandite	3.42	0.25	2.35	0.42	0.60	0.42
010-029B-250-180-pt-73	2	pentlandite	3.94	0.24	2.42	0.27	0.40	0.27
010-029B-250-180-pt-74	2	pentlandite	3.08	0.23	1.67	0.30	0.09	0.30
010-029B-250-180-pt-75	2	pentlandite	4.01	0.24	2.17	0.32	0.11	0.32
010-029B-ii-iii-po-1	2	pyrrhotite	3.33	0.11	1.74	0.17	0.04	0.16
010-029B-ii-iii-po-19	2	pyrrhotite	1.36	0.20	0.71	0.20	0.01	0.18
010-029B-ii-iii-po-21	2	pyrrhotite	3.35	0.11	1.83	0.17	0.12	0.16
010-029B-ii-iii-po-23	2	pyrrhotite	3.51	0.11	1.85	0.20	0.06	0.16
010-029B-ii-iii-po-27	2	pyrrhotite	3.40	0.11	1.97	0.19	0.23	0.16

Supplementary table 4.8.B: S isotope results

Sample ID	group	phase	δ^{34}S V-CDT (‰)	±(2σ)	δ^{33}S V-CDT (‰)	±(2σ)	Δ^{33}S (‰)	±(2σ)
010-029B-ii-iii-po-3	2	pyrrhotite	3.26	0.11	1.65	0.19	-0.02	0.16
010-029B-ii-iii-po-30	2	pyrrhotite	3.47	0.11	1.73	0.20	-0.04	0.16
010-029B-ii-iii-po-33	2	pyrrhotite	3.44	0.12	1.74	0.17	-0.02	0.16
010-029B-ii-iii-po-39	2	pyrrhotite	3.34	0.11	1.67	0.22	-0.04	0.17
010-029B-ii-iii-po-7	2	pyrrhotite	3.36	0.12	1.87	0.18	0.16	0.16
010-029B-ii-iii-po-9	2	pyrrhotite	3.32	0.10	1.76	0.20	0.06	0.16
010-029B-ii-iii-pt-10	2	pentlandite	2.79	0.20	1.42	0.24	0.00	0.22
010-029B-ii-iii-pt-11	2	pentlandite	1.22	0.34	0.50	0.20	-0.12	0.22
010-029B-ii-iii-pt-12	2	pentlandite	2.43	0.27	1.24	0.18	0.00	0.17
010-029B-ii-iii-pt-13	2	pentlandite	4.43	0.14	2.32	0.20	0.06	0.16
010-029B-ii-iii-pt-14	2	pentlandite	3.08	0.15	1.54	0.25	-0.04	0.22
010-029B-ii-iii-pt-15	2	pentlandite	2.87	0.14	1.41	0.19	-0.06	0.16
010-029B-ii-iii-pt-16	2	pentlandite	4.44	0.14	2.42	0.23	0.15	0.20
010-029B-ii-iii-pt-17	2	pentlandite	2.57	0.14	1.33	0.16	0.02	0.16
010-029B-ii-iii-pt-18	2	pentlandite	4.72	0.15	2.36	0.19	-0.05	0.16
010-029B-ii-iii-pt-2	2	pentlandite	4.54	0.12	2.50	0.20	0.18	0.16
010-029B-ii-iii-pt-20	2	pentlandite	4.44	0.13	2.28	0.19	0.01	0.16
010-029B-ii-iii-pt-22	2	pentlandite	4.24	0.14	2.20	0.19	0.03	0.16
010-029B-ii-iii-pt-24	2	pentlandite	4.77	0.14	2.43	0.25	-0.01	0.21
010-029B-ii-iii-pt-25	2	pentlandite	3.31	0.13	1.80	0.19	0.10	0.16
010-029B-ii-iii-pt-26	2	pentlandite	2.89	0.14	1.50	0.22	0.02	0.18
010-029B-ii-iii-pt-29	2	pentlandite	3.78	0.18	2.03	0.24	0.10	0.21
010-029B-ii-iii-pt-31	2	pentlandite	2.59	0.24	1.34	0.22	0.02	0.20
010-029B-ii-iii-pt-32	2	pentlandite	4.23	0.13	2.36	0.18	0.20	0.16
010-029B-ii-iii-pt-34	2	pentlandite	4.55	0.14	2.37	0.18	0.05	0.16
010-029B-ii-iii-pt-35	2	pentlandite	2.99	0.19	1.78	0.20	0.25	0.16
010-029B-ii-iii-pt-36	2	pentlandite	4.60	0.13	2.39	0.25	0.04	0.21
010-029B-ii-iii-pt-37	2	pentlandite	4.64	0.13	2.60	0.20	0.24	0.16

Supplementary table 4.8.B: S isotope results

Sample ID	group	phase	δ^{34}S V-CDT (‰)	±(2σ)	δ^{33}S V-CDT (‰)	±(2σ)	Δ^{33}S (‰)	±(2σ)
010-029B-ii-iii-pt-38	2	pentlandite	4.69	0.13	2.58	0.23	0.18	0.19
010-029B-ii-iii-pt-4	2	pentlandite	4.76	0.12	2.38	0.17	-0.05	0.16
010-029B-ii-iii-pt-5	2	pentlandite	4.60	0.13	2.51	0.20	0.17	0.16
010-029B-ii-iii-pt-6	2	pentlandite	4.62	0.12	2.53	0.17	0.17	0.16
010-029B-ii-iii-pt-8	2	pentlandite	4.11	0.16	2.11	0.19	0.01	0.16
010-030-thick-1-pt-1	2	pentlandite	0.37	0.22	0.45	0.32	0.26	0.25
010-030-thick-1-pt-2	2	pentlandite	0.44	0.22	0.77	0.31	0.54	0.23
010-030-thick-2-pt-3	2	pentlandite	0.57	0.21	0.11	0.26	-0.19	0.20
010-030-thick-3-pt-4	2	pentlandite	-2.54	0.23	-0.85	0.48	0.47	0.44
010-030-thick-4-pt-5	2	pentlandite	-1.21	0.24	-0.69	0.35	-0.07	0.29
Bal-5A_4S_211015_@1	standard	pyrite-B	16.36	0.23	8.29	0.28	-0.15	0.22
Bal-5A_4S_211015_@2	standard	pyrite-B	16.42	0.23	8.50	0.24	0.03	0.18
Bal-5A_4S_211015_@3	standard	pyrite-B	16.40	0.23	8.32	0.26	-0.13	0.19
Bal-5A_4S_211015_@4	standard	pyrite-B	16.33	0.24	8.28	0.22	-0.14	0.18
Bal-5A_4S_211015_@5	standard	pyrite-B	16.29	0.23	8.35	0.24	-0.05	0.18
Bal-5A_4S_211015_@6	standard	pyrite-B	16.30	0.23	8.48	0.27	0.07	0.21
Bal-5A_4S_211015_@7	standard	pyrite-B	16.31	0.23	8.52	0.23	0.10	0.18
Bal-5A_4S_211015_@8	standard	pyrite-B	16.36	0.24	8.53	0.22	0.09	0.18
Bal-5A_4S_mt2088_@31	standard	pyrite-B	16.19	0.24	8.21	0.20	-0.09	0.21
Bal-5A_4S_mt2088_@32	standard	pyrite-B	16.22	0.24	8.21	0.25	-0.11	0.26
Bal-5A_4S_mt2088_@33	standard	pyrite-B	15.99	0.25	8.21	0.25	0.02	0.26
Bal-5A_4S_mt2088_@34	standard	pyrite-B	16.23	0.23	8.27	0.20	-0.05	0.21
Bal-5A_4S_mt2088_@34a	standard	pyrite-B	16.39	0.23	8.40	0.21	0.00	0.22
Bal-5A_4S_mt2088_@34b	standard	pyrite-B	16.31	0.26	8.25	0.21	-0.11	0.23
Bal-5A_4S_mt2088_@35	standard	pyrite-B	16.37	0.23	8.40	0.23	0.01	0.24
Bal-5A_4S_mt2088_@36	standard	pyrite-B	16.25	0.23	8.52	0.20	0.19	0.21
Bal-5A_4S_mt2088_@37	standard	pyrite-B	16.29	0.23	8.29	0.23	-0.06	0.24
Bal-5A_4S_mt2088_@38	standard	pyrite-B	16.22	0.23	8.40	0.21	0.08	0.22

Supplementary table 4.8.B: S isotope results

Sample ID	group phase	δ^{34}S V-CDT (‰)	±(2σ)	δ^{33}S V-CDT (‰)	±(2σ)	Δ^{33}S (‰)	±(2σ)
Bal-5A_4S_mt2088_@39	standard pyrite-B	16.29	0.24	8.27	0.20	-0.08	0.22
Bal-5A_4S_mt2089_@1	standard pyrite-B	16.15	0.11	8.20	0.17	-0.03	0.16
Bal-5A_4S_mt2089_@2	standard pyrite-B	16.11	0.11	8.39	0.17	0.18	0.16
Bal-5A_4S_mt2089_@21	standard pyrite-B	16.11	0.23	8.22	0.23	-0.04	0.24
Bal-5A_4S_mt2089_@4	standard pyrite-B	16.24	0.10	8.28	0.16	0.00	0.16
Bal-5A_4S_mt2089_@5	standard pyrite-B	16.25	0.11	8.24	0.16	-0.04	0.16
Bal-5A_4S_mt2089_@6	standard pyrite-B	16.03	0.12	8.04	0.22	-0.13	0.20
Bal-5C_4S_section-20C_@1	standard pyrite-B	16.22	0.23	8.43	0.26	0.06	0.19
Bal-5C_4S_section-20C_@2	standard pyrite-B	16.24	0.23	8.34	0.23	-0.04	0.18
Bal-5C_4S_section-20C_@3	standard pyrite-B	16.21	0.24	8.30	0.29	-0.06	0.23
Bal-5C_4S_section-20C_@4	standard pyrite-B	15.94	0.23	8.64	0.24	0.41	0.18
Bal-5C_4S_section-20C_@5	standard pyrite-B	15.83	0.23	8.20	0.27	0.04	0.20
Bal-5C_4S_section-20C_@6	standard pyrite-B	15.90	0.23	8.25	0.29	0.04	0.23
Bal-5C_4S_section-22_@1	standard pyrite-B	16.14	0.24	8.38	0.25	0.10	0.26
Bal-5C_4S_section-22_@2	standard pyrite-B	16.29	0.23	8.44	0.21	0.09	0.22
Bal-5C_4S_section-22_@3	standard pyrite-B	16.25	0.23	8.43	0.24	0.10	0.25
Bal-5C_4S_section-22_@4	standard pyrite-B	16.22	0.23	8.62	0.25	0.30	0.26
Bal-5C_4S_section-22_@5	standard pyrite-B	16.22	0.25	8.15	0.27	-0.16	0.28
Bal-5C_4S_section-22_@6	standard pyrite-B	16.19	0.23	8.26	0.27	-0.04	0.28
Is-5A_4S_211015_@1	standard pyrite-I	2.48	0.23	4.42	0.23	3.13	0.18
Is-5A_4S_211015_@4	standard pyrite-I	2.45	0.23	4.41	0.25	3.14	0.18
Is-5A_4S_mt2088_@31	standard pyrite-I	2.52	0.23	4.46	0.22	3.16	0.21
Is-5A_4S_mt2088_@31a	standard pyrite-I	2.50	0.27	3.53	0.28	2.24	0.29
Is-5A_4S_mt2088_@32	standard pyrite-I	2.54	0.22	4.40	0.22	3.09	0.21
Is-5A_4S_mt2088_@33	standard pyrite-I	2.38	0.23	4.31	0.23	3.08	0.22
Is-5A_4S_mt2088_@34	standard pyrite-I	2.49	0.23	3.76	0.25	2.48	0.25
Is-5A_4S_mt2089_@1	standard pyrite-I	2.37	0.11	4.24	0.17	3.03	0.16
Is-5A_4S_mt2089_@2	standard pyrite-I	2.32	0.11	3.65	0.17	2.46	0.16

Supplementary table 4.8.B: S isotope results

Sample ID	group phase	δ^{34}S V-CDT (‰)	±(2σ)	δ^{33}S V-CDT (‰)	±(2σ)	Δ^{33}S (‰)	±(2σ)
Is-5A_4S_mt2089_@21	standard pyrite-I	2.29	0.23	4.14	0.25	2.96	0.25
Is-5A_4S_mt2089_@22	standard pyrite-I	2.25	0.23	3.78	0.27	2.62	0.27
Is-5A_4S_mt2089_@23	standard pyrite-I	2.20	0.23	4.38	0.22	3.25	0.22
Is-5C_4S_section-20C_@1	standard pyrite-I	2.49	0.23	4.53	0.24	3.24	0.18
Is-5C_4S_section-20C_@2	standard pyrite-I	2.48	0.24	4.61	0.23	3.32	0.18
Is-5C_4S_section-20C_@3	standard pyrite-I	2.48	0.23	4.60	0.26	3.31	0.18
Is-5C_4S_section-20C_@4	standard pyrite-I	2.42	0.24	4.70	0.24	3.45	0.18
Is-5C_4S_section-20C_@5	standard pyrite-I	2.22	0.23	4.53	0.27	3.38	0.19
Is-5C_4S_section-22_@1	standard pyrite-I	2.48	0.23	4.68	0.27	3.41	0.26
Is-5C_4S_section-22_@2	standard pyrite-I	2.51	0.23	4.62	0.27	3.33	0.27
Is-5C_4S_section-22_@3	standard pyrite-I	2.47	0.23	4.47	0.22	3.21	0.22
Is-5C_4S_section-22_@4	standard pyrite-I	2.53	0.23	4.71	0.26	3.41	0.25
Is-5C_4S_section-22_@5	standard pyrite-I	2.54	0.23	4.53	0.30	3.23	0.30
Is-5C_4S_section-22_@6	standard pyrite-I	2.52	0.23	4.55	0.30	3.26	0.30
MV_5A_4S_211015_@1	standard pyrrhotite-M	7.00	0.24	5.73	0.31	2.12	0.25
MV_5A_4S_211015_@2	standard pyrrhotite-M	7.04	0.23	5.78	0.27	2.14	0.19
MV_5A_4S_211015_@3	standard pyrrhotite-M	6.95	0.25	5.61	0.26	2.02	0.18
MV_5A_4S_211015_@4	standard pyrrhotite-M	6.99	0.23	5.63	0.26	2.02	0.19
MV_5A_4S_mt2088_@31	standard pyrrhotite-M	6.71	0.24	5.50	0.23	2.05	0.23
MV_5A_4S_mt2088_@32	standard pyrrhotite-M	6.88	0.23	5.59	0.23	2.06	0.22
MV_5A_4S_mt2088_@33	standard pyrrhotite-M	6.80	0.23	5.57	0.21	2.07	0.21
MV_5A_4S_mt2088_@34	standard pyrrhotite-M	6.81	0.23	5.57	0.21	2.07	0.21
MV_5A_4S_mt2088_@35	standard pyrrhotite-M	6.76	0.23	5.63	0.20	2.16	0.20
MV_5A_4S_mt2088_@36	standard pyrrhotite-M	6.78	0.23	5.56	0.22	2.08	0.22
MV_5A_4S_mt2088_@37	standard pyrrhotite-M	6.84	0.23	5.48	0.20	1.96	0.20
MV_5A_4S_mt2088_@37a	standard pyrrhotite-M	6.79	0.25	5.58	0.25	2.09	0.26
MV_5A_4S_mt2088_@37b	standard pyrrhotite-M	6.75	0.24	5.48	0.21	2.01	0.21
MV_5A_4S_mt2088_@38	standard pyrrhotite-M	6.83	0.24	5.58	0.24	2.07	0.24

Supplementary table 4.8.B: S isotope results

Sample ID	group	phase	δ^{34}S V-CDT (‰)	±(2σ)	δ^{33}S V-CDT (‰)	±(2σ)	Δ^{33}S (‰)	±(2σ)
MV_5A_4S_mt2088_@39	standard	pyrrhotite-M	6.81	0.23	5.70	0.22	2.20	0.22
MV_5A_4S_mt2088_@40	standard	pyrrhotite-M	6.95	0.23	5.66	0.21	2.09	0.21
MV_5A_4S_mt2088_@41	standard	pyrrhotite-M	6.96	0.24	5.76	0.25	2.18	0.25
MV_5A_4S_mt2088_@42	standard	pyrrhotite-M	6.93	0.23	5.54	0.22	1.98	0.22
MV_5A_4S_mt2088_@43	standard	pyrrhotite-M	6.93	0.23	5.62	0.21	2.06	0.20
MV_5A_4S_mt2088_@44	standard	pyrrhotite-M	6.96	0.23	5.76	0.21	2.19	0.21
MV_5A_4S_mt2088_@45	standard	pyrrhotite-M	6.90	0.23	5.67	0.21	2.12	0.20
MV_5A_4S_mt2088_@46	standard	pyrrhotite-M	6.91	0.23	5.78	0.21	2.23	0.21
MV_5A_4S_mt2088_@47	standard	pyrrhotite-M	7.18	0.23	5.81	0.21	2.13	0.20
MV_5A_4S_mt2088_@48	standard	pyrrhotite-M	7.09	0.23	5.68	0.23	2.04	0.22
MV_5A_4S_mt2088_@49	standard	pyrrhotite-M	6.91	0.23	5.77	0.22	2.22	0.22
MV_5A_4S_mt2088_@50	standard	pyrrhotite-M	6.83	0.23	5.48	0.22	1.97	0.21
MV_5A_4S_mt2088_@51	standard	pyrrhotite-M	6.99	0.23	5.54	0.21	1.95	0.21
MV_5A_4S_mt2088_@52	standard	pyrrhotite-M	6.94	0.23	5.54	0.25	1.97	0.25
MV_5A_4S_mt2088_@53	standard	pyrrhotite-M	7.06	0.24	5.77	0.22	2.15	0.22
MV_5A_4S_mt2088_@54	standard	pyrrhotite-M	6.84	0.23	5.76	0.25	2.24	0.25
MV_5A_4S_mt2088_@55	standard	pyrrhotite-M	6.89	0.25	5.74	0.24	2.20	0.24
MV_5A_4S_mt2088_@56	standard	pyrrhotite-M	6.87	0.23	5.50	0.22	1.97	0.22
MV_5A_4S_mt2088_@57	standard	pyrrhotite-M	6.95	0.24	5.73	0.27	2.16	0.26
MV_5A_4S_mt2088_@58	standard	pyrrhotite-M	6.84	0.23	5.65	0.25	2.14	0.25
MV_5A_4S_mt2088_@59	standard	pyrrhotite-M	7.03	0.23	5.63	0.22	2.02	0.22
MV_5A_4S_mt2088_@60	standard	pyrrhotite-M	6.93	0.23	5.68	0.28	2.12	0.28
MV_5A_4S_mt2088_@61	standard	pyrrhotite-M	6.93	0.23	5.67	0.33	2.11	0.33
MV_5A_4S_mt2088_@62	standard	pyrrhotite-M	7.00	0.23	5.81	0.29	2.21	0.28
MV_5A_4S_mt2088_@63	standard	pyrrhotite-M	6.99	0.24	5.82	0.31	2.23	0.31
MV_5A_4S_mt2088_@64	standard	pyrrhotite-M	6.90	0.23	5.55	0.29	2.01	0.29
MV_5A_4S_mt2088_@65	standard	pyrrhotite-M	6.98	0.23	5.70	0.25	2.12	0.25
MV_5A_4S_mt2088_@66	standard	pyrrhotite-M	6.89	0.24	5.55	0.32	2.01	0.32

Supplementary table 4.8.B: S isotope results

Sample ID	group	phase	δ^{34}S V-CDT (‰)	±(2σ)	δ^{33}S V-CDT (‰)	±(2σ)	Δ^{33}S (‰)	±(2σ)
MV_5A_4S_mt2088_@67	standard	pyrrhotite-M	6.97	0.24	5.72	0.26	2.14	0.26
MV_5A_4S_mt2089_@1	standard	pyrrhotite-M	6.94	0.11	5.61	0.21	2.07	0.16
MV_5A_4S_mt2089_@10	standard	pyrrhotite-M	7.12	0.13	5.75	0.19	2.12	0.16
MV_5A_4S_mt2089_@11	standard	pyrrhotite-M	6.61	0.12	5.61	0.27	2.24	0.24
MV_5A_4S_mt2089_@12	standard	pyrrhotite-M	6.86	0.12	5.67	0.22	2.17	0.17
MV_5A_4S_mt2089_@2	standard	pyrrhotite-M	7.00	0.11	5.49	0.20	1.92	0.16
MV_5A_4S_mt2089_@21	standard	pyrrhotite-M	6.83	0.23	5.52	0.30	2.00	0.30
MV_5A_4S_mt2089_@22	standard	pyrrhotite-M	6.82	0.23	5.76	0.28	2.26	0.28
MV_5A_4S_mt2089_@23	standard	pyrrhotite-M	6.90	0.24	5.44	0.36	1.90	0.36
MV_5A_4S_mt2089_@24	standard	pyrrhotite-M	6.86	0.23	5.27	0.31	1.75	0.31
MV_5A_4S_mt2089_@25	standard	pyrrhotite-M	6.92	0.23	5.60	0.28	2.05	0.28
MV_5A_4S_mt2089_@26	standard	pyrrhotite-M	6.93	0.23	5.71	0.26	2.15	0.26
MV_5A_4S_mt2089_@27	standard	pyrrhotite-M	6.97	0.23	5.62	0.26	2.04	0.26
MV_5A_4S_mt2089_@28	standard	pyrrhotite-M	6.98	0.23	5.73	0.27	2.15	0.26
MV_5A_4S_mt2089_@29	standard	pyrrhotite-M	6.91	0.27	6.09	0.27	2.55	0.28
MV_5A_4S_mt2089_@3	standard	pyrrhotite-M	6.97	0.11	5.66	0.17	2.10	0.16
MV_5A_4S_mt2089_@30	standard	pyrrhotite-M	6.99	0.23	6.05	0.25	2.46	0.25
MV_5A_4S_mt2089_@30a	standard	pyrrhotite-M	6.89	0.23	5.92	0.23	2.38	0.23
MV_5A_4S_mt2089_@4	standard	pyrrhotite-M	6.71	0.13	5.33	0.27	1.91	0.24
MV_5A_4S_mt2089_@5	standard	pyrrhotite-M	6.93	0.11	5.59	0.16	2.05	0.16
MV_5A_4S_mt2089_@6	standard	pyrrhotite-M	7.04	0.10	5.80	0.16	2.21	0.16
MV_5A_4S_mt2089_@7	standard	pyrrhotite-M	7.02	0.11	5.67	0.18	2.09	0.16
MV_5A_4S_mt2089_@8	standard	pyrrhotite-M	6.96	0.12	5.58	0.18	2.03	0.16
MV_5A_4S_mt2089_@9	standard	pyrrhotite-M	7.00	0.11	5.72	0.19	2.15	0.16
MV_5C_4S_section-20C_@1	standard	pyrrhotite-M	7.10	0.23	5.55	0.28	1.88	0.20
MV_5C_4S_section-20C_@10	standard	pyrrhotite-M	6.71	0.23	5.74	0.34	2.27	0.28
MV_5C_4S_section-20C_@2	standard	pyrrhotite-M	7.02	0.24	5.87	0.25	2.24	0.18
MV_5C_4S_section-20C_@3	standard	pyrrhotite-M	7.07	0.24	5.78	0.24	2.13	0.18

Supplementary table 4.8.B: S isotope results

Sample ID	group	phase	δ^{34}S V-CDT (‰)	±(2σ)	δ^{33}S V-CDT (‰)	±(2σ)	Δ^{33}S (‰)	±(2σ)
MV_5C_4S_section-20C_@4	standard	pyrrhotite-M	7.05	0.23	6.17	0.24	2.52	0.18
MV_5C_4S_section-20C_@7	standard	pyrrhotite-M	6.89	0.23	5.69	0.22	2.13	0.18
MV_5C_4S_section-20C_@8	standard	pyrrhotite-M	6.81	0.24	5.90	0.23	2.38	0.18
MV_5C_4S_section-20C_@8a	standard	pyrrhotite-M	6.83	0.23	5.92	0.29	2.39	0.21
MV_5C_4S_section-20C_@8b	standard	pyrrhotite-M	6.85	0.23	5.56	0.28	2.02	0.21
MV_5C_4S_section-20C_@9	standard	pyrrhotite-M	6.70	0.23	5.86	0.30	2.40	0.23
MV_5C_4S_section-22_@1	standard	pyrrhotite-M	7.10	0.24	5.69	0.22	2.04	0.22
MV_5C_4S_section-22_@10	standard	pyrrhotite-M	7.06	0.23	5.76	0.28	2.13	0.28
MV_5C_4S_section-22_@2	standard	pyrrhotite-M	6.93	0.23	5.61	0.27	2.05	0.27
MV_5C_4S_section-22_@3	standard	pyrrhotite-M	7.06	0.23	5.65	0.29	2.03	0.28
MV_5C_4S_section-22_@4	standard	pyrrhotite-M	7.07	0.23	5.95	0.24	2.32	0.23
MV_5C_4S_section-22_@5	standard	pyrrhotite-M	7.00	0.23	5.72	0.34	2.13	0.34
MV_5C_4S_section-22_@6	standard	pyrrhotite-M	7.02	0.23	5.91	0.34	2.30	0.34
MV_5C_4S_section-22_@7	standard	pyrrhotite-M	6.99	0.23	6.09	0.25	2.51	0.25
MV_5C_4S_section-22_@8	standard	pyrrhotite-M	7.06	0.23	5.71	0.29	2.09	0.28
MV_5C_4S_section-22_@9	standard	pyrrhotite-M	7.13	0.24	5.81	0.28	2.15	0.28
NS-apy1_4S_section-23_@1	standard	arsenopyrite	1.59	0.24	0.78	0.41	-0.03	0.36
NS-apy1_4S_section-23_@2	standard	arsenopyrite	1.65	0.22	1.27	0.44	0.43	0.40
NS-apy1_4S_section-23_@3	standard	arsenopyrite	1.68	0.24	0.30	0.60	-0.56	0.57
NS-apy1_4S_section-23_@4	standard	arsenopyrite	1.48	0.22	0.86	0.44	0.11	0.40
NS-apy1_4S_section-23_@5	standard	arsenopyrite	1.57	0.22	0.62	0.37	-0.17	0.32
NS-apy1_4S_section-23_@6	standard	arsenopyrite	1.51	0.23	0.66	0.30	-0.11	0.23
NS-apy1_4S_section-23_@7	standard	arsenopyrite	1.52	0.24	0.63	0.38	-0.15	0.33
NS-apy1_4S_section-23_@8	standard	arsenopyrite	1.62	0.23	0.80	0.43	-0.02	0.39
Rut-5A_4S_211015_@1	standard	pyrite-R	1.50	0.23	0.59	0.26	-0.18	0.18
Rut-5A_4S_211015_@2	standard	pyrite-R	1.46	0.23	0.70	0.25	-0.06	0.18
Rut-5A_4S_211015_@3	standard	pyrite-R	1.45	0.23	0.64	0.23	-0.12	0.18
Rut-5A_4S_211015_@4	standard	pyrite-R	1.31	0.23	0.58	0.23	-0.10	0.18

Supplementary table 4.8.B: S isotope results

Sample ID	group phase	$\delta^{34}S$ V-CDT (‰)	±(2σ)	$\delta^{33}S$ V-CDT (‰)	±(2σ)	$\Delta^{33}S$ (‰)	±(2σ)
Rut-5A_4S_211015_@5	standard pyrite-R	1.34	0.23	0.74	0.26	0.05	0.18
Rut-5A_4S_211015_@6	standard pyrite-R	1.49	0.23	0.83	0.25	0.06	0.18
Rut-5A_4S_211015_@7	standard pyrite-R	1.38	0.23	0.66	0.21	-0.05	0.18
Rut-5A_4S_211015_@8	standard pyrite-R	1.36	0.23	0.77	0.23	0.06	0.18
Rut-5A_4S_mt2088_@31	standard pyrite-R	1.44	0.23	0.83	0.23	0.09	0.23
Rut-5A_4S_mt2088_@32	standard pyrite-R	1.40	0.23	0.71	0.23	-0.01	0.23
Rut-5A_4S_mt2088_@33	standard pyrite-R	1.31	0.23	0.65	0.21	-0.02	0.21
Rut-5A_4S_mt2088_@34	standard pyrite-R	1.45	0.22	0.69	0.21	-0.05	0.20
Rut-5A_4S_mt2088_@34a	standard pyrite-R	1.43	0.23	0.68	0.20	-0.06	0.19
Rut-5A_4S_mt2088_@34b	standard pyrite-R	1.40	0.23	0.64	0.20	-0.08	0.20
Rut-5A_4S_mt2088_@35	standard pyrite-R	1.47	0.23	0.77	0.25	0.01	0.24
Rut-5A_4S_mt2088_@36	standard pyrite-R	1.46	0.23	0.70	0.23	-0.05	0.22
Rut-5A_4S_mt2088_@37	standard pyrite-R	1.49	0.23	0.59	0.20	-0.17	0.20
Rut-5A_4S_mt2088_@38	standard pyrite-R	1.46	0.23	0.79	0.21	0.03	0.20
Rut-5A_4S_mt2088_@39	standard pyrite-R	1.41	0.23	0.79	0.24	0.06	0.24
Rut-5A_4S_mt2089_@1	standard pyrite-R	1.35	0.10	0.63	0.17	-0.06	0.16
Rut-5A_4S_mt2089_@2	standard pyrite-R	1.38	0.10	0.67	0.16	-0.03	0.16
Rut-5A_4S_mt2089_@21	standard pyrite-R	1.22	0.24	0.54	0.28	-0.09	0.27
Rut-5A_4S_mt2089_@4	standard pyrite-R	1.48	0.11	0.79	0.16	0.03	0.16
Rut-5A_4S_mt2089_@5	standard pyrite-R	1.39	0.12	0.73	0.18	0.02	0.16
Rut-5A_4S_mt2089_@6	standard pyrite-R	1.44	0.11	0.78	0.21	0.05	0.16
Rut-5C_4S_section-20C_@1	standard pyrite-R	1.17	0.23	0.64	0.30	0.03	0.23
Rut-5C_4S_section-20C_@2	standard pyrite-R	1.56	0.23	0.86	0.24	0.05	0.18
Rut-5C_4S_section-20C_@3	standard pyrite-R	1.81	0.23	1.10	0.23	0.17	0.18
Rut-5C_4S_section-20C_@4	standard pyrite-R	1.54	0.23	0.73	0.24	-0.07	0.18
Rut-5C_4S_section-20C_@5	standard pyrite-R	1.52	0.23	0.88	0.23	0.09	0.18
Rut-5C_4S_section-20C_@7	standard pyrite-R	1.34	0.23	0.72	0.25	0.02	0.18
Rut-5C_4S_section-20C_@8	standard pyrite-R	1.29	0.24	0.78	0.25	0.11	0.18

Supplementary table 4.8.B: S isotope results

Sample ID	group phase	δ^{34}S V-CDT (‰)	±(2σ)	δ^{33}S V-CDT (‰)	±(2σ)	Δ^{33}S (‰)	±(2σ)
Rut-5C_4S_section-22_@1	standard pyrite-R	1.50	0.23	0.77	0.24	0.00	0.24
Rut-5C_4S_section-22_@2	standard pyrite-R	1.62	0.23	0.90	0.27	0.07	0.27
Rut-5C_4S_section-22_@3	standard pyrite-R	1.79	0.23	1.09	0.29	0.17	0.29
Rut-5C_4S_section-22_@4	standard pyrite-R	1.32	0.23	0.44	0.28	-0.24	0.27
Rut-5C_4S_section-22_@5	standard pyrite-R	1.27	0.23	0.73	0.26	0.08	0.25
Rut-5C_4S_section-22_@6	standard pyrite-R	1.19	0.23	0.77	0.31	0.16	0.30
S0302A_4S_section-23_@1	standard pyrite-S	-0.11	0.21	-0.24	0.29	-0.18	0.21
S0302A_4S_section-23_@10	standard pyrite-S	-0.12	0.21	-0.04	0.30	0.02	0.22
S0302A_4S_section-23_@11	standard pyrite-S	-0.10	0.22	-0.10	0.25	-0.05	0.20
S0302A_4S_section-23_@12	standard pyrite-S	0.26	0.21	-0.01	0.25	-0.15	0.20
S0302A_4S_section-23_@2	standard pyrite-S	-0.16	0.21	-0.07	0.32	0.01	0.25
S0302A_4S_section-23_@3	standard pyrite-S	-0.09	0.21	-0.06	0.27	-0.01	0.20
S0302A_4S_section-23_@4	standard pyrite-S	-0.02	0.21	0.03	0.25	0.03	0.20
S0302A_4S_section-23_@5	standard pyrite-S	-0.03	0.21	0.10	0.30	0.12	0.23
S0302A_4S_section-23_@6	standard pyrite-S	-0.03	0.21	0.09	0.27	0.11	0.20
S0302A_4S_section-23_@7	standard pyrite-S	0.10	0.21	0.08	0.26	0.03	0.20
S0302A_4S_section-23_@8	standard pyrite-S	-0.01	0.21	-0.10	0.25	-0.09	0.20
S0302A_4S_section-23_@9	standard pyrite-S	0.04	0.21	-0.11	0.29	-0.13	0.22
S0302A-6A_4S_section-30_@1	standard pyrite-S	0.01	0.21	0.06	0.29	0.06	0.21
S0302A-6A_4S_section-30_@2	standard pyrite-S	0.00	0.21	-0.03	0.27	-0.03	0.20
S0302A-6A_4S_section-30_@3	standard pyrite-S	-0.09	0.21	0.25	0.25	0.29	0.20
S0302A-6A_4S_section-30_@4	standard pyrite-S	0.04	0.21	0.21	0.27	0.19	0.20
S0302A-6A_4S_section-30_@5	standard pyrite-S	0.11	0.21	0.10	0.24	0.05	0.20
S0302A-6A_4S_section-30_@6	standard pyrite-S	0.00	0.21	-0.16	0.26	-0.16	0.20
YP136_4S_section-23_@1	standard pyrrhotite-Y	1.57	0.22	0.80	0.24	-0.01	0.20
YP136_4S_section-23_@10	standard pyrrhotite-Y	1.53	0.22	1.21	0.24	0.41	0.20
YP136_4S_section-23_@2	standard pyrrhotite-Y	1.49	0.21	0.80	0.26	0.02	0.20
YP136_4S_section-23_@3	standard pyrrhotite-Y	1.39	0.21	1.03	0.31	0.31	0.24

Supplementary table 4.8.B: S isotope results

Sample ID	group phase	δ^{34}S V-CDT (‰)	±(2σ)	δ^{33}S V-CDT (‰)	±(2σ)	Δ^{33}S (‰)	±(2σ)
YP136_4S_section-23_@4	standard pyrrhotite-Y	1.37	0.22	0.56	0.45	-0.15	0.40
YP136_4S_section-23_@5	standard pyrrhotite-Y	1.41	0.22	0.72	0.34	-0.01	0.28
YP136_4S_section-23_@6	standard pyrrhotite-Y	1.48	0.21	0.83	0.34	0.07	0.28
YP136_4S_section-23_@7	standard pyrrhotite-Y	1.50	0.21	0.86	0.31	0.09	0.24
YP136_4S_section-23_@8	standard pyrrhotite-Y	1.46	0.21	0.88	0.30	0.13	0.22
YP136_4S_section-23_@9	standard pyrrhotite-Y	1.51	0.21	1.06	0.34	0.28	0.27
YP136-6A_4S_section-30_@1	standard pyrrhotite-Y	1.60	0.22	0.99	0.26	0.17	0.20
YP136-6A_4S_section-30_@10	standard pyrrhotite-Y	1.43	0.21	1.07	0.30	0.33	0.22
YP136-6A_4S_section-30_@2	standard pyrrhotite-Y	1.54	0.21	0.91	0.31	0.11	0.24
YP136-6A_4S_section-30_@3	standard pyrrhotite-Y	1.56	0.21	1.12	0.33	0.31	0.26
YP136-6A_4S_section-30_@4	standard pyrrhotite-Y	1.58	0.21	0.84	0.25	0.02	0.20
YP136-6A_4S_section-30_@5	standard pyrrhotite-Y	1.45	0.21	0.74	0.24	-0.01	0.20
YP136-6A_4S_section-30_@6	standard pyrrhotite-Y	1.60	0.21	0.88	0.35	0.05	0.29
YP136-6A_4S_section-30_@7	standard pyrrhotite-Y	1.56	0.21	0.96	0.23	0.15	0.20
YP136-6A_4S_section-30_@8	standard pyrrhotite-Y	1.52	0.21	1.04	0.25	0.25	0.20
YP136-6A_4S_section-30_@9	standard pyrrhotite-Y	1.57	0.21	1.03	0.27	0.22	0.20

Supplementary table 4.8.C: Pb isotope results

											err correl.
Sample #	mineral	Group	$^{207}\mathrm{Pb}/^{206}\mathrm{Pb}$	1σ(%)	$^{208}\mathrm{Pb}/^{206}\mathrm{Pb}$	1σ(%)	$^{206}\mathrm{Pb}/^{204}\mathrm{Pb}$	1σ(%)	$^{207}\mathrm{Pb}/^{204}\mathrm{Pb}$	1σ(%)	$^{207}\mathrm{Pb}/^{206}\mathrm{Pb}$
010-020C-thick-5-pt-15-pb	pt	1	1.04	0.26	2.39	0.21	13.52	0.66	14.04	0.68	0.93
010-020C-iii-pt-63-pb	pt	1	1.05	0.26	2.42	0.21	13.38	0.67	14.04	0.68	0.93
010-020C-iv-pt-28-pb	pt	1	1.04	0.26	2.39	0.21	13.62	0.67	14.11	0.68	0.93
010-020C-ii-pt-111-pb	pt	1	1.02	0.27	2.35	0.22	~~13.87~~	~~0.69~~	~~14.18~~	~~0.71~~	~~0.93~~
010-020C-thick-3-pt-5-pb	pt	1	1.05	0.27	2.41	0.22	13.48	0.72	14.09	0.72	0.93
010-020C-iii-pt-63a-pb	pt	1	1.05	0.29	2.42	0.23	13.33	0.73	13.96	0.75	0.92
010-020C-iii-pt-52-pb	pt	1	1.04	0.31	2.39	0.25	13.54	0.77	14.11	0.80	0.92
010-020C-iii-pt-74-pb	pt	1	1.04	0.31	2.39	0.25	13.67	0.77	14.22	0.79	0.92
010-020C-iv-pt-23-pb	pt	1	1.04	0.30	2.37	0.25	13.57	0.82	14.05	0.84	0.93
010-020C-ii-pt-104-pb	pt	1	1.06	0.31	2.43	0.29	~~13.23~~	~~0.81~~	~~14.01~~	~~0.81~~	~~0.93~~
010-020C-thick-2-pt-3-pb	pt	1	1.05	0.38	2.42	0.32	13.51	1.00	14.16	1.01	0.93
010-020C-iii-pt-60-pb	pt	1	1.05	0.43	2.41	0.34	13.45	1.05	14.08	1.09	0.92
010-020C-iii-pt-76-pb	pt	1	1.04	0.41	2.39	0.36	13.61	1.11	14.23	1.12	0.93
010-020C-iii-po-53-pb	po	1	*1.07*	*1.04*	*2.42*	*0.95*	~~*13.04*~~	~~*2.80*~~	~~*14.04*~~	~~*2.95*~~	~~*0.94*~~
010-020C-thick-4-po-8-pb	po	1	*1.04*	*1.05*	*2.43*	*0.97*	~~*13.55*~~	~~*2.83*~~	~~*14.02*~~	~~*2.84*~~	~~*0.93*~~
010-020C-ii-pt-123-pb	pt	1	~~*1.06*~~	~~*1.68*~~	~~*2.45*~~	~~*1.52*~~	~~*13.71*~~	~~*4.46*~~	~~*14.52*~~	~~*4.46*~~	~~*0.93*~~
010-020C-iv-pt-30-pb	pt	1	~~*1.06*~~	~~*2.03*~~	~~*2.53*~~	~~*1.90*~~	ND	ND	ND	ND	ND
010-020C-thick-4-po-11-pb	po	1	~~*1.06*~~	~~*2.69*~~	~~*2.45*~~	~~*1.98*~~	~~*12.58*~~	~~*5.96*~~	~~*13.08*~~	~~*5.96*~~	~~*0.90*~~
010-020C-iii-po-61-pb	po	1	~~*1.07*~~	~~*3.95*~~	~~*2.66*~~	~~*4.01*~~	ND	ND	ND	ND	ND
010-020C-thick-4-pt-12-pb	pt	1	~~*0.97*~~	~~*3.79*~~	~~*2.32*~~	~~*3.19*~~	ND	ND	ND	ND	ND
010-020C-iii-pt-62-pb	pt	1	~~*1.07*~~	~~*3.84*~~	~~*2.42*~~	~~*3.21*~~	ND	ND	ND	ND	ND
010-020C-iii-po-55-pb	po	1	~~*1.13*~~	~~*6.25*~~	~~*2.63*~~	~~*5.40*~~	ND	ND	ND	ND	ND
010-020C-ii-pt-124-pb	pt	1	~~*0.95*~~	~~*5.93*~~	~~*2.35*~~	~~*6.13*~~	ND	ND	ND	ND	ND
010-020C-ii-pt-134-pb	pt	1	ND	ND	ND	ND	ND	ND	ND	ND	ND
010-020C-ii-pt-125-pb	pt	1	~~*0.84*~~	~~*10.94*~~	~~*2.45*~~	~~*8.96*~~	ND	ND	ND	ND	ND
010-020C-iv-pt-46-pb	pt	1	ND	ND	ND	ND	ND	ND	ND	ND	ND
010-020C-iii-pt-94-pb	pt	1	ND	ND	ND	ND	ND	ND	ND	ND	ND
010-020C-ii-pt-105-pb	pt	1	ND	ND	ND	ND	ND	ND	ND	ND	ND

Supplementary table 4.8.C: Pb isotope results

Sample #	mineral	Group	^{207}Pb/^{206}Pb	1σ(%)	^{208}Pb/^{206}Pb	1σ(%)	^{206}Pb/^{204}Pb	1σ(%)	^{207}Pb/^{204}Pb	1σ(%)	err correl. ^{207}Pb/^{206}Pb
010-020C-ii-pt-132-pb	pt	1	ND	ND	ND	ND	ND	ND	ND	ND	ND
010-020C-ii-pt-103-pb	pt	1	ND	ND	ND	ND	ND	ND	ND	ND	ND
010-020C-iv-pt-50-pb	pt	1	ND	ND	ND	ND	ND	ND	ND	ND	ND
010-020C-iii-pt-56-pb	pt	1	ND	ND	ND	ND	ND	ND	ND	ND	ND
010-020C-ii-pt-135-pb	pt	1	ND	ND	ND	ND	ND	ND	ND	ND	ND
010-022-thick-1-pt-8-pb	pt	1	1.11	0.25	2.57	0.20	12.53	0.64	13.90	0.66	0.93
010-022-thick-7-pt-16-Pb	pt	1	1.11	0.55	2.57	0.26	12.55	0.77	13.95	0.85	0.77
010-022-thick-7-pt-21-Pb	pt	1	1.11	0.56	2.56	0.26	12.54	0.78	13.90	0.86	0.77
010-022-thick-1-pt-7-pb	pt	1	1.11	0.25	2.56	0.21	12.50	0.65	13.85	0.67	0.93
010-022-v-pt-17-pb	pt	1	1.11	0.26	2.56	0.21	12.50	0.65	13.82	0.67	0.92
010-022-thick-6-pt-13-pb	pt	1	1.11	0.26	2.56	0.21	12.56	0.66	13.90	0.68	0.93
010-022-v-pt-9-pb	pt	1	1.11	0.26	2.56	0.21	12.52	0.68	13.88	0.68	0.93
010-022-thick-2-pt-12-pb	pt	1	1.11	0.26	2.56	0.21	12.50	0.66	13.85	0.68	0.93
010-022-thick-2-pt-11-pb	pt	1	1.11	0.27	2.56	0.22	12.57	0.69	13.92	0.71	0.93
010-022-thick-2-pt-10-pb	pt	1	1.11	0.27	2.56	0.22	12.49	0.69	13.86	0.71	0.93
010-022-v-pt-1-pb	pt	1	1.11	0.28	2.56	0.22	12.47	0.72	13.80	0.74	0.93
010-022-thick-7-pt-19-Pb	pt	1	1.11	0.57	2.56	0.28	12.51	0.83	13.86	0.90	0.79
010-022-thick-7-pt-17-Pb	pt	1	1.11	0.57	2.56	0.28	12.52	0.87	13.93	0.93	0.80
010-022-v-pt-3-pb	pt	1	1.11	0.29	2.55	0.24	12.43	0.75	13.76	0.76	0.93
010-022-v-pt-3-pb	pt	1	1.11	0.29	2.55	0.24	12.43	0.75	13.76	0.76	0.93
010-022-v-pt-12-pb	pt	1	1.11	0.29	2.55	0.24	12.49	0.76	13.86	0.79	0.93
010-022-thick-1-pt-6-pb	pt	1	1.11	0.31	2.56	0.26	12.52	0.82	13.89	0.85	0.93
010-022-thick-7-pt-18-Pb	pt	1	1.11	0.61	2.56	0.32	12.53	0.97	13.85	1.02	0.82
010-022-v-pt-11-pb	pt	1	1.11	0.33	2.56	0.28	12.42	0.86	13.75	0.87	0.93
010-022-thick-7-pt-15-Pb	pt	1	1.11	0.60	2.56	0.33	12.67	0.99	13.99	1.05	0.83
010-022-thick-2-pt-9-pb	pt	1	1.11	0.35	2.55	0.29	12.43	0.91	13.77	0.92	0.93
010-022-thick-6-pt-14-pb	pt	1	1.11	0.37	2.56	0.31	12.61	0.96	13.98	0.97	0.93
010-022-thick-7-pt-20-Pb	pt	1	1.11	0.66	2.56	0.40	12.41	1.23	13.81	1.28	0.86

Supplementary table 4.8.C: Pb isotope results

											err correl.
Sample #	mineral	Group	$^{207}Pb/^{206}Pb$	1σ(%)	$^{208}Pb/^{206}Pb$	1σ(%)	$^{206}Pb/^{204}Pb$	1σ(%)	$^{207}Pb/^{204}Pb$	1σ(%)	$^{207}Pb/^{206}Pb$
010-022-v-pt-20-pb	pt	1	*1.12*	*0.66*	*2.56*	*0.52*	*12.06*	*1.70*	*13.39*	*1.68*	*0.92*
010-022-v-pt-13-pb	pt	1	*1.11*	*0.61*	*2.55*	*0.52*	*12.38*	*1.61*	*13.81*	*1.62*	*0.93*
010-022-v-pt-10-pb	pt	1	*1.12*	*0.68*	*2.58*	*0.63*	*12.47*	*1.92*	*13.83*	*1.79*	*0.94*
010-022-v-pt-19-pb	pt	1	*1.07*	*1.49*	*2.51*	*1.28*	~~*11.91*~~	~~*3.92*~~	~~*13.08*~~	~~*3.94*~~	~~*0.93*~~
010-023-thick-3A-pt-6-pb	pt	1	0.99	0.31	2.21	0.26	14.60	0.83	14.44	0.84	0.93
010-023-thick-8-pt-11-pb	pt	1	1.07	0.40	2.44	0.34	13.33	1.06	14.18	1.07	0.93
010-023-thick-1A-pt-3-pb	pt	1	1.07	0.44	2.42	0.37	13.51	1.19	14.38	1.19	0.93
010-023-thick-2A-pt-1-pb	pt	1	1.07	0.46	2.41	0.39	13.18	1.22	14.10	1.23	0.93
010-023-thick-7-pt-7-pb	pt	1	1.07	0.81	2.41	0.50	13.69	1.66	14.47	1.39	0.87
010-023-thick-4-pt-5-pb	pt	1	*1.06*	*0.65*	*2.42*	*0.51*	*13.18*	*1.58*	*14.00*	*1.59*	*0.92*
010-023-thick-8-pt-10-pb	pt	1	*1.07*	*0.61*	*2.44*	*0.52*	*13.36*	*1.73*	*14.39*	*1.94*	*0.95*
010-023-thick-9-pt-12-pb	pt	1	*1.06*	*0.63*	*2.42*	*0.59*	*13.40*	*1.70*	*14.18*	*1.71*	*0.93*
010-023-thick-9-pt-14-pb	pt	1	*1.07*	*0.64*	*2.43*	*0.55*	*13.53*	*1.73*	*14.31*	*1.74*	*0.93*
010-023-thick-8-pt-9-pb	pt	1	*1.06*	*0.82*	*2.41*	*0.93*	~~*13.50*~~	~~*2.32*~~	~~*14.37*~~	~~*2.35*~~	~~*0.94*~~
010-023-thick-1A-pt-2-pb	pt	1	~~*1.05*~~	~~*1.65*~~	~~*2.36*~~	~~*1.41*~~	~~*13.54*~~	~~*4.50*~~	~~*14.57*~~	~~*4.50*~~	~~*0.93*~~
010-023-thick-7-pt-8-pb	pt	1	~~*1.05*~~	~~*2.03*~~	~~*2.42*~~	~~*1.74*~~	~~*14.18*~~	~~*6.12*~~	~~*14.97*~~	~~*6.33*~~	~~*0.95*~~
010-023-thick-4-pt-4-pb	pt	1	~~*1.00*~~	~~*2.18*~~	~~*2.42*~~	~~*2.06*~~	~~*14.09*~~	~~*7.19*~~	~~*14.11*~~	~~*6.86*~~	~~*0.95*~~
010-023-thick-9-pt-13-pb	pt	1	~~*0.99*~~	~~*2.44*~~	~~*2.33*~~	~~*2.60*~~	~~*15.19*~~	~~*6.97*~~	~~*14.12*~~	~~*6.21*~~	~~*0.94*~~
010-029B-250-180-po-67-rr	po	2	1.08	0.25	2.50	0.20	13.05	0.64	14.04	0.65	0.93
010-029B-250-180-pt-72-rr	pt	2	1.07	0.25	2.49	0.20	13.09	0.64	14.05	0.66	0.93
010-029B-ii-iii-pt-10	pt	2	1.07	0.55	2.50	0.26	13.05	0.77	13.90	0.85	0.77
010-029B-250-180-pt-68-rr	pt	2	1.08	0.25	2.50	0.20	13.01	0.64	14.02	0.66	0.93
010-029B-ii-iii-pt-17	pt	2	1.06	0.56	2.50	0.26	12.91	0.78	13.66	0.86	0.77
010-029B-ii-iii-pt-11	pt	2	1.06	0.56	2.51	0.26	12.89	0.78	13.70	0.86	0.77
010-029B-ii-iii-po-27-pb-repeat	po	2	1.07	0.26	2.48	0.21	13.03	0.68	13.99	0.70	0.93
010-029B-ii-iii-po-19	po	2	1.06	0.56	2.50	0.27	12.84	0.80	13.54	0.88	0.78
010-029B-250-180-po-62-rr	po	2	1.08	0.28	2.49	0.23	13.03	0.71	14.06	0.73	0.93
010-029B-ii-iii-pt-15	pt	2	1.06	0.57	2.49	0.28	12.94	0.84	13.67	0.92	0.80

Supplementary table 4.8.C: Pb isotope results

Sample #	mineral	Group	^{207}Pb/^{206}Pb	1σ(%)	^{208}Pb/^{206}Pb	1σ(%)	^{206}Pb/^{204}Pb	1σ(%)	^{207}Pb/^{204}Pb	1σ(%)	err correl. ^{207}Pb/^{206}Pb
010-029B-ii-iii-pt-6	pt	2	1.07	0.58	2.48	0.31	13.11	0.92	14.03	0.96	0.81
010-029B-250-180-pt-45-rr	pt	2	1.08	0.33	2.48	0.28	13.07	0.85	14.08	0.86	0.92
010-029B-ii-iii-pt-28-Pb-repeat	pt	2	1.08	0.44	2.48	0.34	13.12	1.15	14.08	1.14	0.93
010-029B-ii-iii-po-7	po	2	1.07	0.64	2.49	0.38	12.89	1.30	13.79	1.25	0.87
010-029B-250-180-po-52-rr	po	2	1.07	0.50	2.48	0.41	13.26	1.37	14.23	1.34	0.93
010-029B-ii-iii-po-9	po	2	*1.08*	*1.00*	*2.50*	*0.76*	*13.25*	*2.27*	*14.14*	*2.18*	*0.90*
010-029B-ii-iii-po-21	po	2	*1.07*	*1.48*	*2.53*	*1.16*	~~*12.26*~~	~~*3.52*~~	~~*13.27*~~	~~*3.61*~~	~~*0.91*~~
010-029B-ii-iii-pt-2	pt	2	~~*1.08*~~	~~*1.71*~~	~~*2.46*~~	~~*1.46*~~	~~*14.26*~~	~~*5.05*~~	~~*15.11*~~	~~*4.61*~~	~~*0.94*~~
010-029B-ii-iii-pt-13	pt	2	~~*1.07*~~	~~*1.81*~~	~~*2.50*~~	~~*1.42*~~	ND	ND	ND	ND	ND
010-029B-ii-iii-pt-4	pt	2	~~*1.05*~~	~~*2.61*~~	~~*2.46*~~	~~*2.19*~~	~~*15.31*~~	~~*7.63*~~	~~*15.44*~~	~~*7.12*~~	~~*0.94*~~
010-029B-ii-iii-po-1	po	2	~~*1.06*~~	~~*2.88*~~	~~*2.52*~~	~~*2.42*~~	~~*14.12*~~	~~*7.59*~~	~~*14.70*~~	~~*7.59*~~	~~*0.93*~~
010-029B-ii-iii-pt-18	pt	2	~~*1.04*~~	~~*3.52*~~	~~*2.51*~~	~~*2.81*~~	~~*15.94*~~	~~*10.82*~~	~~*16.43*~~	~~*10.96*~~	~~*0.95*~~
010-029B-ii-iii-pt-8	pt	2	~~*1.06*~~	~~*3.40*~~	~~*2.61*~~	~~*3.01*~~	ND	ND	ND	ND	ND
010-029B-ii-iii-pt-20	pt	2	ND	ND	ND	ND	ND	ND	ND	ND	ND
010-030-thick-1-pt-2-pb	pt	2	1.14	0.43	2.65	0.36	11.89	1.20	13.58	1.12	0.93
010-030-thick-4-pt-5-pb	pt	2	*1.10*	*0.57*	*2.57*	*0.51*	*12.71*	*1.43*	*13.97*	*1.43*	*0.92*
010-030-thick-1-pt-1-pb	pt	2	*1.14*	*0.62*	*2.65*	*0.47*	*12.14*	*1.45*	*13.77*	*1.37*	*0.91*
010-030-thick-2-pt-3-pb	pt	2	*1.15*	*0.82*	*2.69*	*0.68*	~~*11.85*~~	~~*2.08*~~	~~*13.88*~~	~~*2.10*~~	~~*0.92*~~
BCR_multiPb_220308_@1	std	2	0.83	0.59	2.06	0.34	18.80	0.98	15.64	1.04	0.830
BCR_multiPb_220308_@2	std	2	0.84	0.59	2.06	0.30	18.55	1.00	15.51	1.06	0.836
BCR_multiPb_220308_@3	std	2	0.84	0.59	2.07	0.30	19.08	0.97	15.92	1.03	0.830
BCR_multiPb_220308_@4	std	2	0.84	0.59	2.07	0.32	18.68	0.96	15.62	1.03	0.828
BCR_multiPb_220308_@5	std	2	0.84	0.59	2.06	0.30	18.75	0.98	15.71	1.04	0.833
BCR_multiPb_220308_@6	std	2	0.83	0.59	2.06	0.30	18.74	0.97	15.55	1.03	0.829
BCR_multiPb_220308_@7	std	2	0.83	0.59	2.07	0.30	18.83	0.95	15.66	1.01	0.820
BCR_multiPb_220308_@8	std	2	0.83	0.59	2.07	0.31	18.68	0.97	15.50	1.04	0.828
BCR_multiPb_220308_@9	std	2	0.83	0.59	2.07	0.30	18.77	0.95	15.52	1.03	0.829
BCR_multiPb_220309_@1	std	2	0.83	0.34	2.07	0.27	18.86	0.90	15.70	0.92	0.930

Supplementary table 4.8.C: Pb isotope results

Sample #	mineral	Group	$^{207}Pb/^{206}Pb$	1σ(%)	$^{208}Pb/^{206}Pb$	1σ(%)	$^{206}Pb/^{204}Pb$	1σ(%)	$^{207}Pb/^{204}Pb$	1σ(%)	err correl. $^{207}Pb/^{206}Pb$
BCR_multiPb_220309_@10	std	2	0.83	0.31	2.06	0.25	18.60	0.84	15.52	0.85	0.934
BCR_multiPb_220309_@11	std	2	0.83	0.31	2.07	0.25	18.68	0.84	15.57	0.85	0.934
BCR_multiPb_220309_@12	std	2	0.83	0.31	2.06	0.25	18.81	0.84	15.58	0.86	0.935
BCR_multiPb_220309_@2	std	2	0.83	0.32	2.06	0.26	18.62	0.88	15.45	0.89	0.935
BCR_multiPb_220309_@3	std	2	0.83	0.32	2.06	0.26	18.92	0.88	15.71	0.90	0.935
BCR_multiPb_220309_@4	std	2	0.83	0.32	2.06	0.26	18.90	0.88	15.73	0.90	0.935
BCR_multiPb_220309_@5	std	2	0.83	0.31	2.06	0.25	18.98	0.83	15.85	0.85	0.934
BCR_multiPb_220309_@6	std	2	0.83	0.31	2.06	0.25	18.81	0.83	15.62	0.85	0.934
BCR_multiPb_220309_@7	std	2	0.83	0.31	2.06	0.25	18.70	0.83	15.55	0.85	0.934
BCR_multiPb_220309_@8	std	2	0.84	0.31	2.07	0.25	18.82	0.84	15.69	0.85	0.934
BCR_multiPb_220309_@9	std	2	0.83	0.31	2.06	0.25	18.92	0.84	15.76	0.85	0.934
BCR_multiPb_220310_@1	std	2	0.83	0.32	2.07	0.26	18.77	0.85	15.66	0.87	0.932
BCR_multiPb_220310_@10	std	2	0.83	0.30	2.07	0.25	18.81	0.83	15.74	0.84	0.934
BCR_multiPb_220310_@11	std	2	0.83	0.30	2.06	0.26	18.62	0.83	15.47	0.84	0.933
BCR_multiPb_220310_@12	std	2	0.83	0.30	2.06	0.25	18.88	0.86	15.69	0.86	0.938
BCR_multiPb_220310_@13	std	2	0.84	0.30	2.07	0.25	18.55	0.86	15.51	0.91	0.943
BCR_multiPb_220310_@14	std	2	0.83	0.30	2.07	0.25	18.66	0.82	15.55	0.84	0.934
BCR_multiPb_220310_@15	std	2	0.83	0.30	2.07	0.25	18.64	0.82	15.50	0.84	0.933
BCR_multiPb_220310_@16	std	2	0.84	0.30	2.07	0.25	18.99	0.82	15.87	0.84	0.934
BCR_multiPb_220310_@17	std	2	0.83	0.30	2.07	0.25	18.79	0.82	15.63	0.84	0.934
BCR_multiPb_220310_@18	std	2	0.83	0.30	2.06	0.25	18.81	0.89	15.63	0.90	0.944
BCR_multiPb_220310_@19	std	2	0.83	0.30	2.06	0.25	18.87	0.82	15.66	0.84	0.934
BCR_multiPb_220310_@2	std	2	0.83	0.31	2.06	0.25	18.70	0.85	15.60	0.87	0.934
BCR_multiPb_220310_@3	std	2	0.83	0.31	2.06	0.26	18.82	0.85	15.66	0.87	0.934
BCR_multiPb_220310_@4	std	2	0.83	0.31	2.07	0.26	18.85	0.84	15.71	0.86	0.934
BCR_multiPb_220310_@5	std	2	0.83	0.31	2.07	0.25	18.64	0.83	15.61	0.85	0.934
BCR_multiPb_220310_@6	std	2	0.83	0.31	2.07	0.25	18.58	0.83	15.50	0.84	0.934
BCR_multiPb_220310_@7	std	2	0.83	0.31	2.07	0.25	18.66	0.83	15.51	0.84	0.934

Supplementary table 4.8.C: Pb isotope results

Sample #	mineral	Group	$^{207}Pb/^{206}Pb$	1σ(%)	$^{208}Pb/^{206}Pb$	1σ(%)	$^{206}Pb/^{204}Pb$	1σ(%)	$^{207}Pb/^{204}Pb$	1σ(%)	err correl. $^{207}Pb/^{206}Pb$
BCR_multiPb_220310_@8	std	2	0.83	0.31	2.07	0.25	18.69	0.90	15.59	0.87	0.940
BCR_multiPb_220310_@9	std	2	0.83	0.31	2.06	0.25	18.76	0.85	15.57	0.85	0.935
BCR_multiPb_220311_@1	std	2	0.83	0.30	2.07	0.25	18.77	0.82	15.64	0.84	0.934
BCR_multiPb_220311_@11	std	2	0.83	0.32	2.06	0.26	18.79	0.86	15.66	0.88	0.934
BCR_multiPb_220311_@2	std	2	0.83	0.30	2.07	0.25	18.65	0.92	15.50	0.91	0.944
BCR_multiPb_220311_@3	std	2	0.84	0.30	2.08	0.25	18.62	0.83	15.63	0.84	0.934
BCR_multiPb_220311_@4	std	2	0.83	0.31	2.07	0.25	18.92	0.84	15.77	0.85	0.934
BCR_multiPb_220311_@5	std	2	0.83	0.31	2.07	0.25	18.79	0.83	15.58	0.85	0.934

Italics - 206Pb < 100 cps

Strikethrough - 206Pb<50 cps (<10 cps for 76 & 86 ratios). Not displayed on figures.

ND - no counts or div/0

pt=pentlandite

po=pyrrhotite

std=standard

cps=counts per second

Supplementary table 4.8.C: Pb isotope results

Sample #	^{208}Pb/^{204}Pb	1σ(%)	err correl. ^{208}Pb/^{206}Pb	^{204}Pb cps	1σ(%)	^{206}Pb cps	1σ(%)	^{207}Pb cps	1σ(%)	^{208}Pb cps	1σ(%)
010-020C-thick-5-pt-15-pb	32.30	0.68	0.95	352.54	5.34	4768.09	5.41	4937.13	5.40	10702.70	5.41
010-020C-iii-pt-63-pb	32.34	0.69	0.95	332.74	5.48	4451.95	5.44	4648.43	5.46	10106.06	5.47
010-020C-iv-pt-28-pb	32.44	0.69	0.95	306.28	6.33	4169.58	6.34	4213.30	6.27	9140.90	6.27
010-020C-ii-pt-111-pb	32.63	0.71	0.95	164.35	4.16	2242.56	3.96	2320.41	4.14	4946.73	3.97
010-020C-thick-3-pt-5-pb	32.44	0.74	0.95	135.12	3.33	1818.15	3.30	1891.51	3.29	4103.77	3.31
010-020C-iii-pt-63a-pb	32.23	0.75	0.95	105.63	10.04	1404.13	10.09	1376.43	8.63	2989.73	8.65
010-020C-iii-pt-52-pb	32.35	0.80	0.95	63.73	2.08	864.62	1.93	897.87	2.01	1939.72	1.94
010-020C-iii-pt-74-pb	32.66	0.79	0.95	61.32	5.36	835.38	5.39	866.33	5.37	1874.13	5.38
010-020C-iv-pt-23-pb	32.17	0.82	0.95	55.35	5.65	757.84	5.70	779.25	5.71	1682.14	5.71
010-020C-ii-pt-104-pb	32.08	0.81	0.94	52.64	7.92	701.52	8.19	711.71	7.80	1541.57	7.84
010-020C-thick-2-pt-3-pb	32.61	1.01	0.95	21.15	4.98	284.01	4.81	302.69	5.02	657.04	5.04
010-020C-iii-pt-60-pb	32.33	1.06	0.95	19.06	7.18	255.92	6.97	267.31	7.10	578.03	7.01
010-020C-iii-pt-76-pb	32.44	1.11	0.95	16.23	3.54	221.30	3.23	229.12	3.23	495.04	3.19
010-020C-iii-po-53-pb	~~*32.16*~~	~~*2.79*~~	~~*0.94*~~	~~*2.41*~~	~~*11.40*~~	~~*33.44*~~	~~*11.55*~~	~~*33.96*~~	~~*11.45*~~	~~*73.49*~~	~~*11.58*~~
010-020C-thick-4-po-8-pb	~~*32.82*~~	~~*2.79*~~	~~*0.94*~~	~~*1.69*~~	~~*3.99*~~	~~*22.88*~~	~~*3.89*~~	~~*23.26*~~	~~*3.62*~~	~~*51.07*~~	~~*3.87*~~
010-020C-ii-pt-123-pb	~~*33.33*~~	~~*4.38*~~	~~*0.94*~~	~~*0.59*~~	~~*9.96*~~	~~*8.38*~~	~~*8.24*~~	~~*8.60*~~	~~*7.97*~~	~~*19.18*~~	~~*8.03*~~
010-020C-iv-pt-30-pb	ND	ND	ND	~~*0.41*~~	~~*8.81*~~	~~*5.24*~~	~~*7.67*~~	~~*5.86*~~	~~*8.31*~~	~~*12.25*~~	~~*7.84*~~
010-020C-thick-4-po-11-pb	~~*29.82*~~	~~*5.84*~~	~~*0.94*~~	~~*0.39*~~	~~*5.70*~~	~~*4.53*~~	~~*4.38*~~	~~*4.90*~~	~~*3.91*~~	~~*10.70*~~	~~*3.92*~~
010-020C-iii-po-61-pb	ND	ND	ND	~~*0.25*~~	~~*37.79*~~	~~*4.09*~~	~~*38.32*~~	~~*4.10*~~	~~*37.53*~~	~~*9.60*~~	~~*37.63*~~
010-020C-thick-4-pt-12-pb	ND	ND	ND	~~*0.11*~~	~~*10.45*~~	~~*1.78*~~	~~*4.34*~~	~~*1.73*~~	~~*4.53*~~	~~*3.83*~~	~~*4.07*~~
010-020C-iii-pt-62-pb	ND	ND	ND	~~*0.11*~~	~~*14.09*~~	~~*1.58*~~	~~*4.92*~~	~~*1.66*~~	~~*5.57*~~	~~*3.44*~~	~~*3.92*~~
010-020C-iii-po-55-pb	ND	ND	ND	~~*0.05*~~	~~*15.40*~~	~~*0.69*~~	~~*7.58*~~	~~*0.75*~~	~~*7.23*~~	~~*1.61*~~	~~*5.74*~~
010-020C-ii-pt-124-pb	ND	ND	ND	~~*0.05*~~	~~*16.48*~~	~~*0.67*~~	~~*7.21*~~	~~*0.63*~~	~~*8.21*~~	~~*1.41*~~	~~*6.78*~~
010-020C-ii-pt-134-pb	ND	ND	ND	~~*0.03*~~	~~*20.22*~~	~~*0.36*~~	~~*15.53*~~	~~*0.33*~~	~~*15.92*~~	~~*0.72*~~	~~*15.68*~~
010-020C-ii-pt-125-pb	ND	ND	ND	~~*0.01*~~	~~*29.28*~~	~~*0.23*~~	~~*7.31*~~	~~*0.18*~~	~~*8.14*~~	~~*0.46*~~	~~*5.18*~~
010-020C-iv-pt-46-pb	ND	ND	ND	~~*0.03*~~	~~*20.38*~~	~~*0.22*~~	~~*15.91*~~	~~*0.23*~~	~~*15.99*~~	~~*0.47*~~	~~*18.20*~~
010-020C-iii-pt-94-pb	ND	ND	ND	~~*0.01*~~	~~*27.74*~~	~~*0.16*~~	~~*18.37*~~	~~*0.13*~~	~~*19.01*~~	~~*0.25*~~	~~*17.65*~~
010-020C-ii-pt-105-pb	ND	ND	ND	~~*0.00*~~	ND	~~*0.06*~~	~~*13.02*~~	~~*0.08*~~	~~*12.33*~~	~~*0.15*~~	~~*8.74*~~

Supplementary table 4.8.C: Pb isotope results

Sample #	^{208}Pb/^{204}Pb	1σ(%)	err correl. ^{208}Pb/^{206}Pb	^{204}Pb cps	1σ(%)	^{206}Pb cps	1σ(%)	^{207}Pb cps	1σ(%)	^{208}Pb cps	1σ(%)
010-020C-ii-pt-132-pb	ND	ND	ND	~~0.00~~	ND	~~0.04~~	~~22.31~~	~~0.04~~	~~21.60~~	~~0.08~~	~~19.57~~
010-020C-ii-pt-103-pb	ND	ND	ND	~~0.01~~	~~33.33~~	~~0.02~~	~~23.69~~	~~0.03~~	~~19.25~~	~~0.06~~	~~14.02~~
010-020C-iv-pt-50-pb	ND	ND	ND	~~0.00~~	ND	~~0.01~~	~~30.15~~	~~0.01~~	~~42.16~~	~~0.01~~	~~25.82~~
010-020C-iii-pt-56-pb	ND	ND	ND	~~0.00~~	ND	~~0.01~~	~~31.62~~	~~0.02~~	~~22.36~~	~~0.03~~	~~20.35~~
010-020C-ii-pt-135-pb	ND	ND	ND	~~0.00~~	ND	~~0.01~~	~~47.99~~	~~0.00~~	ND	~~0.01~~	~~37.88~~
010-022-thick-1-pt-8-pb	32.19	0.67	0.95	977.54	4.46	12269.81	4.47	13535.16	4.46	29560.30	4.45
010-022-thick-7-pt-16-Pb	32.19	0.78	0.94	896.97	4.63	11431.26	4.43	12605.30	4.43	27474.91	4.44
010-022-thick-7-pt-21-Pb	32.11	0.79	0.95	558.95	4.90	6889.94	4.77	7577.86	4.78	16532.70	4.78
010-022-thick-1-pt-7-pb	32.00	0.68	0.95	540.46	5.06	6757.14	5.09	7448.71	5.09	16238.06	5.10
010-022-v-pt-17-pb	31.93	0.68	0.95	453.68	4.80	5668.91	4.75	6242.72	4.74	13605.65	4.75
010-022-thick-6-pt-13-pb	32.06	0.69	0.95	370.67	8.40	4651.64	8.42	5130.60	8.44	11169.45	8.44
010-022-v-pt-9-pb	32.02	0.69	0.95	350.11	4.85	4387.72	4.82	4838.23	4.82	10528.31	4.82
010-022-thick-2-pt-12-pb	31.93	0.69	0.95	342.32	13.25	4284.03	13.25	4719.18	13.23	10282.29	13.26
010-022-thick-2-pt-11-pb	32.17	0.72	0.95	163.04	7.39	2052.61	7.41	2262.29	7.43	4927.06	7.41
010-022-thick-2-pt-10-pb	31.94	0.71	0.95	157.04	5.56	1965.32	5.59	2167.46	5.57	4715.68	5.57
010-022-v-pt-1-pb	31.91	0.72	0.95	126.21	4.49	1576.63	4.47	1738.47	4.45	3785.83	4.44
010-022-thick-7-pt-19-Pb	31.98	0.83	0.94	118.91	5.48	1486.91	5.57	1635.29	5.52	3567.76	5.57
010-022-thick-7-pt-17-Pb	32.07	0.85	0.95	94.18	6.97	1181.26	7.01	1302.40	7.02	2833.81	6.99
010-022-v-pt-3-pb	31.68	0.77	0.95	75.62	6.12	943.49	6.34	1040.97	6.36	2261.66	6.36
010-022-v-pt-3-pb	31.68	0.77	0.95	75.62	6.12	943.49	6.34	1040.97	6.36	2261.66	6.36
010-022-v-pt-12-pb	31.78	0.78	0.95	71.43	6.99	868.76	6.80	960.63	6.78	2139.33	7.02
010-022-thick-1-pt-6-pb	31.99	0.84	0.95	47.55	1.87	595.15	1.69	658.25	1.71	1428.57	1.69
010-022-thick-7-pt-18-Pb	31.99	0.96	0.95	39.39	7.28	493.57	7.23	542.43	7.24	1183.58	7.24
010-022-v-pt-11-pb	31.71	0.87	0.95	38.86	6.07	493.45	6.06	545.12	6.06	1185.08	6.07
010-022-thick-7-pt-15-Pb	32.35	0.99	0.95	30.14	5.48	380.60	5.25	418.41	5.30	914.41	5.28
010-022-thick-2-pt-9-pb	31.67	0.92	0.95	29.66	4.60	369.55	4.72	406.99	4.72	884.46	4.75
010-022-thick-6-pt-14-pb	32.28	0.97	0.95	23.88	4.64	299.69	4.38	330.75	4.44	721.20	4.45
010-022-thick-7-pt-20-Pb	31.90	1.22	0.95	14.17	3.96	181.96	4.03	200.71	3.98	436.85	4.02

Supplementary table 4.8.C: Pb isotope results

Sample #	^{208}Pb/^{204}Pb	1σ(%)	err correl. ^{208}Pb/^{206}Pb	^{204}Pb cps	1σ(%)	^{206}Pb cps	1σ(%)	^{207}Pb cps	1σ(%)	^{208}Pb cps	1σ(%)
010-022-v-pt-20-pb	*30.75*	*1.61*	*0.95*	*6.33*	*16.23*	*77.26*	*16.76*	*84.83*	*16.70*	*185.02*	*16.64*
010-022-v-pt-13-pb	*31.72*	*1.59*	*0.95*	*5.50*	*6.26*	*68.77*	*6.51*	*75.97*	*6.39*	*164.31*	*6.45*
010-022-v-pt-10-pb	*31.79*	*1.77*	*0.94*	*4.20*	*6.77*	*52.23*	*6.88*	*58.18*	*6.61*	*126.44*	*6.79*
010-022-v-pt-19-pb	~~*30.04*~~	~~*4.09*~~	~~*0.95*~~	~~*0.85*~~	~~*7.93*~~	~~*10.44*~~	~~*7.03*~~	~~*11.32*~~	~~*7.16*~~	~~*25.45*~~	~~*7.21*~~
010-023-thick-3A-pt-6-pb	32.25	0.86	0.95	46.23	4.40	675.76	4.49	664.37	4.50	1401.57	4.47
010-023-thick-8-pt-11-pb	32.36	1.07	0.95	18.05	2.66	244.44	2.71	261.37	2.68	558.18	2.63
010-023-thick-1A-pt-3-pb	32.61	1.18	0.95	12.39	4.42	163.29	3.77	173.00	3.81	371.17	3.70
010-023-thick-2A-pt-1-pb	31.75	1.22	0.95	12.21	4.82	161.62	4.69	171.48	4.65	365.16	4.64
010-023-thick-7-pt-7-pb	33.01	1.53	0.95	9.66	9.33	131.60	9.38	139.67	9.34	297.63	9.33
010-023-thick-4-pt-5-pb	*31.96*	*1.57*	*0.95*	*6.27*	*4.73*	*82.53*	*4.46*	*88.77*	*4.55*	*189.79*	*4.51*
010-023-thick-8-pt-10-pb	*32.54*	*1.72*	*0.96*	*5.88*	*3.18*	*78.46*	*2.95*	*83.55*	*2.93*	*179.13*	*2.81*
010-023-thick-9-pt-12-pb	*32.28*	*1.68*	*0.94*	*5.06*	*7.29*	*68.82*	*7.32*	*72.29*	*7.24*	*155.07*	*7.30*
010-023-thick-9-pt-14-pb	*33.21*	*1.81*	*0.95*	*5.16*	*9.15*	*68.64*	*8.40*	*73.04*	*8.51*	*157.19*	*8.48*
010-023-thick-8-pt-9-pb	~~*33.08*~~	~~*2.52*~~	~~*0.93*~~	~~*2.17*~~	~~*14.59*~~	~~*27.61*~~	~~*13.66*~~	~~*29.28*~~	~~*13.78*~~	~~*68.35*~~	~~*14.84*~~
010-023-thick-1A-pt-2-pb	~~*33.08*~~	~~*4.59*~~	~~*0.95*~~	~~*0.64*~~	~~*5.04*~~	~~*8.83*~~	~~*3.67*~~	~~*9.22*~~	~~*3.78*~~	~~*19.34*~~	~~*3.05*~~
010-023-thick-7-pt-8-pb	~~*34.56*~~	~~*6.03*~~	~~*0.96*~~	~~*0.44*~~	~~*8.07*~~	~~*5.56*~~	~~*6.48*~~	~~*5.96*~~	~~*6.43*~~	~~*13.09*~~	~~*6.62*~~
010-023-thick-4-pt-4-pb	~~*33.82*~~	~~*7.32*~~	~~*0.96*~~	~~*0.38*~~	~~*8.13*~~	~~*4.64*~~	~~*5.70*~~	~~*4.85*~~	~~*6.82*~~	~~*10.82*~~	~~*5.98*~~
010-023-thick-9-pt-13-pb	~~*34.67*~~	~~*6.22*~~	~~*0.93*~~	~~*0.33*~~	~~*6.51*~~	~~*4.50*~~	~~*2.49*~~	~~*4.55*~~	~~*2.31*~~	~~*9.96*~~	~~*2.86*~~
010-029B-250-180-po-67-rr	32.52	0.66	0.95	2095.77	6.25	27356.28	6.23	29316.74	6.23	64053.18	6.25
010-029B-250-180-pt-72-rr	32.52	0.67	0.95	1112.71	3.78	14566.23	3.79	15567.38	3.79	33983.93	3.79
010-029B-ii-iii-pt-10	32.57	0.78	0.94	813.98	3.34	10622.81	3.34	11231.80	3.36	24869.03	3.38
010-029B-250-180-pt-68-rr	32.44	0.67	0.95	812.60	8.93	10582.49	8.94	11358.24	8.94	24768.16	8.95
010-029B-ii-iii-pt-17	32.26	0.79	0.94	581.80	3.78	7524.97	3.75	7903.40	3.73	17633.29	3.78
010-029B-ii-iii-pt-11	32.29	0.79	~~0.94~~	561.67	4.55	7242.47	4.51	7640.81	~~4.54~~	~~17017.56~~	~~4.53~~
010-029B-ii-iii-po-27-pb-repeat	32.30	0.70	0.95	377.44	2.53	4910.78	2.50	5249.57	2.50	11434.03	2.50
010-029B-ii-iii-po-19	32.06	0.81	0.94	186.09	8.40	2388.02	8.32	2501.06	8.35	5809.82	8.70
010-029B-250-180-po-62-rr	32.39	0.73	0.95	116.88	2.45	1524.39	2.41	1638.51	2.42	3559.33	2.40
010-029B-ii-iii-pt-15	32.23	0.84	0.95	117.39	2.25	1522.24	2.11	1595.62	2.06	3552.97	2.12

Supplementary table 4.8.C: Pb isotope results

Sample #	^{208}Pb/^{204}Pb	1σ(%)	err correl. ^{208}Pb/^{206}Pb	^{204}Pb cps	1σ(%)	^{206}Pb cps	1σ(%)	^{207}Pb cps	1σ(%)	^{208}Pb cps	1σ(%)
010-029B-ii-iii-pt-6	32.52	0.92	0.94	76.02	8.58	993.91	8.46	1057.83	8.52	2315.93	8.52
010-029B-250-180-pt-45-rr	32.45	0.86	0.95	41.11	3.93	538.37	3.82	578.33	3.83	1254.79	3.86
010-029B-ii-iii-pt-28-Pb-repeat	32.49	1.17	0.96	17.95	8.99	235.54	8.66	252.13	8.73	548.50	8.72
010-029B-ii-iii-po-7	31.96	1.31	0.96	17.81	5.29	229.27	5.46	242.86	5.40	534.49	5.44
010-029B-250-180-po-52-rr	32.70	1.30	0.95	11.09	2.21	148.26	1.77	160.25	2.08	343.52	1.84
010-029B-ii-iii-po-9	*33.17*	*2.15*	*0.94*	*3.80*	*8.81*	*49.89*	*8.77*	*52.94*	*8.64*	*116.96*	*8.74*
010-029B-ii-iii-po-21	~~*31.43*~~	~~*3.47*~~	~~*0.94*~~	~~*1.09*~~	~~*4.55*~~	~~*13.21*~~	~~*3.77*~~	~~*13.78*~~	~~*3.29*~~	~~*31.21*~~	~~*3.49*~~
010-029B-ii-iii-pt-2	~~*34.74*~~	~~*4.52*~~	~~*0.96*~~	~~*0.61*~~	~~*6.97*~~	~~*9.08*~~	~~*7.37*~~	~~*9.48*~~	~~*6.88*~~	~~*20.73*~~	~~*7.06*~~
010-029B-ii-iii-pt-13	ND	ND	ND	~~*0.69*~~	~~*13.52*~~	~~*8.05*~~	~~*14.23*~~	~~*8.58*~~	~~*13.78*~~	~~*18.53*~~	~~*13.85*~~
010-029B-ii-iii-pt-4	~~*37.95*~~	~~*7.51*~~	~~*0.96*~~	~~*0.26*~~	~~*7.74*~~	~~*3.65*~~	~~*4.88*~~	~~*3.79*~~	~~*4.94*~~	~~*8.33*~~	~~*4.47*~~
010-029B-ii-iii-po-1	~~*34.95*~~	~~*7.43*~~	~~*0.95*~~	~~*0.23*~~	~~*7.27*~~	~~*3.03*~~	~~*3.50*~~	~~*3.07*~~	~~*3.30*~~	~~*6.93*~~	~~*3.17*~~
010-029B-ii-iii-pt-18	~~*40.19*~~	~~*10.70*~~	~~*0.97*~~	~~*0.18*~~	~~*8.94*~~	~~*2.23*~~	~~*3.39*~~	~~*2.31*~~	~~*4.26*~~	~~*5.31*~~	~~*3.22*~~
010-029B-ii-iii-pt-8	ND	ND	ND	~~*0.20*~~	~~*10.27*~~	~~*1.94*~~	~~*6.53*~~	~~*2.02*~~	~~*6.48*~~	~~*4.61*~~	~~*5.79*~~
010-029B-ii-iii-pt-20	ND	ND	ND	~~*0.01*~~	~~*65.02*~~	~~*0.03*~~	~~*60.91*~~	~~*0.03*~~	~~*41.12*~~	~~*0.05*~~	~~*54.84*~~
010-030-thick-1-pt-2-pb	31.63	1.14	0.95	10.36	3.60	122.75	3.15	137.73	3.11	306.12	3.21
010-030-thick-4-pt-5-pb	*32.84*	*1.41*	*0.94*	*5.50*	*2.08*	*68.18*	*1.81*	*76.07*	*1.88*	*165.40*	*1.82*
010-030-thick-1-pt-1-pb	*31.99*	*1.46*	*0.95*	*5.38*	*8.90*	*65.54*	*9.15*	*74.33*	*9.04*	*162.75*	*9.03*
010-030-thick-2-pt-3-pb	~~*32.11*~~	~~*2.04*~~	~~*0.95*~~	~~*2.04*~~	~~*5.40*~~	~~*24.17*~~	~~*4.95*~~	~~*27.85*~~	~~*4.93*~~	~~*60.69*~~	~~*4.90*~~
BCR_multiPb_220308_@1	38.72	0.98	0.941	34.73	5.42	655.43	5.38	539.80	5.38	1263.84	5.45
BCR_multiPb_220308_@2	38.25	1.00	0.954	38.20	4.98	709.16	4.91	587.52	4.84	1370.01	4.87
BCR_multiPb_220308_@3	39.37	0.97	0.951	36.87	5.04	699.42	4.81	577.70	4.81	1352.67	4.82
BCR_multiPb_220308_@4	38.75	0.97	0.944	37.65	4.60	715.11	4.71	592.80	4.67	1387.06	4.69
BCR_multiPb_220308_@5	38.66	0.98	0.952	37.97	4.79	712.90	4.70	592.68	4.74	1377.81	4.76
BCR_multiPb_220308_@6	38.52	0.97	0.951	37.36	4.75	701.95	4.80	577.76	4.77	1355.33	4.81
BCR_multiPb_220308_@7	38.82	0.95	0.950	41.55	4.16	782.66	4.15	647.61	4.22	1514.83	4.15
BCR_multiPb_220308_@8	38.66	0.97	0.950	40.80	4.25	762.92	4.30	625.62	4.38	1479.01	4.32
BCR_multiPb_220308_@9	38.84	0.96	0.950	40.01	4.24	749.77	4.15	614.14	4.19	1455.81	4.21
BCR_multiPb_220309_@1	39.05	0.91	0.957	31.39	5.20	593.69	5.12	500.54	5.19	1173.70	5.17

Supplementary table 4.8.C: Pb isotope results

Sample #	^{208}Pb/^{204}Pb	1σ(%)	err correl. ^{208}Pb/^{206}Pb	^{204}Pb cps	1σ(%)	^{206}Pb cps	1σ(%)	^{207}Pb cps	1σ(%)	^{208}Pb cps	1σ(%)
BCR_multiPb_220309_@10	38.23	0.85	0.956	44.06	3.77	822.84	3.88	680.71	3.89	1589.56	3.86
BCR_multiPb_220309_@11	38.64	0.85	0.956	43.78	3.77	822.69	3.86	681.15	3.92	1595.09	3.90
BCR_multiPb_220309_@12	38.63	0.85	0.956	43.94	3.91	825.57	3.99	682.35	3.98	1595.63	3.99
BCR_multiPb_220309_@2	38.31	0.89	0.956	35.35	4.81	661.85	5.00	546.83	4.98	1277.53	4.94
BCR_multiPb_220309_@3	38.88	0.90	0.957	34.42	4.68	661.78	4.87	548.26	4.84	1279.36	4.86
BCR_multiPb_220309_@4	39.04	0.90	0.957	34.10	4.74	655.76	4.76	543.41	4.77	1269.63	4.80
BCR_multiPb_220309_@5	39.10	0.85	0.956	44.36	3.93	838.31	3.77	696.20	3.81	1622.57	3.83
BCR_multiPb_220309_@6	38.63	0.85	0.956	44.78	3.78	839.39	3.74	695.42	3.75	1620.34	3.73
BCR_multiPb_220309_@7	38.59	0.85	0.956	44.49	3.79	834.83	3.77	689.08	3.81	1614.53	3.78
BCR_multiPb_220309_@8	38.71	0.85	0.956	44.07	3.67	827.27	3.69	687.64	3.69	1601.85	3.65
BCR_multiPb_220309_@9	39.08	0.86	0.956	42.68	3.91	816.18	3.79	676.22	3.85	1580.43	3.83
BCR_multiPb_220310_@1	38.79	0.87	0.956	40.20	4.12	759.00	4.17	629.05	4.16	1471.40	4.14
BCR_multiPb_220310_@10	38.92	0.84	0.956	46.30	4.02	869.33	4.01	721.50	4.04	1685.07	4.02
BCR_multiPb_220310_@11	38.49	0.84	0.952	46.77	4.10	872.89	4.06	720.32	4.05	1688.21	4.07
BCR_multiPb_220310_@12	38.92	0.87	0.959	47.07	4.03	884.97	3.98	730.92	4.02	1713.96	4.00
BCR_multiPb_220310_@13	38.34	0.90	0.962	47.31	3.90	881.53	4.03	734.00	4.05	1712.38	4.08
BCR_multiPb_220310_@14	38.64	0.84	0.956	47.07	3.96	883.44	4.05	730.75	4.01	1713.26	4.02
BCR_multiPb_220310_@15	38.41	0.84	0.956	47.59	3.90	887.19	3.90	733.78	3.97	1716.95	3.94
BCR_multiPb_220310_@16	39.34	0.84	0.956	48.34	3.70	917.11	3.86	762.43	3.83	1783.07	3.84
BCR_multiPb_220310_@17	38.91	0.84	0.956	47.83	3.86	898.72	3.86	744.45	3.89	1744.00	3.89
BCR_multiPb_220310_@18	38.89	0.92	0.964	48.64	3.93	918.80	3.88	760.07	3.86	1778.88	3.89
BCR_multiPb_220310_@19	38.92	0.84	0.956	47.58	3.86	896.49	3.84	741.98	3.84	1736.30	3.85
BCR_multiPb_220310_@2	38.62	0.87	0.956	40.53	3.99	761.41	4.00	629.43	4.02	1470.43	4.04
BCR_multiPb_220310_@3	38.80	0.87	0.954	40.56	4.01	764.65	4.01	633.08	3.98	1477.12	3.99
BCR_multiPb_220310_@4	38.89	0.86	0.955	42.59	4.30	803.11	4.27	666.59	4.27	1555.46	4.26
BCR_multiPb_220310_@5	38.66	0.85	0.956	45.01	4.23	842.20	4.18	699.01	4.15	1632.42	4.16
BCR_multiPb_220310_@6	38.41	0.85	0.956	45.80	4.18	851.20	4.04	706.91	4.03	1651.86	4.03
BCR_multiPb_220310_@7	38.50	0.85	0.956	45.78	4.12	856.43	4.14	709.05	4.17	1662.36	4.17

Supplementary table 4.8.C: Pb isotope results

			err correl.								
Sample #	$^{208}Pb/^{204}Pb$	1σ(%)	$^{208}Pb/^{206}Pb$	^{204}Pb cps	1σ(%)	^{206}Pb cps	1σ(%)	^{207}Pb cps	1σ(%)	^{208}Pb cps	1σ(%)
BCR_multiPb_220310_@8	38.59	0.91	0.962	44.28	4.24	841.60	4.14	697.75	4.14	1632.71	4.16
BCR_multiPb_220310_@9	38.59	0.85	0.955	45.59	4.23	852.87	4.23	706.39	4.22	1651.92	4.25
BCR_multiPb_220311_@1	38.68	0.84	0.956	47.07	4.18	878.54	3.95	729.96	4.00	1702.13	3.99
BCR_multiPb_220311_@11	38.76	0.88	0.956	38.15	4.26	717.54	4.18	594.87	4.25	1388.28	4.23
BCR_multiPb_220311_@2	38.47	0.89	0.963	46.19	4.07	862.68	3.98	715.42	3.94	1674.39	3.97
BCR_multiPb_220311_@3	38.63	0.84	0.955	46.62	3.93	872.73	3.88	727.57	3.87	1699.53	3.92
BCR_multiPb_220311_@4	39.18	0.85	0.956	45.16	4.15	854.13	4.00	707.36	3.99	1655.34	4.04
BCR_multiPb_220311_@5	38.76	0.85	0.956	45.24	4.21	851.60	4.14	704.67	4.16	1648.73	4.12

Italics - 206Pb < 100 cps

Strikethrough - 206Pb<50 cps (<10 cps for 76 & 86 ratios). Not displayed on figures.

ND - no counts or div/0

pt=pentlandite

po=pyrrhotite

std=standard

cps=counts per second

Chapter 5

Conclusions and outlook

5.1. Conclusions

This thesis set out to elucidate the nature of geodynamic processes that formed the cores of the Earth's first lasting cratons in the Eoarchean. This controversial subject was explored primarily through multiple sulfur isotope analysis of igneous lithologies found in the North Atlantic Craton's Eoarchean Itsaq Gneiss Complex (IGC) in southern West Greenland. Taken together, the results presented in the previous three chapters demonstrate that examples of all studied lithologies contain mass independently fractionated sulfur (MIF-S). Indeed, only a minority of the analyzed lithologies lack evidence for MIF-S in the form of nonzero $\Delta^{33}S$ values that fall outside the range typically produced by mass dependent processes, per LaFlamme et al. (2018b). This implies that most, if not all, igneous lithologies found in the IGC contain material reworked from the Earth's surface in the Eoarchean. Taken together, the sheer abundance of evidence for surface-derived material in Eoarchean igneous lithologies including TTGs, metabasalts, and peridotites presented in the last three chapters (Figure 5.1) forms an argument of its own in favor of geodynamic processes recycling material from Earth's surface in the Eoarchean. At least in the IGC, incorporation of surface-derived material during the formation of igneous lithologies was more the rule than the exception. This implies extensive reworking of material from Earth's surface into Earth's deep interior took place in the Eoarchean, including, as appears very likely given the probable mantle origins of the SOISB peridotites discussed in the previous two chapters, the Earth's mantle.

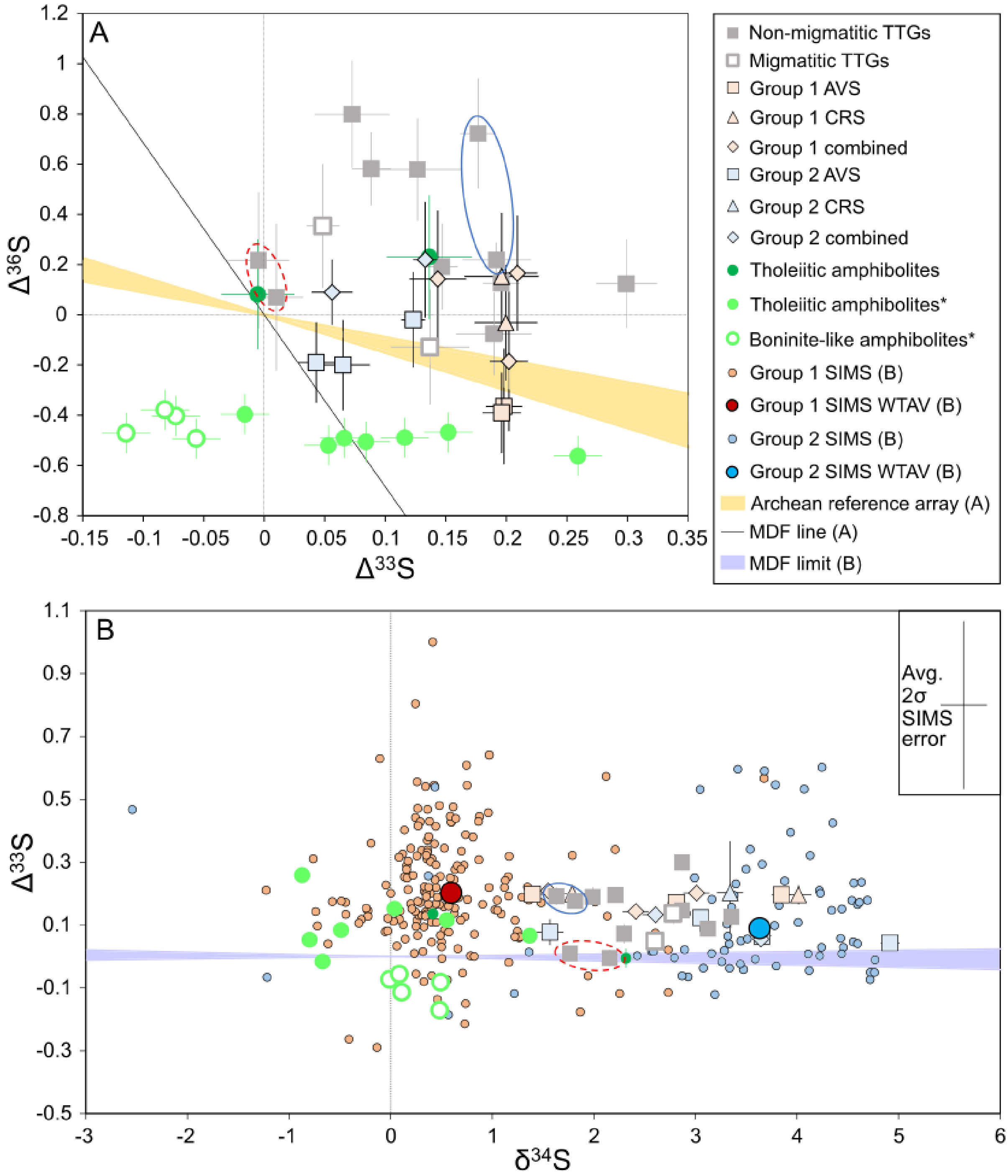

Figure 5.1: Compilation of all sulfur isotope results from the previous three chapters, including bulk TTG results from the second chapter, bulk Group 1 and Group 2 peridotite results from the third chapter, and Group 1 and Group 2 in-situ results collected with SIMS from the fourth chapter, along with ISB metabasalt results from Siedenberg et al. (2016), marked in the legend with asterisks. The Archean reference array covering typical values of sulfur subject to MIF-S in the Archean (Farquhar et al., 2000; Ono, 2017; Zerkle et al., 2012) and a line representing mass dependent fractionation caused by processes such as microbial sulfate reduction (Ono et al., 2006) are also shown for comparison in A. In B, the typical range of isotopic compositions resulting from mass dependent fractionation (MIF) (LaFlamme et al., 2018b) is also shown. SIMS results only appear in B because Δ^{36}S was not

measured with SIMS. As in the second chapter, TTG duplicate bulk measurements are connected with ellipses, and as in the third chapter, peridotite duplicate bulk measurements are shown as weighted averages.

These findings agree with and support a growing body of evidence presented in recent years for the early onset of crustal recycling in the Eoarchean (e.g., Antonelli et al., 2021; Drabon et al., 2022; Garde et al., 2020; Hastie et al., 2023; Nutman, 2023; Nutman et al., 2021; Windley et al., 2021), including processes similar to modern subduction in which plates override one another, forming settings similar to mantle wedges that this thesis suggests the SOISB peridotites came from. Models of crust formation that do not include the horizontal movement of plates such as vertical stacking of basalt flows and reworking of crust in large, plateau-like structures (e.g., Johnson et al., 2017; Webb et al., 2020) are not applicable at least to the studied IGC. Such models do not allow for the extensive recycling of crust into the mantle prior to eclogitization and removal of elements such as sulfur. This leaves no mechanism for mantle rocks to be overprinted by surface-derived sulfur, as the SOISB peridotites were according to the model proposed in this thesis.

It should be noted that, while this thesis finds strong evidence for horizontal tectonic processes active in the IGC in the Eoarchean, that is, the horizontal movement of plates over one another with the potential to form mantle wedges in between, this does not mean that no other tectonic processes were active in the Eoarchean. Other processes of crust formation and reworking also operated in the Eoarchean and subsequently. Even on the modern Earth, the Hawaiian Islands serve as a limited example of vertical crust-building processes similar to those invoked by models that do not include horizontal tectonics, including the formation of evolved, quartz-bearing lithologies such as tonalites in such settings (Fodor, 2001). Furthermore, unambiguous evidence for vertical tectonic processes including internal reworking of Archean crust to form TTGs may be found in Archean terranes outside the IGC, notably dome and keel structures found in Australia's East Pilbara Terrane (e.g., Roberts and Tikoff, 2021). Such TTG-forming vertical tectonic processes were active throughout the Archean including the Neoarchean (e.g., Liu et al., 2023). The type of vertical reworking of the crust that formed dome and keel structures allowed supracrustal rocks including sediments to be reworked into TTGs, and this process could explain the presence of MIF-S in TTGs as shown in the second chapter of this thesis if the sulfur isotope results from those rocks were taken only by themselves. However, the interpretation of the geodynamic mechanisms that introduced MIF-S to the IGC TTGs presented in this thesis, informed by geological context and prior studies, is different. What vertical tectonism of this kind also cannot explain is the introduction of MIF-S into mantle peridotites, as this thesis presents evidence for in the third and fourth chapters. Another process is necessary here, one including horizontal as well as vertical displacement of plates relative to one another. It would be a mistake to look at one Archean craton and extrapolate from evidence for a single geodynamic process found there that this was the only process operating on Earth at this time to the exclusion of all others.

While we may say that the horizontal tectonic processes active in the Eoarchean IGC were similar to modern plate tectonics, insofar as plates very likely overrode one another and were at least at times subducted into the mantle, it is not necessarily the case that a fully modern system of continuously moving tectonic plates across the globe was active in the Eoarchean. The horizontal tectonic processes that formed the IGC may well have been restricted in space and time, and did not necessarily operate continuously or across the entire planet (e.g., O'Neill and Zhang, 2019). Researchers arguing for a relatively recent beginning to modern “plate tectonics” often define the term more narrowly than any scenario in which plates override one another horizontally or even subduct, for example, by arguing that plate tectonics requires sustained, extensive subduction of plates into the deep mantle (e.g., Stern et al., 2016) or a global network of plates defined by narrow boundaries (e.g., Brown et al., 2020). Therefore, arguments about the timing of the onset of modern “plate tectonics” can devolve into semantics if terms are not carefully defined and agreed upon (e.g., Hawkesworth et al., 2020). This thesis does not claim that plate tectonics in a fully modern sense began in the Eoarchean or any other specific time defined as much by use of language as any discernable process or set of processes. Enough to say that like the modern Earth, the Eoarchean Earth was a geodynamically diverse planet with multiple processes of crustal formation and reworking in operation (e.g., Kuang et al., 2023; Figure 5.2). This thesis finds that the processes active at this time included the horizontal movement and overriding of plates, along with the formation of mantle wedge-like environments above subducting portions of plates in the IGC. The geodynamic processes identified in this thesis have been described in past chapters as modern-like or horizontal tectonics.

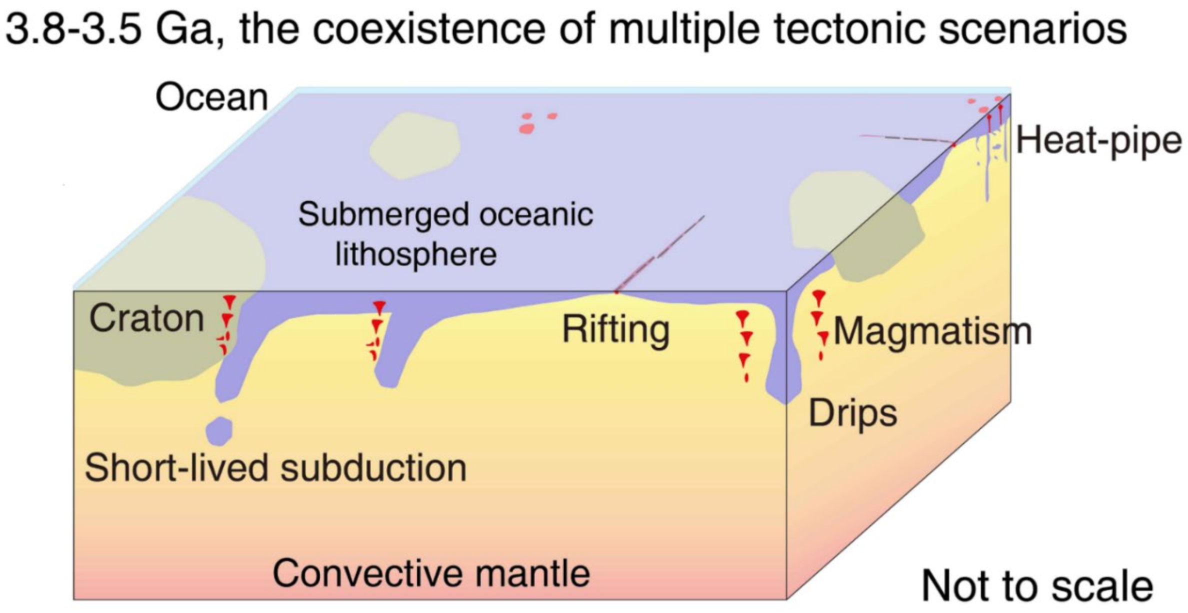

Figure 5.2: Multiple geodynamic processes operating in the Eoarchean, reprinted from Kuang et al. (2023).

5.2. Outlook for future research

The sulfur isotopic compositions of TTGs and peridotites from the IGC are best explained by the incorporation and mixing of two distinct surface-derived sources. One of these endmembers is sediment with positive $\Delta^{33}S$. Such sediment is well represented in the IGC, notably in the Isua Supracrustal Belt (e.g., Baublys et al., 2004; Mojzsis et al., 2003; Papineau and Mojzsis, 2006; Whitehouse, 2013; Whitehouse et al., 2005). The second surface-derived endmember is expected to have low to negative $\Delta^{33}S$ and positive $\delta^{34}S$, consistent with Archean seawater sulfate derived deposits such as barites that have been identified in Paleoarchean (e.g., Roerdink et al., 2012) and Mesoarchean terranes (e.g., Bao et al., 2007; Farquhar et al., 2000; Montinaro et al., 2015). Barite deposits of Eoarchean age with isotopic compositions similar to those found in the Paleoarchean and Mesoarchean have not yet been identified. However, multiple sulfur isotope values consistent with seawater-derived sulfate have been found in the ISB in pyrite grains within a rock described as a quartz-biotite gneiss (Hu et al., 2003; Siedenberg et al., 2016). Recent studies have shown that Phanerozoic barite deposits may be replaced by pyrite, along with carbonate and silicate accessory minerals that contain Ba such as witherite, hyalophane, and cymerite during diagenesis (Fernandes et al., 2017; Grema et al., 2022). Diagenesis and metamorphism, notably in the reducing environment of the Eoarchean, may have had similar effects on Eoarchean barite deposits. If Ba enriched accessory minerals can be found in association with pyrite in Eoarchean lithologies, notably where pyrite grains containing sulfur with high $\delta^{34}S$ and negative $\Delta^{33}S$ values consistent with Archean seawater have been identified, it would demonstrate that barite deposits, possibly similar to those observed in Paleoarchean and later settings, also formed in the Eoarchean. It is also possible that future work may identify relatively well-preserved deposits of Eoarchean barite. Such deposits may represent the missing Eoarchean seawater sulfate endmember invoked in previous chapters.

Some sulfide compositions in the SOISB peridotites, measured by microprobe and reported in the fourth chapter of this thesis, may represent either Fe-rich pentlandite or horomanite, a sulfide with crystallography that is distinct from pentlandite and has been reported to occur in peridotites with origins in the mantle (Kitakaze et al., 2011; Ozawa, 2004). This thesis suggests that the SOISB peridotites likely also have mantle origins, and the possibility that horomanite exists along with pentlandite within the SOISB peridotites should therefore also be considered. Micro X-Ray diffraction (µXRD) analysis of sulfide grains with compositions consistent with horomanite could determine whether horomanite is present in the SOISB peridotites. Improved constraints on sulfide crystallography may lead to improved SIMS $\delta^{34}S$ measurement accuracy of SOISB peridotite sulfides, as well as sulfides hosted in other peridotites, through better standardization. It should be noted that any potential instrumental mass fractionation resulting from the possible presence of horomanite in the SOISB peridotites is mass dependent, and therefore should not influence any reported $\Delta^{33}S$ values in this thesis.

Finally, a number of lithologies from southern West Greenland were measured for bulk multiple sulfur isotopes as part of this research that did not fit into any previous chapter, and the results are presented here as a potential starting point or addition to future studies of the region. These include additional boninite-like and tholeiitic amphibolites from the ISB, some of which were measured for major and trace elements in Szilas et al. (2015) and for H and O isotope compositions in Pope et al. (2012). Samples measured in these previous studies are indicated in Table 5.1 at the end of this chapter. One sample of magnesite found in association with meatbasalt in Isua was also analyzed. Four banded iron formation (BIF) samples from the ISB were also analyzed, as well as an organic carbon bearing, black, slaty metaturbidite from the same ISB locality where ^{13}C depleted carbon was identified in a different sample of similar metasedimentary rock, possibly indicating the presence of life >3.7 Ga (Rosing, 1999). For some of these samples, sequential extraction and separate analysis of acid volatile monosulfide sulfur (AVS) and chromium reducible disulfide sulfur (CRS) was attempted, following the same extraction methods modified from Canfield et al. (1986) and

Tuttle et al. (1986) as well as analytical methods following Siedenberg et al. (2016) described in the Methods section of Chapter 3. For other samples all sulfide sulfur was extracted for combined analysis in one step following the extraction and analysis methods of Siedenberg et al. (2016) described in the Methods sections of Chapters 2 and 3. The results of successful extractions and multiple sulfur isotope analyses of extracted sulfur are presented accordingly in Figure 5.3 and Table 5.1, in the latter alongside five concurrently measured IAEA-S1 standards.

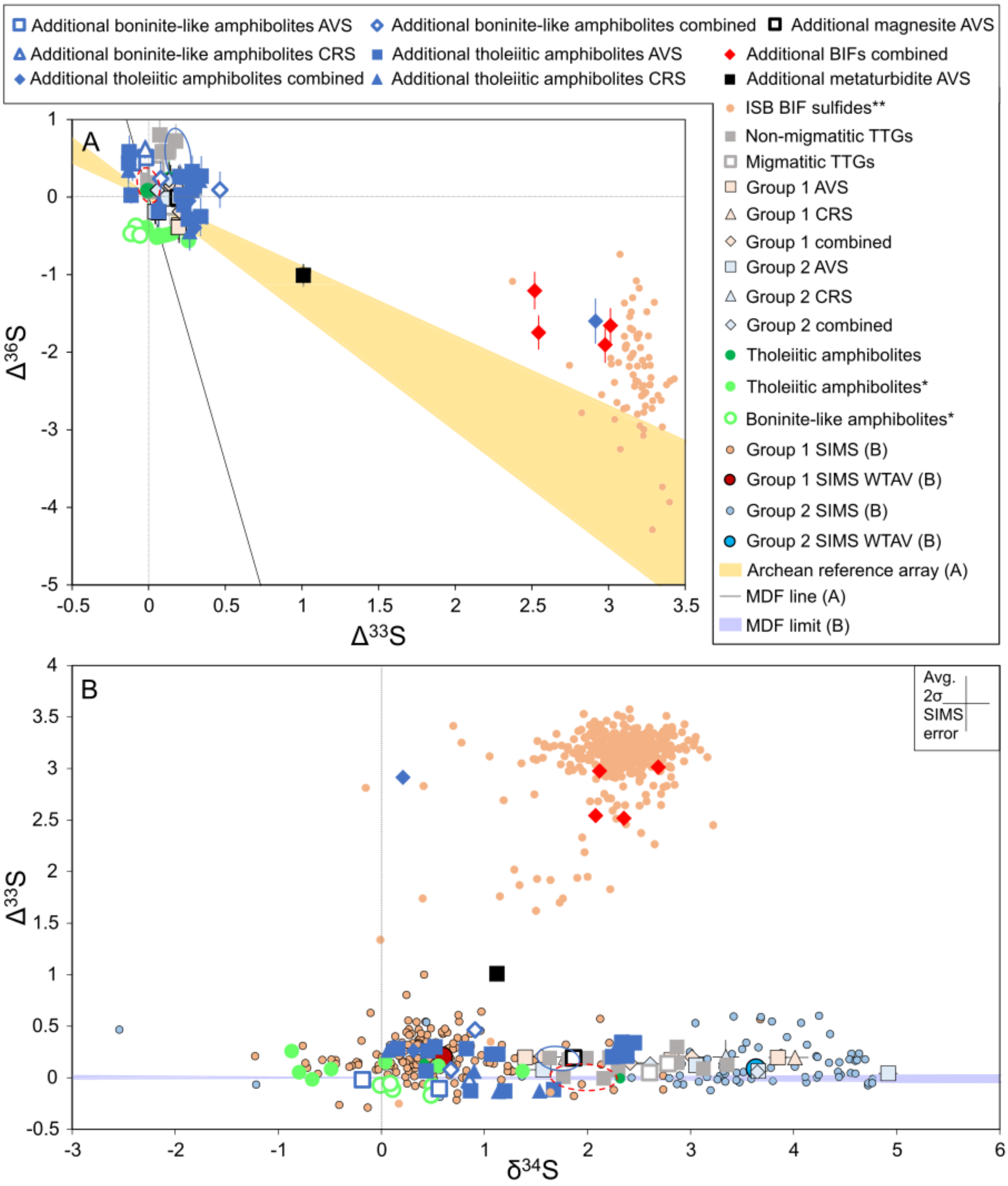

Figure 5.3: Additional bulk results plotted with all data from Figure 5.1 and banded iron formation (BIF) in-situ sulfide data from existing literature (Mojzsis et al., 2003; Whitehouse, 2013; marked with a double asterisk) shown for comparison. Acid volatile sulfur (AVS) and chromium reducible sulfur (CRS) were sometimes extracted separately, and in other cases combined sulfide sulfur was extracted in one step, as in samples in the third chapter. Note that the average 2σ SIMS error shown in B applies to measurements from the fourth chapter of this thesis. SIMS errors associated with literature data are found in Mojzsis et al. (2003) and Whitehouse (2013).

The BIF bulk results overlap with published SIMS analyses of sulfides in ISB lithologies of the same kind (Mojzsis et al., 2003; Whitehouse, 2013), with positive Δ^{33}S typical of sediments including sulfide subject to MIF-S in the Archean atmosphere and falling above the Archean reference array in Δ^{33}S-Δ^{36}S space (Figure 5.3). This offset from the Archean reference array, also observed in the majority of published SIMS results shown for comparison that include Δ^{36}S analyses (Whitehouse, 2013) in Figure 5.3, may be the result of mass dependent Rayleigh fractionation processes (Ono et al., 2006). Whether or not these mass dependent processes were biologically mediated is unclear. The boninite-like and tholeiitic amphibolites largely overlap with other IGC igneous lithologies published in previous chapters and Siedenberg et al. (2016). While none of the additional metabasalts display Δ^{36}S values as high as the highest observed in the TTGs, it is notable that some do have positive Δ^{36}S and negative Δ^{33}S (Figure 5.3). This suggests that these metabasalts contain sulfur that includes and in some cases is dominated by a seawater sulfate derived endmember with negative Δ^{33}S and elevated Δ^{36}S. This endmember may have had a sulfur isotope composition similar to Mesoarchean barites from South Africa's Fig Tree Group invoked in the second chapter (Bao et al., 2007; Farquhar et al., 2000; Montinaro et al., 2015). Notably, the additional data include the first ISB tholeiitic amphibolies with negative, sulfate dominated bulk Δ^{33}S yet reported. One ISB amphibolite sample, an outlier with a Δ^{33}S value of +2.91‰, is strongly dominated by sedimentary sulfur and falls within the range of BIF samples (Figure 5.3). The metaturbidite from the locality where ^{13}C depleted carbon was reported by Rosing (1999) falls on the Archean reference array (Figure 5.3A), unlike the analyzed BIF samples. This suggests that if any life was present in this locality and was responsible for fractionating carbon, it did not also significantly fractionate sulfur via biologically mediated Rayleigh distillation processes described by Ono et al. (2006). Δ^{33}S in this sample is not as strongly positive in the in the metaturbidite as in the BIF samples, indicating the former may include magmatic sulfur in addition to sulfur subject to MIF, possibly from an originally magmatic terrigenous component the BIF samples lack.

The additional amphibolite results further demonstrate the ubiquity of MIF-S in igneous lithologies in the IGC, buttressing the case for widespread recycling of surface-derived material into the magmatic system in the Eoarchean. The additional amphibolites with negative $\Delta^{33}S$ are of particular interest as the sulfur these rocks contain appears to be dominated by seawater sulfate, similar to the boninite-like metabasalts reported by Siedenberg et al. (2016). The existence of such an endmember in the Eoarchean is consistent with interpretations of results in previous chapters and further suggests that future work may allow this endmember to be found and characterized in the IGC, possibly in the form of barite such as that found in Paleoarchean and younger deposits elsewhere (e.g., Bao et al., 2007; Farquhar et al., 2000; Montinaro et al., 2015; Roerdink et al., 2012). Even if Eoarchean barite cannot be found in the IGC, barite's alteration products, such as hyalophane and cymrite, may still be identified in IGC rocks following the methods of Fernandes et al. (2017) and Grema et al. (2022). If such Ba-rich minerals can be identified, associated sulfides may carry the isotopic signature of the as-yet uncharacterized Eoarchean sulfate endmember. Together with careful in-situ analysis of sulfide mineralogy, ideally including μXRD, the isotope composition of this endmember may be determined in such sulfides via in-situ analytical methods such as SIMS. The characterization of this endmember may allow for constraints on the relative contribution of different surface-derived sulfur sources to IGC lithologies and offer new insights into the processes that formed these rocks.

Table 5.1: Summary of additional bulk S isotope analyses

sample name	extraction	sample type	description	other analyses published in	provided by
06-07AA	AVS	Boninite-like metabasalt	boninite cumulate	Szilas et al. 2015	Boyd
06-07AA	CRS	Boninite-like metabasalt	boninite cumulate	Szilas et al. 2015	Boyd
B03	combined	Boninite-like metabasalt	Isua boninite		Szilas
B09	combined	Boninite-like metabasalt	Isua boninite		Szilas
ECP01-10	AVS	Boninite-like metabasalt	boninite cumulate	Szilas et al. 2015	Boyd
208262	AVS	Tholeiitic metabasalt	Isua greenschist		Szilas
208262	AVS	Tholeiitic metabasalt	Isua greenschist		Szilas
208265	AVS	Tholeiitic metabasalt	Isua Lens A (tholeiitic cumulate)		Szilas
07-07	AVS	Tholeiitic metabasalt	Isua Metabasalt	Szilas et al. 2015; Pope et al. 2012	Boyd
07-07	CRS	Tholeiitic metabasalt	Isua Metabasalt	Szilas et al. 2015; Pope et al. 2012	Boyd
208299 2	combined	Tholeiitic metabasalt	Isua amphibolite		Szilas
AJ31 DAP	AVS	Tholeiitic metabasalt	Powder		Boyd
AJ31 Ocelli	AVS	Tholeiitic metabasalt	Ocelli and amygdule		Boyd
AJ34 B	combined	Tholeiitic metabasalt	Isua Metabasalt		Boyd
AJ35	AVS	Tholeiitic metabasalt	Powder		Boyd
AJ35	CRS	Tholeiitic metabasalt	Powder		Boyd
AJ36	combined	Tholeiitic metabasalt	Isua Metabasalt		Boyd
AJ37	AVS	Tholeiitic metabasalt	Powder		Boyd
AJ37	CRS	Tholeiitic metabasalt	Powder		Boyd
AJ38	combined	Tholeiitic metabasalt	Isua Metabasalt		Boyd
ECP03-10 CI	AVS	Tholeiitic metabasalt	basalt cumulate	Szilas et al. 2015; Pope et al. 2012	Boyd
ECP03-10 CI	CRS	Tholeiitic metabasalt	basalt cumulate	Szilas et al. 2015	Boyd
ECP03-10 CII	AVS	Tholeiitic metabasalt	Szilas basalt cumulate	Szilas et al. 2015; Pope et al. 2012	Boyd
ECP03-10 CII	CRS	Tholeiitic metabasalt	Szilas basalt cumulate	Szilas et al. 2015; Pope et al. 2012	Boyd
ECP03-10A	AVS	Tholeiitic metabasalt	basalt cumulate	Szilas et al. 2015; Pope et al. 2012	Szilas
ECP08-07A	AVS	Tholeiitic metabasalt	powder	Szilas et al. 2015	Boyd
ECP08-08	AVS	Tholeiitic metabasalt	basalt cumulate	Szilas et al. 2015; Pope et al. 2012	Szilas
ECP08-08	AVS	Tholeiitic metabasalt	basalt cumulate	Szilas et al. 2015; Pope et al. 2012	Boyd

Table 5.1: Summary of additional bulk S isotope analyses

sample name	extraction	sample type	description	other analyses published in	provided by
ECP08-08	CRS	Tholeiitic metabasalt	basalt cumulate	Szilas et al. 2015; Pope et al. 2012	Szilas
ECP07-A Mag.	AVS	Magnesite	Magnesite		Boyd
2008	AVS	Sediment (metaturbidite)	Isua metasediment (Rosing 1999 locality)		Szilas
207529	combined	Sediment (BIF)	Isua BIF (long section)		Szilas
207534	combined	Sediment (BIF)	Isua BIF with sulfide		Szilas
207537	combined	Sediment (BIF)	Isua BIF with sulfide		Szilas
207540	combined	Sediment (BIF)	Isua BIF with sulfide		Szilas
IAEA-S1		standard	standard		
IAEA-S1		standard	standard		
IAEA-S1		standard	standard		
IAEA-S1		standard	standard		
IAEA-S1		standard	standard		

Table 5.1: Summary of additional bulk S isotope analyses

sample name	extraction	sample type	$\delta^{34}S$ [‰]	$2\sigma(\delta^{34}S)$ [‰]	$\Delta^{33}S$ [‰]	$2\sigma(\Delta^{33}S)$ [‰]	$\Delta^{36}S$ [‰]	$2\sigma(\Delta^{36}S)$ [‰]
06-07AA	AVS	Boninite-like metabasalt	-0.18	0.02	-0.02	0.03	0.51	0.07
06-07AA	CRS	Boninite-like metabasalt	0.85	0.01	-0.02	0.03	0.62	0.13
B03	combined	Boninite-like metabasalt	0.91	0.01	0.46	0.03	0.09	0.23
B09	combined	Boninite-like metabasalt	0.67	0.01	0.08	0.02	0.24	0.22
ECP01-10	AVS	Boninite-like metabasalt	0.56	0.01	-0.11	0.03	0.44	0.23
208262	AVS	Tholeiitic metabasalt	1.13	0.01	0.23	0.03	-0.10	0.18
208262	AVS	Tholeiitic metabasalt	1.07	0.02	0.23	0.03	0.01	0.13
208265	AVS	Tholeiitic metabasalt	2.24	0.01	0.20	0.04	0.26	0.16
07-07	AVS	Tholeiitic metabasalt	0.43	0.01	0.07	0.02	-0.19	0.20
07-07	CRS	Tholeiitic metabasalt	0.90	0.02	0.06	0.02	-0.06	0.13
208299 2	combined	Tholeiitic metabasalt	1.66	0.02	2.91	0.04	-1.60	0.29
AJ31 DAP	AVS	Tholeiitic metabasalt	0.82	0.01	0.28	0.02	0.08	0.20
AJ31 Ocelli	AVS	Tholeiitic metabasalt	0.16	0.01	0.28	0.03	0.33	0.20
AJ34 B	combined	Tholeiitic metabasalt	0.21	0.01	0.30	0.02	0.10	0.09
AJ35	AVS	Tholeiitic metabasalt	0.45	0.01	0.26	0.03	-0.29	0.19
AJ35	CRS	Tholeiitic metabasalt	0.06	0.01	0.27	0.04	-0.45	0.25
AJ36	combined	Tholeiitic metabasalt	0.12	0.01	0.26	0.03	-0.05	0.28
AJ37	AVS	Tholeiitic metabasalt	0.52	0.01	0.30	0.02	0.15	0.12
AJ37	CRS	Tholeiitic metabasalt	0.48	0.02	0.31	0.03	0.23	0.19
AJ38	combined	Tholeiitic metabasalt	0.31	0.01	0.30	0.02	-0.40	0.20
ECP03-10 CI	AVS	Tholeiitic metabasalt	0.87	0.01	-0.13	0.03	0.58	0.21
ECP03-10 CI	CRS	Tholeiitic metabasalt	1.14	0.01	-0.13	0.02	0.35	0.29
ECP03-10 CII	AVS	Tholeiitic metabasalt	1.20	0.02	-0.13	0.03	0.44	0.20
ECP03-10 CII	CRS	Tholeiitic metabasalt	1.53	0.01	-0.13	0.03	0.50	0.17
ECP03-10A	AVS	Tholeiitic metabasalt	1.67	0.00	-0.11	0.03	0.02	0.11
ECP08-07A	AVS	Tholeiitic metabasalt	2.38	0.01	0.21	0.03	0.03	0.12
ECP08-08	AVS	Tholeiitic metabasalt	2.45	0.01	0.34	0.03	-0.25	0.25
ECP08-08	AVS	Tholeiitic metabasalt	2.33	0.01	0.34	0.03	0.27	0.26

Table 5.1: Summary of additional bulk S isotope analyses

sample name	extraction	sample type	$\delta^{34}S$ [‰]	$2\sigma(\delta^{34}S)$ [‰]	$\Delta^{33}S$ [‰]	$2\sigma(\Delta^{33}S)$ [‰]	$\Delta^{36}S$ [‰]	$2\sigma(\Delta^{36}S)$ [‰]
ECP08-08	CRS	Tholeiitic metabasalt	2.30	0.02	0.33	0.04	0.22	0.15
ECP07-A Mag.	AVS	Magnesite	1.87	0.02	0.19	0.04	-0.01	0.17
2008	AVS	Sediment (metaturbidite)	1.12	0.02	1.01	0.03	-1.01	0.15
207529	combined	Sediment (BIF)	2.35	0.01	2.52	0.03	-1.21	0.24
207534	combined	Sediment (BIF)	2.08	0.01	2.54	0.04	-1.75	0.22
207537	combined	Sediment (BIF)	2.12	0.02	2.98	0.02	-1.91	0.23
207540	combined	Sediment (BIF)	2.69	0.01	3.01	0.03	-1.66	0.22
IAEA-S1		standard	-0.28	0.02	0.08	0.02	-0.91	0.31
IAEA-S1		standard	-0.23	0.01	0.07	0.04	-0.50	0.11
IAEA-S1		standard	-0.23	0.02	0.07	0.04	-0.54	0.21
IAEA-S1		standard	0.06	0.01	0.08	0.03	-0.30	0.17
IAEA-S1		standard	-0.29	0.02	0.07	0.03	-0.34	0.23

Results are reported relative to the Vienna Canyon Diablo Troilite (V-CDT).

References

André, L., Abraham, K., Hofmann, A., Monin, L., Kleinhanns, I.C., Foley, S., 2019. Early continental crust generated by reworking of basalts variably silicified by seawater. Nature Geoscience 12, 769-773.

Appel, P.W.U., Rollinson, H.R., Touret, J.L.R., 2001. Remnants of an Early Archaean (>3.75 Ga) sea-floor, hydrothermal system in the Isua Greenstone Belt. Precambrian Research 112, 27-49.

Allwood, A.C., Walter, M.R., Burch, I.W. and Kamber, B.S., 2007. 3.43 billion-year-old stromatolite reef from the Pilbara Craton of Western Australia: Ecosystem-scale insights to early life on Earth. Precambrian Research 158, 198-227.

Amelin, Y., Kamo, S.L., Lee, D.-C., 2010. Evolution of early crust in chondritic or nonchondritic Earth inferred from U–Pb and Lu–Hf data for chemically abraded zircon from the Itsaq Gneiss Complex, West Greenland. This article is one of a series of papers published in this Special Issue on the theme of Geochronology in honour of Tom Krogh. Can. J. Earth Sci. 48, 141–160.

Amelin, Y., Lee, D.-C., Halliday, A.N. and Pidgeon, R.T., 1999. Nature of the Earth's earliest crust from hafnium isotopes in single detrital zircons. Nature 399, 252-255.

Antonelli, M.A., Kendrick, J., Yakymchuk, C., Guitreau, M., Mittal, T., Moynier, F., 2021. Calcium isotope evidence for early Archaean carbonates and subduction of oceanic crust. Nature Communications 12, 2534.

Antonelli, M.A., Kim, S.-T., Peters, M., Labidi, J., Cartigny, P., Walker, R.J., Lyons, J.R., Hoek, J., Farquhar, J., 2014. Early inner solar system origin for anomalous sulfur isotopes in differentiated protoplanets. Proceedings of the National Academy of Sciences 111, 17749.

Appel, P.W.U., Moorbath, S. and Taylor, P.N., 1978 Least radiogenic terrestrial lead from Isua, West Greenland. Nature 272, 524-526.

Augustin, C.T., Mungall, J.E., Schutesky, M.E., Ernst, R. and Garcia, V.B., 2022. Petrological and geochemical characteristics of the mafic–ultramafic Americano do Brasil Complex, central Brazil, and the implications for its genesis. Ore Geology Reviews 150, 105126.

Bao, H., Rumble, D. and Lowe, D.R., 2007. The five stable isotope compositions of Fig Tree barites: Implications on sulfur cycle in ca. 3.2Ga oceans. Geochimica et Cosmochimica Acta 71, 4868-4879.

Baublys, K.A., Golding, S.D., Young, E., Kamber, B.S., 2004. Simultaneous determination of δ^{33}S V-CDT and δ^{34}S V-CDT using masses 48, 49 and 50 on a continuous flow isotope ratio mass spectrometer. Rapid Communications in Mass Spectrometry 18, 2765–2769.

Baumgartner, R.J., Van Kranendonk, M.J., Wacey, D., Fiorentini, M.L., Saunders, M., Caruso, S., Pages, A., Homann, M. and Guagliardo, P., 2019. Nano−porous pyrite and organic matter in 3.5-billion-year-old stromatolites record primordial life. Geology 47, 1039-1043.

Bédard, J.H., 2006. A catalytic delamination-driven model for coupled genesis of Archaean crust and sub-continental lithospheric mantle. Geochimica et Cosmochimica Acta 70, 1188–1214.

Bennett, V.C., Nutman, A.P. and Esat, T.M., 2002. Constraints on mantle evolution from ^{187}Os/^{188}Os isotopic compositions of Archean ultramafic rocks from southern West Greenland (3.8 Ga) and Western Australia (3.46 Ga). Geochimica et Cosmochimica Acta 66, 2615-2630.

Betts, H.C., Puttick, M.N., Clark, J.W., Williams, T.A., Donoghue, P.C.J. and Pisani, D., 2018. Integrated genomic and fossil evidence illuminates life's early evolution and eukaryote origin. Nature Ecology & Evolution 2, 1556-1562.

Bouvier, A., Vervoort, J.D., Patchett, P.J., 2008. The Lu–Hf and Sm–Nd isotopic composition of CHUR: Constraints from unequilibrated chondrites and implications for the bulk composition of terrestrial planets. Earth Planet. Sci. Lett. 273, 48–57.

Bowring, S.A. and Williams, I.S., 1999 Priscoan (4.00–4.03 Ga) orthogneisses from northwestern Canada. Contributions to Mineralogy and Petrology 134, 3-16.

Brown, M., Johnson, T., 2019. Metamorphism and the evolution of subduction on Earth. American Mineralogist 104, 1065-1082.

Brown, M., Johnson, T. and Gardiner, N.J., 2020. Plate Tectonics and the Archean Earth. Annual Review of Earth and Planetary Sciences 48, 291-320.

Bucholz, C.E., Biasi, J.A., Beaudry, P., Ono, S., 2020. Sulfur isotope behavior during metamorphism and anatexis of Archean sedimentary rocks: A case study from the Ghost Lake batholith, Ontario, Canada. Earth and Planetary Science Letters 549, 116494.

Cabral, R.A., Jackson, M.G., Rose-Koga, E.F., Koga, K.T., Whitehouse, M.J., Antonelli, M. A., Farquhar, J., Day, J.M.D., Hauri, E.H., 2013. Anomalous Sulphur isotopes in plume lavas reveal deep mantle storage of Archaean crust. Nature 496, 490-493.

Canfield, D.E., Raiswell, R., Westrich, J.T., Reaves, C.M., Berner, R.A., 1986. The use of chromium reduction in the analysis of reduced inorganic sulfur in sediments and shales. Chemical Geology 54, 149–155.

Caruso, S., Fiorentini, M.L., Champion, D.C., Lu, Y., Ueno, Y., Smithies, R.H., 2022a. Sulfur isotope systematics of granitoids from the Yilgarn Craton shed new light on the fluid reservoirs of Neoarchean orogenic gold deposits. Geochimica et Cosmochimica Acta 326, 199–213.

Caruso, S., Fiorentini, M.L., Champion, D.C., Lu, Y., Ueno, Y. and Smithies, R.H., 2022b. Sulfur isotope systematics of granitoids from the Yilgarn Craton sheds new light on the fluid reservoirs of Neoarchean orogenic gold deposits. Geochimica et Cosmochimica Acta 326, 199-213.

Cates, N.L., Ziegler, K., Schmitt, A.K. and Mojzsis, S.J., 2013. Reduced, reused and recycled: Detrital zircons define a maximum age for the Eoarchean (ca. 3750–3780Ma) Nuvvuagittuq Supracrustal Belt, Québec (Canada). Earth and Planetary Science Letters 362, 283-293.

Cavosie, A.J., Valley, J.W. and Wilde, S.A., 2019. Chapter 12 - The Oldest Terrestrial Mineral Record: Thirty Years of Research on Hadean Zircon From Jack Hills, Western Australia, in: Van Kranendonk, M.J., Bennett, V.C., Hoffmann, J.E. (Eds.), Earth's Oldest Rocks (Second Edition). Elsevier, pp. 255-278.

Chaudhuri, T., Wan, Y., Mazumder, R., Ma, M. and Liu, D., 2018. Evidence of Enriched, Hadean Mantle Reservoir from 4.2-4.0 Ga zircon xenocrysts from Paleoarchean TTGs of the Singhbhum Craton, Eastern India. Scientific Reports 8, 7069.

Coggon, J.A., Luguet, A., Fonseca, R.O.C., Lorand, J.-P., Heuser, A., Appel, P.W.U., 2015. Understanding Re–Os systematics and model ages in metamorphosed Archean ultramafic rocks: a single mineral to whole-rock investigation. Geochimica et Cosmochimica Acta 167, 205–240.

Condie, K.C., 2019. Chapter 11 - Earth's Oldest Rocks and Minerals, in: Van Kranendonk, M.J., Bennett, V.C., Hoffmann, J.E. (Eds.), Earth's Oldest Rocks (Second Edition). Elsevier, pp. 239-253.

Corriveau, L. and Spry, P.G., 2014. 13.7 - Metamorphosed Hydrothermal Ore Deposits, in: Holland, H.D., Turekian, K.K. (Eds.), Treatise on Geochemistry (Second Edition). Elsevier, Oxford, pp. 175-194.

Craig, J.R., 1973. Pyrite-pentlandite assemblages and other low temperature relations in the Fe-Ni-S system. American Journal of Science 273-A, 496-510.

Crowley, J.L., 2003. U–Pb geochronology of 3810–3630 Ma granitoid rocks south of the Isua greenstone belt, southern West Greenland. Precambrian Research 126, 235-257.

Cui, P.-L., Sun, J.-G., Sha, D.-M., Wang, X.-J., Zhang, P., Gu, A.L. and Wang, Z.-Y., 2013. Oldest zircon xenocryst (4.17 Ga) from the North China Craton. International Geology Review 55, 1902-1908.

Damer, B., 2016. A Field Trip to the Archaean in Search of Darwin's Warm Little Pond, Life 6, 21.

Darwin, C.R., 1871. To J. D. Hooker. Darwin Correspondence Project, Letter no. 7471, https://www.darwinproject.ac.uk/letter/?docId=letters/DCP-LETT-7471.xml, accessed on 27 September, 2023.

Delavault, H., Chauvel, C., Thomassot, E., Devey, C.W., Dazas, B., 2016. Sulfur and lead isotopic evidence of relic Archean sediments in the Pitcairn mantle plume. Proceedings of the National Academy of Sciences 113, 12952-12956.

Deng, Z., Chaussidon, M., Guitreau, M., Puchtel, I.S., Dauphas, N., Moynier, F., 2019. An oceanic subduction origin for Archaean granitoids revealed by silicon isotopes. Nature Geoscience 12, 774-778.

Dietz, R.S. and Holden, J.C., 1970. Reconstruction of Pangaea: Breakup and dispersion of continents, Permian to Present. Journal of Geophysical Research (1896-1977) 75, 4939-4956.

Ding, T., Valkiers, S., Kipphardt, H., De Bièvre, P., Taylor, P.D.P., Gonfiantini, R., Krouse, R., 2001. Calibrated sulfur isotope abundance ratios of three IAEA sulfur isotope reference materials and V-CDT with a reassessment of the atomic weight of sulfur. Geochimica et Cosmochimica Acta 65, 2433-2437.

Dodd, M.S., Papineau, D., Grenne, T., Slack, J.F., Rittner, M., Pirajno, F., O'Neil, J. and Little, C.T.S., 2017. Evidence for early life in Earth's oldest hydrothermal vent precipitates. Nature 543, 60-64.

Dottin III, J.W., Labidi, J., Jackson, M.G. and Farquhar, J., 2021. Sulfur Isotope Evidence for a Geochemical Zonation of the Samoan Mantle Plume. Geochemistry, Geophysics, Geosystems 22, e2021GC009816.

Dottin III, J.W., Labidi, J., Jackson, M.G., Woodhead, J. and Farquhar, J., 2020a. Isotopic Evidence for Multiple Recycled Sulfur Reservoirs in the Mangaia Mantle Plume. Geochemistry, Geophysics, Geosystems 21, e2020GC009081.

Dottin III, J.W., Labidi, J., Lekic, V., Jackson, M.G. and Farquhar, J., 2020b. Sulfur isotope characterization of primordial and recycled sources feeding the Samoan mantle plume. Earth and Planetary Science Letters 534, 116073.

Drabon, N., Byerly, B.L., Byerly, G.R., Wooden, J.L., Wiedenbeck, M., Valley, J.W., Kitajima, K., Bauer, A.M. and Lowe, D.R., 2022. Destabilization of Long-Lived Hadean Protocrust and the Onset of Pervasive Hydrous Melting at 3.8 Ga. AGU Advances 3, e2021AV000520.

Eskesen, B., Fassmer, K., Münker, C., Ulrich, T., Szilas, K., Wagner, S., Hoffmann, J.E. and Nagel, T.J., 2023. Neoarchean synkinematic metamorphic peak in the Isua supracrustal belt (West Greenland). Geology.

Evans, K.A., Tomkins, A.G., Cliff, J., Fiorentini, M.L., 2014. Insights into subduction zone sulfur recycling from isotopic analysis of eclogite-hosted sulfides. Chemical Geology 365, 1-19.

Farquhar, J., Bao, H., Thiemens, M., 2000. Atmospheric Influence of Earth's Earliest Sulfur Cycle. Science 289, 756–758.

Farquhar, J., Peters, M., Johnston, D.T., Strauss, H., Masterson, A., Wiechert, U., Kaufman, A.J., 2007. Isotopic evidence for Mesoarchaean anoxia and changing atmospheric sulphur chemistry. Nature 449, 706-709.

Farquhar, J. and Wing, B.A., 2003. Multiple sulfur isotopes and the evolution of the atmosphere. Earth and Planetary Science Letters 213, 1-13.

Farquhar, J., Wing, B.A., McKeegan, K.D., Harris, J.W., Cartigny, P., Thiemens, M.H., 2002. Mass-Independent Sulfur of Inclusions in Diamond and Sulfur Recycling on Early Earth. Science 298, 2369-2372.

Farquhar, J., Zerkle, A.L., Bekker, A., 2011. Geological constraints on the origin of oxygenic photosynthesis. Photosynthesis Research 107, 11-36.

Fernandes, N.A., Gleeson, S.A., Magnall, J.M., Creaser, R.A., Martel, E., Fischer, B.J. and Sharp, R., 2017. The origin of Late Devonian (Frasnian) stratiform and stratabound mudstone-hosted barite in the Selwyn Basin, Northwest Territories, Canada. Marine and Petroleum Geology 85, 1-15.

Fike, D.A., Bradley, A.S. and Rose, C.V., 2015. Rethinking the Ancient Sulfur Cycle. Annual Review of Earth and Planetary Sciences 43, 593-622.

Fisher, C.M., Vervoort, J.D., 2018. Using the magmatic record to constrain the growth of continental crust—the Eoarchean zircon Hf record of Greenland. Earth Planet. Sci. Lett. 488, 79–91.

Fodor, R.V., 2001. The Role of Tonalite and Diorite in Mauna Kea Volcano, Hawaii, Magmatism: Petrology of Summit-Region Leucocratic Xenoliths. Journal of Petrology 42, 1685-1704.

Fonseca, R.O.C., Mallmann, G., O'Neill, H.S.C., Campbell, I.H., Laurenz, V., 2011. Solubility of Os and Ir in sulfide melt: Implications for Re/Os fractionation during mantle melting. Earth Planet. Sci. Lett. 311, 339–350.

Frei, R., Polat, A., Meibom, A., 2004. The Hadean upper mantle conundrum: evidence for source depletion and enrichment from Sm-Nd, Re-Os, and Pb isotopic compositions in 3.71 Gy boninite-like metabasalts from the Isua Supracrustal Belt, Greenland. Geochimica et Cosmochimica Acta 68, 1645–1660.

Frei, R. and Rosing, M.T., 2001. The least radiogenic terrestrial leads; implications for the early Archean crustal evolution and hydrothermal–metasomatic processes in the Isua Supracrustal Belt (West Greenland). Chemical Geology 181, 47-66.

Friend, C., Bennett, V., Nutman, A., 2002. Abyssal peridotites >3,800 Ma from southern West Greenland: field relationships, petrography, geochronology, whole-rock and mineral chemistry of dunite and harzburgite inclusions in the Itsaq Gneiss complex. Contributions to Mineralogy and Petrology 143, 71–92.

Friend, C.R.L., Nutman, A.P., 2011. Dunites from Isua, Greenland: A ca. 3720 Ma window into subcrustal metasomatism of depleted mantle. Geology 39, 663-666.

Froude, D.O., Ireland, T.R., Kinny, P.D., Williams, I.S., Compston, W., Williams, I.R. and Myers, J.S., 1983. Ion microprobe identification of 4,100–4,200 Myr-old terrestrial zircons. Nature 304, 616-618.

Garde, A.A., Windley, B.F., Kokfelt, T.F. and Keulen, N., 2020. Archaean Plate Tectonics in the North Atlantic Craton of West Greenland Revealed by Well-Exposed Horizontal Crustal Tectonics, Island Arcs and Tonalite-Trondhjemite-Granodiorite Complexes. Frontiers in Earth Science 8.

Gardiner, N.J., Kirkland, C.L., Hollis, J., Szilas, K., Steenfelt, A., Yakymchuk, C., Heide-Jørgensen, H., 2019. Building Mesoarchaean crust upon Eoarchaean roots: the Akia Terrane, West Greenland. Contributions to Mineralogy and Petrology 174, 20.

Ge, R.-F., Wilde, S.A., Zhu, W.-B. and Wang, X.-L., 2023. Earth's early continental crust formed from wet and oxidizing arc magmas. Nature.

Grassineau, N.V., Abell, P., Appel, P.W.U., Lowry, D., Nisbet, E.G., 2006. Early life signatures in sulfur and carbon isotopes from Isua, Barberton, Wabigoon (Steep Rock), and Belingwe Greenstone Belts (3.8 to 2.7 Ga), in: Kesler, S.E., Ohmoto, H. (Eds.), Evolution of Early Earth's Atmosphere, Hydrosphere, and Biosphere - Constraints from Ore Deposits. Geological Society of America, p. 0.

Grema, H.M., Magnall, J.M., Whitehouse, M.J., Gleeson, S.A. and Schulz, H.-M., 2022. The Formation of Highly Positive δ^{34}S Values in Late Devonian Mudstones: Microscale Analysis of Pyrite (δ^{34}S) and Barite (δ^{34}S, δ^{18}O) in the Canol Formation (Selwyn Basin, Canada). Frontiers in Earth Science 9.

Guitreau, M., Blichert-Toft, J., Martin, H., Mojzsis, S.J., Albarède, F., 2012. Hafnium isotope evidence from Archean granitic rocks for deep-mantle origin of continental crust. Earth Planet. Sci. Lett. 337-338, 211–223.

Hasenstab-Dübeler, E., Tusch, J., Hoffmann, J.E., Fischer-Gödde, M., Szilas, K., Münker, C., 2022. Temporal evolution of ^{142}Nd signatures in SW Greenland from high precision MC-ICP-MS measurements. Chem. Geol. 121141.

Harrison, T.M., Blichert-Toft, J., Müller, W., Albarède, F., Holden, P. and Mojzsis, S.J., 2005. Heterogeneous Hadean Hafnium: Evidence of Continental Crust at 4.4 to 4.5 Ga. Science 310, 1947-1950.

Hartmann, W.K. and Davis, D.R., 1975. Satellite-sized planetesimals and lunar origin. Icarus 24, 504-515.

Hastie, A.R., Fitton, J.G., Bromiley, G.D., Butler, I.B., Odling, N.W.A., 2016. The origin of Earth's first continents and the onset of plate tectonics. Geology 44, 855-858.

Hastie, A.R., Law, S., Bromiley, G.D., Fitton, J.G., Harley, S.L. and Muir, D.D., 2023. Deep formation of Earth's earliest continental crust consistent with subduction. Nature Geoscience.

Hawkesworth, C., Cawood, P.A. and Dhuime, B., 2019. Rates of generation and growth of the continental crust. Geoscience Frontiers 10, 165-173.

Hawkesworth, C.J., Cawood, P.A. and Dhuime, B., 2020. The Evolution of the Continental Crust and the Onset of Plate Tectonics. Frontiers in Earth Science 8.

Hiess, J., Nutman, A.P., Bennett, V.C., Holden, P., 2008. Ti-in-zircon thermometry applied to contrasting Archean metamorphic and igneous systems. Chem. Geol. 247, 323–338.

Hoffmann, J.E., 2017. Oxygenation by a changing crust. Nature Geoscience 10, 713-714.

Hoffmann, J.E., Münker, C., Næraa, T., Rosing, M.T., Herwartz, D., Garbe-Schönberg, D., Svahnberg, H., 2011a. Mechanisms of Archean crust formation inferred from high precision HFSE systematics in TTGs. Geochimica et Cosmochimica Acta 75, 4157–4178.

Hoffmann, J.E., Münker, C., Polat, A., Rosing, M.T., Schulz, T., 2011b. The origin of decoupled Hf–Nd isotope compositions in Eoarchean rocks from southern West Greenland. Geochimica et Cosmochimica Acta 75, 6610–6628.

Hoffmann, J.E., Münker, C., Polat, A., König, S., Mezger, K., Rosing, M.T., 2010. Highly depleted Hadean mantle reservoirs in the sources of early Archean arc-like rocks, Isua supracrustal belt, southern West Greenland. Geochimica et Cosmochimica Acta 74, 7236–7260.

Hoffmann, J.E., Nagel, T.J., Münker, C., Næraa, T., Rosing, M.T., 2014. Constraining the process of Eoarchean TTG formation in the Itsaq Gneiss complex, southern West Greenland. Earth and Planetary Science Letters 388, 374–386.

Hoffmann, J.E., Wilson, A.H., 2017. The origin of highly radiogenic Hf isotope compositions in 3.33 Ga Commondale komatiite lavas (South Africa). Chem. Geol. 455, 6–21.

Hoffmann, J.E., Zhang, C., Moyen, J.-F., Nagel, T.J., 2019. Chapter 7 - The Formation of Tonalites–Trondjhemite–Granodiorites in Early Continental Crust, in: Van Kranendonk, M.J., Bennett, V.C., Hoffmann, J.E. (Eds.), Earth's Oldest Rocks (Second Edition). Elsevier, pp. 133-168.

Hu, G., Rumble, D. and Wang, P.-l., 2003. An ultraviolet laser microprobe for the in situ analysis of multisulfur isotopes and its use in measuring Archean sulfur isotope mass-independent anomalies. Geochimica et Cosmochimica Acta 67, 3101-3118.

Hulston, J.R. and Thode, H.G., 1965. Variations in the S^{33}, S^{34}, and S^{36} contents of meteorites and their relation to chemical and nuclear effects. Journal of Geophysical Research (1896-1977) 70, 3475-3484.

Jenner, F.E., Bennett, V.C., Nutman, A.P., Friend, C.R.L., Norman, M.D., Yaxley, G., 2009. Evidence for subduction at 3.8 Ga: Geochemistry of arc-like metabasalts from the southern edge of the Isua Supracrustal Belt. Chemical Geology 261, 83-98.

Johnson, T.E., Brown, M., Gardiner, N.J., Kirkland, C.L., Smithies, R.H., 2017. Earth’s first stable continents did not form by subduction. Nature 543, 239.

Johnson, T.E., Brown, M., Kaus, B.J.P., Van Tongeren, J.A., 2013. Delamination and recycling of Archaean crust caused by gravitational instabilities. Nat. Geosci. 7, 47.

Johnson, T.E., Kirkland, C.L., Lu, Y., Smithies, R.H., Brown, M. and Hartnady, M.I.H., 2022. Giant impacts and the origin and evolution of continents. Nature 608, 330-335.

Johnston, D.T., 2011. Multiple sulfur isotopes and the evolution of Earth's surface sulfur cycle. Earth-Science Reviews 106, 161-183.

Johnston, D.T., Farquhar, J., Habicht, K.S., Canfield, D.E., 2008. Sulphur isotopes and the search for life: strategies for identifying Sulphur metabolisms in the rock record and beyond. Geobiology 6, 425–435.

Kamber, B.S., 2007. Chapter 2.4 The Enigma of the Terrestrial Protocrust: Evidence for Its Former Existence and the Importance of Its Complete Disappearance, in: van Kranendonk, M.J., Smithies, R.H., Bennett, V.C. (Eds.), Developments in Precambrian Geology. Elsevier, pp. 75-89.

Kamber, B.S., Collerson, K.D., Moorbath, S. and Whitehouse, M.J., 2003. Inheritance of early Archaean Pb-isotope variability from long-lived Hadean protocrust. Contributions to Mineralogy and Petrology 145, 25-46.

Kanehira, K., Yui, S., Sakai, H., Sasaki, A., 1973. Sulphide globules and sulphur isotope ratios in the abyssal tholeiite from the Mid-Atlantic Ridge near 30°N latitude. Geochemical Journal 7, 89-96.

Kasting, J.F., 2019. Chapter 3 - Early Earth Atmosphere and Oceans, in: Van Kranendonk, M.J., Bennett, V.C., Hoffmann, J.E. (Eds.), Earth's Oldest Rocks (Second Edition). Elsevier, pp. 49-61.

Kiseeva, E.S., Fonseca, R.O.C. and Smythe, D.J., 2017. Chalcophile Elements and Sulfides in the Upper Mantle. Elements 13, 111-116.

Kitakaze, A., 1998. Sulfide minerals from the Horoman peridotite, Hokkaido, Japan. Journal of Mineralogy, Petrology and Economic Geology 93, 369-379.

Kitakaze, A., Itoh, H. and Komatsu, R., 2011. Horomanite, $(Fe,Ni,Co,Cu)_9S_8$, and samaniite, $Cu_2(Fe,Ni)_7S_8$, new mineral species from the Horoman peridotite massif, Hokkaido, Japan. Journal of Mineralogical and Petrological Sciences 106, 204-210.

Klein, F. and Bach, W., 2009. Fe–Ni–Co–O–S Phase Relations in Peridotite–Seawater Interactions. Journal of Petrology 50, 37-59.

König, S., Münker, C., Schuth, S., Luguet, A., Hoffmann, J.E., Kuduon, J., 2010. Boninites as windows into trace element mobility in subduction zones. Geochimica et Cosmochimica Acta 74, 684–704.

Korenaga, J., 2021. Was There Land on the Early Earth?, Life 11, 1142.

Kuang, J., Morra, G., Yuen, D.A., Kusky, T., Jiang, S., Yao, H. and Qi, S., 2023. Metamorphic constraints on Archean tectonics. Precambrian Research 397, 107195.

Kubota, Y., Matsu'ura, F., Shimizu, K., Ishikawa, A. and Ueno, Y., 2022. Sulfur in Archean komatiite implies early subduction of oceanic lithosphere. Earth and Planetary Science Letters 598, 117826.

Labidi, J., Cartigny, P., Jackson, M.G., 2015. Multiple sulfur isotope composition of oxidized Samoan melts and the implications of a sulfur isotope ‘mantle array’ in chemical geodynamics. Earth and Planetary Science Letters 417, 28-39.

Labidi, J., Dottin, J.W., Clog, M., Hemond, C. and Cartigny, P., 2022. Near-zero ^{33}S and ^{36}S anomalies in Pitcairn basalts suggest Proterozoic sediments in the EM-1 mantle plume. Earth and Planetary Science Letters 584, 117422.

LaFlamme, C., Fiorentini, M.L., Lindsay, M.D. and Bui, T.H., 2018a. Atmospheric sulfur is recycled to the crystalline continental crust during supercontinent formation. Nature Communications 9, 4380.

LaFlamme, C., Jamieson, J.W., Fiorentini, M.L., Thébaud, N., Caruso, S. and Selvaraja, V., 2018b. Investigating sulfur pathways through the lithosphere by tracing mass independent fractionation of sulfur to the Lady Bountiful orogenic gold deposit, Yilgarn Craton. Gondwana Research 58, 27-38.

LaFlamme, C., Martin, L., Jeon, H., Reddy, S.M., Selvaraja, V., Caruso, S., Bui, T.H., Roberts, M.P., Voute, F., Hagemann, S., Wacey, D., Littman, S., Wing, B., Fiorentini, M. and Kilburn, M.R., 2016. In situ multiple sulfur isotope analysis by SIMS of pyrite, chalcopyrite, pyrrhotite, and pentlandite to refine magmatic ore genetic models. Chemical Geology 444, 1-15.

Lewis, J.A., Hoffmann, J.E., Schwarzenbach, E.M., Strauss, H., Li, C., Münker, C. and Rosing, M.T., 2023. Sulfur isotope evidence from peridotite enclaves in southern West Greenland for recycling of surface material into Eoarchean depleted mantle domains. Chemical Geology 633, 121568.

Lewis, J.A., Hoffmann, J.E., Schwarzenbach, E.M., Strauss, H., Liesegang, M. and Rosing, M.T., 2021. Sulfur isotope evidence for surface-derived sulfur in Eoarchean TTGs. Earth and Planetary Science Letters 576, 117218.

Li, J.-L., Schwarzenbach, E.M., John, T., Ague, J.J., Huang, F., Gao, J., Klemd, R., Whitehouse, M.J. and Wang, X.-S., 2020. Uncovering and quantifying the subduction zone sulfur cycle from the slab perspective. Nature Communications 11, 514.

Li, J.-L., Schwarzenbach, E.M., John, T., Ague, J.J., Tassara, S., Gao, J., Konecke, B.A., 2021. Subduction zone sulfur mobilization and redistribution by intraslab fluid–rock interaction. Geochimica et Cosmochimica Acta 297, 40-64.

Li, R., Xia, X., Yang, S., Chen, H. and Yang, Q., 2019. Off-Mount Calibration and One New Potential Pyrrhotite Reference Material for Sulfur Isotope Measurement by Secondary Ion Mass Spectrometry. Geostandards and Geoanalytical Research 43, 177-187.

Lin, M., Zhang, X., Li, M., Xu, Y., Zhang, Z., Tao, J., Su, B., Liu, L., Shen, Y. and Thiemens, M.H., 2018. Five-S-isotope evidence of two distinct mass-independent sulfur isotope effects and implications for the modern and Archean atmospheres. Proceedings of the National Academy of Sciences 115, 8541-8546.

Liou, P., Guo, J., Mitchell, R.N., Spencer, C.J., Li, X., Zhai, M., Evans, N.J., Li, Y., McDonald, B.J., Jin, M., 2022. Zircons underestimate mantle depletion of early Earth. Geochimica et Cosmochimica Acta 317, 538–551.

Liseroudi, M.H., Ardakani, O.H., Pedersen, P.K., Stern, R.A., Wood, J.M. and Sanei, H., 2021. Microbial and thermochemical controlled sulfur cycle in the Early Triassic sediments of the Western Canadian Sedimentary Basin. Journal of the Geological Society 178, jgs2020-2175.

Liu, B., Liu, Y., Li, S., Neubauer, F., Liang, C. and Guan, Q., 2023. Vertical tectonics of a Neoarchean gneiss dome in the eastern North China Craton. Geological Journal 58, 3181-3190.

Löcht, J.v.d., 2019. Geochemistry and petrology of ~ 3.8 Ga mafic - ultramafic enclaves in the Itsaq Gneiss Complex, SW Greenland, Department of Geosciences. University of Cologne, Cologne, Germany.

Lorand, J.P., 1989. Mineralogy and chemistry of Cu-Fe-Ni sulfides in orogenic-type spinel peridotite bodies from Ariege (Northeastern Pyrenees, France). Contributions to Mineralogy and Petrology 103, 335-345.

Lorand, J.P., Keays, R.R. and Bodinier, J.L., 1993. Copper and Noble Metal Enrichments Across the Lithosphere—Asthenosphere Boundary of Mantle Diapirs: Evidence from the Lanzo Lherzolite Massif. Journal of Petrology 34, 1111-1140.

Lowe, D.R., 1983. Restricted shallow-water sedimentation of Early Archean stromatolitic and evaporitic strata of the Strelley Pool Chert, Pilbara Block, Western Australia. Precambrian Research 19, 239-283.

Ludwig, K., 2012. User's Manual for ISOPLOT version 3.75-4.15. In: A Geochronological Toolkit for Microsoft Excel, 5. Berkeley Geochronology Center special Publication, p. 71.

Maltese, A. and Mezger, K., 2020. The Pb isotope evolution of Bulk Silicate Earth: Constraints from its accretion and early differentiation history. Geochimica et Cosmochimica Acta 271, 179-193.

Maruyama, S., Santosh, M. and Azuma, S., 2018. Initiation of plate tectonics in the Hadean: Eclogitization triggered by the ABEL Bombardment. Geoscience Frontiers 9, 1033-1048.

McIntyre, T., Pearson, D.G., Szilas, K., Morishita, T., 2019. Implications for the origins of Eoarchean ultramafic rocks of the North Atlantic Craton: a study of the Tussaap Ultramafic complex, Itsaq Gneiss complex, southern West Greenland. Contrib. Mineral. Petrol. 174, 96.

McIntyre, T., Waterton, P., Vezinet, A., Szilas, K., Pearson, D.G., 2021. Extent and age of Mesoarchean components in the Nagssugtoqidian orogen, West Greenland: Implications for tectonic environments and crust building in cratonic orogenic belts. Lithos 396-397, 106182.

Miyazaki, Y. and Korenaga, J., 2022. A wet heterogeneous mantle creates a habitable world in the Hadean. Nature 603, 86-90.

Mojzsis, S.J., Coath, C.D., Greenwood, J.P., McKeegan, K.D., Harrison, T.M., 2003. Mass-independent isotope effects in Archean (2.5 to 3.8 Ga) sedimentary sulfides determined by ion microprobe analysis. Geochimica et Cosmochimica Acta 67, 1635-1658.

Monster, J., Appel, P.W.U., Thode, H.G., Schidlowski, M., Carmichael, C.M., Bridgwater, D., 1979. Sulfur isotope studies in early Archaean sediments from Isua, West Greenland: Implications for the antiquity of bacterial sulfate reduction. Geochimica et Cosmochimica Acta 43, 405-413.

Montinaro, A., Strauss, H., Mason, P.R.D., Roerdink, D., Münker, C., Schwarz-Schampera, U., Arndt, N.T., Farquhar, J., Beukes, N.J., Gutzmer, J., Peters, M., 2015.

Paleoarchean sulfur cycling: Multiple sulfur isotope constraints from the Barberton Greenstone Belt, South Africa. Precambrian Research 267, 311-322.

Moore, W.B. and Webb, A.A.G., 2013. Heat-pipe Earth. Nature 501, 501-505.

Nadeau, S., Chen, W., Reece, J., Lachhman, D., Ault, R., Faraco, M., Fraga, L., Reis, N. and Betiollo, L., 2013. Guyana: the Lost Hadean crust of South America? Brazilian Journal of Geology 43, 601-606.

Næraa, T., Scherstén, A., Rosing, M.T., Kemp, A.I.S., Hoffmann, J.E., Kokfelt, T.F., Whitehouse, M.J., 2012. Hafnium isotope evidence for a transition in the dynamics of continental growth 3.2 Gyr ago. Nature 485, 627-630.

Nagel, T.J., Hoffmann, J.E., Münker, C., 2012. Generation of Eoarchean tonalite-trondhjemite-granodiorite series from thickened mafic arc crust. Geology 40, 375-378.

Nebel, O., Capitanio, F.A., Moyen, J.F., Weinberg, R.F., Clos, F., Nebel-Jacobsen, Y.J. and Cawood, P.A., 2018. When crust comes of age: on the chemical evolution of Archaean, felsic continental crust by crustal drip tectonics. Philosophical Transactions of the Royal Society A: Mathematical, Physical and Engineering Sciences 376, 20180103.

Nutman, A.P., 2023. Forming the oldest-surviving crust. Nature Geoscience 16, 762–763.

Nutman, A.P., Allaart, J.H., Bridgwater, D., Dimroth, E. and Rosing, M., 1984. Stratigraphic and geochemical evidence for the depositional environment of the early archaean isua supracrustal belt, southern west greenland. Precambrian Research 25, 365-396.

Nutman, A.P. and Bennett, V.C., 2019. Chapter 17 - The 3.9–3.6 Ga Itsaq Gneiss Complex of Greenland, in: Van Kranendonk, M.J., Bennett, V.C., Hoffmann, J.E. (Eds.), Earth's Oldest Rocks (Second Edition). Elsevier, pp. 375-399.

Nutman, A.P., Bennett, V.C., Friend, C.R.L., Horie, K., Hidaka, H., 2007a. ~3,850 Ma tonalites in the Nuuk region, Greenland: geochemistry and their reworking within an Eoarchaean gneiss complex. Contrib. Mineral. Petrol. 154, 385–408.

Nutman, A.P., Friend, C.R.L., Horie, K., Hidaka, H., 2007b. Chapter 3.3 the Itsaq Gneiss complex of Southern West Greenland and the Construction of Eoarchaean Crust at Convergent Plate Boundaries. In: van Kranendonk, M.J., Smithies, R.H., Bennett, V. C. (Eds.), Developments in Precambrian Geology. Elsevier, pp. 187–218.

Nutman, A.P., Bennett, V.C., Friend, C.R.L., Norman, M.D., 1999. Meta-igneous (nongneissic) tonalites and quartz-diorites from an extensive ca. 3800 Ma terrain south of the Isua supracrustal belt, southern West Greenland: constraints on early crust formation. Contrib. Mineral. Petrol. 137, 364–388.

Nutman, A.P., Bennett, V.C., Friend, C.R.L., Van Kranendonk, M.J. and Chivas, A.R., 2016. Rapid emergence of life shown by discovery of 3,700-million-year-old microbial structures. Nature 537, 535-538.

Nutman, A.P., Bennett, V.C., Friend, C.R.L. and Yi, K., 2020. Eoarchean contrasting ultra-high-pressure to low-pressure metamorphisms (<250 to >1000 °C/GPa) explained by tectonic plate convergence in deep time. Precambrian Research 344, 105770.

Nutman, A.P. and Friend, C.R.L., 2007. Adjacent terranes with ca. 2715 and 2650Ma high-pressure metamorphic assemblages in the Nuuk region of the North Atlantic Craton, southern West Greenland: Complexities of Neoarchaean collisional orogeny. Precambrian Research 155, 159-203.

Nutman, A.P., Friend, C.R.L., 2009. New 1:20,000 scale geological maps, synthesis and history of investigation of the Isua supracrustal belt and adjacent orthogneisses, southern West Greenland: A glimpse of Eoarchaean crust formation and orogeny. Precambrian Research 172, 189-211.

Nutman, A.P., McGregor, V.R., Friend, C.R.L., Bennett, V.C., Kinny, P.D., 1996. The Itsaq Gneiss Complex of southern West Greenland; the world's most extensive record of early crustal evolution (3900-3600 Ma). Precambrian Research 78, 1-39.

Nutman, A.P., Scicchitano, M.R., Friend, C.R.L., Bennett, V.C. and Chivas, A.R., 2021. Isua (Greenland) ~3700 Ma meta-serpentinite olivine Mg# and δ^{18}O signatures show connection between the early mantle and hydrosphere: Geodynamic implications. Precambrian Research 361, 106249.

Ohmoto, H., Lasaga, A.C., 1982. Kinetics of reactions between aqueous sulfates and sulfides in hydrothermal systems. Geochimica et Cosmochimica Acta 46, 1727-1745.

Ohmoto, H., Rye, R.O., 1979. Isotopes of sulfur and carbon, in: Barnes, H.L. (Ed.), Geochemistry of Hydrothermal Ore Deposits. John Wiley and Sons, New York, pp. 509-567.

O'Neil, J., Carlson, R.W., Francis, D. and Stevenson, R.K., 2008. Neodymium-142 Evidence for Hadean Mafic Crust. Science 321, 1828-1831.

O'Neil, J., Carlson, R.W., Papineau, D., Levine, E.Y. and Francis, D., 2019. Chapter 16 - The Nuvvuagittuq Greenstone Belt: A Glimpse of Earth's Earliest Crust, in: Van Kranendonk, M.J., Bennett, V.C., Hoffmann, J.E. (Eds.), Earth's Oldest Rocks (Second Edition). Elsevier, pp. 349-374.

O'Neil, J.R., 1986. Theoretical and experimental aspects of isotopic fractionation. Reviews in Mineralogy 16, 1-40.

O'Neill, C. and Debaille, V., 2014. The evolution of Hadean–Eoarchaean geodynamics. Earth and Planetary Science Letters 406, 49-58.

O'Neill, C. and Zhang, S., 2019. Chapter 4 - Modeling Early Earth Tectonics: The Case for Stagnant Lid Behavior, in: Van Kranendonk, M.J., Bennett, V.C., Hoffmann, J.E. (Eds.), Earth's Oldest Rocks (Second Edition). Elsevier, pp. 65-80.

O’Neil, J., Carlson, R.W., Paquette, J.-L. and Francis, D., 2012. Formation age and metamorphic history of the Nuvvuagittuq Greenstone Belt. Precambrian Research 220-221, 23-44.

Ono, S., 2017. Photochemistry of Sulfur Dioxide and the Origin of Mass-Independent Isotope Fractionation in Earth's Atmosphere. Annual Review of Earth and Planetary Sciences 45, 301-329.

Ono, S., Wing, B., Johnston, D., Farquhar, J., Rumble, D., 2006. Mass-dependent fractionation of quadruple stable sulfur isotope system as a new tracer of sulfur biogeochemical cycles. Geochimica et Cosmochimica Acta 70, 2238-2252.

Ozawa, K., 2004. Thermal History of the Horoman Peridotite Complex: A Record of Thermal Perturbation in the Lithospheric Mantle. Journal of Petrology 45, 253-273.

Palme, H., O’Neill, H.S.C., 2014. 3.1 - cosmochemical estimates of mantle composition. In: Holland, H.D., Turekian, K.K. (Eds.), Treatise on Geochemistry (Second Edition). Elsevier, Oxford, pp. 1–39.

Papineau, D., Mojzsis, S.J., 2006. Mass-independent fractionation of sulfur isotopes in sulfides from the pre-3770 Ma Isua Supracrustal Belt, West Greenland. Geobiology 4, 227-238.

Patchett, P.J., Tatsumoto, M., 1980. Hafnium isotope variations in oceanic basalts. Geophys. Res. Lett. 7, 1077–1080.

Polat, A. and Hofmann, A.W. 2003. Alteration and geochemical patterns in the 3.7–3.8 Ga Isua greenstone belt, West Greenland. Precambrian Research 126, 197-218.

Polat, A., Hofmann, A.W., Münker, C., Regelous, M. and Appel, P.W.U., 2003. Contrasting geochemical patterns in the 3.7–3.8 Ga pillow basalt cores and rims, Isua greenstone belt, Southwest Greenland: implications for postmagmatic alteration processes. Geochimica et Cosmochimica Acta 67, 441-457.

Polat, A., Hofmann, A.W., Rosing, M.T., 2002. Boninite-like volcanic rocks in the 3.7–3.8 Ga Isua greenstone belt, West Greenland: geochemical evidence for intra-oceanic subduction zone processes in the early Earth. Chemical Geology 184, 231-254.

Pope, E.C., Bird, D.K. and Rosing, M.T., 2012. Isotope composition and volume of Earth's early oceans. Proceedings of the National Academy of Sciences 109, 4371-4376.

Puchtel, I.S., Walker, R.J., Brandon, A.D., Nisbet, E.G., 2009. Pt–Re–Os and Sm–Nd isotope and HSE and REE systematics of the 2.7Ga Belingwe and Abitibi komatiites. Geochimica et Cosmochimica Acta 73, 6367–6389.

Ranjan, S., Todd, Z.R., Rimmer, P.B., Sasselov, D.D. and Babbin, A.R., 2019. Nitrogen Oxide Concentrations in Natural Waters on Early Earth. Geochemistry, Geophysics, Geosystems 20, 2021-2039.

Ranta, E., Gunnarsson-Robin, J., Halldórsson, S.A., Ono, S., Izon, G., Jackson, M.G., Reekie, C.D.J., Jenner, F.E., Guðfinnsson, G.H., Jónsson, Ó.P. and Stefánsson, A., 2022. Ancient and recycled sulfur sampled by the Iceland mantle plume. Earth and Planetary Science Letters 584, 117452.

Richards, J.R. and Appel, P.W.U., 1987. Age of the "least radiogenic" galenas at Isua, west Greenland. Chemical Geology: Isotope Geoscience section 66, 181-191.

Rizo, H., Boyet, M., Blichert-Toft, J., Rosing, M., 2011. Combined Nd and Hf isotope evidence for deep-seated source of Isua lavas. Earth Planet. Sci. Lett. 312, 267–279.

Roberts, N.M. and Tikoff, B., 2021. Internal structure of the Paleoarchean Mt Edgar dome, Pilbara Craton, Western Australia. Precambrian Research 358, 106163.

Roerdink, D.L., Mason, P.R.D., Farquhar, J. and Reimer, T., 2012. Multiple sulfur isotopes in Paleoarchean barites identify an important role for microbial sulfate reduction in the early marine environment. Earth and Planetary Science Letters 331-332, 177-186.

Rollinson, H., 2010. Coupled evolution of Archean continental crust and subcontinental lithospheric mantle. Geology 38, 1083–1086.

Rollinson, H., 2021. No plate tectonics necessary to explain Eoarchean rocks at Isua (Greenland). Geology 50, 147-151.

Rosas, J.C. and Korenaga, J., 2018. Rapid crustal growth and efficient crustal recycling in the early Earth: Implications for Hadean and Archean geodynamics. Earth and Planetary Science Letters 494, 42-49.

Rosing, M.T., 1999. ^{13}C-Depleted Carbon Microparticles in >3700-Ma Sea-Floor Sedimentary Rocks from West Greenland. Science 283, 674-676.

Savarino, J., Romero, A., Cole-Dai, J., Bekki, S. and Thiemens, M.H., 2003. UV induced mass-independent sulfur isotope fractionation in stratospheric volcanic sulfate. Geophysical Research Letters 30.

Salters, V.J.M., Stracke, A., 2004. Composition of the depleted mantle. Geochem. Geophys. Geosyst. 5.

Schwarzenbach, E.M., Caddick, M.J., Petroff, M., Gill, B.C., Cooperdock, E.H.G., Barnes, J.D., 2018a. Sulphur and carbon cycling in the subduction zone mélange. Scientific Reports 8, 15517.

Schwarzenbach, E.M., Gill, B.C., Johnston, D.T., 2018b. Unraveling multiple phases of sulfur cycling during the alteration of ancient ultramafic oceanic lithosphere. Geochimica et Cosmochimica Acta 223, 279-299.

Scherer, E., Münker, C., Mezger, K., 2001. Calibration of the Lutetium-Hafnium Clock. Science 293, 683–687.

Siedenberg, K., Strauss, H., Hoffmann, E.J., 2016. Multiple sulfur isotope signature of early Archean oceanic crust, Isua (SW-Greenland). Precambrian Research 283, 1-12.

Smit, M.A. and Mezger, K. (2017) Earth’s early O2 cycle suppressed by primitive continents. Nature Geoscience 10, 788.

Smithies, R.H., Champion, D.C., Van Kranendonk, M.J., 2009. Formation of Paleoarchean continental crust through infracrustal melting of enriched basalt. Earth and Planetary Science Letters 281, 298-306.

Söderlund, U., Patchett, P.J., Vervoort, J.D., Isachsen, C.E., 2004. The ^{176}Lu decay constant determined by Lu–Hf and U–Pb isotope systematics of Precambrian mafic intrusions. Earth Planet. Sci. Lett. 219, 311–324.

Stern, R.A. and Bleeker, W., 1998. Age of the World's Oldest Rocks Refined Using Canada's SHRIMP: The Acasta Gneiss Complex, Northwest Territories, Canada. Geoscience Canada 25.

Stern, R.J., 2005. Evidence from ophiolites, blueschists, and ultrahigh-pressure metamorphic terranes that the modern episode of subduction tectonics began in Neoproterozoic time. Geology 33, 557-560.

Stern, R.J., Leybourne, M.I. and Tsujimori, T., 2016. Kimberlites and the start of plate tectonics. Geology 44, 799-802.

Stracke, A., Bourdon, B., 2009. The importance of melt extraction for tracing mantle heterogeneity. Geochimica et Cosmochimica Acta 73, 218–238.

Strauss, H., 2002. The Isotopic Composition of Precambrian Sulphides—Seawater Chemistry and Biological Evolution, Precambrian Sedimentary Environments, pp. 67-105.

Strauss, H., 2003. Sulphur isotopes and the early Archaean sulphur cycle. Precambrian Research 126, 349-361.

Su, W., Schwarzenbach, E.M., Chen, L., Li, Y., John, T., Gao, J., Chen, F., Hu, X., 2019. Sulfur isotope compositions of pyrite from high-pressure metamorphic rocks and related veins (SW Tianshan, China): Implications for the sulfur cycle in subduction zones. Lithos 348-349, 105212.

Sugitani, K., Mimura, K., Takeuchi, M., Lepot, K., Ito, S. and Javaux, E.J., 2015. Early evolution of large micro-organisms with cytological complexity revealed by microanalyses of 3.4 Ga organic-walled microfossils. Geobiology 13, 507-521.

Szilas, K., Kelemen, P.B., Rosing, M.T., 2015. The petrogenesis of ultramafic rocks in the >3.7Ga Isua supracrustal belt, southern West Greenland: Geochemical evidence for two distinct magmatic cumulate trends. Gondwana Research 28, 565-580.

Tashiro, T., Ishida, A., Hori, M., Igisu, M., Koike, M., Méjean, P., Takahata, N., Sano, Y. and Komiya, T., 2017. Early trace of life from 3.95 Ga sedimentary rocks in Labrador, Canada. Nature 549, 516-518.

Thiemens, M., Sprung, P., Fonseca, R., Leitzke, F. and Münker, C., 2019. Early Moon formation inferred from hafnium–tungsten systematics. Nature Geoscience 12.

Thomassot, E., O'Neil, J., Francis, D., Cartigny, P., Wing, B.A., 2015. Atmospheric record in the Hadean Eon from multiple sulfur isotope measurements in Nuvvuagittuq Greenstone Belt (Nunavik, Quebec). Proceedings of the National Academy of Sciences 112, 707.

Tomkins, A.G., 2010. Windows of metamorphic sulfur liberation in the crust: Implications for gold deposit genesis. Geochimica et Cosmochimica Acta 74, 3246-3259.

Tomkins, A.G., Evans, K.A., 2015. Separate zones of sulfate and sulfide release from subducted mafic oceanic crust. Earth and Planetary Science Letters 428, 73-83.

Touret, J.L.R., 2003. Remnants of early Archaean hydrothermal methane and brines in pillow-breccia from the Isua Greenstone Belt, West Greenland. Precambrian Research 126, 219-233.

Tusch, J., Hoffmann, J.E., Hasenstab, E., Fischer-Gödde, M., Marien, C.S., Wilson, A.H. and Münker, C., 2022. Long-term preservation of Hadean protocrust in Earth's mantle. Proceedings of the National Academy of Sciences 119, e2120241119.

Tuttle, M.L., Goldhaber, M.B., Williamson, D.L., 1986. An analytical scheme for determining forms of Sulphur in oil shales and associated rocks. Talanta 33, 953–961.

Valley, J.W., Cavosie, A.J., Ushikubo, T., Reinhard, D.A., Lawrence, D.F., Larson, D.J., Clifton, P.H., Kelly, T.F., Wilde, S.A., Moser, D.E. and Spicuzza, M.J., 2014. Hadean age for a post-magma-ocean zircon confirmed by atom-probe tomography. Nature Geoscience 7, 219-223.

van de Löcht, J., Hoffmann, J.E., Li, C., Wang, Z., Becker, H., Rosing, M.T., Kleinschrodt, R. and Münker, C., 2018. Earth's oldest mantle peridotites show entire record of late accretion. Geology 46, 199-202.

van de Löcht, J., Hoffmann, J.E., Rosing, M.T., Sprung, P. and Münker, C., 2020. Preservation of Eoarchean mantle processes in ~3.8 Ga peridotite enclaves in the Itsaq Gneiss Complex, southern West Greenland. Geochimica et Cosmochimica Acta 280, 1-25.

van Hunen, J. and Moyen, J.-F., 2012. Archean Subduction: Fact or Fiction? Annual Review of Earth and Planetary Sciences 40, 195-219.

Van Kranendonk, M.J., Bennett, V.C. and Hoffmann, J.E., 2019a. Earth's Oldest Rocks, Second ed. Elsevier, Amsterdam, Netherlands.

Van Kranendonk, M.J., Smithies, R.H. and Champion, D.C., 2019b. Chapter 19 - Paleoarchean Development of a Continental Nucleus: The East Pilbara Terrane of the Pilbara Craton, Western Australia, in: Van Kranendonk, M.J., Bennett, V.C., Hoffmann, J.E. (Eds.), Earth's Oldest Rocks (Second Edition). Elsevier, pp. 437-462.

Vervoort, J.D., Blichert-Toft, J., 1999. Evolution of the depleted mantle: Hf isotope evidence from juvenile rocks through time. Geochimica et Cosmochimica Acta 63, 533–556.

Vezinet, A., Pearson, D.G., Thomassot, E., 2021. Effects of contamination on whole-rock isochrons in ancient rocks: a numerical modelling approach. Lithos 386-387, 106040.

Vezinet, A., Pearson, D.G., Thomassot, E., Stern, R.A., Sarkar, C., Luo, Y., Fisher, C.M., 2018. Hydrothermally-altered mafic crust as source for early Earth TTG: Pb/Hf/O isotope and trace element evidence in zircon from TTG of the Eoarchean Saglek Block, N. Labrador. Earth and Planetary Science Letters 503, 95-107.

Vezinet, A., Thomassot, E., Pearson, D.G., Stern, R.A., Luo, Y., Sarkar, C., 2019. Extreme $\delta^{18}O$ signatures in zircon from the Saglek Block (North Atlantic Craton) document reworking of mature supracrustal rocks as early as 3.5 Ga. Geology 47, 605-608.

Wacey, D., Kilburn, M.R., Saunders, M., Cliff, J. and Brasier, M.D., 2011. Microfossils of sulphur-metabolizing cells in 3.4-billion-year-old rocks of Western Australia. Nature Geoscience 4, 698-702.

Wacey, D., Noffke, N., Cliff, J., Barley, M.E., Farquhar, J., 2015. Micro-scale quadruple sulfur isotope analysis of pyrite from the ~3480Ma Dresser Formation: New insights into sulfur cycling on the early Earth. Precambrian Research 258, 24-35.

Wan, Y., Dong, C., Xie, H., Wilde, S.A., Liu, S., Li, P., Ma, M., Li, Y., Wang, Y., Wang, K. and Liu, D., 2023. Hadean to early Mesoarchean rocks and zircons in the North China Craton: A review. Earth-Science Reviews 243, 104489.

Wang, Z., Becker, H., Gawronski, T., 2013. Partial re-equilibration of highly siderophile elements and the chalcogens in the mantle: a case study on the Baldissero and Balmuccia peridotite massifs (Ivrea Zone, Italian Alps). Geochimica et Cosmochimica Acta 108, 21–44.

Waterton, P., Guotana, J.M., Nishio, I., Morishita, T., Tani, K., Woodland, S., Legros, H., Pearson, D.G. and Szilas, K., 2022. No mantle residues in the Isua Supracrustal Belt. Earth and Planetary Science Letters 579, 117348.

Webb, A.A.G., Müller, T., Zuo, J., Haproff, P.J. and Ramírez-Salazar, A., 2020. A non–plate tectonic model for the Eoarchean Isua supracrustal belt. Lithosphere 12, 166-179.

Whitehouse, M.J., 2013. Multiple Sulfur Isotope Determination by SIMS: Evaluation of Reference Sulfides for Δ^{33}S with Observations and a Case Study on the Determination of Δ^{36}S. Geostandards and Geoanalytical Research 37, 19-33.

Whitehouse, M.J., Kamber, B.S., Fedo, C.M. and Lepland, A., 2005. Integrated Pb- and S-isotope investigation of sulphide minerals from the early Archaean of southwest Greenland. Chemical Geology 222, 112-131.

Whitehouse, M.J., Nemchin, A.A. and Pidgeon, R.T., 2017. What can Hadean detrital zircon really tell us? A critical evaluation of their geochronology with implications for the interpretation of oxygen and hafnium isotopes. Gondwana Research 51, 78-91.

Whitney, D.L. and Evans, B.W., 2010. Abbreviations for names of rock-forming minerals. American Mineralogist 95, 185-187.

Wiechert, U., Halliday, A.N., Lee, D.C., Snyder, G.A., Taylor, L.A. and Rumble, D., 2001. Oxygen Isotopes and the Moon-Forming Giant Impact. Science 294, 345-348.

Wilde, S.A., Valley, J.W., Peck, W.H. and Graham, C.M., 2001. Evidence from detrital zircons for the existence of continental crust and oceans on the Earth 4.4 Gyr ago. Nature 409, 175-178.

Windley, B.F., Kusky, T. and Polat, A., 2021. Onset of plate tectonics by the Eoarchean. Precambrian Research 352, 105980.

Woodhead, J.D. and Hergt, J.M., 2000. Pb-Isotope Analyses of USGS Reference Materials. Geostandards Newsletter 24, 33-38.

Zerkle, A.L., Claire, M.W., Domagal-Goldman, S.D., Farquhar, J., Poulton, S.W., 2012. A bistable organic-rich atmosphere on the Neoarchaean Earth. Nature Geoscience 5, 359-363.

Zuo, A.J., Webb, A., Chin, E.J., Ackerman, L., Harvey, J., Haproff, P.J., Mueller, T., Wang, Q., Hickman, A.H., Sorger, D., Ramirez-Salazar, A., 2022. Early earth's phaneritic ultramafic rocks: Mantle slices or crustal cumulates? Geochemistry, Geophysics, Geosystems 23, e2022GC010519.

jonathanaaronlewis@gmail.com

Jonathan A. Lewis

Geoscientist and Ph.D. candidate

Academic Background

Freie Universität Berlin, Berlin, Germany March 2019-February 2024
PhD in earth sciences
Thesis: An investigation into Eoarchean geodynamics via multiple sulfur isotopes

Washington University in St. Louis, St. Louis, MO, USA
Degree May 2012
MA in earth and planetary science
Thesis: Sub-kilometer scale environmental variability during the mid-Holocene on Sai Island, Sudan

Salem State University, Salem, MA, USA
Degree May 2010
BS in geological sciences, Summa Cum Laude
Thesis: A multi-proxy study of a five meter sediment core from Sluice Pond, Lynn, MA

Brandeis University, Waltham, MA, USA
Degree May 2007
BA in classical archaeology and ancient history, economics, Cum Laude, Dean’s Award, Honor Grant

Profile

Broadly trained geoscientist with a strong focus on light stable isotope geochemistry. Experienced in field and laboratory methods applicable to earth science and archaeology including work with C, O, and S isotopes. Proven record of scientific publications in internationally recognized journals as well as presentations at national and international conferences in Europe and the United States. Native English speaker, German language skill at an A2 level with intent to learn more.

Experience

Research Assistant (Wissenschaftlicher Mitarbeiter) / Guest Researcher March 2019-present
Freie Universität Berlin, Berlin, Germany

- Doctoral research focused on elucidating Eoarchean geodynamic processes via isotope geochemistry
- Wrote and edited scientific papers in collaboration with colleagues, including two published first-author papers
- Extracted sulfur from rock samples for isotopic analysis via wet chemical methods
- Analyzed rock samples for multiple sulfur and lead isotope compositions via IRMS and SIMS
- Performed petrographic analysis on rock samples via optical and electron microscopy
- Performed compositional analysis on sulfides and other minerals via electron microprobe analysis

Field Technician / Geologist March 2018-August 2018
OHI Engineering/Aerotek, Mansfield, MA, USA

- Conducted Phase I environmental site assessments and subsurface investigations
- Provided contractor oversight to ensure correct implementation of a release abatement measure
- Collected environmental groundwater and soil samples

Geotechnical Technician II April 2017-February 2018
Thielsch Engineering, Cranston, RI, USA

- Conducted geotechnical tests on soil samples
- Conducted unconfined compression and elastic modulus tests on rock samples
- Collected environmental air, water, and soil samples and performed air monitoring in the field
- Oversaw geotechnical subsurface borings, collected associated samples, and generated boring logs
- Wrote environmental monitoring reports and geotechnical SOPs based on ASTM standards

Environmental Scientist / Geologist I November 2014-April 2017

Arcadis, Midland, TX and Warwick, RI, USA

- Prepared various reports, permit applications, health and safety plans, and job safety analyses
- Performed Phase I environmental site assessments and Phase II subsurface investigations
- Collected groundwater, surface water, air, and soil samples for various analyses

Surface Mud Logger September 2013-November 2014

Weatherford Surface Logging Systems, Midland, TX, USA

- Analyzed gas from drilling operations, determining composition and ensuring safe total gas concentrations
- Collected and analyzed rock cuttings to determine lithology and the presence of hydrocarbons
- Maintained contact with senior geologist and rig personnel, preparing multiple reports per day

Research Assistant August 2012-August 2013

Southern Illinois University, Carbondale, IL, USA

- Collected and analyzed water and precipitate samples from an experimental acid mine drainage remediation system and a nearby stream

Research / Teaching Assistant September 2010-August 2012

Washington University in St. Louis, St. Louis, MO, USA

- Sampled and conducted granulometric, petrographic, and isotopic ($\delta^{18}O$ and $\delta^{13}C$) analysis on paleosols
- Fieldwork included support for two archaeological field seasons in Sudan and one in Mongolia
- Published work included maps of isotope compositions made with GIS
- Developed and presented lab lectures and provided academic support for students outside of class

Tutor September 2008-May 2010

Salem State University Math Lab and Student Academic Support Services, Salem, MA, USA

- Provided tutoring for students in geology, math, academic English writing, and other subjects

Peer-Reviewed Journal Publications

- **Lewis, J.A.,** Hoffmann, J.E., Schwarzenbach, E.M., Strauss, H., Li, C., Münker, C. and Rosing, M.T. (2023) Sulfur isotope evidence from peridotite enclaves in southern West Greenland for recycling of surface material into Eoarchean depleted mantle domains. Chemical Geology 633, 121568. DOI: https://doi.org/10.1016/j.chemgeo.2023.121568

- **Lewis, J.A.,** Hoffmann, J.E., Schwarzenbach, E.M., Strauss, H., Liesegang, M. and Rosing, M.T. (2021) Sulfur isotope evidence for surface-derived sulfur in Eoarchean TTGs. Earth and Planetary Science Letters 576, 117218. DOI: https://doi.org/10.1016/j.epsl.2021.117218

- Adelsberger, K.A., **Lewis, J.,** Dodd, J.P., Hill, D., Smith, J.R. and Garcea, E.A.A. (2020) Mid-Holocene environmental change and human occupation at Sai Island, Northern Sudan. Geoarchaeology 35, 803-818. DOI: https://doi.org/10.1002/gea.21812

- Hubeny, J.B., McCarthy, F.M.G., **Lewis, J.,** Drljepan, M., Morissette, C., King, J.W., Cantwell, M., Hudson, N.M. and Crispo, M.L. (2015) The paleohydrology of Sluice Pond, NE Massachusetts, and its regional significance. Journal of Paleolimnology 53, 271-287. DOI: https://doi.org/10.1007/s10933-015-9824-8

Invited Talks

- Insights into Eoarchean crustal recycling via multiple sulfur isotope analysis of igneous lithologies from southern West Greenland (2023 State Key Laboratory of Isotope Geochemistry, Guangzhou Institute of Geochemistry, Chinese Academy of Sciences), online oral presentation by **J. Lewis**

Conference Presentations

- In-situ analysis of lead and multiple sulfur isotopes in southern West Greenland peridotite sulfide grains reveal evidence for Eoarchean crustal recycling (2023 GeoBerlin BGR and DGGV annual meeting, Berlin, Germany), oral presentation by **J.A. Lewis,** E.M. Schwarzenbach, M. Liesegang, J. van de Löcht, A. Schwarz, H. Strauss, C. Münker, M.T. Rosing, M.J. Whitehouse, H. Jeon, J.E. Hoffmann

- In-situ lead and multiple sulfur isotope analyses of sulfides in Eoarchean peridotites provide evidence for early crustal recycling (2023 Goldschmidt annual meeting, Lyon, France), poster presentation by **J.A. Lewis,** E.M. Schwarzenbach, M. Liesegang, J. van de Löcht, A. Schwarz, H. Strauss, C. Münker, M.T. Rosing, M.J. Whitehouse, H. Jeon, J.E. Hoffmann

- In-situ sulfur and lead isotope measurements confirm Eoarchean origin of surface-derived sulfur in southern West Greenland peridotites (2023 SPP 1833 General meeting, Köln, Germany), poster presentation by **J.A. Lewis,** E.M. Schwarzenbach, M. Liesegang, J. van de Löcht, A. Schwarz, H. Strauss, C. Münker, M.T. Rosing, M.J. Whitehouse, H. Jeon, J.E. Hoffmann

- In-situ sulfur and lead isotope evidence for Eoarchean crustal recycling in southern West Greenland peridotites (2022 GeoMin Köln DMG and DGGV annual meeting, Köln, Germany), oral presentation by **J.A. Lewis,** E.M. Schwarzenbach, M. Liesegang, J. van de Löcht, A. Schwarz, H. Strauss, C. Münker, M.T. Rosing, M.J. Whitehouse, H. Jeon, J.E. Hoffmann

- Contrasting messages from sulfur and oxygen isotopes on the origin of Eoarchean crust (2022 GeoMin Köln DMG and DGGV annual meeting, Köln, Germany), oral presentation by J.E. Hoffmann, **J.A. Lewis,** E.M. Schwarzenbach, H. Strauss

- Sulfur and Hafnium Isotope evidence for Early Horizontal Tectonics in Eoarchean Peridotites (2022 European Geophysical Union annual meeting), oral presentation by **J. Lewis,** J.E. Hoffmann, E.M. Schwarzenbach, H. Strauss, C. LI, C. Münker, M.T. Rosing, DOI: https://doi.org/10.5194/egusphere-egu22-5226

- Sulfur and hafnium isotope constraints on depletion and refertilization history of Eoarchean mantle peridotites (2022 SPP 1833 annual meeting, Tübingen, Germany), oral presentation by **J. Lewis,** J.E. Hoffmann, E.M. Schwarzenbach, H. Strauss, C. LI, C. Münker, M.T. Rosing

- Evidence for surface-derived sulfur in Eoarchean TTGs from the Itsaq Gneiss Complex, SW Greenland (Goldschmidt 2021 annual meeting, Lyon, France), online oral presentation by **J.A. Lewis,** J.E. Hoffmann, E.M. Schwarzenbach, H. Strauss, H. Vrijmoed, M.T. Rosing

- Evidence for recycled surface-derived sulfur in Earth's oldest mantle peridotites from southern West Greenland (Goldschmidt 2021 annual meeting, Lyon, France), online oral presentation by J.E. Hoffmann, **J.A. Lewis,** E.M. Schwarzenbach, H. Strauss, M. Liesegang, M.T. Rosing

- Eoarchean TTGs from the Itsaq Gneiss Complex, SW Greenland host recycled, surface derive d sulfur (2021 SPP 1833 annual meeting, virtual), online presentation by **J. Lewis,** J.E. Hoffmann, E.M. Schwarzenbach, H. Strauss, M. Liesegang, M.T. Rosing

- Elucidating Eoarchean geodynamic processes by multiple sulfur isotopes (2019 SPP 1833 General meeting, Köln, Germany), poster presentation by **J. Lewis,** J. E. Hoffmann, E.M. Schwarzenbach, H. Strauss, M.J. Whitehouse, C. Münker, M.T. Rosing, A. Schwarz

- Geoarchaeological Evidence of Mid- to Late-Holocene Environments at Sai Island, Sudan (2017 GSA Annual Meeting, Seattle, Washington, USA), poster presentation by K. A. Adelsberger, **J. Lewis,** D. N. Hill, J.P. Dodd, J. R. Smith, E.A.A. Garcea, DOI: https://doi.org/10.1130/abs/2017AM-299092

- Paleoenvironmental implications of the isotope geochemistry and granulometry of quaternary alluvial sediments and associated plaeosols from Sai Island, Sudan (2011 GSA Annual Meeting, Minneapolis, MN, USA), poster presentation by **J. Lewis,** J. Smith, E.A.A. Garcea

- Holocene Stratigraphy and Climate History of Sluice Pond, MA (2011 GSA Annual Meeting, Minneapolis, MN, USA), poster presentation by J. B. Hubeny, F.M.G. McCarthy, **J. Lewis,** M. Cantwell, C. Morissette, M.L. Crispo, R. Zanatta

- A multi-proxy study of a five meter sediment core from Sluice Pond, Lynn, MA: Comparison of lithostratigraphic and seismic records (2010 GSA joint Northeastern/Southeastern meeting, Baltimore, MD, USA; also presented at the 2010 North Shore chapter Sigma Xi Research Symposium, Salem, MA, USA), poster presentation by **J. Lewis**, J.B. Hubeny

Awards and Honors

- Geological Society of America Outstanding Undergraduate Student Poster Award (2010 GSA Northeastern/Southeastern meeting)

Memberships

- European Association of Geochemistry
- Deutsche Mineralogische Gesellschaft